Summer 8-19-2022

Microstructural Analysis for Dynamic Pulverization and Asymmetric Damage at the Base of Seismogenic Strike-slip Faults

Bo Ra Song
University of Maine, bora.song@maine.edu

MICROSTRUCTURAL ANALYSIS FOR DYNAMIC PULVERIZATION AND ASYMMETRIC DAMAGE AT THE BASE OF SEISMOGENIC STRIKE-SLIP FAULTS

By

Bo Ra Song

B.S. Korea University, South Korea, 1998

M.S. Korea University, South Korea, 2005

A DISSERTATION

Submitted in Partial Fulfillment of the

Requirements for the Degree of

Doctor of Philosophy

(in Earth and Climate Sciences)

The Graduate School

The University of Maine

August 2022

Advisory Committee:

Scott E. Johnson, Professor of Earth and Climate Sciences, Co-Advisor

Peter O. Koons, Professor of Earth and Climate Sciences, Co-Advisor

Christopher C. Gerbi, Professor of Earth and Climate Sciences

Martin G. Yates, Laboratory Manager and Instructor of Earth and Climate Sciences

Senthil S. Vel, Arthur O. Willey Professor of Mechanical Engineering

Phaedra Upton, Geodynamics Team Leader of GNS Science, New Zealand

MICROSTRUCTURAL ANALYSIS FOR DYNAMIC PULVERIZATION AND ASYMMETRIC DAMAGE AT THE BASE OF SEISMOGENIC STRIKE-SLIP FAULTS

By Bo Ra Song

Dissertation Advisors: Dr. Scott E. Johnson and Dr. Peter O. Koons

An Abstract of the Dissertation Presented
in Partial Fulfillment of the Requirements for the
Degree of Doctor of Philosophy
(in Earth and Climate Sciences)
August 2022

Although the mechanics of continental, seismogenic strike-slip faults have been primarily studied around active faults near Earth's surface, large earthquakes on these faults commonly extend to depths between 10 and 20 km. At the base of seismogenic strike-slip faults, interaction and feedback between coseismic brittle fracturing and post- and interseismic viscous flow affect transient and long-term changes in stress cycling, fluid and heat transport, fault strength, and associated strain localization and deformation mechanisms. A primary goal of my dissertation is to explore the deeper structures of damage zones near the base of the seismogenic zone and to better understand the influence of the damaged rocks on rupture dynamics, by examining microstructures of exhumed fault rocks. My study area, the Sandhill Corner shear zone that is the longest strand of the Paleozoic Norumbega fault system in Maine, USA, represents large-displacement, seismogenic strike-slip faults at frictional-to-viscous transition depths (corresponding to temperatures of ~400–500 °C). The shear zone contains mutually overprinting pseudotachylyte and mylonite, and juxtaposes quartzofeldspathic mylonites and mica-rich schists.

I analyzed fractured and fragmented garnet grains using particle size distributions, microfracture patterns, and electron backscatter diffraction fabrics. Microstructural studies of fragmented garnets reveal asymmetric distribution of dynamic pulverization with a width of ~70 m in the Sandhill Corner shear zone, and these results imply that the same damage processes observed around active seismogenic strike-slip

faults operate at the base of the seismogenic zone. Garnet microstructures formed during earthquake cycles at the frictional-viscous transition can also provide evidence for dynamic pulverization even though the particle size distribution is modified by quasi-static fragmentation during post- and interseismic shearing.

Elastic and seismic properties of the quartzofeldspathic rock and the mica-rich schist are quantified using the Thermo-Elastic and Seismic Analysis (TESA) numerical toolbox. The results illustrate how elastic contrast across bimaterial faults separating two different anisotropic materials affects preferred rupture propagation and asymmetric damage distribution. Strong anisotropy occurs in fault zones where preferentially aligned phyllosilicate minerals are a major component of the modal mineralogy. My findings suggest that the orientation and proportion of preferentially aligned phyllosilicates, or other highly anisotropic minerals, should be considered when investigating fault ruptures in anisotropic rocks.

ACKNOWLEDGMENTS

I would like to acknowledge my gratitude for generous financial support from the National Science Foundation, and for the persistent efforts of my advisor Scott Johnson, whose research grants made this possible. Additional supports were provided by the University of Maine, through a Michael J. Eckardt Dissertation Fellowship, a Summer Dissertation Fellowship, and numerous Teaching Assistantships.

This dissertation has benefitted immensely from the help and support of many people. Specific acknowledgements associated with published works are noted at the end of each related chapter. Here, I would like to acknowledge those who have made my journey fruitful and rewarding.

My first and foremost thanks goes to my co-advisors Scott Johnson and Peter Koons who inspired and encouraged me not only academically, but personally as well. Scott offered unwavering support while allowing me complete freedom to forge my own path and pursue my interests and ideas. He has taught me so much during my time here, including interpreting geology in the field, observing microstructures together, shaping my understanding of the physics of the natural world, as well as making sure my writing was clear, coherent, and accurate. Thank you, Scott, for being not just a Ph.D. advisor, but a supportive friend as I faced both professional and personal challenges. Thank you for being the "best man" when Won Joon and I got married, and thank you for providing space your own backyard garden for us to plant our choice of greens, and for sharing many healthy foods including berries, peaches, smoked sprats, elk osso, and your home-made Kimchi. Peter, through his own excellence in research and teaching, has set an example to all students in his research group and classroom, not least myself. He challenges yet encourages students to find creative ways to solve problems with his enthusiasm, scientific rigor, hard work and enjoyment of the process. Thank you, Peter, for introducing me to the numerical modeling world and helping me frame my research in a way that is relevant to the big questions in geology/geodynamics. It was very impressive to hear about the life and missionary work of your grandfather Edwin Wade Koons in South Korea. He was one of the pioneer missionaries who made an impact on shaping modern higher education in South Korea. This may sound silly, but I owe a debt of gratitude to your family.

I would like to thank Christopher Gerbi, Martin Yates, Senthil Vel, and Phaedra Upton for serving on my advisory committee. I thank Chris for his creative approach and important questions, which helped me think critically and sharpen my research ideas. Marty taught me the essential skill of scanning electron microscope analysis, and his advice helped me make my research goals realistic and achievable. Many thanks go to Senthil for being a tremendous resource of knowledge and expertise in mathematical analysis, and for bringing a unique and crucial perspective to my work. I am indebted to Phaedra for allowing me to use her numerical codes on strain partitioning simulations, and for always being so approachable and available for lengthy discussions. It is a privilege to have each of these insightful minds focused on my work.

Although my name is the only one appearing on this dissertation, it would not have been feasible without the help and mentorship of many scientists working together. I would like to offer special thanks to Edward Grew and Alicia (Cici) Cruz-Uribe for insightful discussions and research advice during group meetings. I would also like to thank current and previous research students of the Solid Earth and Geodynamics groups in the School of Earth and Climate Sciences, including but not limited to: Erik Anderson, Cemil Arkula, Steven Bernsen, Annie Boucher, Clara Deck, He (Jackie) Feng, Maura Foley, Brett Gerard, Natalie Harmon, Laura Hartman, James Hodge, Kate Hruby, Michael McMormick, Stephanie Mills, Bipush Osti, Tyler Pollock, Nicholas Richmond, Samuel Roy, Deborah Shulman, Won Joon Song, Steven Spreitzer, Jesse Walters, Lauren Wheeler, and Nicholas Whiteman for scientific discussions, your friendship, and encouragement. I also thank Nancy Price at SUNY Plattsburgh, and Walter Sullivan (Bill) at Colby College for providing their rock samples and thin sections.

Considering my scientific development in the years before coming to the United States, I would also like to thank my previous mentors, Youngdo Park, Jae-Young Yu, and Meehye Lee, who opened my eyes to Earth and Climate Sciences, and guided me toward the right academic track when I needed it.

I would not have survived in my graduate life had I not taken time for relaxation and the appreciation of beauty with my wonderful friends. Hence, I want to thank Hyun Kyung Bae, Yoon Kyung Cho, Violet Clark, Jung-Yoon Kim, Bethany Leavitt, Jong-Won Lee, Joon Taek Lee, Min Jeong Lee, Jin

Hee Park, and Ji-Hyun Yoon. Thank you all for providing just the right amount of distractions and keeping me sane. I'm especially grateful to Min Jeong Lee for showing me how to have fun and dream big. Special thanks to Jin Hee Park for lending a listening ear when I need it most, and enduring long conversations on the phone. Also, a very special thanks to Bethany Leavitt for spending time with me when I felt like an "alien" for taking me on nature walks, and for gardening together. I'll never forget the moment when we walked along the riverside and watched the pair of bald eagles cruising down the Penobscot river together on an ice flow.

My family back in Korea, including my parents, sister, brother, brothers-in-law, sisters-in-law, nephews and nieces, are the best support crew ever. Your constant encouragement and faith in me means more than you will ever know. Being so far away from home was tough at times and I am really looking forward to spending more time with you again sometime soon. I respectfully thank my parents Jae Man Song and Kum Ran Park for being the best parents by loving me unconditionally and supporting me in whatever I do through every step of my life.

Finally, there's my husband, Won Joon. These past years have been unpredictable and disrupted at times (particularly the last two years while quarantined at home in the midst of a global pandemic), but they have been mostly fun thanks to you. Thank you for being there for me every step of the way. I'm so grateful for your support and encouragement with all of my work, including carrying all the heavy rocks, reading through and revising my messy drafts, editing figures and tables, and cooking our daily meals. You make me smile every day and you're my rock.

TABLE OF CONTENTS

LIST OF TABLES

LIST OF FIGURES

CHAPTER 1

INTRODUCTION

1.1. Rock Damage Adjacent to Large-Displacement, Seismogenic Strike-Slip Faults in Continental Lithosphere

Seismogenic continental strike-slip fault systems are important targets for scientific study owing partly to the hazards that they present for humans, but also because they are rich sources of information about how interactions among rock rheology, kinematic boundary conditions and associated stress fields lead to long-term strain localization (Handy et al., 2007). The structure and rheology of faults change with depth as fracture and frictional sliding progressively give way to temperature- and strain-rate-dependent creep. This frictional-to-viscous transition (FVT) controls the coupling of stress and deformation between the middle and upper crust in fault zones and is closely associated with the earthquake cycle. The state of stress, rheology, and kinematic partitioning at FVT depths in active fault zones exert first-order influence on the overlying faults. For this reason, the study of fault rocks exhumed from FVT depths is essential for developing modern concepts related to faulting and active seismicity. Important as they are, our understanding of key parameters in the FVT below seismogenic faults is poor. In particular, we have a poor understanding of the dynamic states of stress that occur during rupture propagation and how the energy released during rupture is distributed in the vicinity of the rupture (Johnson et al., 2021b — Appendix C of this dissertation). We do know that some component of this energy goes into fragmentation and surface-area generation, and documenting this process forms a significant focus of my dissertation.

Large-scale faults are not simple planar surface but have a complex structure including fault core and surrounding damage zones (e.g., Chester and Logan, 1986). The fault core represents the high-strain narrow zone that accommodates most of the displacement. Fault damage zones surrounding the core consist of highly fractured and pulverized rocks. In large-displacement strike-slip faults, fault damage zones can extend to tens of meters to kilometers (e.g., Faulkner et al., 2011; Savage and Brodsky, 2011). Damage zones with significant reduction of seismic velocities (e.g., Walsh, 1965; Lockner et al., 1977; Cochran et

al., 2009) can trap seismic waves (Li et al., 1994) and thus alter dynamic fault stresses during earthquakes, which affect rupture mode, rupture characteristics (such as pulse-like rupture and supershear rupture), and near-field ground motion. (e.g., Harris and Day, 1997; Spudich and Olsen, 2001; Huang and Ampuero, 2011; Huang et al., 2014). Therefore, information about the structures along and across faults is essential for our understanding of the fault dynamics and future rupture scenarios.

Large-displacement strike-slip faults commonly juxtapose materials having different elastic properties. These so-called bimaterial faults can significantly modify various aspects of fault dynamics and earthquake rupture, including stress variations, preferred direction of rupture propagation (unilateral or bilateral), and rupture speeds (sub-Rayleigh or supershear rupture) (e.g., Weertman, 1980; Ben-Zion, 2001; Ranjith and Rice, 2001; Shi and Ben-Zion, 2006). It is thus important to understand how such variations in material properties across faults influence the dynamics of earthquake rupture.

To understand complicated 3D fault structures and fault zone dynamic processes, many studies have investigated modern large-displacement strike-slip faults such as the San Andreas fault in California, and the North Anatolian fault in Türkiye (e.g., Dor et al., 2006a, 2006b, 2008; Rempe et al., 2013). However, the deeper structures of damage zones, near the base of seismogenic zone (within the FVT), and the influence of the damaged rocks on rupture dynamics are poorly known because the roots of such faults are rarely exposed at Earth's surface. In this dissertation, I present detailed studies of the Sandhill Corner shear zone, which is the largest strand of the exhumed Norumbega fault system in Maine, USA. The shear zone kinematics indicate dominantly simple shear, and mineral assemblages and microstructures indicate a deformation temperature of ~400–500 °C at the time the shear zone was seismically active. For these and other reasons, this part of the Norumbega fault system is a suitable analog for rocks near the base of the seismogenic zone in modern large-displacement strike-slip faults.

1.2. Major Research Questions

Following are questions that I aim to address through the research described in my dissertation.

1. Does strong coseismic damage occur at the base of the seismogenic zone in continental strike-slip faults? (Chapter 2)
2. What is the width of the resulting damage zones at that depth? (Chapter 2)
3. What are the microstructural characteristics of highly fractured and pulverized rocks in coseismic damage zones at FVT depths? (Chapter 3)
4. How do the microstructural characteristics compare to those formed at the surface along continental strike-slip faults? (Chapter 3)
5. Can fragment size statistics of fragmented minerals like garnet be used to distinguish between dynamic and quasi-static damage? (Chapter 3)
6. What is the best way to describe the elastic contrast of anisotropic rocks across a bimaterial fault that allows comparison with theory and numerical experiments aimed at elastically isotropic bimaterial interfaces? (Chapter 4)
7. How does asymmetric damage around an anisotropic bimaterial fault relate to elastic contrast and rupture directivity? (Chapter 4)

1.3. Structure of This Dissertation

My dissertation is focused on microstructural observations and numerical analysis of rocks from the Sandhill Corner shear zone in an attempt to: (1) investigate fragmented garnet grains for estimating the extent and type (dynamic versus quasi-static) of damage zone surrounding the shear zone, (2) characterize microstructures of the fragmented garnet grains to evaluate whether particle size distributions and microfracture intensity can still be used to fingerprint dynamic fragmentation after fragmented grains are highly displaced and rotated during postseismic tectonic shearing, and (3) quantitatively evaluate the elastic/seismic properties of rocks separated by the shear zone to explore the relationship among elastic contrast, rupture propagation direction, and damage asymmetry.

For my first topic (Chapter 2), I documented fragment size distributions of garnet using image analysis based on backscattered electron (BSE) images from a scanning electron microscope. I also documented that damage zones induced by dynamic ruptures are strongly asymmetrically distributed either side of the shear zone. My results imply that the same damage processes that occur along seismogenic strike-slip faults in the uppermost continental crust also operate near the base of the seismogenic zone (B. R. Song et al., 2020).

For my second topic (Chapter 3), I compared garnet grains deformed under two different conditions: (1) coseismic fragmentation followed by post- and interseismic shearing and (2) quasi-static shearing. To evaluate the usefulness of electron backscatter diffraction (EBSD)-based analysis on rock fragmentation, I used both BSE-image- and EBSD-based analyses to estimate particle size distribution. Differences in microfracture patterns (intensity and orientation) and particle size distributions between two different rocks (one from the Sandhill Corner shear zone and another from a regionally deformed terrane in California) were used to discuss the possible effects of comminution associated with postseismic or regional tectonic flow on these quantifiable parameters.

For my third topic (Chapter 4), I calculated elastic properties and seismic wave speeds of the two elastically anisotropic rocks across the Sandhill Corner shear zone and illustrated how elastic contrast in large-displacement bimaterial faults affects preferred rupture directivity and asymmetric damage distribution (B. R. Song et al., 2022).

1.4. Research Contributions

One of the main contributions of this dissertation is the development (and validation) of robust and generalized methodologies for the microstructural analysis of dynamically fragmented mineral grains. The established methods provide useful ways to study complex microstructures induced by shock penetration and dynamic fragmentation of various types of brittle materials (such as ceramics, glasses, concretes and rocks) in a wide range of areas including fault gouge formation and off-fault rock damage in geology,

magma explosion in volcanology, impacts and collisions of asteroid/meteorites in planetary and space science, rock explosions in mining industries, and impact of hard projectiles used in military applications.

I have also made advances in understanding asymmetric off-fault damage and earthquake rupture directivity in elastically anisotropic rocks. Microstructures of natural polycrystalline rocks (quartzofeldspathic rock and mica schist) and crystal preferred orientations of minerals were obtained through electron backscatter diffraction fabrics (EBSD) technique, and bulk (homogenized) stiffness tensors and seismic wave velocities derived from EBSD maps were calculated using the Thermo-Elastic and Seismic Analysis (TESA) numerical toolbox. This work offers a different perspective on rupture dynamics and bimaterial effects compared to existing work that focusses on elastically isotropic materials and opens new avenues of application for seismic anisotropy of natural polycrystalline rocks.

CHAPTER 2

COSEISMIC DAMAGE RUNS DEEP IN CONTINENTAL STRIKE-SLIP FAULTS[1]

2.1. Chapter Abstract

Coseismic off-fault damage and pulverization significantly influence the mechanical and transport properties, and in turn the rupture dynamics, of faults. Although field-based, laboratory, and numerical studies help elucidate the structure of damage zones adjacent to modern strike-slip faults, the vertical extent of these zones remains an open question. To address this question, we analyzed particle size distribution and microfracture density of fragmented garnets from the Sandhill Corner shear zone, a strand of an ancient, seismogenic, strike-slip fault system exhumed from frictional-to-viscous transition depths (400–500 °C). The shear zone has mutually overprinting pseudotachylyte and mylonite, and juxtaposes quartzofeldspathic and schist units. The inner parts of the quartzofeldspathic and schist units (~63 m and ~5 m wide from the lithologic contact, respectively) have two-dimensional *D*-values ≥ 1.5, which indicates dynamic fragmentation during rupture propagation. Similar to the particle size distribution analysis, microfracture density data from the garnets show progressive but asymmetric increase toward the core in each unit. Our results suggest that coseismic damage extends down to the base of the seismogenic zone in mature strike-slip faults, and the asymmetric distribution of damage may indicate preferred rupture directivity as proposed for some modern strike-slip faults.

2.2. Chapter Introduction

Highly fractured and pulverized rocks are common in damage zones adjacent to active or recently active seismogenic strike-slip faults (e.g., Rockwell et al., 2009; Mitchell et al., 2011; Wechsler et al., 2011; Morton et al., 2012; Rempe et al., 2013; Muto et al., 2015). Field-based geological data, geophysical data, laboratory experiments, and numerical simulations have helped to elucidate the structure and spatial extent

[1] The content of this chapter has been published in: Song, B.R, Johnson, S.E., Song, W.J., Gerbi, C.C., Yates, M.G., 2020, Earth and Planetary Science Letters, 539, 116226, https://doi.org/10.1016/j.epsl.2020.116226.

of coseismic damage zones (e.g., Cochran et al., 2009; Yuan et al., 2011; Sagy and Korngreen, 2012; Xu and Ben-Zion, 2017). However, the maximum depth to which this dynamic damage occurs, and the width of the resulting damage zones at depth, remain open questions. Based on evidence from field observations, Aben et al. (2017a) suggested that pulverization can extend to a depth of ~10 km or less. On the other hand, recent analysis of past earthquakes in southern California estimated the production of rock damage at a depth of 10–15 km (Ben-Zion and Zaliapin, 2019), and Incel et al. (2019) found experimental evidence for pulverization of garnet at upper mantle depths. Studies from exhumed seismogenic shear zones also documented the occurrence of pulverization at middle and lower crustal depths in thrust (e.g., Trepmann and Stöckhert, 2002; Jamtveit et al., 2019), normal (e.g., Soda and Okudaira, 2018), and strike-slip fault systems (e.g., Sullivan and Peterman, 2017). However, there has not been a systematic study of the lateral extent of coseismic rock damage at the base of mature strike-slip faults.

Damage zones significantly change the mechanical properties of rocks and reduce seismic velocities (e.g., Walsh, 1965; Lockner et al., 1977; Cochran et al., 2009). Seismic waves trapped in low velocity damage zones can produce complex pattern of slip and rupture propagation such as oscillations of stick-slip behavior, short rise-time pulse-like rupture, and supershear rupture, as well as amplifying near-fault ground motion (e.g., Harris and Day, 1997; Spudich and Olsen, 2001; Huang et al., 2014). Therefore, the width and depth extent of damage zones is fundamentally important for assessing seismic hazard. Damage zones at depth also influence transient and long-term changes in fluid flow (e.g., Mitchell and Faulkner, 2012), heat transport (e.g., Morton et al., 2012), and overall fault rock rheology (e.g., Handy et al., 2007).

This paper provides measurements of particle size distribution (PSD) and fracture density for fragmented garnets across an ancient seismogenic strike-slip fault/shear zone exhumed from depths corresponding to temperatures of 400–500 °C (~13–17 km if the geothermal gradient was 30 °C/km), and we use these data to define the lateral extent of high-energy dynamic deformation. Several studies inferred damage related to the seismogenic cycle at depth based on deformation microstructure in quartz (e.g., Trepmann et al., 2007; Price et al., 2016). However, quartz at these temperatures deforms by both brittle

and viscous processes that overprint one another during co-, post- and interseismic cycles, and the mutually overprinting deformation mechanisms can obscure the record of brittle coseismic damage. Garnet, in contrast, does not deform viscously at such low temperatures, and so can preserve coseismic microfractures in the deeper reaches of the seismogenic zone (e.g., Jamtveit et al., 2019). Thus, PSD and fracture density of garnet across the fault/shear zone may provide convincing evidence for coseismic damage and pulverization, and allow characterization of the spatial gradient and extent of the damage as a function of distance from the shear zone core. We also calculated fabric intensity (using M-index; Skemer et al., 2005) of fragmented garnets to obtain information about their post-fragmentation rotation caused by viscous flow of the surrounding matrix during post- and interseismic cycles.

The microstructures of fragmented garnet have been used to infer coseismic damage at frictional-to-viscous transition (FVT) depths (at temperatures of ~300–350 °C; Trepmann and Stöckhert, 2002) and in the deeper crust (corresponding to temperatures of 650–700 °C; Jamtveit et al., 2019). Feldspar fragmentation has also been reported at FVT depths (>400 °C; Sullivan and Peterman, 2017) and in the deeper crust (~600–750 °C; Soda and Okudaira, 2018). However, most of these studies did not present PSD analysis, which has been widely used to infer high-energy dynamic processes in the brittle upper crust (e.g., Rockwell et al., 2009; Wechsler et al., 2011; Buhl et al., 2013; Hossain and Kruhl, 2015; Muto et al., 2015). Fracturing of brittle minerals (e.g., garnet) hosted in a ductile matrix is not uncommon in foliated metamorphic rocks (e.g., Ji et al., 1997b), and can be caused by quasi-static deformation processes. However, at dynamic stresses with increasing energy, the relative abundance of smaller fragments increases, while the relative abundance of larger fragments decreases (e.g., Muto et al., 2015 and references therein). Thus, the PSD resulting from dynamic fragmentation is distinct from that resulting from quasi-static processes, and therefore a slope in a cumulative log–log plot of PSD (see Section 2.4) can be used to infer the process of fragmentation. Soda and Okudaira (2018) used PSDs of fine-grained feldspar, but the study of fragmented feldspar is more challenging because its fracturing can be controlled by cleavage, possibly leading to significant directional anisotropy in the microfractures. Jamtveit et al. (2019) analyzed PSDs of

fragmented garnets around pseudotachylyte veins and documented cm-wide damage zones. Here, we describe garnet fragmentation using PSD analysis at the base of a mature strike-slip fault (the Sandhill Corner shear zone) in an attempt to define the spatial extent of off-fault damage and pulverization.

2.3. The Sandhill Corner Shear Zone (SCSZ)

The northeast-trending SCSZ is the longest continuous strand of the Norumbega fault system, which is a Paleozoic, crustal-scale, large-displacement, right-lateral strike-slip fault system in the northern Appalachians, USA (Figure 2.1). A kinematic vorticity number of 0.97 in the SCSZ was reported by Johnson et al. (2009), indicating approximately strike-slip flow (subsimple shear). The ~230 m-wide shear zone consists of a quartzofeldspathic (QF) unit (protomylonite to mylonite) and a sheared schist unit. The shear zone core is a ~5 m-wide zone of ultramylonite/phyllonite rock, containing abundant deformed and undeformed pseudotachylyte veins (locally >50 % of rock volume), and coincident with the lithologic contact between the QF and schist units (Figures 2.2a and 2.2b; Price et al., 2012). The SCSZ, especially within the immediate vicinity of the core, preserves evidence for the mutual overprinting of pseudotachylyte and mylonite (Price et al., 2012), which reflects coeval frictional and viscous deformation during seismogenic cycles (e.g., Handy et al., 2007). Based on quartz (dislocation creep and subgrain rotation recrystallization) and feldspar (fracturing) deformation, Price et al. (2016) estimated that mylonitic deformation, overprinting previous higher-temperature microstructures outside the shear zone, occurred at temperatures of 400–500 °C. Plagioclase in and near the core displays multiple generations of microfractures and fragmentation down to submicron scale with little or no internal strain (Figures 2.2c, 2.2d and 2.2e). Garnet is fragmented in various styles: intact, split into several pieces, and partially and pervasively fractured. Some fragmented garnets within and near the core underwent moderate to extreme post-fragmentation shearing and stretching, leading to aspect ratios of the fragment mass exceeding 8 (e.g., sample BB16 in Figure 2.3).

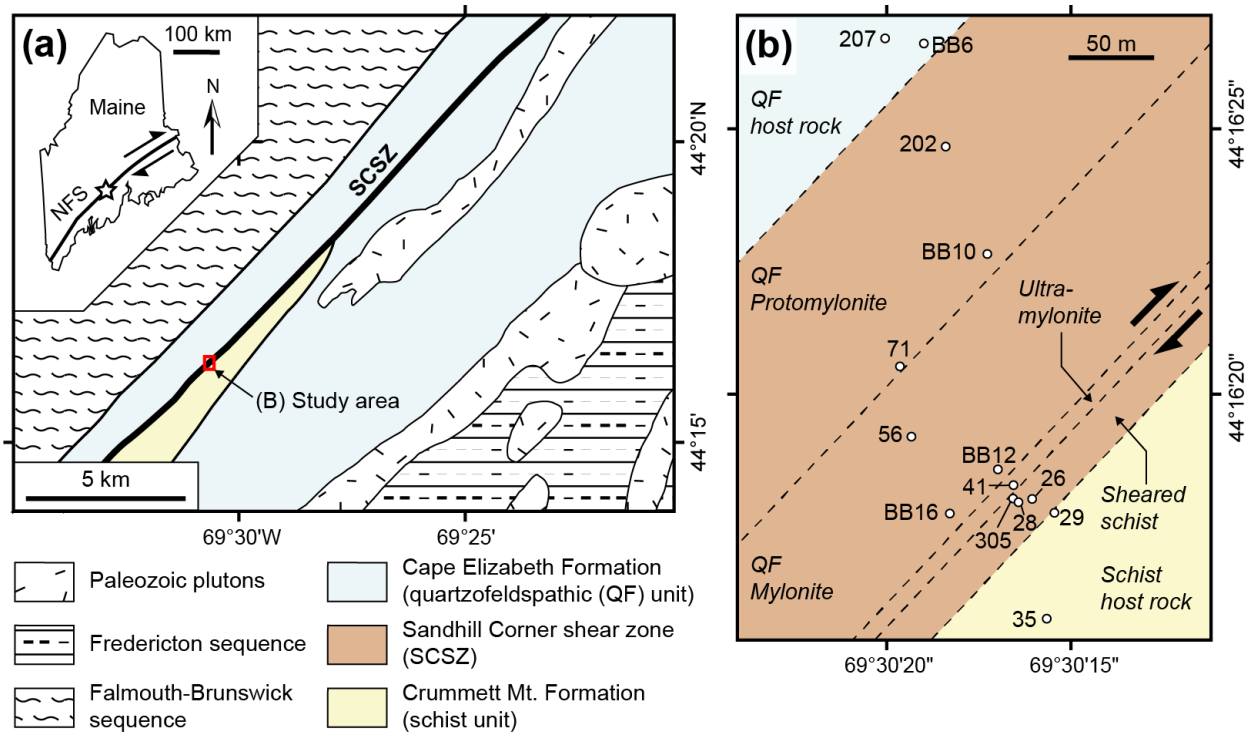

Figure 2.1 Geologic maps of the Sandhill Corner shear zone (SCSZ) in the Norumbega fault system (NFS). Modified from Price et al. (2016). (a) Regional geologic setting of the study area. The SCSZ is located in the central part of the NFS (denoted by a star in the inset map of Maine, USA). The red box indicates the study area. (b) Study area and sample locations. The core of the shear zone (ultramylonite) is the lithologic contact between quartzofeldspathic (QF) and schist units. White dots correspond to sample locations, and paired arrows indicate shear sense.

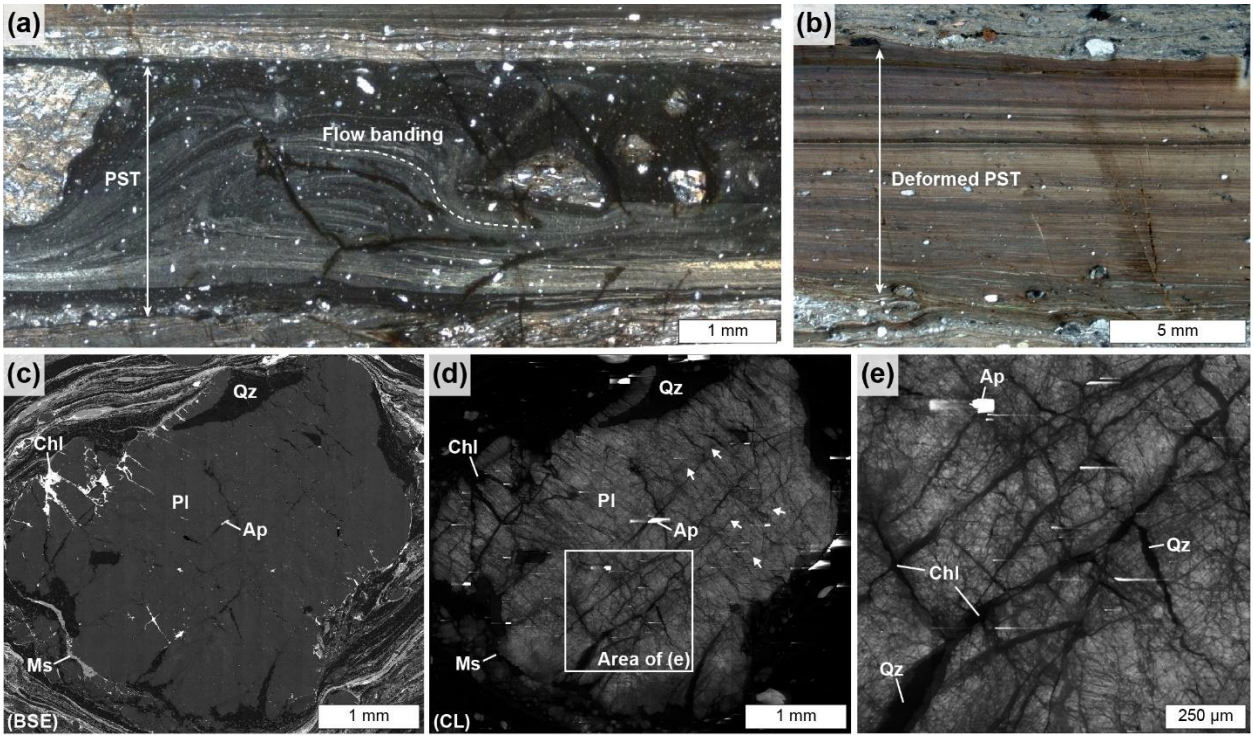

Figure 2.2 Rock microstructures in or near the shear zone core. (a) Photomicrograph (cross-polarized light) of undeformed pseudotachylytes (PST). The undeformed PST contains flow banding (dashed curve) that shows melt flow structure. (b) Photomicrograph (cross-polarized light) of deformed PST. Internal layers of the deformed PST are generally concordant with the external mylonitic foliation of the shear zone. (c) Backscattered electron (BSE) image of shattered plagioclase in the QF mylonite near the shear zone core. Microfractures are partly filled with quartz, chlorite and apatite. (d) Cathodoluminescence (CL) image of (c). Healed microfracture networks appear as dark CL bands (arrows). (e) CL image of area outlined in (d) showing extreme fragmentation. Micron and submicron-sized fragments are observed. Mineral abbreviations are: Ap = apatite, Chl = chlorite, Ms = Muscovite, Pl = plagioclase, Qz = quartz.

2.4. Methods

We analyzed 15 thin-sections of garnet-bearing rock samples across the SCSZ (Figure 2.1b). The rock samples were cut perpendicular to the main foliation and parallel to the stretching lineation (XZ plane), except one sample (BB16-a) that was cut perpendicular to both foliation and lineation (YZ plane). All the sections were polished mechanically with 0.3 µm alumina suspension and chemically in 0.02 µm colloidal silica suspension, and then were coated with a thin layer of carbon to prevent electron charging. They were used to acquire backscattered electron (BSE) images and electron backscatter diffraction (EBSD) maps of garnet from a Tescan Vega II scanning electron microscope at the University of Maine, USA.

We measured two-dimensional PSD of fragmented garnet from BSE images using a technique similar to that reported in Keulen et al. (2007). We selected one highly fragmented garnet from each thin section and collected high-resolution BSE images (4,000× magnification) to cover the whole area of each garnet. We stitched 40 to 426 images, depending on garnet size, to create a single image. For stretched garnets with rotated fragments, we chose to analyze relatively less rotated areas that contain a wide range of fragment sizes (red boxes in Figure 2.3) to minimize the effect of post- and interseismic deformation on PSD (see Section 2.5.2). For segmented bitmap of garnet and its image analysis, we used ImageSXM (https://www.liverpool.ac.uk/~sdb/ImageSXM/) with a macro ('Lazy Erode Dilate'; https://micro.earth.unibas.ch/support/LazyMacros/) and ImageJ (https://imagej.nih.gov/ij/). During ranking filter processes through the macro, the bitmaps were manually modified to maintain the original fragment shapes by comparing with the BSE images. For example, hairline microfractures that could not be automatically identified were manually traced. For sample BB12 which showed unclear fracture lines too thin to identify in the BSE image at 4,000× magnification (especially true for fine fragments < 6 μm in that sample), additional BSE images at 10,000× magnification were collected in sub-areas containing fine fragments. Cross-sectional areas of fragments were measured in the processed bitmaps after removing fragments smaller than 20 pixel^2 (equivalent to 0.34 μm and 0.14 μm in size for magnifications of 4,000× and 10,000×, respectively). The number of analyzed fragments in each garnet ranged from ~200 to ~12,000. To restore the 'eroded' outline of each fragment during the segmentation, the pixel values equivalent to its perimeter were added to the area. Then, we calculated area-equivalent diameters, which are taken as particle size in our PSD analysis. PSD data are commonly analyzed using a power-law function within a specific range of particle sizes (Mandelbrot, 1982). This power-law relationship can be quantified by the cumulative frequency curve in log–log plot of $N\ (>d) = kd^{-D}$, where $N\ (>d)$ is the number of particles greater than diameter d, k is a constant, and the exponent D (D-value in two dimensions here) is the negative slope of a best-fit line over a linear part of the plot (Turcotte, 1986). For comparison purposes, three-dimensional D-values of other studies were converted to two-dimensional D-values by subtracting one (Sammis et al., 1987). On a log(cumulative frequency) – log(size) plot, we used 20 bins per order of magnitude of particle

size. In sample BB12, the PSD data from two magnifications were combined into a single plot, multiplying the frequency in each bin at 10,000× magnification by a factor to the particle numbers at 4,000× magnification. To correct for variation in overlapping bins of two magnifications, the average frequency of the overlapping bins is used.

We also measured microfracture density of garnets in the stitched BSE images through a linear scanline method, widely used to characterize fracture networks (e.g., Anders and Wiltschko, 1994; Mitchell et al., 2011). To minimize the effect of operator sampling bias, we used 8 to 12 randomly oriented scanlines drawn across each garnet (Anders and Wiltschko, 1994). The garnet microfracture density (#/mm) is defined as the total number of microfractures that intersect scanlines divided by the total scanline length. In the case of dilated microfractures separating garnet fragments, the scanline length within each dilated fracture was subtracted from the total scanline length.

EBSD patterns of garnets were collected in an EDAX-TSL EBSD system at an acceleration voltage of 20 kV, a sample tilt of 70°, and a working distance of 25 mm, using a step size between 1 and 2 μm. EDAX-TSL OIM Analysis 6 software was used to construct EBSD maps and obtain misorientation angle distributions. The misorientation index (M-index; Skemer et al., 2005) was calculated to represent fabric intensity of fragmented garnets. The M-index is defined as the difference between the observed distribution of misorientation angles for pairs of randomly selected data points ("random-pair") and the misorientation angle distribution for a random fabric ("theoretical random") (Skemer et al., 2005). The M-index ranges from 0 for random fabric to 1 for single crystal fabric. When particles of a mineral show a strong crystallographic preferred orientation, its M-index is close to 1. If the particles are heterogeneously rotated, the M-index can be close to 0. The results of PSD, microfracture density, and M-index for all 15 garnet samples are documented in Table 2.1.

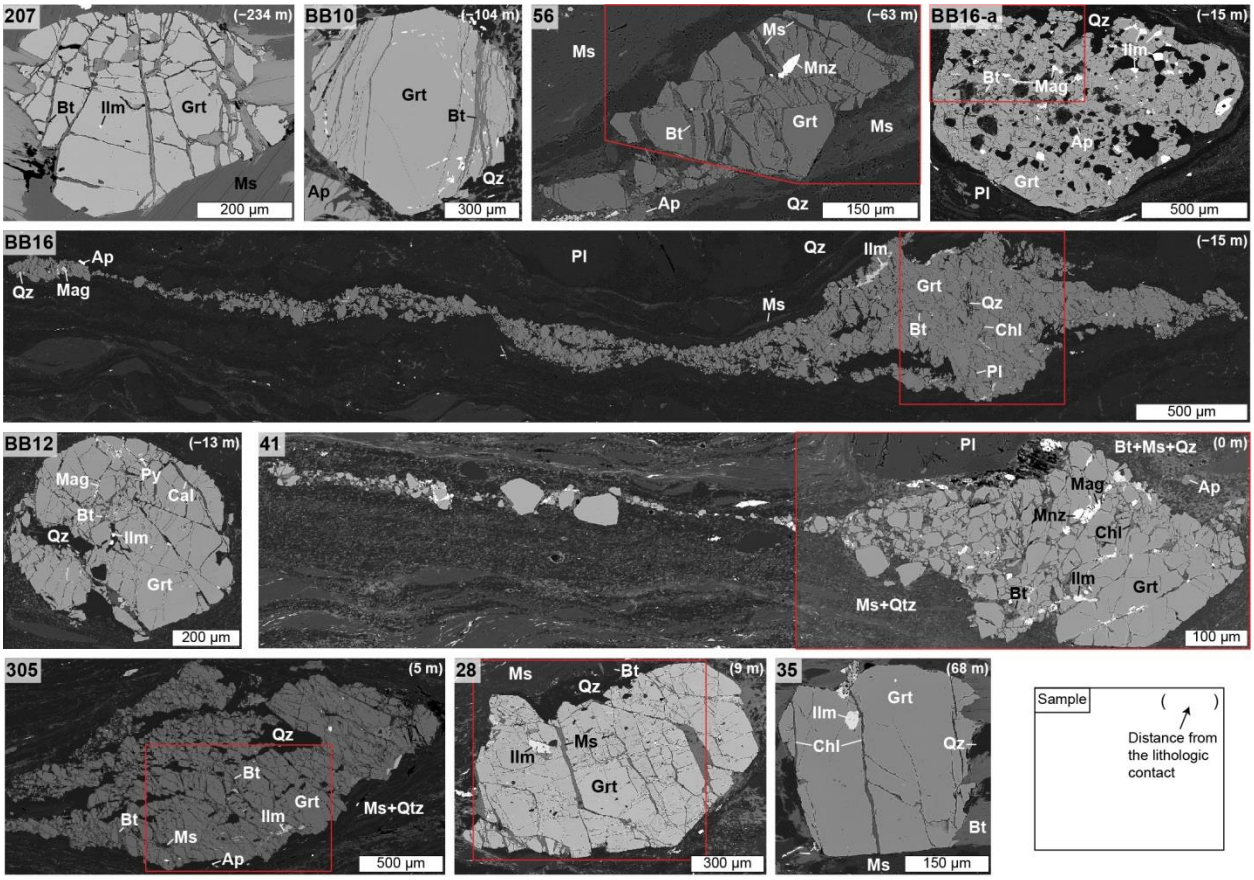

Figure 2.3 BSE images of ten representative garnet samples. Red boxes show the analysis areas of particle size distribution (PSD). The images are arranged from the QF host rock, through the shear zone core, to the schist host rock. Perpendicular distance for each sample was measured from the lithologic contact between the QF and schist units, and is shown in the upper-right corner of each image. Negative value of distance indicates the QF area. Note that while garnets in the host rocks and the outer shear zone (samples 207, BB10, 28 and 35) show one or more sets of preferred microfracture orientations, the inner shear zone garnets (samples 56, BB16-a, BB16, BB12, 41 and 305) have a large number of microfractures without preferred orientation. See Figure 2.4 for all the analyzed garnet samples. As fracture-filling minerals, quartz, micas (locally chloritized), calcite and feldspar are displayed in gray to dark gray, and oxides, phosphates and sulfides are shown in bright white. Mineral abbreviations are: Ap = apatite, Bt = biotite, Cal = calcite, Chl = chlorite, Grt = garnet, Ilm = ilmenite, Mag = magnetite, Mnz = monazite, Ms = Muscovite, Pl = plagioclase, Py = pyrite, Qz = quartz.

Table 2.1 Summary of two-dimensional *D*-value, microfracture density, and M-index data for all the fragmented garnet samples.

Lithology	Distance from the unit contact (m)*	Sample	*D*-value				Microfracture density (#/mm)	M-index
				Diameter, d range (μm)	*D*	R^2		
QF† host	-234.32	207		$1 < d \leq 63.10$	0.88	0.995	43.81	0.958
	-215.45	BB6		$1 < d \leq 70.79$	0.72	0.992	17.77	0.980
QF SCSZ§	-165.02	202		$3.16 < d \leq 39.81$	0.47	0.993	18.52	0.917
	-103.77	BB10		$1 < d \leq 22.39$	0.89	0.991	36.98	0.999
	-96.06	71		$1 < d \leq 22.39$	0.90	0.990	61.42	0.996
	-62.98	56	$D_<$	$1 < d \leq 8.91$	1.19	0.996	120.12	0.823
			$D_>$	$8.91 < d \leq 31.62$	1.50	0.992		
	-15.47	BB16-a	$D_<$	$2.24 < d \leq 10$	1.04	0.994	113.59	0.655
			$D_>$	$10 < d \leq 22.39$	1.96	0.991		
	-15.47	BB16	$D_<$	$1.26 < d \leq 10$	1.15	0.991	155.07	0.236
			$D_>$	$10 < d \leq 44.67$	2.36	0.996		
	-12.72	BB12	$D_<$	$1 < d \leq 10$	0.86	0.993	94.11	0.972
			$D_>$	$10 < d \leq 56.23$	1.84	0.994		
Contact	0	41	$D_<$	$1.59 < d \leq 10$	1.10	0.992	113.72	0.308
			$D_>$	$10 < d \leq 31.62$	1.88	0.997		
Schist SCSZ	5.46	305	$D_<$	$1.26 < d \leq 10$	0.84	0.992	123.01	0.755
			$D_>$	$10 < d \leq 35.48$	1.71	0.992		
	9.01	28	$D_<$	$1 < d \leq 11.22$	0.69	0.997	60.51	0.842
			$D_>$	$11.22 < d \leq 35.48$	1.37	0.991		
	13.50	26		$1 < d \leq 31.62$	0.77	0.994	67.71	0.998
Schist host	28.46	29		$1 < d \leq 199.53$	1.12	0.997	25.12	0.925
	67.82	35		$1 < d \leq 44.67$	0.88	0.994	21.79	0.985

*Perpendicular distance was measured from the lithological contact between the QF† and schist units, and negative values indicate the QF† area.

†QF = quartzofeldspathic unit.

§SCSZ = Sandhill Corner shear zone.

2.5. Garnet Fragmentation

2.5.1. Microstructures

Garnet microfractures in the host rocks and the “outer” shear zone (see Section 2.5.2) show one or more sets of preferred orientation (Figures 2.3 and 2.4). For example, sample BB10 has one set of oriented microfractures, perpendicular to the local foliation. On the other hand, qualitatively, microfractures in the “inner” shear zone samples (see Section 2.5.2) show no obvious preferred orientation (Figures 2.3 and 2.4). Garnets in the inner shear zone including the core are highly fragmented down to the submicron range and, in most cases, sheared (e.g., see samples BB16 and 41 in Figure 2.3). Sheared and thus rotated fragments appear sub-angular to sub-rounded in shape. However, the fragments of sample BB12, the least sheared garnet in the inner shear zone, display little or no shear offset, thereby maintaining the original particle shape, and have angular, wedge-like shapes (Figure 2.3). Dilatant microfractures of garnets in the SCSZ and host rocks are filled primarily with quartz and micas (locally chloritized), but include very minor quantities of feldspar, calcite, oxides, sulfides and/or phosphates (Figure 2.3).

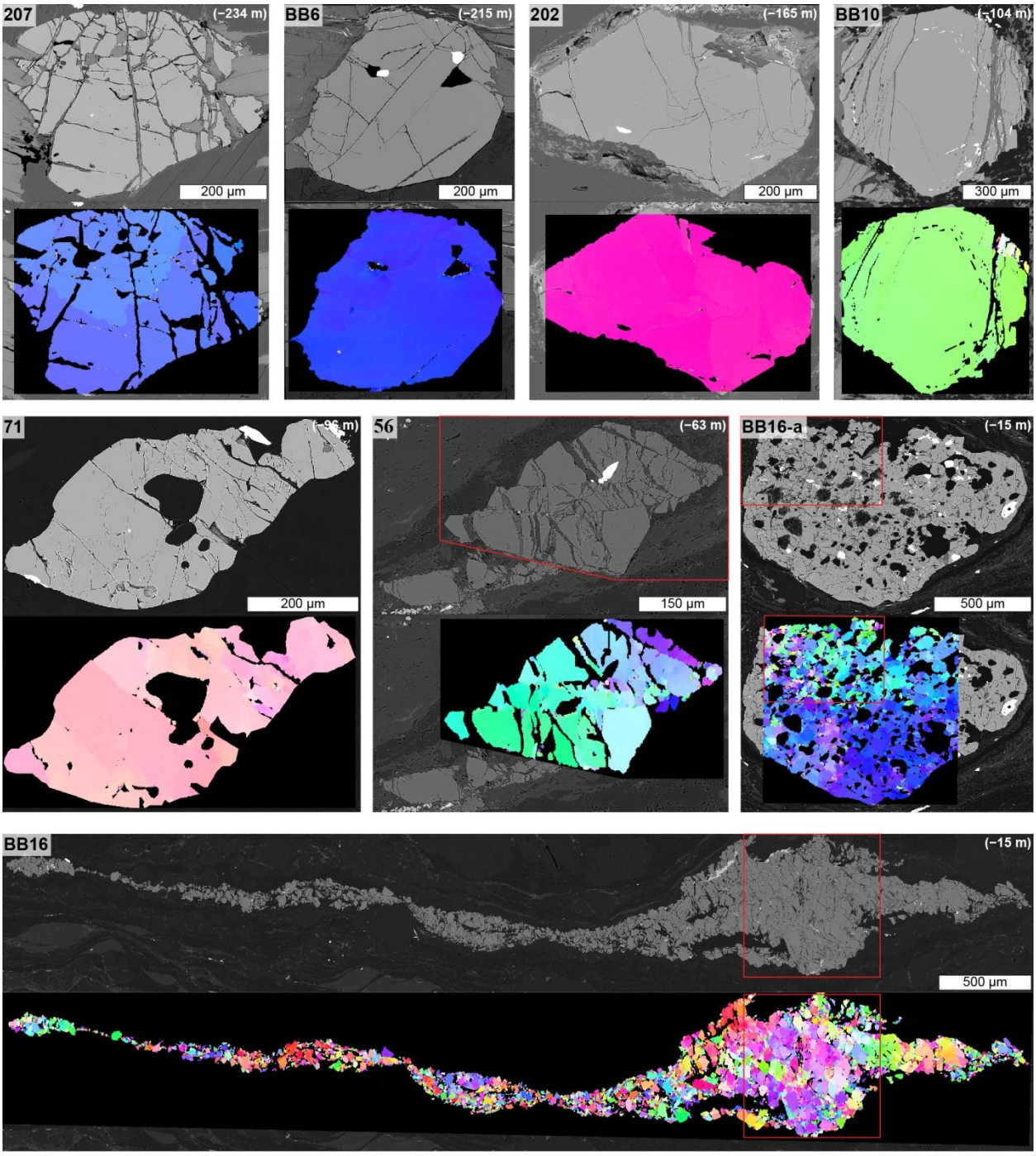

Figure 2.4 Microstructures of all the analyzed garnet samples. *Upper panels*: BSE images. Red boxes indicate analysis areas of particle size distribution. *Lower panels*: EBSD inverse pole figure (IPF) maps of garnet showing crystal orientation aligned with Y-direction, overlaid on the BSE image for each sample. Red boxes indicate analysis areas of M-index. The figures are arranged from the QF host rock (upper left), through the shear zone core, to the schist host rock (lower right). Note that while garnets in the host rocks and the outer shear zone (samples 207, BB6, 202, BB10, 71, 28, 26, 29 and 35) show one or a few sets of preferred microfracture orientations, the inner shear zone garnets (samples 56, BB16-a, BB16, BB12, 41 and 305) have a large number of microfractures without obvious preferred orientation.

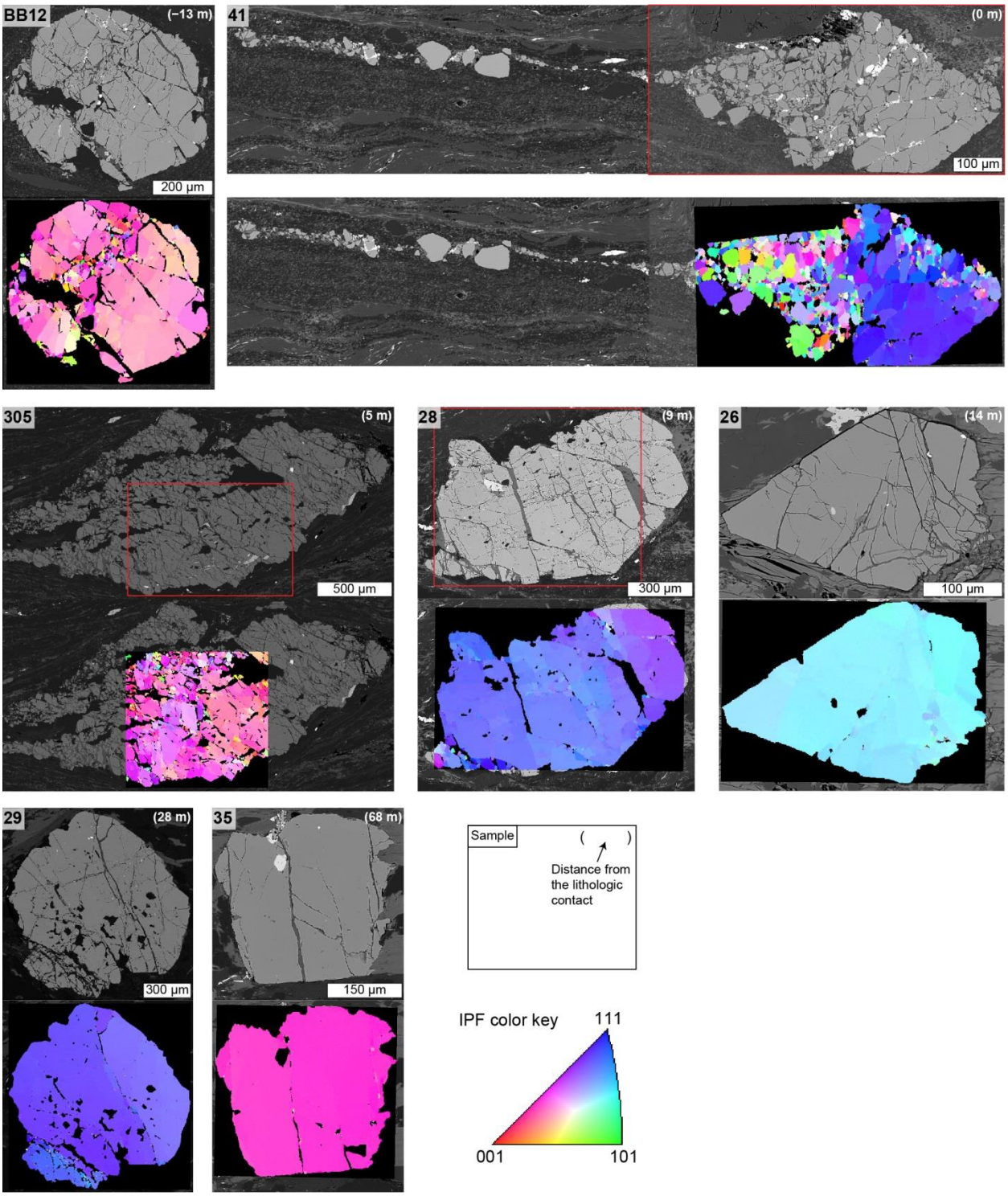

Figure 2.4 (Continued)

2.5.2. Particle Size Distribution (PSD), Microfracture Density, and Fabric Intensity

The cumulative PSDs of fragmented garnets from the host rocks and the outer shear zone in both the QF and schist units generally show a single power-law distribution over the majority of the size range, more than one order of magnitude, with R-square values larger than 0.99 indicating an excellent correlation (Figures 2.5a, 2.5c and 2.6). Their *D*-values are less than 1.50, between 0.47 and 1.12 (samples 207, BB6, 202, BB10, 71, 26, 29 and 35 in Figures 2.6 and 2.7a). However, the PSDs of the inner shear zone samples do not exhibit a single power-law with a constant slope; the data are better fit by two different domains of smaller and larger particle sizes, for which we denote two *D*-values as $D_<$ and $D_>$, respectively (Keulen et al., 2007; see Figures 2.5b, 2.5d and 2.6). The boundary between two power-law domains was chosen at a particle diameter of ~10 μm, based on inspection of the distribution data (Table 2.1). In the inner shear zone, the fitted *D*-values for smaller fragments ($D_<$) range from 0.84 to 1.19, while the *D*-values for larger fragments ($D_>$) are equal to or higher than 1.50, between 1.50 and 2.36 (samples 56, BB16-a, BB16, BB12, 41 and 305 in Figures 2.6 and 2.7a). *D*-values in the study area (or $D_>$-values for the samples with two power-laws) tend to increase toward the shear zone core (Figure 2.7a). We call the area with *D*- or $D_>$-values ≥ 1.5 an "inner" shear zone because of its proximity to the core, whereas the shear zone rocks with *D*- or $D_>$-values < 1.5 are considered as "outer" shear zone. One garnet (sample 28) in the schist unit shows two power-law distributions with relatively low *D*-values ($D_<$ = 0.69 and $D_>$ = 1.37), but is considered an outer shear zone rock due to the $D_>$-value < 1.5 (Figure 2.6). The inner shear zone is asymmetrically distributed around the shear zone core with widths in the QF and schist units of ~63 m and ~5 m, respectively (Figure 2.7a).

Microfracture density of fragmented garnets also generally increases toward the shear zone core from the host rocks (Figure 2.7b). The host rock garnets have relatively few microfractures corresponding to microfracture density between 17.77 and 43.81 mm^{-1}. In the outer shear zone, microfracture density ranges from 18.52 to 67.71 mm^{-1}. The inner shear zone garnets show enhanced microfracture density from 94.11 mm^{-1} to 155.07 mm^{-1}. The trends of garnet microfracture density from two host rock units to the core exhibit exponential increases and also an asymmetric distribution (Figure 2.7b).

The M-index fabric intensity for most garnet samples is very high exceeding 0.8, but stretched garnets in the inner shear zone show lower values (Figures 2.7c and 2.8). The aspect ratio of fragmented garnet appears to inversely correlate with the M-index (Figure 2.9). While garnets with little to no strain (e.g., sample BB12 in Figure 2.9a) exhibit high M-index values close to 1 (M-index of BB12 = 0.972 in Figure 2.9b), the highly stretched fragmented garnets near and in the core (e.g., samples BB16 and 41 in Figure 2.9a) exhibit very low M-index values (M-index of BB16 = 0.236 and M-index of 41 = 0.308 in Figure 2.9b). Relatively slightly stretched garnets such as sample 305 (Figure 2.9a) in the inner shear zone show intermediate M-index values (M-index of 305 = 0.755 in Figure 2.9b).

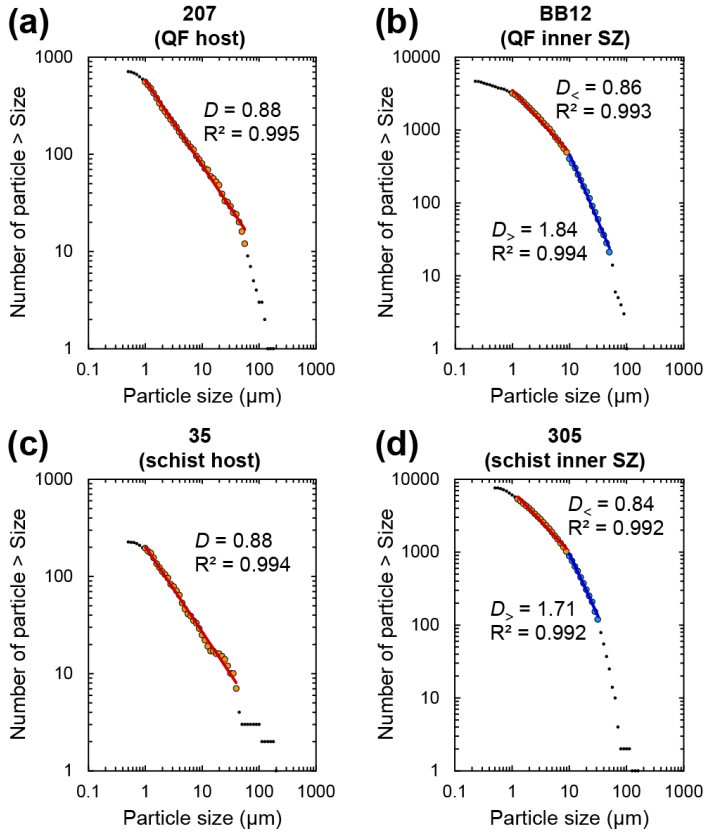

Figure 2.5 Particle size distribution (PSD) results of four representative garnet samples. Cumulative size frequency distribution is plotted in log–log space against fragment diameter. Best-fit power-law lines are drawn with *D*-values and R^2 correlation coefficients. The host rock samples in (a) and (c) can be fit by a single power-law distribution (red lines) over more than one order of magnitude, whereas highly fragmented garnets of the inner shear zone (SZ) in (b) and (d) follow two power-law distributions (red and blue lines). Measurements from truncated data (very fine fragments) or censored data (large fragments) were excluded from the analysis (black dots). See Figure 2.6 for all the analyzed garnet samples.

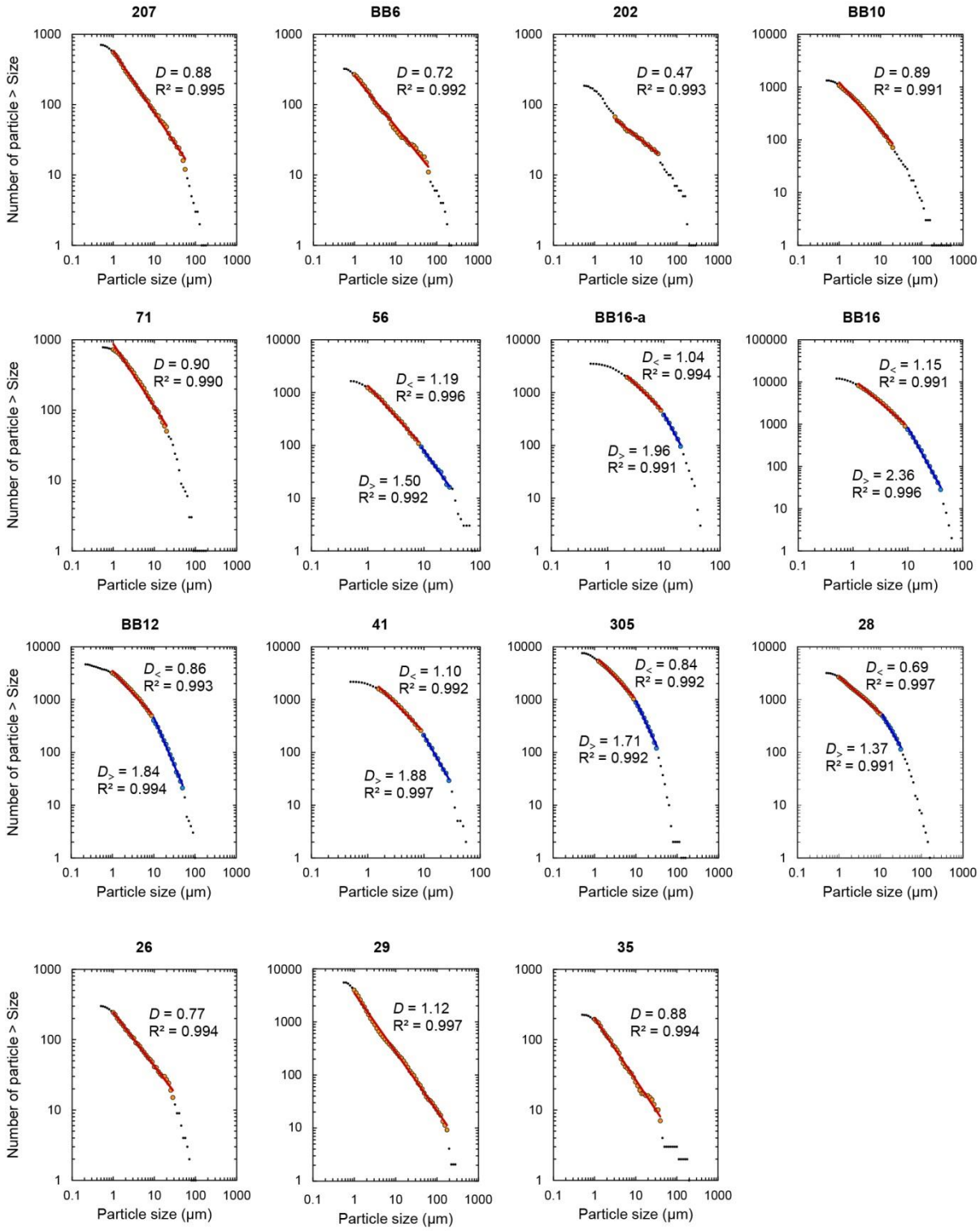

Figure 2.6 Particle size distributions (PSDs) of all the analyzed garnet samples. The cumulative size frequency against fragment diameter is plotted in log–log space with best-fit power-law line, *D*-value, and R^2. The plots are arranged from the QF host rock (upper left), through the shear zone core, to the schist host rock (lower right). The inner shear zone has *D*- or $D_>$-values ≥1.50, and the outer shear zone and the host rocks show *D*- or $D_>$-values <1.50.

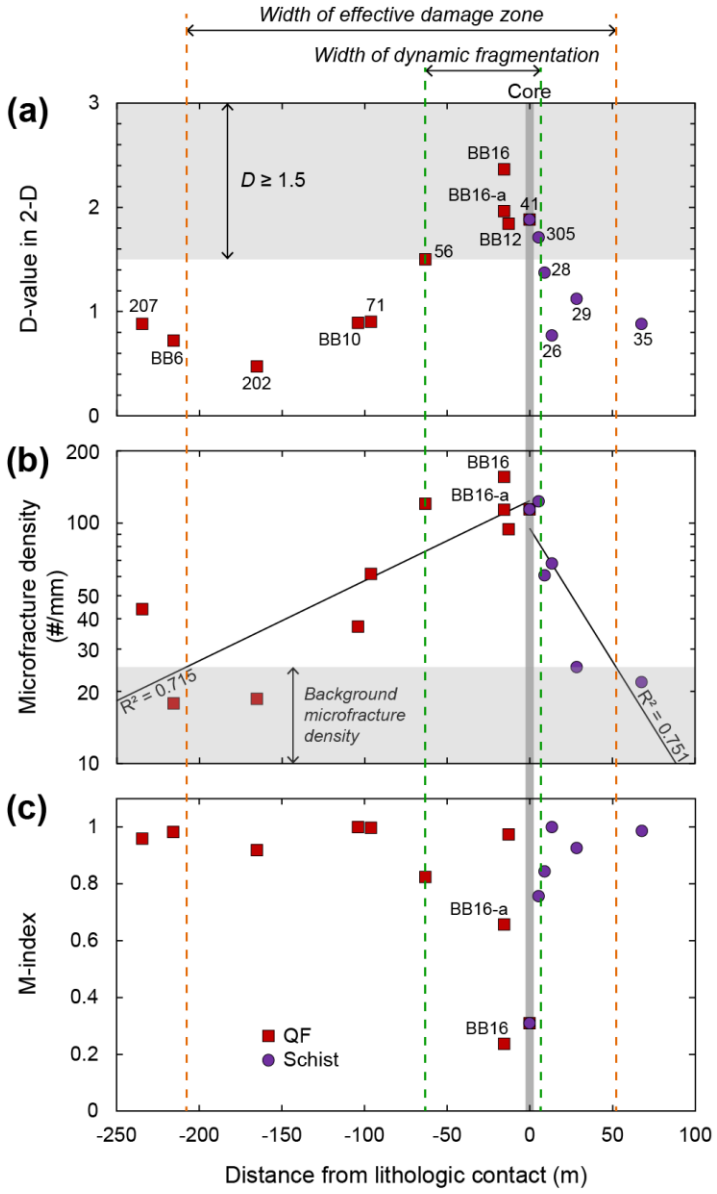

Figure 2.7 Summary graphs of the analyzed data for all the fragmented garnet samples, against distance from the QF/schist lithologic contact. (a) Two-dimensional *D*-value plot. $D_{>}$ for the larger particle size is plotted where there are two power-law trends. The region of *D*-value ≥ 1.5, above the threshold of dynamic fragmentation, is highlighted in light gray, and the width of a dynamically fragmented zone (the inner shear zone) is determined by samples with *D*-value ≥ 1.5 (marked by green dashed lines). Note highly asymmetric distribution of the dynamic fragmentation zone around the shear zone core (highlighted by dark gray). (b) Microfracture density plot. Note the logarithmic scale on the y-axis. Best-fit exponential lines are drawn for two lithologic units. Background microfracture density, below the fracture density value of sample 29 (schist host), is highlighted in light gray for reference. The width of effective damage zone is determined by the best fit lines above the background microfracture density (marked by orange dashed lines). Note asymmetric distribution of the effective damage zone around the shear zone core. (c) M-index fabric intensity plot. The M-index for most samples is very high in excess of 0.8, except four samples in the inner shear zone (BB16-a, BB16, 41 and 305). Legend for the QF and schist units is displayed in (c). Sample numbers are shown in (a), and only two sample numbers at a same distance are provided in (b) and (c).

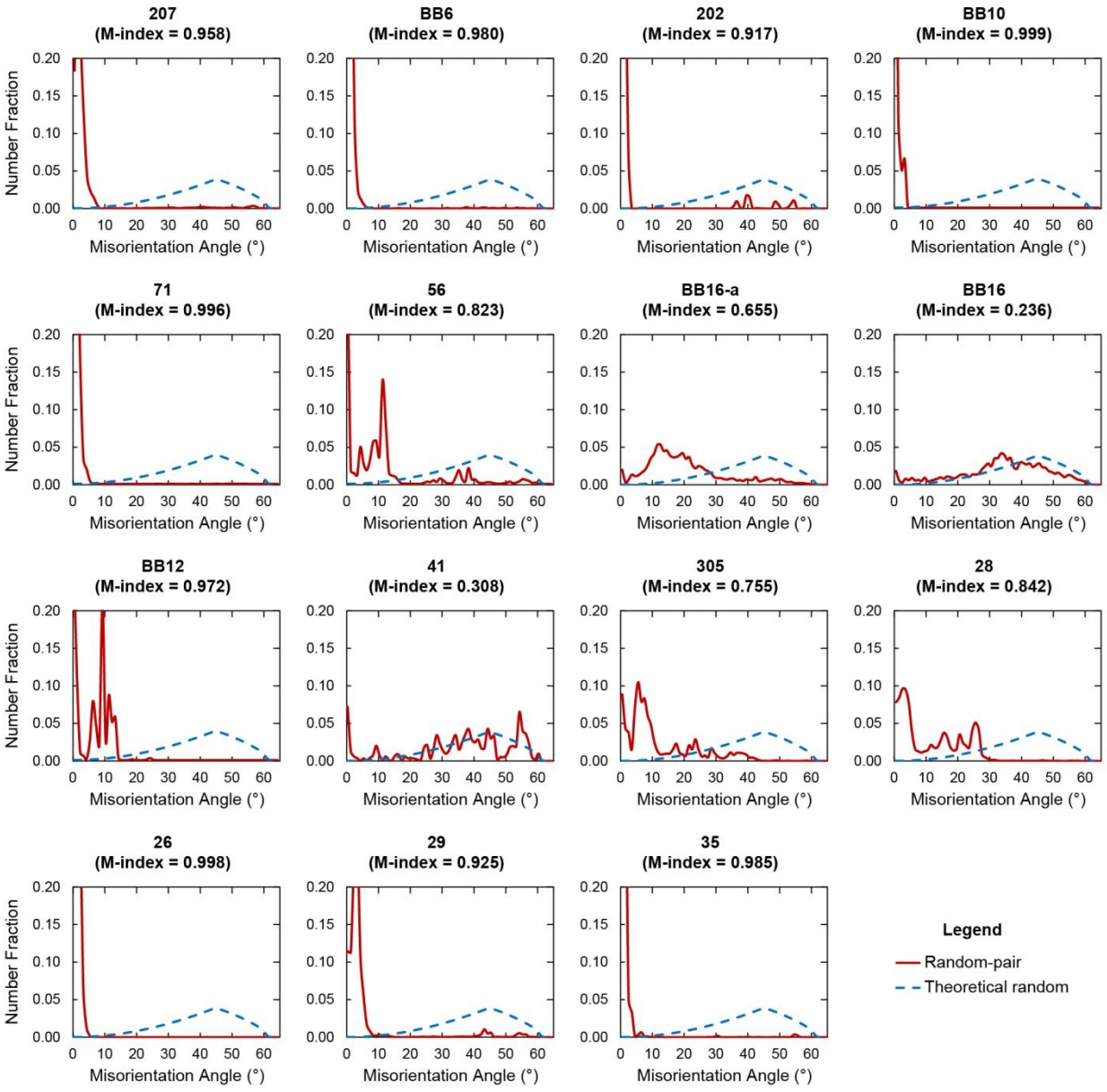

Figure 2.8 Misorientation angle distribution and M-index of all the analyzed garnet samples. Random-pair (red solid curve) indicates the observed misorientation distribution for pairs of randomly selected data points. Theoretical random (blue dashed curve) indicates the misorientation distribution for a random fabric. The M-index is the difference between the random-pair and the theoretical random, and ranges from 0 for random fabric to 1 for single crystal fabric (Skemer et al., 2005). The plots are arranged from the QF host rock (upper left), through the shear zone core, to the schist host rock (lower right).

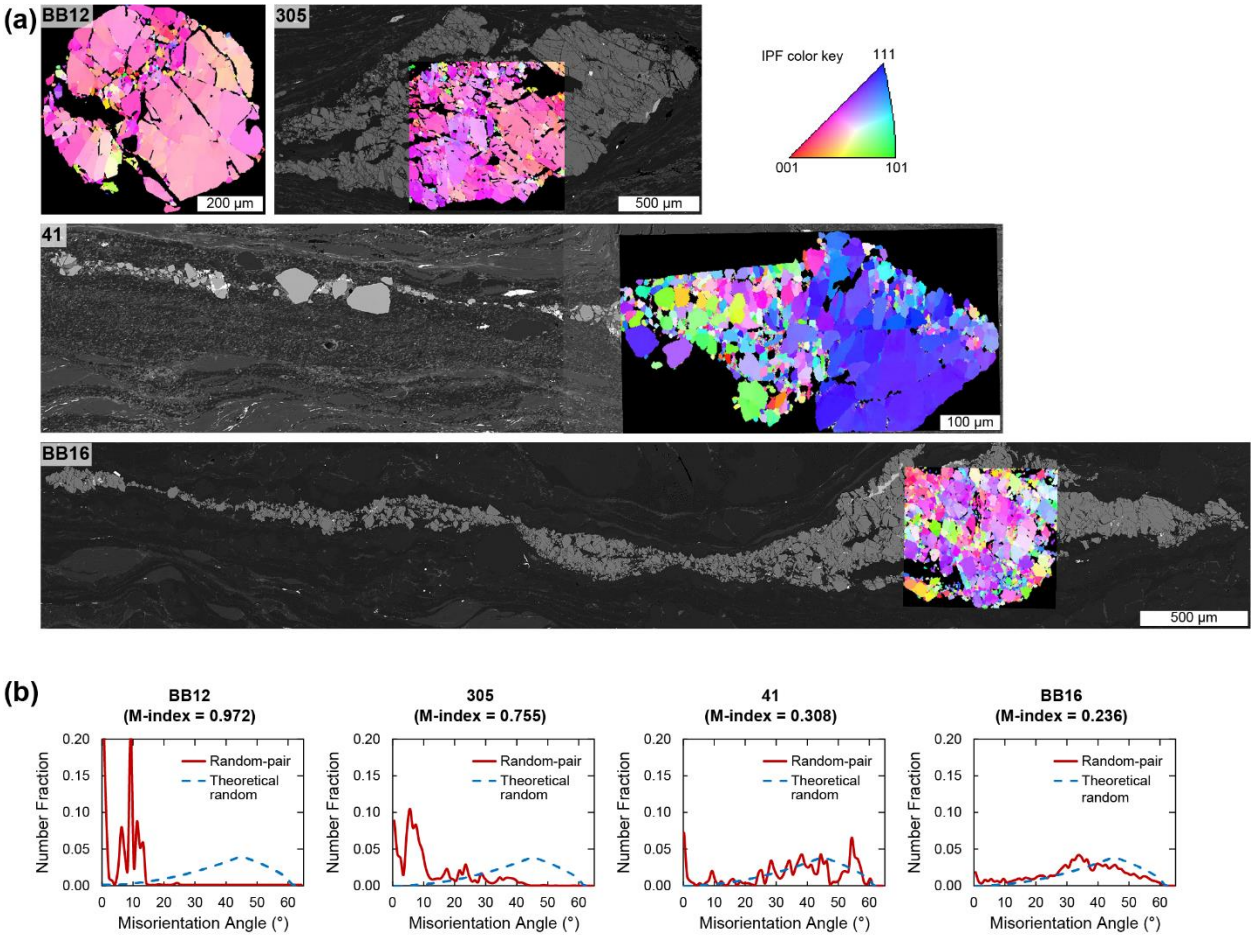

Figure 2.9 Electron backscatter diffraction (EBSD) analysis for four inner shear zone samples. (a) EBSD inverse pole figure (IPF) maps of garnet showing crystal orientation aligned with Y-direction. Analyzed IPF maps are overlaid on the BSE image for each sample. The figures are arranged in order of increasing aspect ratio of fragmented garnet. (b) Misorientation angle distributions with M-index values of the analyzed IPF maps in (a). Note an inverse correlation between the aspect ratio and M-index of fragmented garnet.

2.6. Discussion

2.6.1. Development of High *D*-Values in the SCSZ

The magnitude of *D* is generally related to fragmentation process and energy. Hydraulic brecciation produces low *D*-values less than ~1.3 (Clark et al., 2006), high-energy fracturing during catastrophic explosion generates high *D*-value equal to or greater than 1.5 (Schoutens, 1979; Turcotte, 1986), and mature shear-related fault rocks such as gouge exhibit *D*-values near 1.6 predicted by the constrained comminution

model (Sammis et al., 1987). Therefore, high $D_{>}$-values ≥ 1.5 of the inner shear zone garnets, similar to those reported for the explosive fragmentation, may indicate high-energy dynamic fragmentation.

Sample BB12 in the inner shear zone shows the $D_{>}$-value of 1.84 (Figure 2.5b), which is comparable with the *D*-value of 1.72 for pulverized quartz from the Arima-Takatsuki Tectonic Line, Japan (Muto et al., 2015). By considering its unique damage microstructure: (1) intense fracturing, (2) angular fragments down to the micron and submicron scales (Figure 2.3), and (3) a large M-index value (0.972) indicating very little to no relative fragment rotation (Figure 2.9), we propose that the high $D_{>}$-values of QF and schist samples in and near the core reflect dynamic damage during earthquake rupture.

Sample BB16 in the XZ plane parallel to the lineation shows a $D_{>}$-value of 2.36 while $D_{>}$-value of sample BB16-a in the YZ plane is much lower (1.96) (Figures 2.6 and 2.7a). Those two samples at the same distance from the lithologic contact display distinct microstructures: sample BB16 is strongly sheared, similar to fragmented and cataclastic garnets observed by Trepmann and Stöckhert (2002), whereas sample BB16-a is relatively less deformed. $D_{>}$-values more than 2 were reported in naturally and experimentally produced gouge (e.g., Keulen et al., 2007) and deformed sandstone by shock recovery experiment (Buhl et al., 2013), resulting from further shear displacement (and thus more strain) and high strain rate impact. Given that only highly stretched garnet (sample BB16) shows $D_{>}$-value greater than 2 in the SCSZ, we suggest that postseismic viscous flow of the matrix can yield such high *D*-value by surface abrasion combined with rotation and cataclastic flow of the fragments (e.g., Trepmann and Stöckhert, 2002, 2003). This argument is further supported by a very low M-index value (0.236) in BB16, indicating nearly random fabric (Figure 2.9). Similarly, sample 41 in the shear zone core may have experienced an increase in $D_{>}$-value by shear displacement as evidenced by its low M-index value (0.308) (Figure 2.9).

2.6.2. Insights Into Fragmentation Processes From PSDs

In the cumulative PSD graphs, the fragmented garnets in the inner shear zone do not show a single power-law over a large range. Instead, they show a slightly ‘curved’ distribution with a slope change (Figures 2.5b, 2.5d and 2.6). This is not uncommon in other PSD studies on pulverized fault zone rocks

(e.g., Rockwell et al., 2009; Wechsler et al., 2011). The curved distribution can be separated into two power-law regimes, with a lower *D*-value ($D_<$) for smaller fragments and a higher value ($D_>$) for larger fragments (Figures 2.5b, 2.5d and 2.6). The power-law behavior is lost for very fine and large fragments. For the very fine fragments, this is possibly due to the resolution limit, whereas the large fragments suffer from insufficient sampling and the restriction to fragments smaller than the initial size of the garnet (Pickering et al., 1995).

The two-power-law fit has been used in a wide range of fragmentation studies including explosive magmatic fragmentation, meteoric shock and impact fragmentation, shearing comminution, and drilling comminution (e.g., Carpinteri and Pugno, 2002; Keulen et al., 2007; Roy et al., 2012; Hossain and Kruhl, 2015). Keulen et al. (2007) suggested that two power-laws with a slope change at a diameter between 1.8 and 4 μm represent the grinding limit of quartz (1.7 μm; Prasher, 1987) in shearing comminution. We calculated the grinding limit ($= 30\times(K_{IC}/H)^2$) of garnet based on crack nucleation (Hagan, 1981) using the hardness (H) and toughness (resistance to fracture, K_{IC}) of Whitney et al. (2007). Garnet has a lower limit value than quartz (0.26 μm for almandine-pyrope) and thus, in our samples, the particle size at which the slope changes is much larger (~10 μm) than the grinding limit of garnet.

Our possible explanations for the two power-law distributions in garnet include the following. First, we suggest that the change in slope is more likely related to two-stage dynamic fragmentation (Carpinteri and Pugno, 2002; Taşdemir, 2009). The primary stage is a high energy, high strain-rate volume fragmentation, typically generating coarse, through-going, wedge-shaped fragments in a 3D volume (Wittel et al., 2008). In the secondary stage, finer fragmented material forms at the surfaces of coarser fragments by low energy surface fragmentation or attrition (Carpinteri and Pugno, 2002). Sample BB12 in Figure 2.10 supports these volume and surface fragmentations. Wedge-shaped coarser fragments are more spatially distributed with *D*-value close to 2 ($D_> = 1.84$) whereas fine fragments are concentrated between the coarser fragments with *D*-value close to 1 ($D_< = 0.86$) (Figure 2.10). Therefore, these two power-law distributions presumably reflect a two-stage process of dynamic fragmentation mechanism (dynamic tensile fracturing and then frictional grain-boundary sliding), as reported by the experimental study of Aben et al. (2016).

The second possibility is that PSDs produced by dynamic fragmentation may be modified by chemical erosion after the fragmentation. Fracture-filling minerals are mainly quartz, micas and chlorite (Figure 2.3). In the inner shear zone samples, fracture-filling biotite is partly or extensively replaced by chlorite, possibly consuming adjacent garnet. During chemical alteration, small garnet fragments along fractures can completely dissolve and disappear while large fragments experience the rounding of sharp corners and edges. The lower slope for smaller fragments is likely to reflect this chemical erosion during hydrothermal alteration. The thermal erosion model proposed by Roy et al. (2012) supports secondary post-fragmentation processes modifying the original PSD, decreasing the slope of the PSDs preferably at smaller sizes. However, even with secondary modification, it is inferred that the slope of coarser fragments ($D_{>}$-value) still indicates the original primary dynamic fragmentation process. We note that two power-law distributions of a garnet in the outer shear zone (sample 28) may reflect a relatively high degree of post-fragmentation modification (Figure 2.6).

In addition, we also consider $D_{<}$- and $D_{>}$-values to have been produced by two different primary fragmentation processes. One process can be fluid-assisted microfracturing possibly during post- and interseismic periods, leading to the *D*-values close to 1, which may be the primary process that occurred in the host rock and the outer shear zone garnets. We interpret the second process to be earthquake-induced dynamic fragmentation. In this stage, more intensive fragmentation occurs within preferred size intervals (>~10 μm) likely owing to high confining pressure, in agreement with the experimental evidence of Yuan et al. (2011).

Lastly, the curved distribution may be fit by a Weibull distribution (exponential-like function represented by Rosin and Rammler, 1933) generated by multiple fragmentations during successive earthquakes, instead of a single earthquake, thus showing parameters of both power-law and lognormal distributions. However, there is no clear evidence for superimposed fracture sets of different generations in the garnets we examined, nor in the other studies noted above where two different *D*-values were identified in single samples.

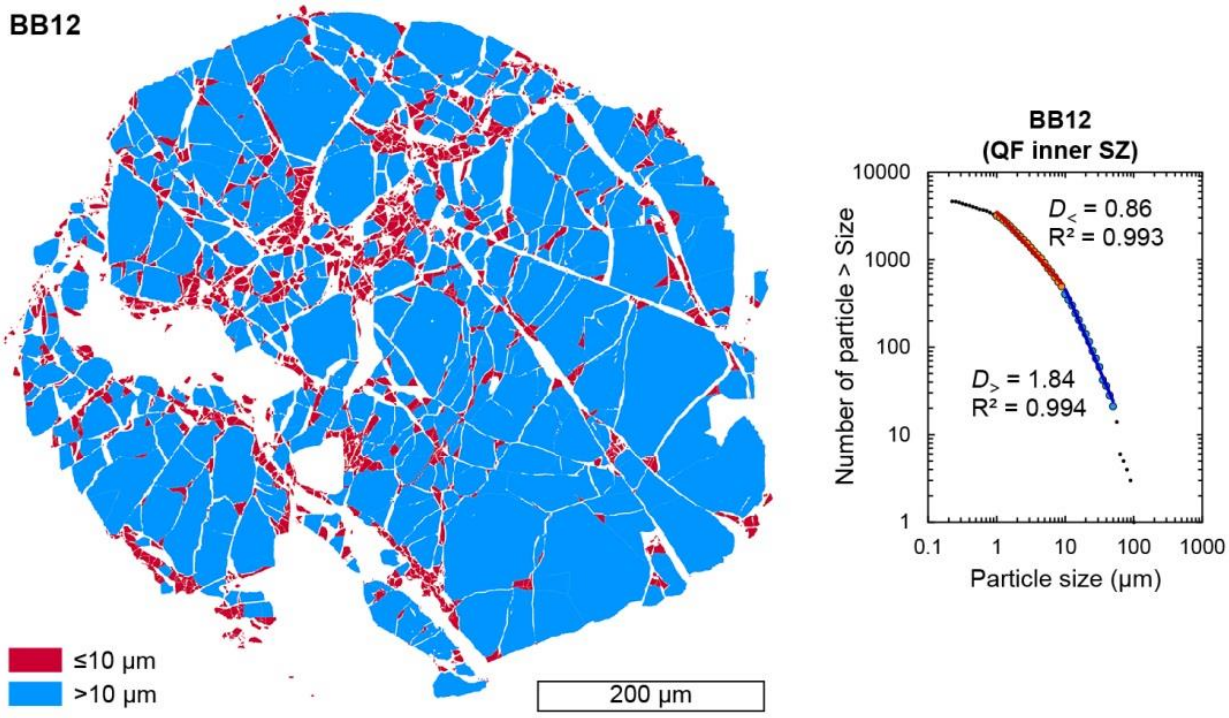

Figure 2.10 Bicolor map of the processed bitmap for BB12 garnet, highlighting fragment distributions for two different size ranges with a breakpoint at 10 μm. Red and blue colors in the map indicate fragments ≤10 μm and >10 μm, respectively, corresponding to $D_<$ and $D_>$ in the PSD plot (*right panel*). The plot is taken from Figure 4b.

2.6.3. Overview of Coseismic Damage at FVT Depths

The inner shear zone was defined as a zone with *D*-values ≥ 1.5, above the threshold considered to indicate high-energy fragmentation processes. We therefore attribute the ~70 m-wide inner shear zone with $D \geq 1.5$ (~63 m wide in QF and ~5 m in schist) to dynamic stresses generated during rupture propagation (Figure 2.7a). Garnet microstructures also strongly suggest transition from non-dynamic to dynamic damage at the boundary between the outer and inner shear zones, such as considerable reduction of fragment size and changes in microfracture orientation from preferred to no apparent preferred orientations (Figure 2.3).

The microfracture density that decreases with increasing distance from the QF/schist contact outlines the spatial extent of the outer effective damage zone (e.g., Mitchell and Faulkner, 2012). The microfracture density drops to the background levels at ~207 m and ~53 m from the contact in the QF and

schist units, respectively, when background levels are taken as less than the microfracture density of sample 29 (schist host) (Figure 2.7b). Sample 207 in the QF host rock shows a relatively high microfracture density, which we attribute to heterogeneous localized deformation. In the outer shear zone, fragmented garnets with microfracture density higher than the background values show *D*-values less than 1.5 (Figures 2.7a and 2.7b). Therefore, damage in the outer shear zone may result from a quasi-static deformation such as hydraulic microfracturing (Clark et al., 2006).

Our interpretation based on the garnet microstructures, *D*-values, and microfracture density is supported by the appearance of deformed pseudotachylyte in the inner shear zone (Figure 2.2). The cycles of pseudotachylyte and mylonitic deformation indicate a long history of repeated coseismic slip and post- and interseismic viscous deformation at FVT depths (e.g., Handy et al., 2007; Price et al., 2012).

2.7. Chapter Conclusions and Implications

The SCSZ of the Norumbega fault system preserves previously undocumented characteristics of large-displacement, strike-slip faults at FVT depths. The subdivisions of the SCSZ (the host rock, the fractured outer shear zone, the dynamically fragmented inner shear zone, and the shear zone core) correlate with the pattern of damage zone around active or recently active strike-slip faults at shallow depths (e.g., Mitchell et al., 2011; Rempe et al., 2013). In the QF unit of the SCSZ, the transition from the outer to inner shear zone occurs at ~63 m from the lithologic contact with prominent changes in microstructures, *D*-values, and microfracture densities. Such a transition is also observed across mature fault systems that are currently or recently active. For example, the boundary between fractured and pulverized zones are located at ~50 m and ~200 m from the fault core of the San Andreas fault and Arima-Takatsuki Tectonic Line, respectively (Mitchell et al., 2011; Rempe et al., 2013). In particular, we propose that the highly fragmented and sheared garnet near the SCSZ core (e.g., sample BB16) might correlate with the "pulverized and sheared" unit adjacent to the San Andreas fault core of Rempe et al. (2013). If this correlation is valid, then our results suggest that intense coseismic damage extends through the entire seismogenic zone in large-displacement,

strike-slip faults/shear zones, although healing processes and elastic strength recovery at depth may generally render it undetectable to seismological investigations after a relatively short time (e.g., Li et al., 2006).

Although garnet is relatively abundant in the schist, it is relatively rare in the QF rocks. However, we believe that the observed microfracturing and fragmentation in garnet occurred in other mineral phases such as quartz and feldspar (Figures 2.2c, 2.2d and 2.2e) during earthquake rupture. Such processes could facilitate chemical reactions and fluid-induced mineralogical changes during post- and interseismic periods. Thus, coseismic damage can affect episodic evolution of the shear zone rheology and therefore long-term weakening and strain localization of viscous deformation at depth (e.g., Handy et al., 2007). These may in turn contribute to long-term slip localization in the brittle upper crust developing along a mature seismogenic fault zone.

A final point of importance is the pronounced asymmetry of damage around the SCSZ core. While the damaged inner shear zone with $D \geq 1.5$ is ~63 m wide in the QF unit (northwest side), it is ~5 m wide in the schist unit (southeast side). Such asymmetric damage distribution is commonly found around active large-displacement, strike-slip faults that juxtapose rocks with dissimilar properties that form a bimaterial interface (e.g., Rockwell et al., 2009; Mitchell et al., 2011; Rempe et al., 2013). Dynamic rupture models have shown that bimaterial faults can host ruptures with preferred direction, producing more pronounced damage on the stiffer side (e.g., Dalguer and Day, 2009; Xu and Ben-Zion, 2017). If the strong asymmetry of damage in the SCSZ reflects rupture dynamics, then the right-lateral slip along the shear zone would indicate southwest preferred directivity of rupture propagation in the area. The asymmetric damage observed in the SCSZ exhumed from FVT depths may imply that the same damage processes of seismogenic strike-slip faults occurring in the uppermost crust operate through the entire seismogenic zone.

2.8. Chapter Acknowledgments

We thank Tom Mitchell and an anonymous reviewer for helpful comments that improved the manuscript. This research was supported by National Science Foundation grants EAR-0820946, EAR-1347087 and EAR-1727090. B. R. Song was supported in part by a Michael J. Eckardt Dissertation Fellowship from the University of Maine.

CHAPTER 3

EFFECT OF POST-FRAGMENTATION VISCOUS SHEAR STRAIN ON PARTICLE SIZE DISTRIBUTION FOR DYNAMIC AND QUASI-STATIC FRAGMENTATION

3.1. Chapter Abstract

Particle size distribution (PSD) analysis of fragmented minerals has been used to estimate energy sources or loading conditions. For example, three-dimensional *D*-value (negative slope in log-log plot of the cumulative PSD) ≥2.5 is considered high strain-rate dynamic loading whereas *D*-value <2.5 indicates low-energy quasi-static loading. However, PSD can be modified if secondary deformation occurs. Although pulverized minerals observed in active faults near Earth's surface show no or little relative rotation and shearing, the original crystal shapes of coseismically fragmented/pulverized grains are rarely preserved in seismogenic faults at the frictional-to-viscous transition (FVT) due to post- and interseismic flow. Thus, caution should be taken when analyzing *D*-value of fragmented minerals with various aspect ratios from the seismogenic faults at FVT depths. To evaluate whether PSD analysis of the fragmented brittle minerals at the FVT can still be used for an indicator of dynamic loading when it is modified by post- and interseismic shearing, I analyze dynamically fragmented garnet with various aspect ratios from the Sandhill Corner shear zone and compare with quasi-statically fragmented garnet from aseismically deformed "L-tectonites". My results show *D*-values (in 3D) between 2.5 and 4 for the dynamically deformed rocks and less than 2.5 for the L-tectonites even with high aspect ratio. Fracture patterns are also analyzed for both rocks. My findings indicate that PSD is a useful tool for evaluating energy source or loading condition of brittle minerals irrespective of the degree of shearing.

3.2. Chapter Introduction

Pervasive damage caused by coseismic fracturing and fragmentation (so-called pulverization) has been recognized along the active large-displacement strike-slip faults such as the San Andreas fault (Wilson et al., 2005; Dor et al., 2006a, 2006b, 2009; Rockwell et al., 2009; Wechsler et al., 2011; Rempe et al.,

2013; Muto et al., 2015), the Garlock fault (Rockwell et al., 2009), and the San Jacinto fault (Dor et al., 2006b; Wechsler et al., 2009) in USA, the North Anatolian fault in Türkiye (Dor et al., 2008), and the Arima-Takatsuki Tectonic Line in Japan (Mitchell et al., 2011; Muto et al., 2015).

In upper crustal faults near Earth's surface where all rock materials exhibit brittle behavior, pulverized rocks are generally recognized by a lack of in-situ shear strain (Rockwell et al., 2009; Mitchell et al., 2011; Wechsler et al., 2011; Rempe et al., 2013; Muto et al., 2015). Thus, pulverized rocks commonly preserve the original shapes of the constituent minerals. In frictional-to-viscous transition (FVT) zones at middle crustal depth, however, some mineral phases deform brittley while some others behave viscously, depending on conditions of pressure, temperature, differential stress, and strain rate. Strong minerals such as garnet and feldspar are broken down by microfracturing and fragmentation during earthquake ruptures and undergo granular flow during post- and interseismic periods due to viscous flow of the surrounding fine-grained matrix. Over multiple earthquake cycles, consequently, strong minerals adjacent to the fault/shear zone core experience shearing and secondary grain-size reduction.

It is difficult to distinguish whether rocks in faults/shear zones are deformed by seismic (dynamic) or aseismic (quasi-static) loading (e.g., Sibson, 1989; Cowan, 1999; Rowe and Griffith, 2015). Pseudotachylite (quenched friction melt) is the most accepted indicator to determine whether slip occurs at seismic or aseismic rate (Cowan, 1999, and references therein), but is not always observed in natural fault/shear zones. Pulverized rocks observed in large-displacement strike-slip faults have been considered as a direct signature indicating earthquake-related deformation (e.g., Rowe and Griffith, 2015). To identify pulverized rocks, particle size distribution (PSD) analysis is commonly used (e.g., Muto et al., 2015; B. R. Song et al., 2020) since higher energy source generally produces more finer particles.

It is often documented that the PSD of fractured materials follows a power law (e.g., Sammis et al., 1987; Crum, 1990; Perugini et al., 2007; Buhl et al., 2013) and the exponent *D* (the negative slope of a best-fit line over the cumulative frequency curve in log-log plot) of the PSD has been correlated with different deformation modes for given energy or strain-rates (e.g., Jebrak, 1997; Barnett, 2004; Buhl et al., 2013). The quantitative relation between strain-rate and resulting PSD is a topic of ongoing research (e.g., Johnson

et al., 2021b), but the general idea is that at increased strain rate, rapid growth of elastic strain energy exceeds the required fracture energy, thus triggering more defects in the deformed material, causing rapid increase in the number of microfractures that nucleate, grow, and branch out, which results in increase of small fragments and thus likely influences *D*-values (Grady and Kipp, 1985; Sharon et al., 1996; Grady, 2010). Table 3.1 shows a compilation of published results on the three-dimensional *D*-values for rocks deformed under high and low strain-rate settings. High strain-rate experiments to simulate shock-induced fragmentation indicate correlation between *D*-value and strain-rate; the *D*-value increases with increasing impact energy (Lange et al., 1984; Buhl et al., 2013). Studies on natural rock fragmentation provide a broad range of *D*-values between 1.88 and 3.98 (Table 3.1). Studies on dynamic fragmentation induced by volcanic explosion, impact, and earthquake rupture reported a wide range of *D*-values between 1.97 and 3.98 (Rousell et al., 2003; Barnett, 2004; Farris and Paterson, 2007; Key and Schultz, 2011; Hossain and Kruhl, 2015; Muto et al., 2015; B. R. Song et al., 2020). In contrary, fluid induced brecciation under low strain-rate loading shows relatively low *D*-values between 2.17 and 2.34 (Clark et al., 2006). Low strain-rate shear experiments of Biegel et al. (1989), simulating fault gouge formation, show power-law PSDs with *D*-value of 2.6, which supports the constrained comminution model (Sammis et al., 1986). On the other hand, natural fault rocks such as gouge, cataclasite and breccia show a large range of *D*-values from 1.88 to 3.6 (Sammis et al., 1987; Sammis and Biegel, 1989; Blenkinsop, 1991; An and Sammis, 1994; Shao and Zou, 1996; Monzawa and Otsuki, 2003; Storti et al., 2003; Billi and Storti, 2004; Chester et al., 2005; Ma et al., 2006; Keulen et al., 2007; Pittarello et al., 2008; Balsamo and Storti, 2011; Fondriest et al., 2012), which cannot be explained by self-similar evolution of cataclastic shear ($D = 2.58$; Sammis et al., 1986). In addition, high *D*-values may be related to increasing strain (e.g., Blenkinsop, 1991; Storti et al., 2003; Keulen et al., 2007), and this shear-related modification makes it difficult to distinguish from high strain-rate fragmentation.

At middle crustal depths, dynamically pulverized rocks often experience shearing during post- and interseismic periods (B. R. Song et al., 2020), making it difficult to distinguish dynamic fragmentation from the type of microfracturing experienced by rocks undergoing quasi-static shear deformation. To identify

the difference between microstructures of dynamically pulverized and sheared rocks versus quasi-statically fractured and fragmented rocks, I compare fractured and fragmented garnet grains in a seismically pulverized rock from the Sandhill Corner shear zone and a tectonically deformed rock from the Pigeon Point high-strain zone.

In this chapter, using the samples described above, I investigate garnet PSD by both image-based and electron backscatter diffraction (EBSD)-based analyses. For PSD analysis, a backscattered electron (BSE) image has been widely used with image analysis software such as ImageJ to detect microfractures and identify fragments. However, since the gray-scale values in BSE images represent relative mass density or composition, hairline microfractures appearing as irregular brightness and blemishes cannot be automatically identified if the microfractures have no clearly defined edges. Thus, image-based analysis, especially for partially healed or fused fractures, requires painstaking manual modification procedures, making it slow and inefficient. This also affects the reliability of measurements because identifying fragment boundaries is often subjective, prone to human error. EBSD-based analysis is a feasible alternative that can measure fragment size in a fast and more reliable way. The advantage of using EBSD is its ability to assess fragment boundaries based on crystallographic orientation.

Table 3.1 Published three-dimensional *D*-values in analysis of particle size distribution for different deformation modes.

Category	Type of deformation	*D*-value in 3D*	Reference
Natural deformation	Volcanic explosion	2.14–3.57	Barnett (2004)
	Volcanic explosion	3.34–3.77	Farris & Paterson (2007)
	Impact	2.2–2.8	Rousell et al. (2003)
	Impact	2.55	Key and Schultz (2011)
	Impact	2.20–3.98	Hossain and Kruhl (2015)
	Earthquake rupture	1.97–2.92	Muto et al. (2015)
	Earthquake rupture	2.50–3.36	B. R. Song et al. (2020)
	Hydrostatic load	2.17–2.34	Clark et al. (2006)
	Comminution	2.60	Sammis et al. (1987)
	Comminution	2.60	Sammis & Biegel (1989)
	Comminution	2.27–3.1	Blenkinsop (1991)
	Comminution	2.4–3.6	An & Sammis (1994)
	Comminution	2.60	Shao & Zou (1996)
	Comminution	2.70–3.30	Monzawa & Otsuki (2003)
	Comminution	1.88–3.49	Storti et al. (2003)
	Comminution	2.09–2.93	Billi & Storti (2004)
	Comminution	3.00	Chester et al. (2005)
	Comminution	3.30	Ma et al. (2006)
	Comminution	2.6–3.4	Keulen et al. (2007)
	Comminution	2.80	Pittarello et al. (2008)
	Comminution	2.64–3.02	Balsamo & Storti (2011)
	Comminution	2.49–2.56	Fondriest et al. (2012)
Experiment (high strain-rate)	Nuclear explosion	2.50	Schoutens (1979)
	Impact	2.4–2.62	Fujiwara et al. (1977)
	Impact	2.44–2.71	Lange et al. (1984)
	Crater	1.84–2.74	Buhl et al. (2013)
	Shock recovery	3.42	Buhl et al. (2013)
Experiment (low strain-rate)	Hydrostatic load 20 MPa	2.40	Marone & Scholz (1989)
	Hydrostatic load 100 MPa	2.80	Marone & Scholz (1989)
	Shear test	2.60	Marone & Scholz (1989)
	Shear test	2.60	Biegel et al. (1989)
	Tri axial compression	2.9–3.5	Hadizadeh & Johnson (2003)
	Tri axial compression	2.4–3.3	Heilbronner & Keulen (2006)
	Tri axial compression	2.4–3.3	Keulen et al. (2017)
	Rotary shear	2.54–3.26	Stunitz et al. (2010)

*Two-dimensional *D*-value is converted to three-dimensional *D*-values by adding one ($D_{3d} = D_{2d} + 1$) (Mandelbrot, 1982; Sammis et al., 1987).

3.3. Geological Overview and Sample Selection

3.3.1. Dynamically Deformed Sandhill Corner Shear Zone (SCSZ)

The SCSZ is a strand of the Norumbega fault system in Maine (Figure 3.1) that is an ancient, large-displacement, strike-slip fault/shear zone system exhumed from frictional-to-viscous transition depths (400–500 °C). The mutual overprinting of pseudotachylyte and mylonite (Price et al., 2012; W. J. Song et al., 2020) indicates that the SCSZ was active at temperatures of 400–500 °C (Price et al., 2012). Dynamic pulverization of inner shear zone garnets (see Chapter 2), abundances of fluid inclusion with low-high-low trend (W. J. Song et al., 2020), muscovite kink-band with high degree of asymmetry, small width, and large range of external rotation (Anderson et al, 2021) also provide evidence of coseismic dynamic loading. I selected BB12 sample from the QF inner shear zone (~13 m from the lithologic contact between QF and schist units; Figure 3.1) showing highly fractured and fragmented garnets with various degrees of aspect ratios.

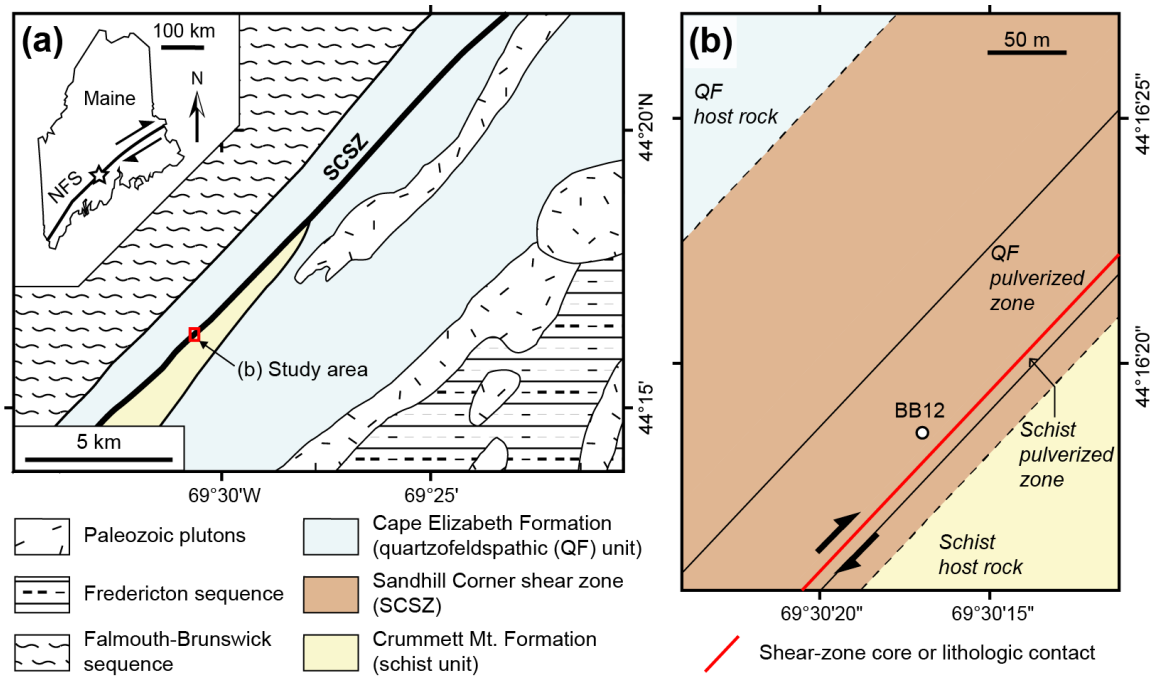

Figure 3.1 Sample location (BB12) of dynamically deformed Sandhill Corner shear zone in the Norumbega fault system (NFS), Maine, USA.

3.3.2. Quasi-Statically Deformed Pigeon Point High-Strain Zone (PPHSZ)

The PPHSZ is a subhorizontal to gently dipping structure with intense viscous deformation associated with a thrust-fault system, located in the southeastern Klamath Mountains, California (Figure 3.2; Wright and Fahan, 1988; Sullivan, 2009). The high-strain zone is likely related to magmatic heating (Sullivan, 2009). L-tectonites showing pure or nearly pure linear fabrics in the PPHSZ were deformed during regional greenschist- to amphibolite-facies metamorphism and display strong mineral shape fabrics parallel to lineation (Figure 3.2b; Sullivan, 2009). Sample WHF-4A consists mostly of garnet, hornblende, plagioclase, quartz and biotite, where garnet grains appear as elongate fractured and fragmented aggregates.

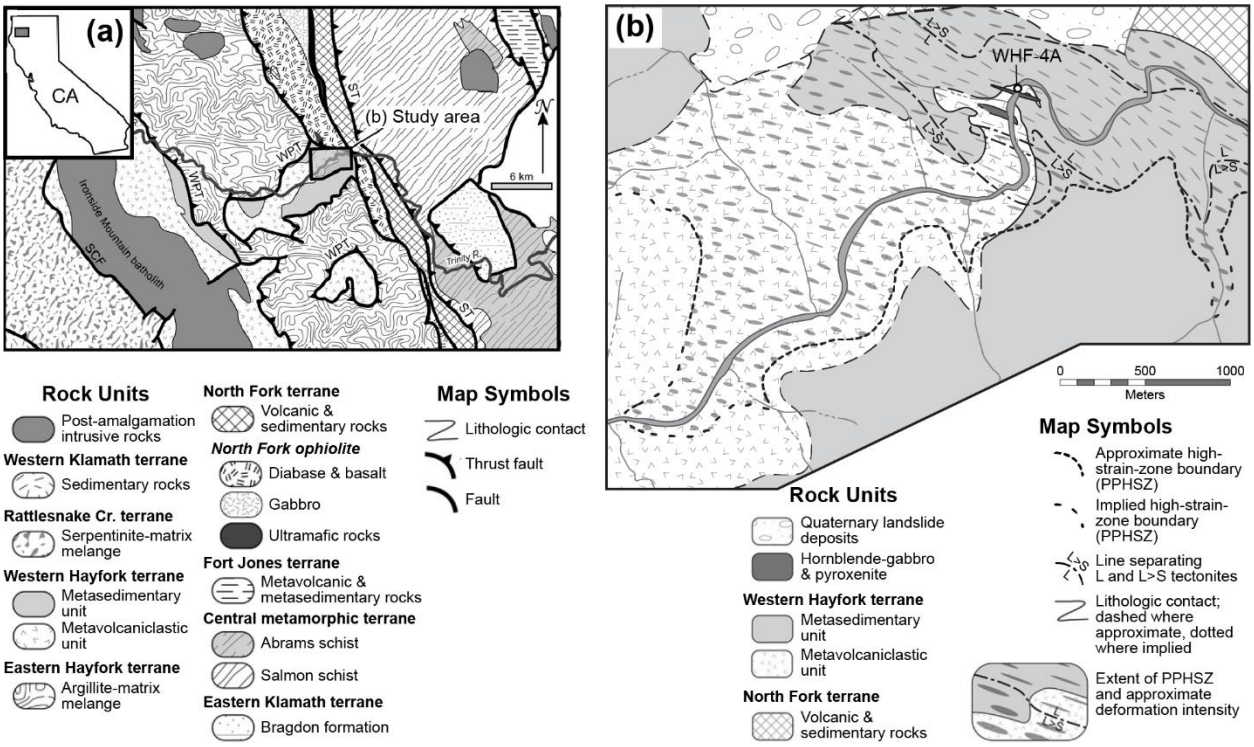

Figure 3.2 Sample location (WHF-4A) of quasi-statically deformed Pigeon Point high-strain zone (PPHSZ), California, USA. (a) Regional geologic map. SCF = Salt Creek fault; ST = Siskyou thrust; WPT = Wilson Point thrust. (b) Sample location, marked by white dot, in the PPHSZ. L = linear fabric; S = foliation fabric. After Sullivan (2009).

3.4. Methods

Garnet-bearing rock samples were collected from the inner shear zone of the SCSZ and the L-tectonite in the PPHSZ. Thin sections were cut perpendicular to the main foliation and parallel to the stretching lineation, and polished mechanically with 0.3 μm alumina suspension and chemically in 0.02 μm colloidal silica suspension before being thin carbon coated. BSE images and EBSD maps of fragmented garnets were collected using a Tescan Vega II scanning electron microscope equipped with an EDAX-TSL EBSD system at the University of Maine, USA. The EBSD was run with an acceleration voltage of 20 kV, a sample tilt of 70°, and a working distance of 25 mm, using a step size between 1 and 2 μm.

Using stitched BSE images, I measured microfracture intensity and microfracture orientation in fragmented garnets. I chose a circular scanline method described by Heidrick and Titley (1982) and Davis et al. (2012). Circles are drawn on a fractured and fragmented garnet and data are collected from all fractures intersecting the circumference of the circle. Documenting microfractures in this way minimizes sampling biases by orientation, censoring, or truncation (Mauldon et al., 2001; Zeeb et al., 2013).

All acquired EBSD data were post-processed using EDAX-TSL OIM Analysis 5.31 software, following the procedure described by Johnson et al. (2021a). Grain size of 5 analysis points for a 1 μm step size and 3 points for a 1.5 or 2 μm step size were used. Defining critical misorientation angle is an important step in the study of particle size distribution by EBSD. 'Grain' boundaries are usually defined as angle of 10–15° (e.g., Humphreys, 2001). However, substructure such as intragranular microfracture can separate grains into fragments with little rotation of crystal lattice orientation far lower than 10°. The fragmented garnet was originally a single grain which means it ideally had no internal strain without deformation. Thus, with no or little strain, two adjacent fragments can have only very small degree of misorientation although it depends on their fragmentation history. In this study, misorientation angle of 0.3° is used as a critical misorientation angle to define almost all fragments, which show very good agreement with the BSE image.

Two-dimensional particle size distributions (PSDs) were analyzed using two different methods, BSE-image and EBSD-based analyses. The 2D *D*-values are converted to 3D *D*-values by adding one ($D_{3d} = D_{2d} + 1$), which are used throughout this chapter (Mandelbrot, 1982; Sammis et al., 1987). The BSE-

image analysis I used here is similar to the PSD analysis described in Chapter 2.4. Since garnet grains in the PPHSZ L-tectonite are much larger than those in the SCSZ inner shear zone rock, relatively lower resolution images (1000× and 2000× magnifications) were combined with higher resolution (4000× magnification) images. With BSE-image analysis, cross-sectional areas of five garnet grains were measured: three from the SCSZ inner shear zone rock (BB12-g1, BB12-g4, and BB12-g6) and two from the PPHSZ L-tectonite (WHF4AC1-g1 and WHF4AC1-g2). As addressed in the Introduction, EBSD-based analysis is a relatively faster and more reliable method. I analyzed PSDs of ten fragmented garnets using EBSD-based analysis.

Fabric intensity of fragmented garnet was represented by the misorientation index (M-index; Skemer et al., 2005). The M-index is obtained by the difference between the observed distribution of random-pair misorientation angles and the distribution of theoretical random misorientation angles (Skemer et al., 2005). The M-index ranges from 0 for random fabric to 1 for single crystal fabric.

The aspect ratio is calculated as the ratio of the major axis to the minor axis of the best fitting ellipse. Binary images of fragmented garnets were automatically collected from original BSE images, using ImageJ (image processing software). With thresholding, garnet fragments were separated from background features. After removing noises and filling holes between fragments, the best fitting ellipse was generated (Figure 3.3).

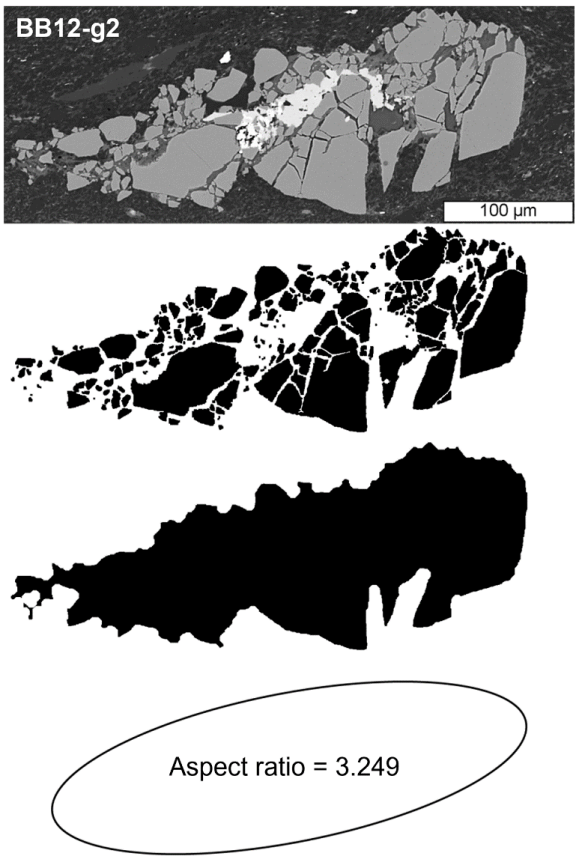

Figure 3.3 An example of aspect ratio calculation for fragmented garnet from BSE image.

3.5. Results

3.5.1. Microstructures of Heterogeneously Fragmented Garnet Grains

3.5.1.1. SCSZ Inner Shear Zone Rocks

Figure 3.4 is a BSE image of a foliation-perpendicular and lineation-parallel section of sample BB12 collected from the inner shear zone of the SCSZ. The BB12 sample from the quartzofeldspathic mylonite is primarily composed of quartz, plagioclase, and mica, with sparse garnets. Six garnets in sample BB12 show highly heterogeneous microstructures (Figure 3.5). They are fractured and fragmented, and appear stretched owing to cataclastic flow induced by viscous deformation of the matrix. We can divide those garnets into three groups based on strain (Figure 3.5). A fragmented garnet at middle left of the section (g1) that well preserves its original euhedral shape of garnet crystal with little rotation is classified by group

I. Four aggregates of fragmented garnets at middle center (g2) and right side (g3–g5) that have augen- or fish-shapes with long tails are included in group II. Group III garnet is highly fragmented and stretched one, such as garnet aggregates at bottom left (g6). Garnets show no evidence for compositional zoning.

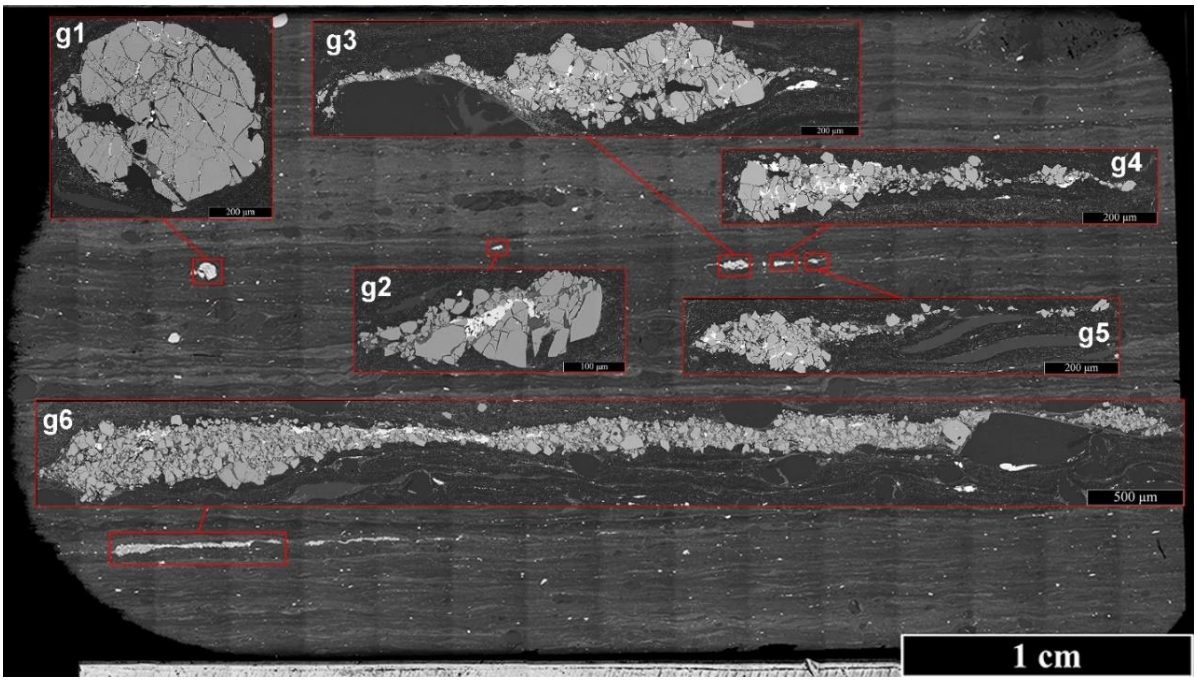

Figure 3.4 Microstructure of the SCSZ inner shear zone rock (BB12) that was dynamically deformed. Various aspect ratios for garnet grains are observed. BSE images.

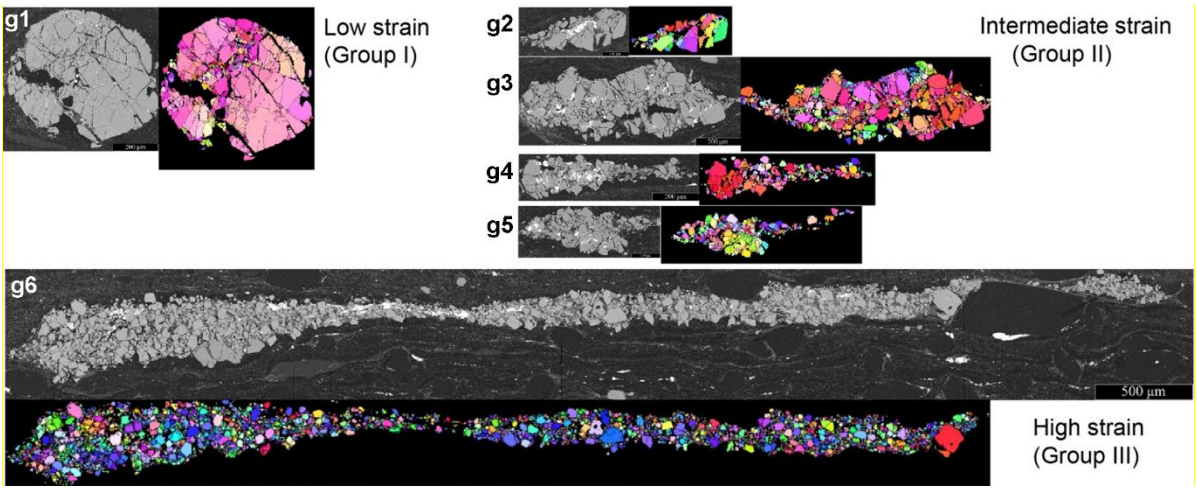

Figure 3.5 Heterogeneous garnet microstructures in the SCSZ inner shear zone rock (BB12). BSE images and EBSD maps.

3.5.1.2. PPHSZ L-Tectonite

Figure 3.6 is a BSE image of a lineation-parallel section of sample WHF-4A from the PPHSZ. The WHF-4A sample is garnet amphibolite including aggregates of fractured and fragmented garnet grains. Except for one (g1), most fractured and fragmented garnets are highly elongated. Compositional zoning is not observed within the thin section.

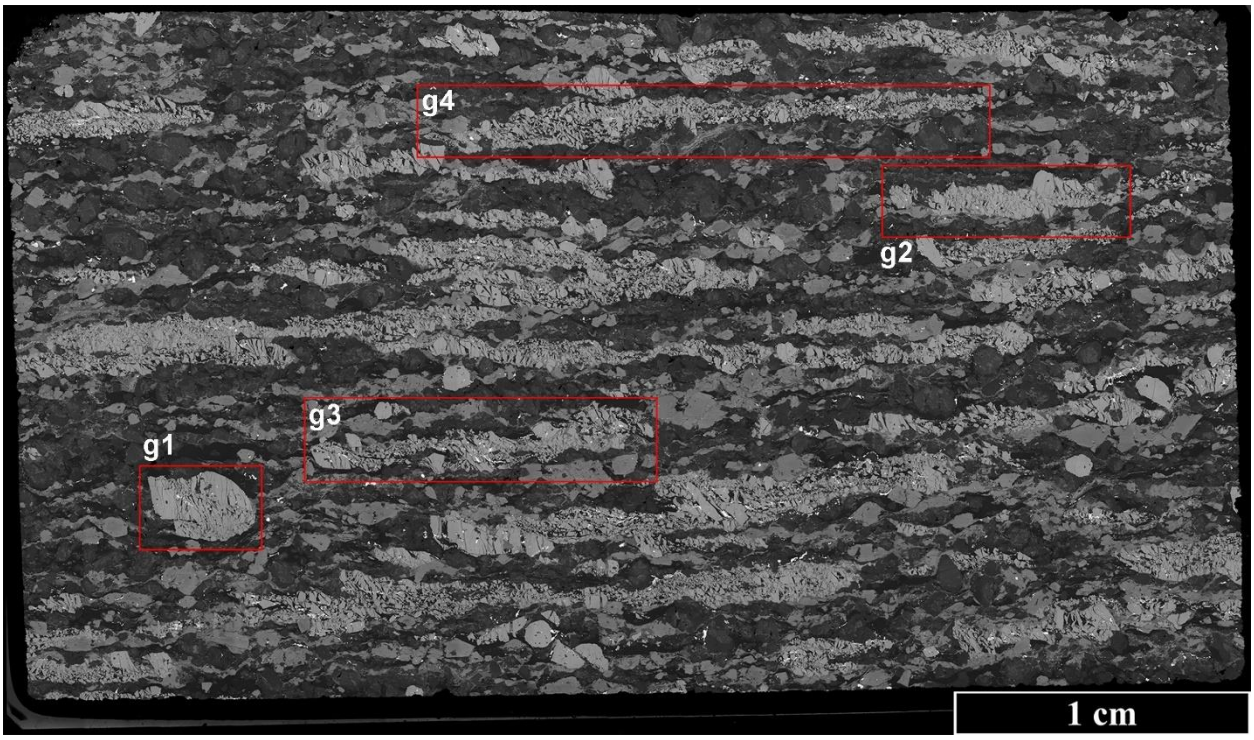

Figure 3.6 Microstructure of the PPHSZ L-tectonite (WHF-4A) that was quasi-statically deformed. Various aspect ratios for garnet grains are observed. BSE image.

3.5.2. Microfracture Intensity and Orientation

3.5.2.1. SCSZ Inner Shear Zone Rocks

BB12 garnets have relatively high microfracture intensities in the range between 111.8 mm^{-1} and 226.7 mm^{-1} (Figure 3.7). The least stretched garnet (BB12-g1) in group I has the lowest value of 111.8 mm^{-1} and BB12-g5, one of group II garnets, shows the highest value (226.7 mm^{-1}).

There are some variations, but BB12 garnets tend to show week preferred orientation of microfracture. Rose diagrams and histograms in Figures 3.8, 3.9a and 3.10a show frequency of observed microfracture orientation from 0° to 360° and from 0° to 180° in 10° classes, respectively. 0° is perpendicular to the lineation direction and angle is measured clockwise. The unstretched (group I) and highly stretched (group III) garnets show weaker preferred orientation than garnets in group II. For example, maximum value group of BB12-g1 are 7.7% between 1–10° and 41–50° and second highest value group are 7.0% between 31–40° and 71–80° while the minimum value is 3.0% between 91–100°. Difference between the maximum and minimum values is 4.7%. On the other hand, BB12-g4 shows relatively strong (sub-horizontal) preferred orientation with the maximum frequency of 13.1% between 81–90° and the minimum value of 1.6% between 171–180°. The difference between the maximum and minimum frequencies of BB12-g4 is 11.5%. BB12-g2 and g5 appear two conjugate sets of microfracture preferred orientation: sub-vertical and sub-horizontal.

3.5.2.2. PPHSZ L-Tectonite

WHF-4A garnets show relatively low intensities of microfractures compared to BB12 garnets within the narrow range between 57.8 mm^{-1} and 85.6 mm^{-1}. The most unstretched garnet (WHF-4A-g1) has the lowest value of 57.8 mm^{-1}, g2 and g3 are in 65.8 mm^{-1} and 69.5 mm^{-1}, respectively, and g4 shows the highest value of 85.6 mm^{-1}. Even the highest value of intensity in WHF-4A (85.6 mm^{-1}) is lower than the lowest value in BB12 (111.8 mm^{-1}) with difference of 26.2 mm^{-1}. Gradual increase in microfracture intensity is observed with increasing apparent aspect ratio (Figure 3.7).

Microfractures in WHF-4A garnets tend to show strong preferred orientation. Rose diagrams and histograms in Figure 3.8, 3.9b and 3.10b showing frequency of observed microfracture orientation indicate that microfractures are aligned subvertical to 90°, the transport direction (lineation). For example, the maximum value of WHF-4A-g1 is 12.5% between 171–180° and the second highest value is 11.2% between 1–10°. More than 23% of total microfractures are oriented in the range between 1–10° and 171–180°. The minimum value group are 3.4% between 71–80° and 131–140°. Difference between the maximum and

minimum values is 7.8%. Even in WHF-4A-g3, showing the second highest value of 7.9% between 81–90° and relatively week preferred orientation, the maximum value of 9.7% is between 1–10°, and more than 30% of frequency is between 1–20° and 161–180°. The difference between the maximum and minimum values of frequency in WHF-4A-g3 is 6.1%.

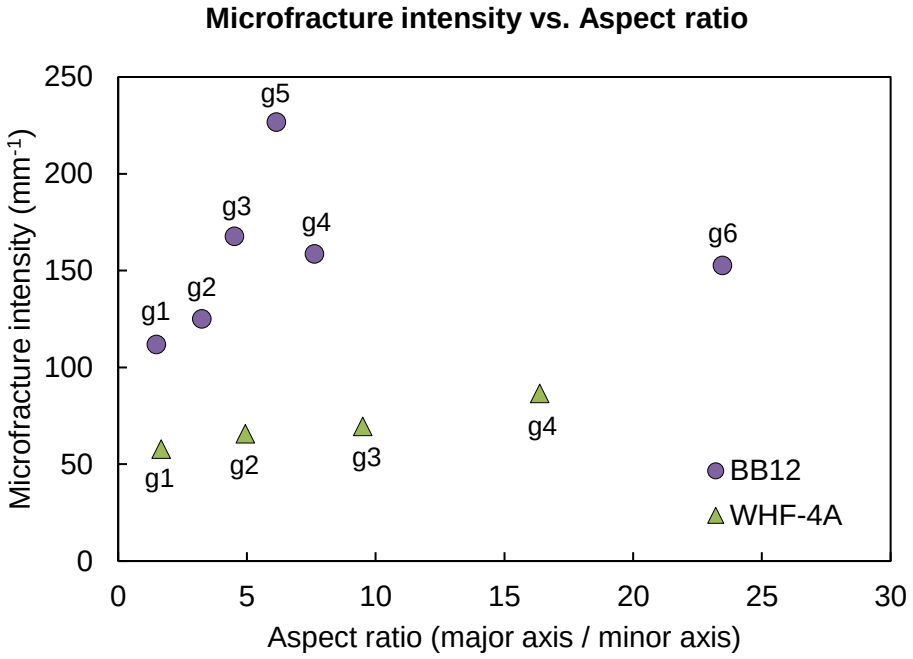

Figure 3.7 Plots of garnet microfracture intensities for the SCSZ inner shear zone rock (BB12) and the PPHSZ L-tectonite (WHF-4A) with ret to aspect ratio.

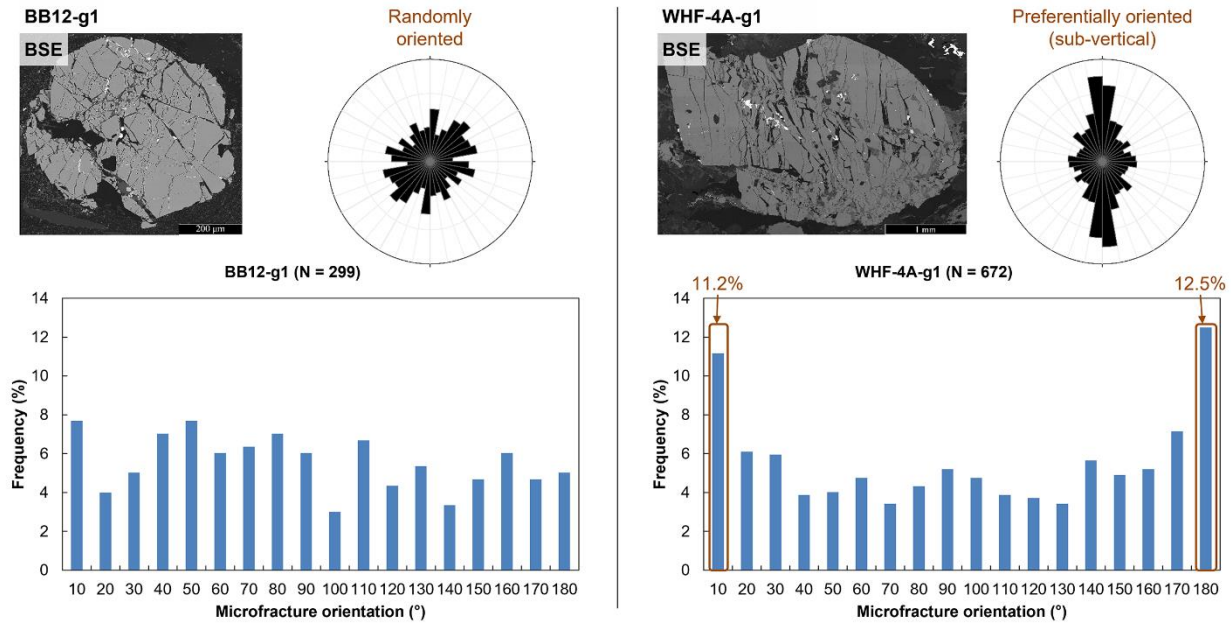

Figure 3.8 Comparison of microfracture orientation between unstretched samples for BB12 (*left*) and WHF-4A (*right*). The SCSZ sample (BB12-g1) shows more random orientation of microfracture than the L-tectonite sample (WHF-4A-g1).

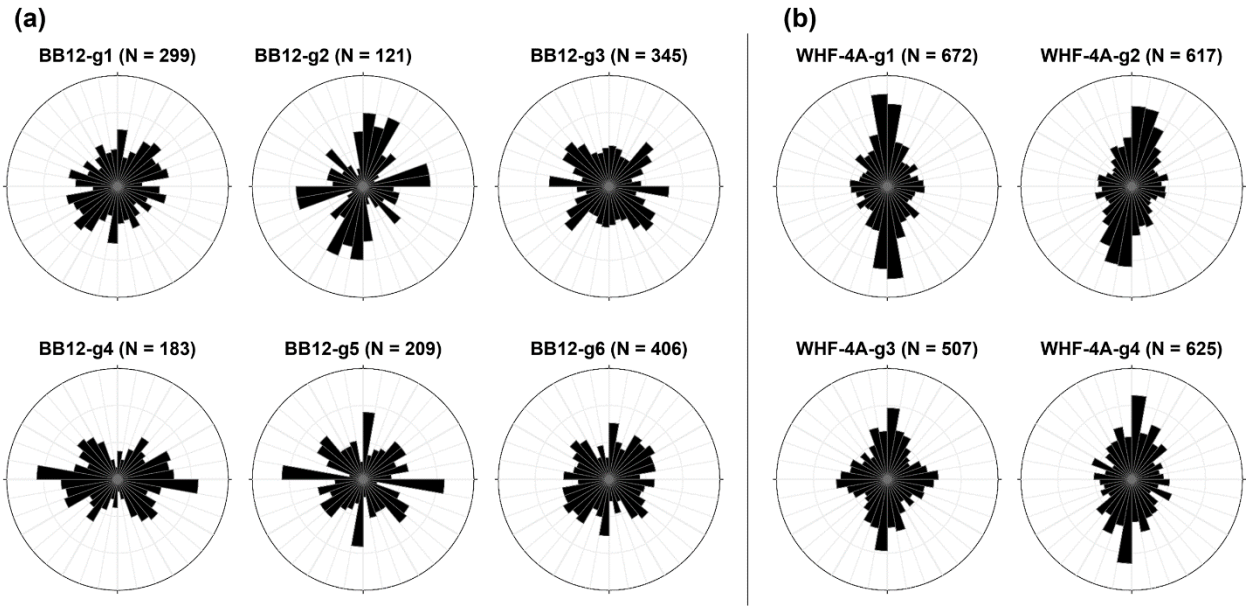

Figure 3.9 Rose diagrams showing garnet microfracture orientations for (a) the SCSZ inner shear zone rock (BB12) and (b) the PPHSZ L-tectonite (WHF-4A). The SCSZ samples have less preferred orientations than the L-tectonite samples.

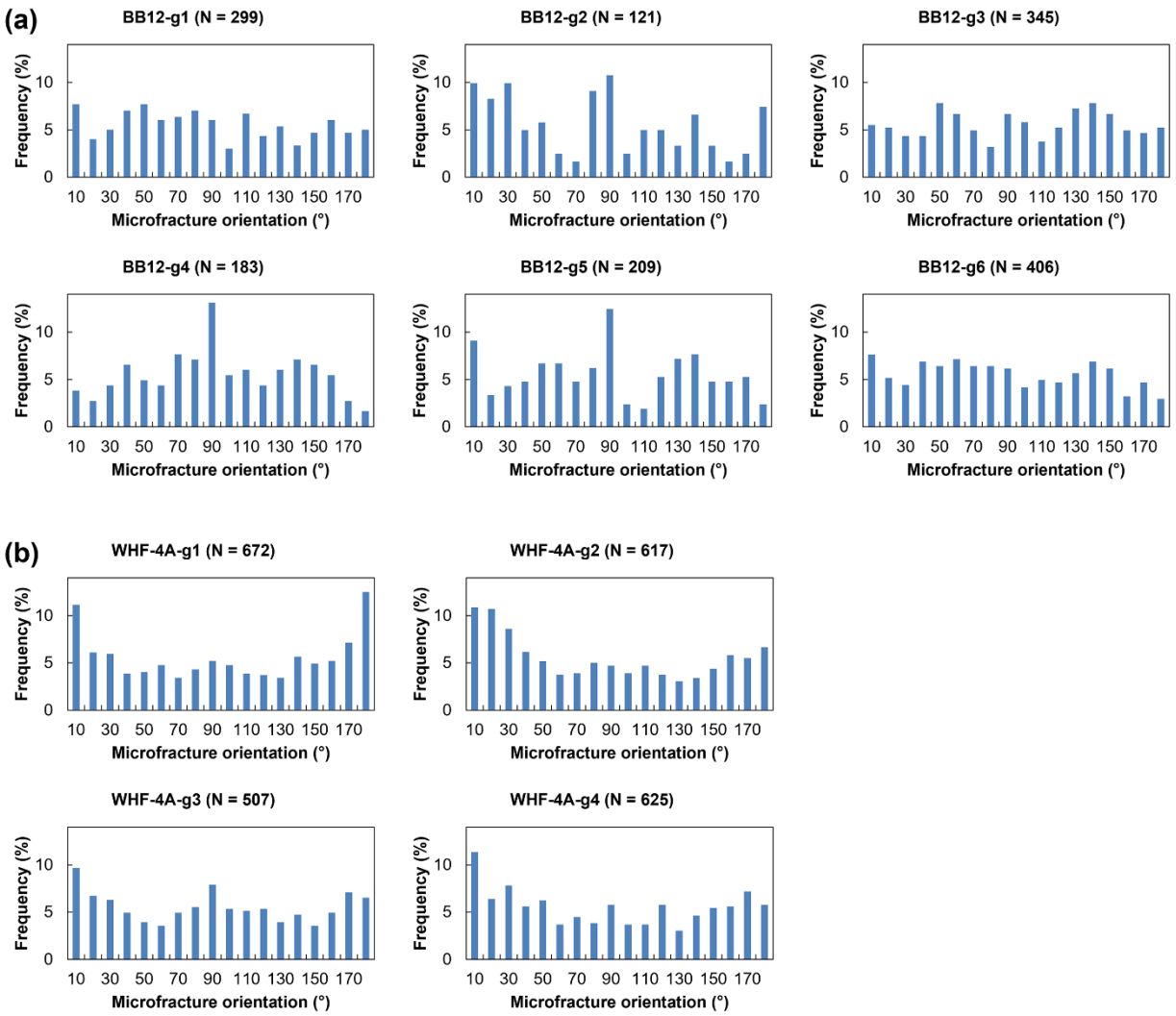

Figure 3.10 Histograms showing frequency versus garnet microfracture orientations for (a) the SCSZ inner shear zone rock (BB12) and (b) the PPHSZ L-tectonite (WHF-4A).

3.5.3. Particle Size Distribution (PSD), Fabric Intensity, and Aspect Ratio

3.5.3.1. SCSZ Inner Shear Zone Rocks

For BB12 sample, using BSE-image-based analysis, PSDs were analyzed from three garnets (BB12-g1, g4 and g6). Using EBSD-based analysis, PSDs of six garnets (BB12-g1 to BB12-g6) were analyzed. PSDs of BSE-image-based analysis exhibit strong two power law relationships with two different domains of smaller (<~10 μm) and larger (>~10 μm) fragment sizes (Figure 3.11; also see Chapter 2). However, in the case of EBSD-based analysis, PSDs for smaller fragment sizes do not exhibit such a good fit whereas PSDs for larger fragment sizes show a strong power law behavior (Figure 3.11). Figure 3.11 shows comparison of $D_{>}$-values from BSE-image-based and EBSD-based PSD analyses. In both cases, BB12-g1 shows relatively low values ($D_{>}$-values of 2.84 and 2.80, respectively) comparing with BB12-g4 ($D_{>}$-values of 3.31 and 3.01, respectively) and BB12-g6 ($D_{>}$-values of 3.16 and 3.35, respectively). Group I garnet with little rotation has $D_{>}$-value smaller than 3 whereas stretched group II and III garnets have $D_{>}$-value larger than 3 with the exception of BB12-g2 (Figures 3.11 and 3.12).

Fabric intensities (M-index) and aspect ratios were also analyzed using the EBSD method. Here, I use $D_{>}$-values obtained from EBSD-based PSD analysis. BB12-g1 with small $D_{>}$-value of 2.80 has the lowest aspect ratio (1.48) and highest M-index (0.800). In contrast, BB12-g6 with $D_{>}$-value of 3.35 has the highest aspect ratio (23.47) and lowest M-index close to 0 (0.054). As aspect ratios increase, $D_{>}$-values generally increase (Figure 3.12) whereas M-indexes tend to decrease (Figures 3.13 and 3.14).

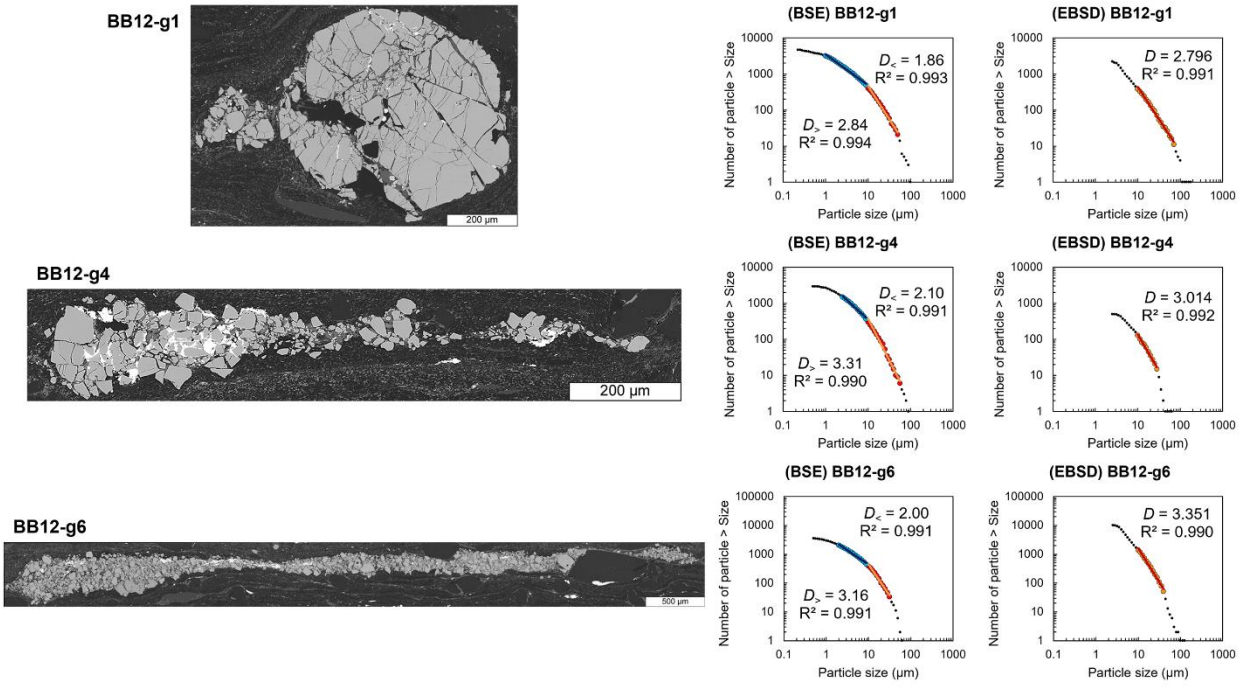

Figure 3.11 Comparison of 3D *D*-values between BSE- and EBSD-based calculations for the SCSZ inner shear zone samples (BB12-g1, g4, and g6).

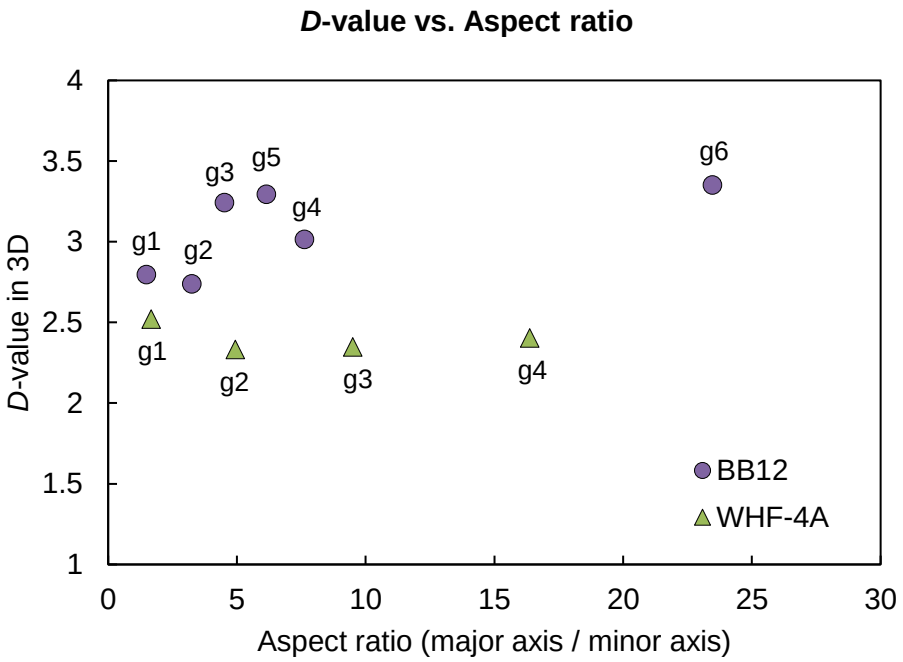

Figure 3.12 Plot of *D*-values for the SCSZ inner shear zone rock (BB12) and the PPHSZ L-tectonite (WHF-4A) with respect to aspect ratio.

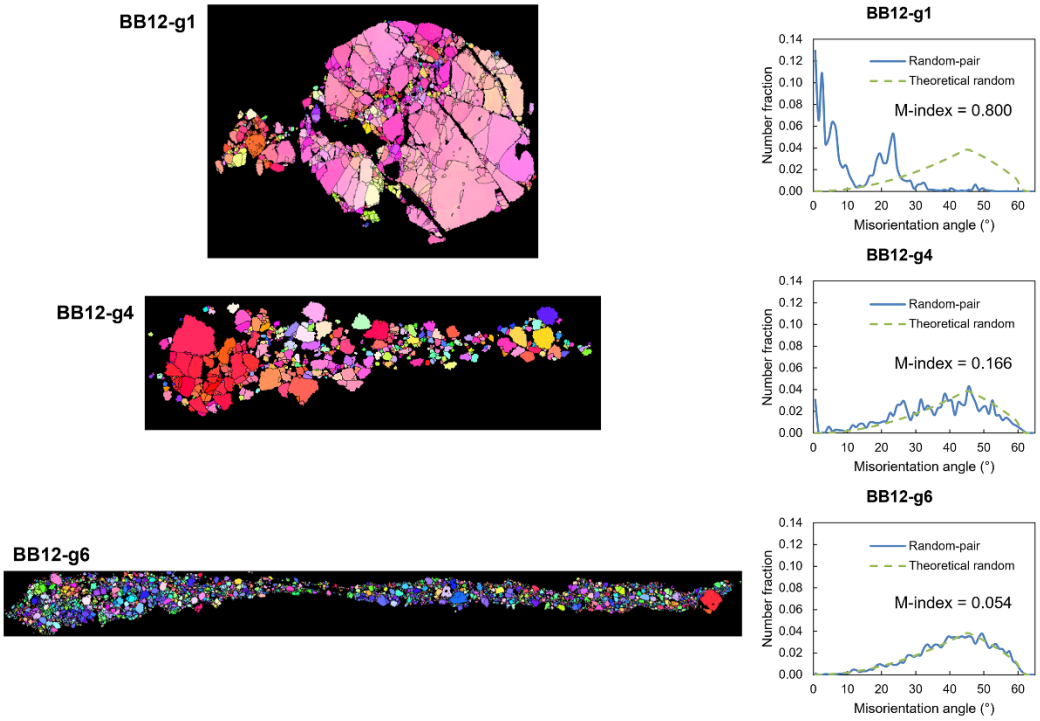

Figure 3.13 Random-pair misorientation distributions and M-index values for the SCSZ inner shear zone samples (BB12-g1, g4, and g6).

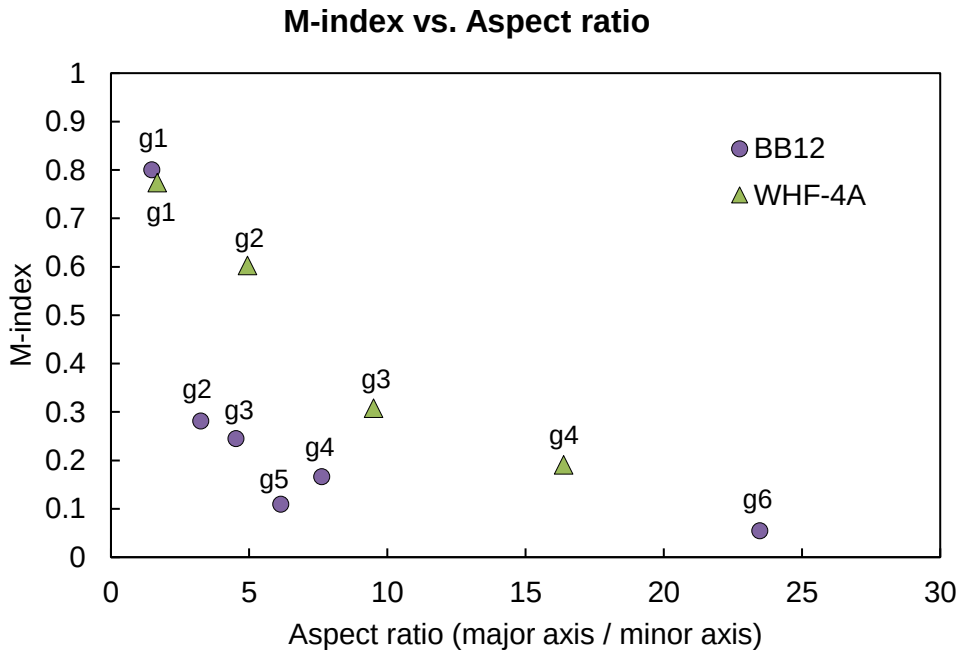

Figure 3.14 Plot of M-index for the SCSZ inner shear zone rock (BB12) with respect to aspect ratio.

3.5.3.2. PPHSZ L-Tectonite

For the WHF-4A sample, PSDs were analyzed by BSE-image-based analysis from two garnets (WHF-4A-g1 and g2) and by EBSD-based analysis from tour garnets (WHF-4A-g1 to g4). In contrast to BB12 garnets, PSDs of BSE-image-based analysis exhibit one power law relationship covering both smaller and larger fragment sizes (Figure 3.15). For example, the best-fit power-law line of WHF-4A-g1 is drawn with *D*-value of 2.30 over fragment diameters (*d*) between 7.9 μm and 79.4 μm. In the case of EBSD-based analysis, similar to BB12 garnets, PSDs for smaller fragment sizes do not exhibit such a good fit whereas PSDs for larger fragment sizes show a strong power law behavior (Figure 3.15). Figure 3.15 shows comparison of *D*-values from BSE-image-based and EBSD-based PSD analyses. In the least stretched WHF-4A-g1, *D*-value from BSE-image-based analysis (2.30) is smaller than that obtained from EBSD-based analysis (2.52). However, in the more stretched WHF-4A-g2, *D*-value from BSE-image-based analysis (2.38) is larger than that obtained from EBSD-based analysis (2.33). All the garnet grains in the PPHSZ show *D*-values less than 2.6 (Figure 3.12 and 3.15).

M-indexes and aspect ratios were also analyzed using the EBSD method. When related to EBSD-based *D*-values, WHF-4A-g1 with lowest aspect ratio (1.67) has highest M-index (0.773). In contrast, WHF-4A-g4 with highest aspect ratio (23.47) shows lowest M-index (0.190). As aspect ratios increase, $D_{>}$-values are relatively constant (Figure 3.12) whereas M-indexes decrease (Figures 3.14 and 3.16).

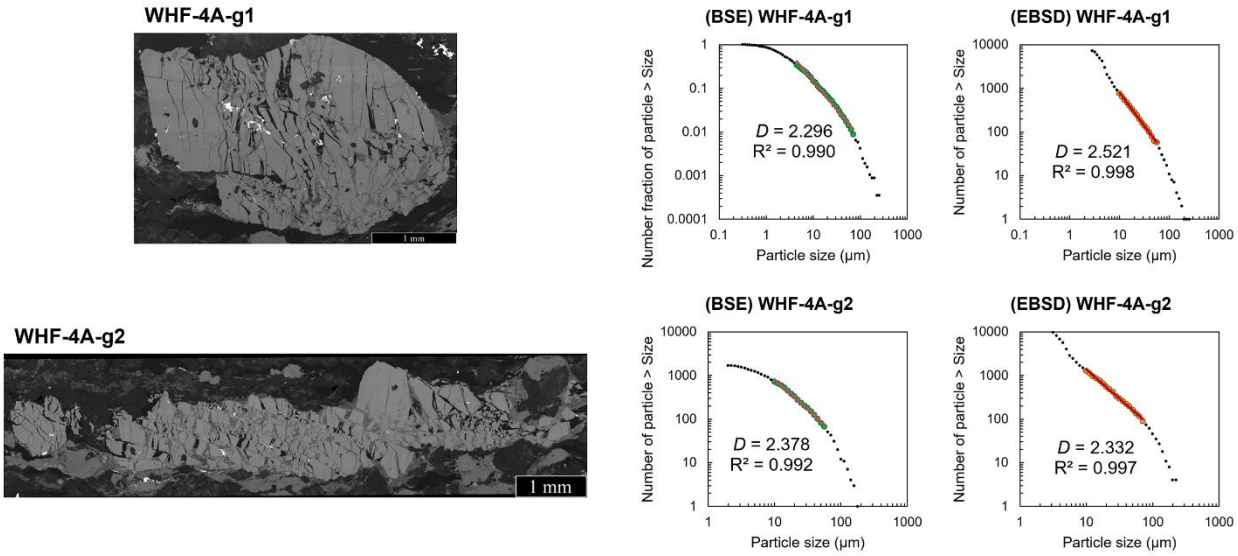

Figure 3.15 Comparison of 3D *D*-values between BSE- and EBSD-based calculations for the PPHSZ L-tectonite samples (WHF-4A-g1 and g2).

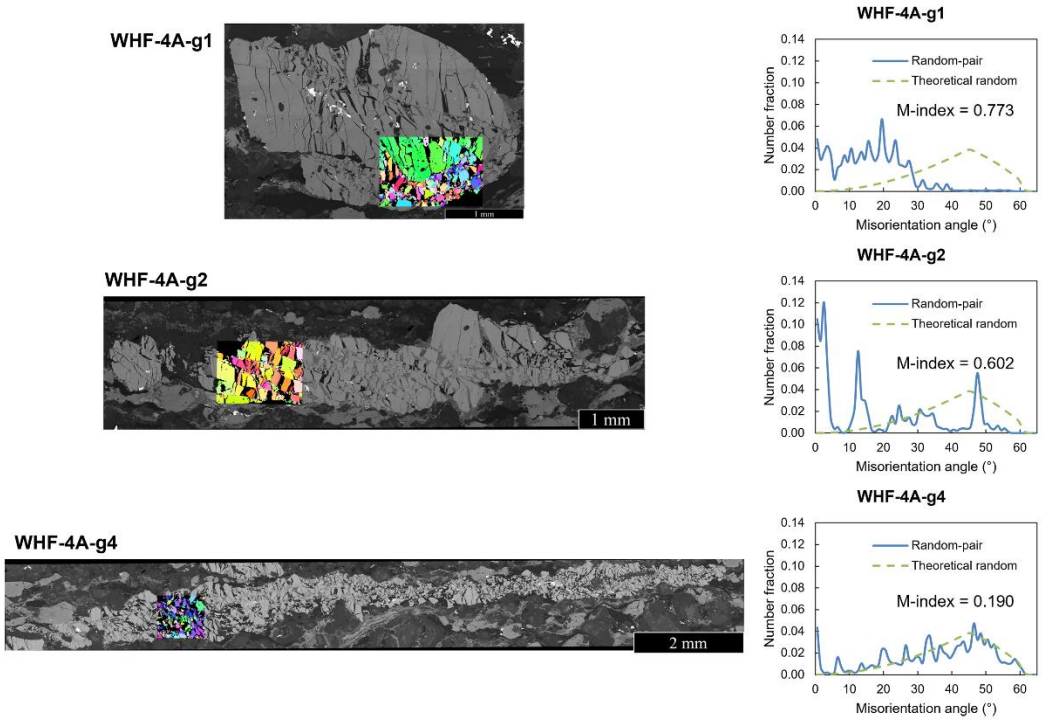

Figure 3.16 Random-pair misorientation distributions and M-index values for the PPHSZ L-tectonite samples (WHF-4A-g1, g2, and g4).

3.6. Discussion

3.6.1. Comparison of BSE-Image- and EBSD-Based PSD Analyses

In this study, I chose to fit my data to cumulative power-law distributions for both BSE-image-based and EBSD-based analyses. In BSE-image-based analyses, all samples maintain some degree of curvature over their measured range, showing progressive slope reduction towards the smaller fragments. Therefore, an empirical distribution using an exponential or exponential-like relation (such as Gamma, Rosin-Rammler, Weibull, and Voronoi) or lognormal relation may fit the wider range of fragment size from less than a micron (e.g., d = 0.4 μm) to tens of microns.

In the defense industry, fragment size of metals and other more ductile materials subjected to high-velocity impact (or explosive) loadings are often characterized by exponential or exponential-like distributions (e.g., Bennett, 1936; Gilvarry, 1961; Lienau, 1936; Botvina, 2011). However, for brittle solids such as ceramics and glasses under dynamic loading conditions, fragmentation typically follows power-law distributions (e.g., Schuhmann, 1940; Grady and Kipp, 1987). Using a wide range of natural and experimental fault rocks, Phillips and Williams (2021) demonstrated that lognormal relations best describe particle size distributions of fault rocks. However, a fractal (power-law) distribution is more extensively used to quantify and describe the fragmentation of geological materials, including fault gouge and off-fault-rock pulverization (e.g., Sammis et al., 1987; Chester et al., 2005; Rockwell et al., 2009; Wechsler et al., 2011; Muto et al., 2015), impacts and collisions of asteroid/meteorites (e.g., Donnison and Sugden, 1984; Buhl et al., 2013), magma explosion during volcanic eruptions (e.g., Dellino and Liotino, 2002 ; Kueppers et al., 2006; Perugini et al., 2011; Perugini and Kueppers, 2012), rock explosions in mining (e.g., Taşdemir. 2009), and the break-up of sea ice (e.g., Rampal et al., 2019).

In EBSE-based analysis, defining the boundary is critical for determining fragment size. Traditionally, grain boundaries are defined as angle of 10–15° (e.g., Humphreys, 2001). However, if fragments have not experienced shear deformation of the surrounding matrix, they can exhibit very small misorientation angles. Therefore, a misorientation angle of 10° is too high to identify fragment boundaries.

To identify fragments, I measured misorientation angle between all pixel pairs. After comparing with BSE images, I selected a misorientation angle of 0.3° as the cutoff. Thus, all areas showing misorientation greatere than 0.3° with neighboring areas are considered boundaries enclosing individual fragments.

$D_{>}$-values measured from the EBSD-based analysis are comparable with those from the BSE-image-based analysis. However, $D_{<}$-values from the EBSD-based analysis are much higher than the values from the BSE-image-based analysis. With such a small critical misorientation angle of 0.3°, topography near the fragment boundaries can be defined as artificial small grains that consequently increase the number of small fragments and lead to an increase in $D_{<}$-values. Therefore, in this EBSD-based PSD analysis, only $D_{>}$-values are reliable. With that, in case of EBSD-based PSD analysis, only $D_{>}$-values will be discussed in following sections.

As shown in Section 3.5.3.1, in BB12 sample, BSE-image-based PSDs of three garnets show two power law distributions with two different slopes: mild slope with $D_{<}$-values close to 2 for the smaller fragment sizes (d <~10 μm) and stepper slope with $D_{>}$-values higher than 2.8 for the larger ones (d >~10 μm). Although EBSD-based analysis of PSDs is a fast method, the mild slope with $D_{<}$-value is not detectable because of its limit described above. However, the mild slope for the smaller fragment sizes is associated with secondary surface fragmentation (see Chapter 2), and thus it is independent to determine whether or not the fragmentation is induced by dynamic loading.

3.6.2. Dynamic Versus Quasi-Static Fragmentation

3.6.2.1. Microfracture Intensity and Orientation

Microfracture patterns (intensity and orientation) of quasi-static and dynamic fragmentation were significantly different. Microfracture intensity values were significantly higher for dynamically fragmented garnets in BB12 sample of the SCSZ (between 111.82 and 240.60) compared to quasi-statically deformed

garnets in WHF-4A (between 57.76 and 85.64) (Figure 3.7). As shown in Figures 3.8, 3.9 and 3.10, microfractures in the SCSZ sample usually occur without dominant orientation while microfractures in the L-tectonite sample show strong sub-vertical orientation (limited to the range of 1–10° and 171–180°.

With increasing strain rate, the transition of fracturing to fragmentation occurs from sparse fracturing to pervasive shattering and pulverization (e.g., Yuan et al., 2011). Thus, rocks under dynamic, high-rate loading display significantly higher microfracture intensity compared to quasi-statically fractured rocks. Dynamic microfractures propagate in the radial direction owing to branching (e.g., Sagy et al., 2001; Griffith et al., 2009; Fineberg et al., 1992; Fineberg and Marder, 1999) while quasi-static microfractures display a distinct preferred orientation approximately perpendicular to the slip direction, implying the average orientation of maximum principal stress (e.g., Friedman, 1963; Engelder, 1974).

3.6.2.2. Particle Size Distribution and *D*-value

Typical *D*-values (in three-dimensional measurement) for shearing-induced fragmentation range between ~2.3 and 3.1 with average *D*-value of 2.6 (Blenkinsop, 1991). *D*-value of ~2.6 is commonly observed in many natural and experimental fault gouges (e.g., Biegel et al., 1989; Marone and Scholz, 1989; Sammis et al., 1986,1987; Sammis and Biegel, 1989) and predicted by the constrained comminution model of Sammis et al. (1986). In the constrained comminution model, neighboring particles constrain particle movement, and the relative size of neighboring particles controls probability of particle fracturing. In the constrained comminution theory, fragmentation is predicted when similar size particles are juxtaposed. *D*-values of 2.30–2.52 in the L-tectonite sample indicate comminution during shear displacement of fragments.

The particle size distribution with *D*-values ranging between 2.74 and 3.35 suggests that pulverization of sample BB12 in the inner shear zone of the SCSZ is not simply a consequence of shearing. Rocks fragmented by explosion often have *D*-values greater than 2.5 and even above 3 (e.g., Barnett, 2004; Bjork et al., 2009; O'keefe and Ahrens, 1985; Schoutens, 1979).

3.6.2.3. Effect of Shear Strain

With shearing, continued attrition and grinding at the fragment surface causes reduction of fragment size, resulting in increase of microfracture intensity (Figure 3.7). Rotation and flow during shear displacement cause fragments to align preferentially along flow (Jebrak, 1997), and thus in both quasi-statically and dynamically fragmented samples, with increasing aspect ratio, microfracture orientation tends to appear some degree of preferred orientation parallel to horizontal direction.

Plot of *D*-value versus aspect ratio (Figure 3.12) shows *D*-value increase with strain in both quasi-statically and dynamically fragmented garnets. With increase of displacement during shear flow, continued attrition and grinding at the fragment surface causes reduction of fragment size, resulting in increase of the proportion of smaller fragments, as noted in experiments investigating gouge formation (Engelder, 1974). Since *D*-values describe the abundance of smaller particles relative to larger particles, increasing the proportion of smaller fragments creates a steeper slope with a higher *D*-value. It is also supported by the inverse correlation between the average fragment size and *D*-value. Garnet WHF-4A-g1 with the lowest aspect ratio among four garnets in the sample has the highest *D*-value in measurement of EBSD-based analysis although all *D*-values are in similar ranges. This is because the EBSD-based *D*-value of WHF-4A-g1 is estimated within a small area that shows relatively high rotation. The BSE-image based *D*-value measured from the entire area of WHF-4A-g1 reveals slightly lower value compared to other three garnets in WHF-4A sample.

3.6.3. Comparison of PSD With Other Studies of Shear-Related Fragmentation

It is difficult to determine whether rock fragmentation in faut/shear zones is produced by seismic (dynamic) or aseismic (quasi-static) loading (Cowan, 1999; Sibson, 1989). A wide range of fault rock studies demonstrates that most cataclasites and gouges may have resulted from seismic deformation, but their PSDs (or *D*-values) are not distinguishable from those of aseismic shear fragmentation. Based on experimentally sheared granitoid gouges, Stunitz et al. (2010) concluded that *D*-values of fault rocks are independent of slip rates for shear strain (Υ) >20. Keulen et al. (2007, 2008) showed that *D*-value of gouge

developed by high-speed experiments (at slip rates between 0.65 and 1.28 m/s) ranges between 3.24 and 3.26, whereas low-speed experiments (at slip rates of ~1 μm/s) produced *D*-value of 2.89–3.33. On the other hand, Marone and Scholz (1989) observed *D*-value of ~2.6 for small displacement (Υ = 1.5–2).

Three-dimensional *D*-values of the SCSZ and PPHSZ samples are compared with other natural fault rocks and experimentally sheared rocks in Figure 3.17. *D*-values measured from breccias, gouges, and cataclasites of natural faults are highlighted by the light green area (*D* = 1.88–3.6; Sammis et al., 1987; Sammis and Biegel, 1989; Blenkinsop, 1991; An and Sammis, 1994; Shao and Zou, 1996; Monzawa and Otsuki, 2003; Storti et al., 2003; Billi and Storti, 2004; Chester et al., 2005; Ma et al., 2006; Keulen et al., 2007; Pittarello et al., 2008; Balsamo and Storti, 2011; Fondriest et al., 2012). Experimentally sheared rocks are highlighted by dark green area, showing *D*-value of 2.54–3.26 (Biegel et al., 1989; Marone and Scholz, 1989; Stunitz et al., 2010). *D*-value of 2.6 predicted by the constrained comminution theory is also presented by black dashed line in Figure 3.17.

The dynamically pulverized garnets with different aspect ratios in the SCSZ have 3D *D*-values (2.74–3.35) higher than the comminution theory and within the range of natural fault rocks. Comparing with the shear experiments, most SCSZ garnets show *D*-values corresponding to the range of the experiments, but two garnets including one with highest aspect ratio have *D*-values above the experimental values. In contrast, the quasi-statically deformed garnets of L-tectonite in the PPHSZ show *D*-values lower than the comminution theory and the shear experiments although they are within the range of natural fault rocks. The fact that the dynamically and quasi-statically fragmented and sheared garnets are separated by the value predicted by comminution theory implies that PSD analysis can still be useful for an indicator of dynamic loading at the FVT regardless of post-fragmentation shear strain.

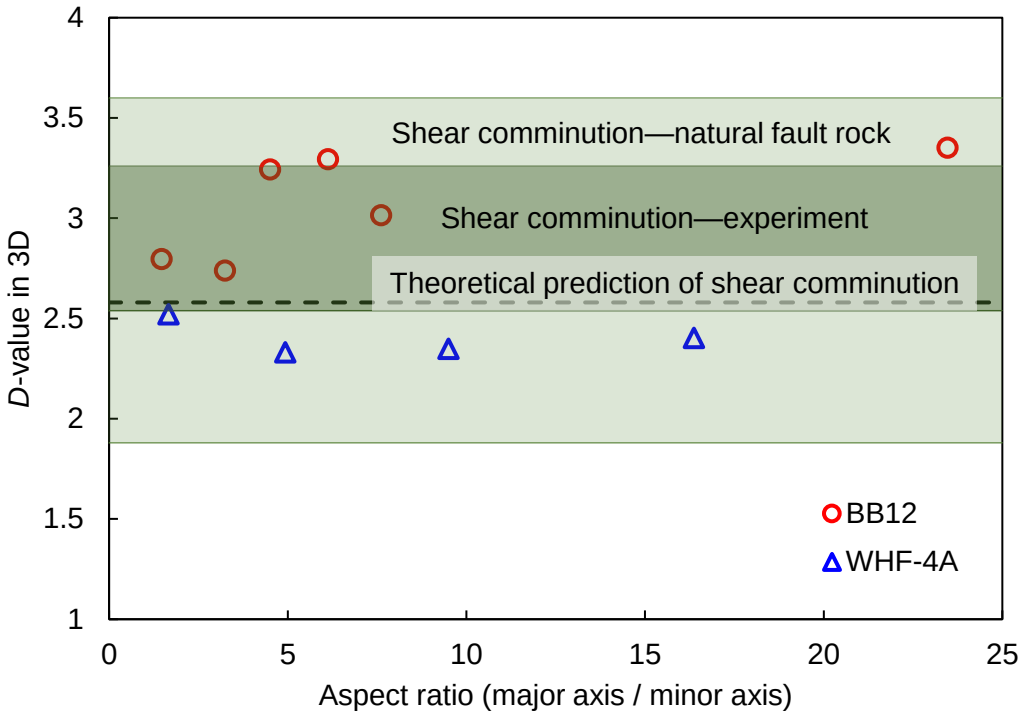

Figure 3.17 Comparison of 3D *D*-values with other natural fault rocks and experimentally sheared rocks. Theoretical *D*-value of shear comminution is marked by dashed line. Red circles are the dynamically deformed SCSZ samples (BB12) and blue triangles are quasi-statically deformed L-tectonite samples (WHF-4A).

3.7. Chapter Conclusions

This chapter has presented microfracture intensity, microfracture orientation, and particle size distribution data of fractured and fragmented garnet grains from seismogenic shear zone (the SCSZ) and tectonic structure (the PPHSZ) to compare rock fragmentation under dynamic and quasi-static loadings. The results demonstrate that dynamically pulverized garnets in the SCSZ rock show high intensity and weak preferred orientation of microfractures whereas quasi-statically sheared garnets in the PPHSZ rock have relatively low intensity and strong preferred orientation of microfractures. Pulverized garnets experiencing dynamic fragmentation with/without shear strain reveal *D*-values in 3D between 2.5 and 3.5. In contrast, fractured and fragmented garnets under quasi-static shear deformation show *D*-values in 3D

less than 2.5. A change in fragmentation process from volumetric shattering during dynamic rupture to surface crushing and grinding during comminution leads to significant difference in microfracture pattern and particle size distribution.

CHAPTER 4

ELASTIC CONTRAST, RUPTURE DIRECTIVITY, AND DAMAGE ASYMMETRY IN AN ANISOTROPIC BIMATERIAL STRIKE-SLIP FAULT AT MIDDLE CRUSTAL DEPTHS[2]

4.1. Chapter Abstract

Mature faults with large cumulative slip often separate rocks with dissimilar elastic properties and show asymmetric damage distribution. Elastic contrast across such bimaterial faults can significantly modify various aspects of earthquake rupture dynamics, including normal stress variations, rupture propagation direction, distribution of ground motions, and evolution of off-fault damage. Thus, analyzing elastic contrasts of bimaterial faults is important for understanding earthquake physics and related hazard potential. The effect of elastic contrast between isotropic materials on rupture dynamics is relatively well studied. However, most fault rocks are elastically anisotropic, and little is known about how the anisotropy affects rupture dynamics. We examine microstructures of the Sandhill Corner shear zone, which separates quartzofeldspathic rock and micaceous schist with wider and narrower damage zones, respectively. This shear zone is part of the Norumbega fault system, a Paleozoic, large-displacement, seismogenic, strike-slip fault system exhumed from middle crustal depths. We calculate elastic properties and seismic wave speeds of elastically anisotropic rocks from each unit having different proportions of mica grains aligned sub-parallel to the fault. Our findings show that the horizontally polarized shear wave propagating parallel to the bimaterial fault (with fault-normal particle motion) is the slowest owing to the fault-normal compliance and therefore may be important in determining the elastic contrast that affects rupture dynamics in anisotropic media. Following results from subshear rupture propagation models in isotropic media, our results are consistent with ruptures preferentially propagated in the slip direction of the schist, which has the slower horizontal shear wave and larger fault-normal compliance.

[2] The content of this chapter has been published in: Song, B.R, Song, W.J., Johnson, S.E., Gerbi, C.C., Vel, S.S., 2022, Journal of Geophysical Research: Solid Earth, 127, e2021JB023821, https://doi.org/10.1029/2021JB023821.

4.2. Chapter Plain Language Summary

Earthquake faults that separate geologic materials with different elastic properties are referred to as bimaterial faults. Elastic contrast across bimaterial faults can modify rupture dynamics including rupture propagation direction and earthquake intensity and is therefore important for understanding potential earthquake hazards. The effects of elastic contrast between elastically isotropic materials (same elastic properties in all directions) on rupture propagation are reasonably well understood. However, rocks separated by natural faults are typically elastically anisotropic (having different elastic properties in different directions), and we know relatively little about the effects of this anisotropy on rupture propagation. To better understand the effects of elastic anisotropy, we analyze anisotropic rocks with different mica proportions collected from both sides of an ancient strike-slip earthquake fault, in which mica grains are aligned sub-parallel to the fault. We calculate the velocities of seismic waves in these rocks and their elastic contrast. We find that analysis of the horizontal shear wave propagating parallel to the sub-vertical fault plane gives results that are consistent with rupture propagation theory for isotropic materials. Thus, the shear-wave propagation direction should be considered when measuring seismic velocities and calculating elastic contrasts to investigate rupture along natural faults in anisotropic rocks.

4.3. Chapter Introduction

A bimaterial interface separating different materials is common along mature faults. Examples include strike-slip faults separating tectonic plates with different rock types (e.g., Allam et al., 2014), subduction zones separating continental and oceanic crust (e.g., Turcotte and Schubert, 2014), and in the context of glacial earthquakes, ice-rock interfaces at the base of glaciers (e.g., Weertman, 2005; Danesi et al., 2007). When considering strike-slip faults, rupture along a bimaterial interface is fundamentally different from rupture along a homogeneous interface (e.g., Weertman, 1980: Adams, 1995; Andrews and Ben-Zion, 1997; Rice et al., 2001; Shi and Ben-Zion, 2006; Ampuero and Ben-Zion, 2008; Brener et al., 2016). On a planar interface in a homogeneous isotropic medium bounded by similar materials with identical elastic stiffness and density, the shear source radiation moves with a symmetric disturbance on

both sides of the interface. In this case, no coupling occurs between shear slip and normal stress on the interface, and therefore no change in normal stress occurs on the interface (Figure 4.1a; e.g., Ben-Zion, 2001). In contrast, for an isotropic bimaterial planar interface bounded by materials with different elastic stiffness and density, the symmetry of the near-tip stress and displacement fields across the interface are broken (Figure 4.1b; e.g., Ben-Zion, 2001). As a result, variations of normal stress are theoretically expected to couple to perturbations of in-plane slip on the interface ("bimaterial coupling"). Due to the bimaterial coupling in mode II (in-plane shear) ruptures, the sense of normal stress variation on the interface during propagation in one direction is reverse of the sense in the opposite direction. For a standard subshear rupture propagating in the slip direction of the more compliant material (so-called "positive" direction), normal stress can be dynamically reduced near the rupture tip. This normal stress reduction produces dilation and spatially localized pulse-like slip at the leading edge of the rupture tip, facilitating rupture propagation (Figures 4.1b and 4.1c; e.g., Weertman, 1980; Andrews and Ben-Zion, 1997; Ben-Zion and Huang, 2002). In the opposite "negative" direction (the slip direction of the stiffer material) of a subshear rupture, dynamic increase in normal stress at the trailing edge of the rupture tip causes compression that arrests the slip motion behind the rupture front, suppressing rupture propagation in the negative direction (Figure 4.1c; e.g., Shi and Ben-Zion, 2006; Ampuero and Ben-Zion, 2008). For these reasons, rupture propagation during bimaterial rupture is expected to be predominantly unidirectional (e.g., Andrews and Ben-Zion, 1997; Ampuero and Ben-Zion, 2008; Dalguer and Day, 2009; Erickson and Day, 2016; Xu and Ben-Zion, 2017).

Preferred rupture propagation (or rupture directivity) along bimaterial faults is of great interest in seismology and earthquake engineering communities because of its effect on near-fault ground motions (e.g., Brietzke et al., 2009). In near-field regions of bimaterial faults, the subshear rupture propagating in a positive direction generates pulse-like ground motions from shear waves characterized by large amplitudes, long periods, and short durations (e.g., Bertero et al., 1978; Boatwright and Boore, 1982; Bernard et al., 1996; Yazdani et al., 2017; Zhai et al., 2018). These motions are distinct from ordinary non-pulse-like ground motions that are commonly observed in far-field regions. An important feature of the impulsive

shear-wave motions is large particle displacements normal to the fault relative to those parallel to the fault (Figure 4.1c; e.g., Somerville et al., 1997; Ben-Zion, 2001). Moreover, the long-period average pulse-like motions in both fault-normal and fault-parallel directions in the near field are more intense than the far-field motions (e.g., Bray et al., 2009). Consequently, the pulse-like near-field ground motions in the positive direction of bimaterial faults are potentially more destructive and can cause serious damage to human-made structures (e.g., Hall et al., 1995; Kalkan and Kunnath, 2006; Champion and Liel, 2012). Therefore, accurately predicting rupture directivity and resultant ground motions are of growing importance for estimating the seismic hazard near faults.

Rupture directivity also influences the distribution of off-fault rock damage. Ruptures in a homogeneous isotropic medium that propagate bilaterally without a preferred direction produce rock damage (tensile fractures with preferred orientation) primarily in the two tensile quadrants of the radiated seismic field (Figure 4.1d; e.g., Poliakov et al., 2002; Dalguer et al., 2003; Andrews, 2005; Ben-Zion and Shi, 2005; Rice et al., 2005; Griffith et al., 2009; Thomas et al., 2017; Xu and Ben-Zion, 2017; Thomas and Bhat, 2018; Okubo et al., 2019). Thus, a relatively symmetrical distribution of damage is expected around the homogeneous fault after multiple rupture events with different hypocenter locations. In contrast, the cumulative effect of multiple rupture propagation events with a preferred direction along isotropic bimaterial faults generates asymmetric damage, with more damage on the stiffer side of the fault, or in the tensile quadrant for each wrinkle-like pulse propagating in the positive direction (Figure 4.1e; e.g., Ben-Zion and Shi, 2005; Xu and Ben-Zion, 2017). Highly fractured and pulverized rocks in the damage zones of bimaterial faults typically exhibit tensile microfractures with little apparent preferred orientation (Figure 4.1e; e.g., Rempe et al., 2013; Xu and Ben-Zion, 2017).

In the above context, analyzing contrasts in elastic and seismic properties of bimaterial faults is an important step towards a better understanding of rupture directivity and related hazard potential. In elastically isotropic media, the effect of elastic contrast between two different materials (e.g., bimaterial coupling) is relatively well studied through theoretical and numerical experiments (e.g., Weertman, 1980; Andrews and Ben-Zion, 1997; Cochard and Rice, 2000; Adda-Bedia and Ben Amar, 2003; Ampuero and

Ben-Zion, 2008). However, most crustal rocks are elastically anisotropic and show seismic anisotropy, or directional dependence of seismic velocity (e.g., Babuška and Cara, 1991; Christensen and Mooney, 1995; Almqvist and Mainprice, 2017). The anisotropy causes change of elastic contrast between natural rocks depending on direction, and even a switch of relative strength (e.g., from stiffer to more compliant rock) might occur in certain directions. Although some workers investigated damage asymmetry in natural bimaterial faults and discussed their preferred rupture propagation directions (e.g., Dor et al., 2006a, 2006b; Dor et al., 2008; Mitchell et al., 2011; Rempe et al., 2013; B. R. Song et al., 2020), they did not analyze elastic or seismic contrast of the anisotropic rocks. In the present study, we investigate potential effects of elastic contrast (represented by difference in seismic wave velocity) on rupture directivity and damage distribution in bimaterial faults/shear zones separating dissimilar and elastically anisotropic rocks. We calculate elastic properties and seismic wave velocities of two anisotropic rocks (quartzofeldspathic rock and mica-rich schist) juxtaposed across the deeply exhumed, seismogenic Sandhill Corner shear zone, an ancient strike-slip fault that exhibits strongly asymmetric damage distribution (B. R. Song et al., 2020; Johnson et al., 2021b). We determine elastic contrast of the anisotropic rocks and conclude that the horizontally polarized shear wave propagating parallel to the fault may be the most relevant wave to consider when comparing our results to isotropic bimaterial rupture models. To further explore and generalize our results, synthetic microstructures with mica preferred orientation are used to conduct sensitivity analysis on the effect of modal mineralogy (i.e., mica proportion from 0% to 100%) on seismic contrast and rupture directivity. We compare our results of seismic anisotropy and contrast to published data of other natural rocks with various mica contents.

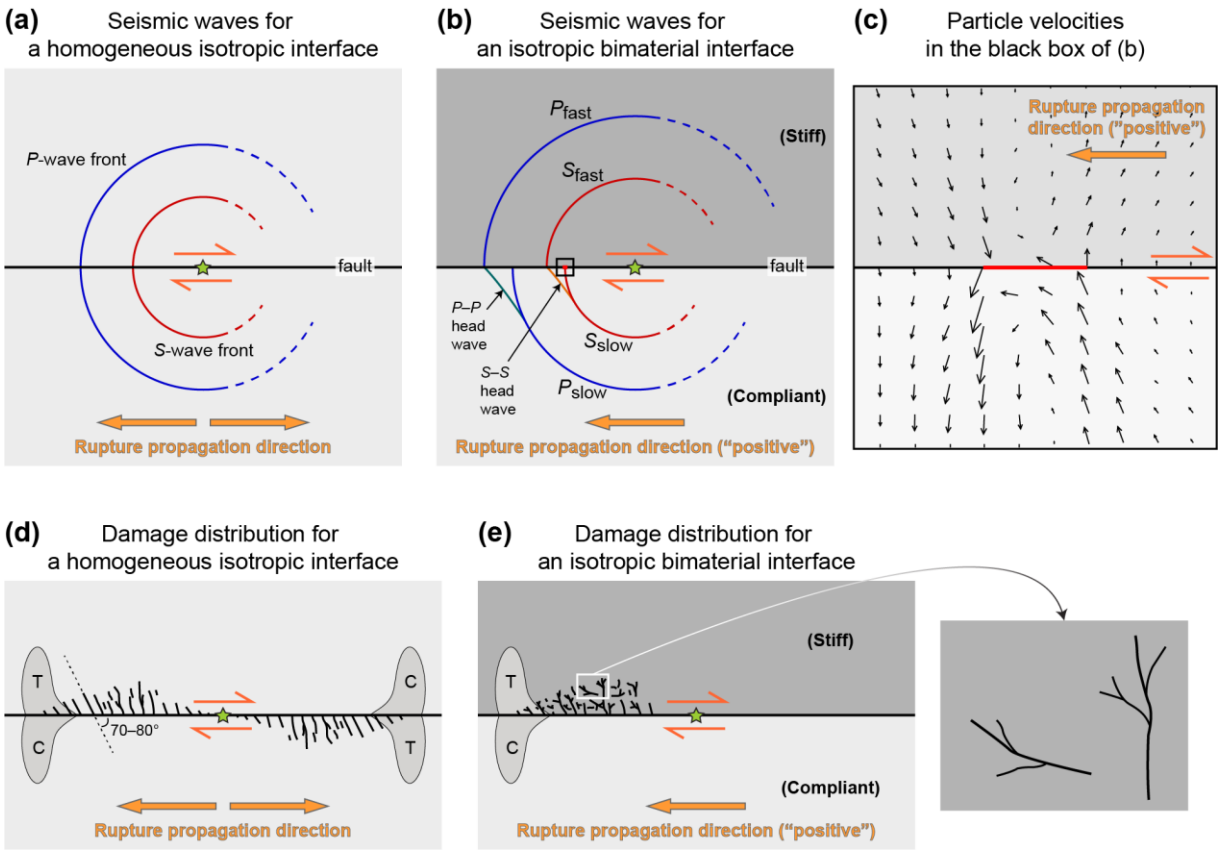

Figure 4.1 Plan view illustration of seismic waves, particle velocities, and damage distributions generated by subshear rupture along right-lateral strike-slip faults in elastically isotropic media. (a) *P*- and *S*-wave fronts at a given time for a homogeneous isotropic interface between identical solids, showing symmetry with respect to the interface. Rupture is propagating in both directions (left and right). (b) *P*- and *S*-wave fronts at a given time for an isotropic bimaterial interface in stiff (upper block) and compliant (lower block) materials. The compliant block has slower *P*- and *S*-wave fronts (P_{slow} and S_{slow}, respectively) and two different head wave fronts (*P*-to-*P* between P_{fast} and P_{slow} and *S*-to-*S* between S_{fast} and S_{slow}). A wrinkle-like rupture pulse (small red bar within the black box) is propagating to the left. In (a) and (b), the left-propagating wave fronts (solid lines) are traced from the numerical simulations of particle velocities by Ben-Zion (2001), and the corresponding right-propagating wave fronts (dashed lines) are extrapolated from these results. (c) Enlarged view of the black box in (b) showing asymmetric particle velocities (black arrows) near the rupture pulse. Note larger particle velocities in the more compliant material (below the interface) than in the stiffer material (above the interface). Consequently, tension and compression occur near the rupture tips in the "positive" and "negative" directions, respectively (left and right sides of the red bar), allowing rupture propagation to the "positive" direction (the slip direction of the more compliant material). After Ben-Zion (2001) and Dor et al. (2006b). (d) Simplified schematic drawing of damage (fracture) distribution generated by a crack-like rupture in a homogeneous isotropic medium. Off-fault fractures are produced in rocks on both sides of the fault but on the tensile (T) rather than compressional (C) side of each rupture front. Although the fractures here are oriented at high angles (70–80°) to the fault, the angle could vary with the stress state around the fault. Modified from Ben-Zion and Shi (2005), Griffith et al. (2009), and Okubo et al. (2019). (e) Simplified schematic drawing of damage (fracture) distribution generated by a wrinkle-like rupture propagating to the left in an isotropic bimaterial medium. Off-fault fractures are produced only in the tensile (T) quadrant on the stiffer side of the fault and have little apparent preferred orientation. Modified from Ben-Zion and Shi (2005) and Xu and Ben-Zion (2017). Green stars in (a), (b), (d) and (e) indicate nucleation point.

4.4. The Sandhill Corner Shear Zone of the Norumbega Fault System

4.4.1. Geologic Setting

The Sandhill Corner shear zone (SCSZ) is located in the south-central portion of the Norumbega fault system in the northeastern Appalachians of North America (Figure 4.2a). Field and geochronological studies suggest that the Norumbega fault experienced regional scale, orogen-parallel, dextral strike-slip shear deformation in the late Paleozoic (Ludman et al., 1999; West, 1999; Wang and Ludman, 2004). Although total displacement along the fault system is uncertain, estimates of 25–300 km have been reported on the basis of map relations and shear strain analysis (Swanson, 1992; Hubbard, 1999; Wang and Ludman, 2004). The Norumbega fault spans a length of nearly 450 km from southwestern Maine, USA to central New Brunswick, Canada (Figure 4.2a; e.g., Newberg, 1985; Hussey et al., 1986; Swanson et al., 1986; Hussey, 1988; Swanson, 1992; Pankiwskyj, 1996; Ludman, 1998) and possibly extends up to ~1200 km from Connecticut, USA to the Gulf of St. Lawrence, Canada (Figure 4.2a; Ludman, 1998; Goldstein and Hepburn, 1999), comparable to the overall length of the San Andreas fault, California, USA. Seismic reflection profiles suggest that strands of the Norumbega fault crosscut the Moho (e.g., Doll et al., 1996).

The SCSZ in the study area (Figures 4.2a and 4.2b) is a ~230 m wide shear zone that contains quartz- and feldspar-rich mylonitic rocks of the Cape Elizabeth Formation on the northwest side and sheared mica-rich schist of the Crummett Mountain Formation on the southeast side (Grover and Fernandes, 2003; West and Peterman, 2004; Price et al., 2016), and thus can be referred to as a bimaterial fault/shear zone. Pseudotachylyte is observed within ~40 m of the shear zone core in the quartzofeldspathic (QF) rocks and within ~5 m of the core in the schist (Price et al., 2012; W. J. Song et al., 2020). The mylonitic foliation of the SCSZ is subvertical and northeast-trending, having subhorizontal stretching lineation (Figure 4.2c). The QF and schist host rocks show sub-parallel foliation to that of the SCSZ (Figure 4.2c). The seismogenic parts of the shear zone were active at temperatures of 400–500 °C (Price et al., 2016), indicating it was exhumed from middle crustal depths. Mean kinematic vorticity number of 0.97 and microstructures of shear bands, muscovite fish and mantled feldspar porphyroclasts in the SCSZ indicate approximately strike-slip

flow with dextral sense of shear (West and Hubbard, 1997; Johnson et al., 2009). These observations ensure that the maximum principal stress was oriented at an angle somewhat larger than 45° from the fault plane, allowing direct comparisons with dynamic rupture modeling in Section 4.7.2.

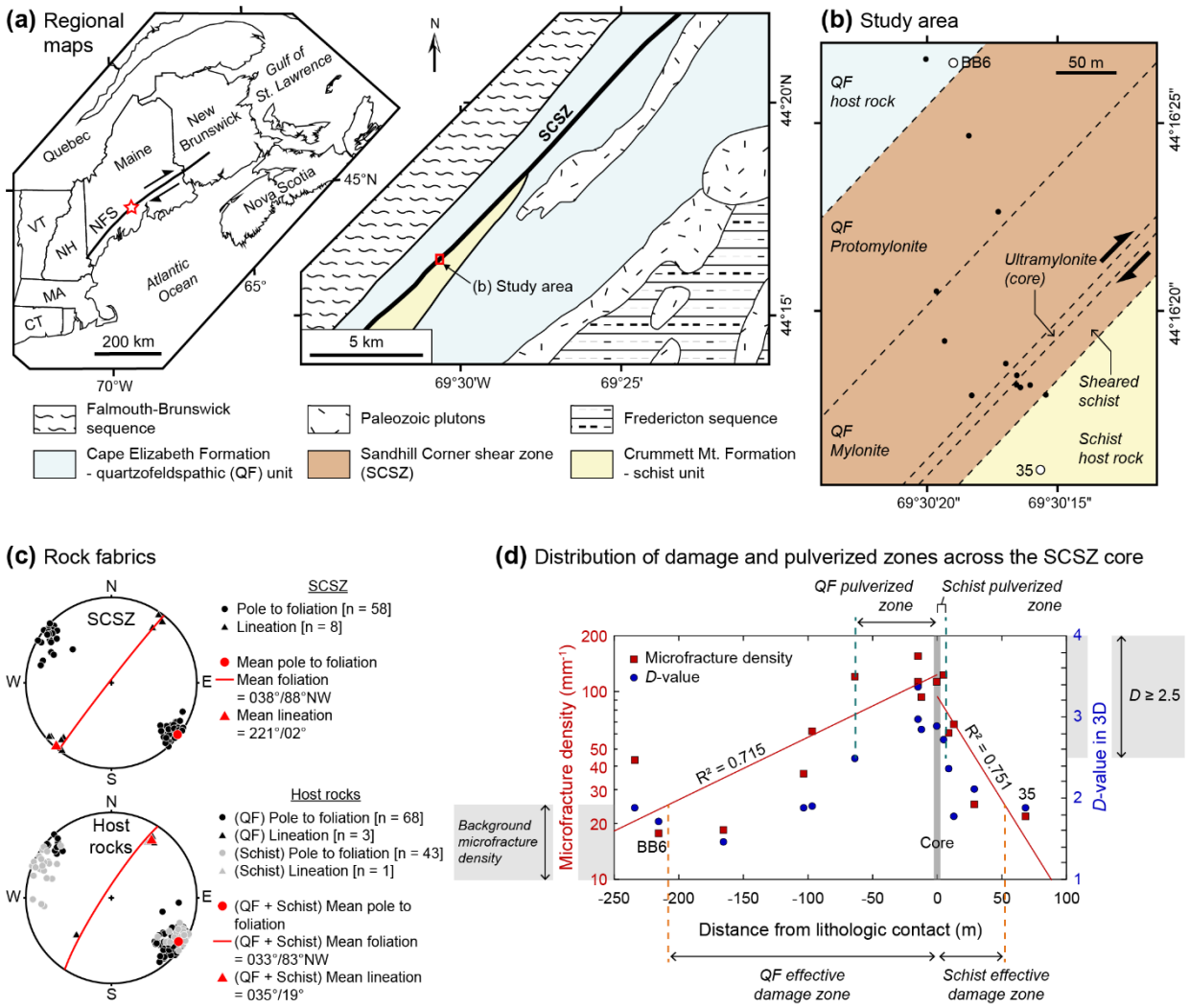

Figure 4.2 Geologic setting and damage distribution of the Sandhill Corner shear zone (SCSZ) in the Norumbega fault system (NSF). (a) Regional geologic maps of the right-lateral NSF and SCSZ (red star). The SCSZ near the study area (red box) separates two lithologic units (Cape Elizabeth Formation and Crummett Mt. Formation). Modified from Price et al. (2016). CT, Connecticut; MA, Massachusetts; NH, New Hampshire; VT, Vermont. (b) Study area and two host rock sample locations (white circles; BB6 and 35) for the present study. Samples for analyses of microfracture density and fragment size distribution in (d) are also marked by black circles (B. R. Song et al., 2020). The core of the shear zone (ultramylonite) is the lithologic contact between quartzofeldspathic (QF) and schist units. (c) Foliation and lineation of the SCSZ (upper panel) and host rocks (lower panel) plotted by equal-area, lower hemisphere projection. Mean values (strike/dip and trend/plunge, respectively) of mylonitic foliation and stretching lineation in the SCSZ indicate a northeast-trending, sub-vertical, strike-slip fault/shear zone. The host rocks show mean foliation sub-parallel to that of the SCSZ. Data from Grover and Fernandes (2003), and West and Peterman (2004). (d) Plots of microfracture density (red squares) and three-dimensional *D*-value (blue circles) for garnet samples in (b) against perpendicular distance from the QF/schist lithologic contact (data from B. R. Song et al., 2020; negative distance indicates the QF unit). The widths of effective damage zones are determined by the best fit lines above the background microfracture density. *D*-value is taken from the exponent of a power-law trend in the cumulative size distribution of garnet fragments. The widths of pulverized zones are determined by samples with *D*-value ≥ 2.5. Note highly asymmetric distribution of the effective damage and pulverized zones around the shear zone core.

4.4.2. Asymmetric Damage Distribution

Rocks within the SCSZ contain highly fractured and fragmented garnet grains. B. R. Song et al. (2020) analyzed the width of effective damage either side of the lithologic contact/shear-zone core based on the microfracture density measurements of the fractured or fragmented garnets. The damage distribution is highly asymmetric: ~207 m and ~53 m wide in the QF and schist units, respectively (Figure 4.2d). Using fragment size distribution analysis with three-dimensional *D*-value greater than 2.5, the boundaries between fractured and pulverized zones are located at ~63 m in the QF and ~5 m in the schist unit from the lithologic contact, indicating highly asymmetric distribution of pulverized zones as well (Figure 4.2d; B. R. Song et al., 2020). The wider pulverized zone determined by fragmented garnet in the QF unit is comparable to the dynamic strain-rate region (~60 m wide) determined by muscovite kink-band geometries (Anderson et al., 2021) and the coseismic damage zone (~90 m wide) determined by spatial abundance of fluid inclusions in the QF rocks (W. J. Song et al., 2020). Johnson et al. (2021b) have summarized these relations and their implications for energy expenditure in the earthquake source.

4.5. Methods

4.5.1. Sample Selection

One representative host-rock sample was chosen from either side of the SCSZ (BB6 and 35) to estimate elastic and seismic properties of the shear zone (Figures 4.2b and 4.3). The QF and schist host rocks have the same major minerals with quartz + feldspars + biotite + muscovite > ~95 modal%. The protomylonite and mylonite in the shear zone were derived from the QF host rock, and all share a similar mineralogy with only varying minor accessory minerals. Mica-rich schist that has a planar foliation defined by alternating mica-rich and quartz/feldspar-rich layers is the protolith of sheared schist in the shear zone. We compare elastic properties of the host rocks as they best represent the initial or early states of the bimaterial contact in development of the shear zone. A more accurate representation of the elastic properties could be determined by averaging the measured elastic properties of multiple host-rock samples on either side of the shear zone, but results from the selected samples are adequate for our purposes in the present

study. Due to the small grain size, we did not assess the elastic properties of the highly strained mylonitic/ultramylonitic rocks adjacent to the shear-zone core. The QF/schist contact continues for ~5.8 km to the NE and >~6.2 km to the SW from the study area (Figure 4.2a). The full length of the contact to the SW is unknown due to lack of outcrop. Thus, we are confident that the damage distribution evaluated herein reflects the elastic contrast between these two units as opposed to being inherited from some earlier part of the displacement history.

To help interpretation of seismic velocities for the complex natural samples, we also generate two simplified synthetic microstructures by changing the crystal orientations, pixel coordinates and phase information, as described by Naus-Thijssen et al. (2011b). The synthetic microstructures contain quartz, plagioclase, biotite and muscovite, and have nearly identical modal mineral abundance to the natural rock samples. The quartz and plagioclase grains have hexagonal shape and random crystallographic orientation while the rectangular mica grains show strong preferred shape and c-axis orientations parallel and perpendicular to the foliation, respectively. Specifically, the basal (001) planes of mica grains are oriented with a mean angle of zero degrees with respect to both the $x1$ (lineation direction) and $x3$ (direction parallel to the foliation and perpendicular to the lineation) axes with deviation angle of ±10° (see Figure 4.4 for the coordinate system), but the [100] and [010] axes of mica are randomly oriented within the basal (001) planes. All grains/phases in the synthetic microstructures are randomly distributed in the $x1$-$x2$ coordinate plane.

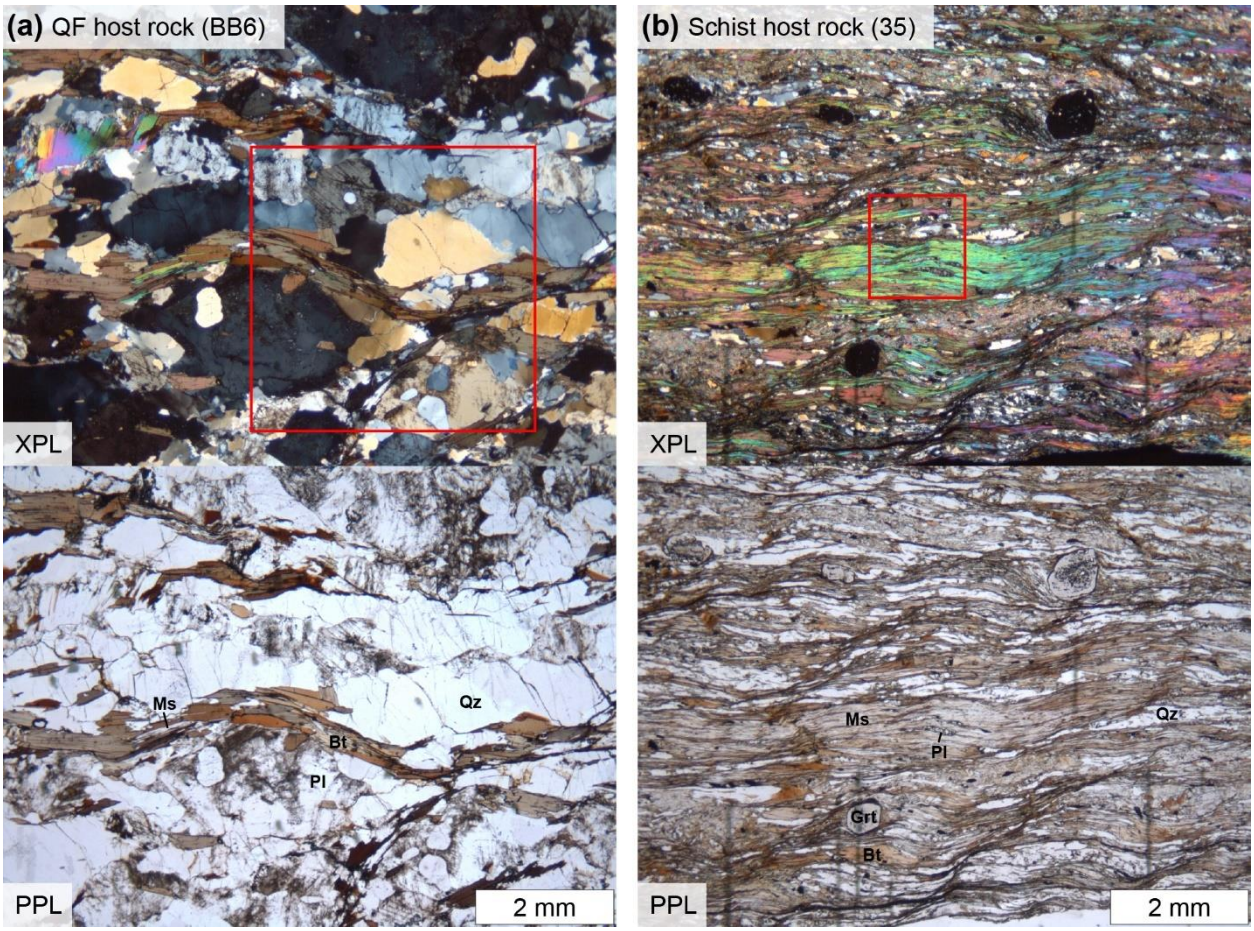

Figure 4.3 Photomicrographs of two host rock samples cut perpendicular to the foliation and parallel to the lineation. (a) Quartzofeldspathic (QF) host rock (sample BB6) with lower mica content. (b) Schist host rock (sample 35) with higher mica content. Red boxes present the analysis regions by EBSD (see Figure 4.7a). XPL, cross-polarized light; PPL, plane-polarized light; Qz, quartz; Pl, plagioclase; Bt, biotite; Ms, muscovite; Grt, garnet. Dark gray vertical stripes in (b) are scratches on the slide glass.

(a) TESA toolbox interface

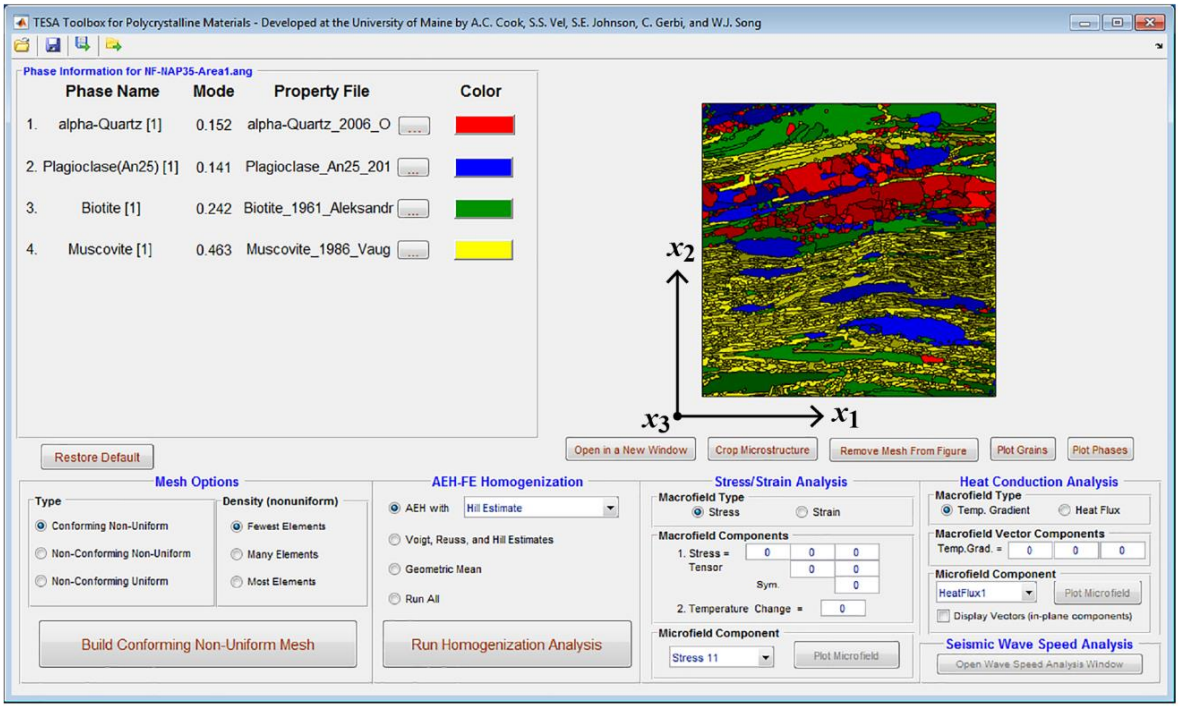

(b) Seismic wave speed analysis in TESA

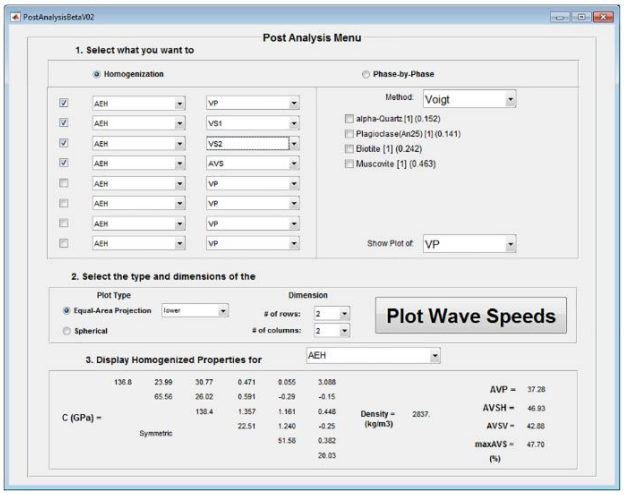

(c) Coordinate system

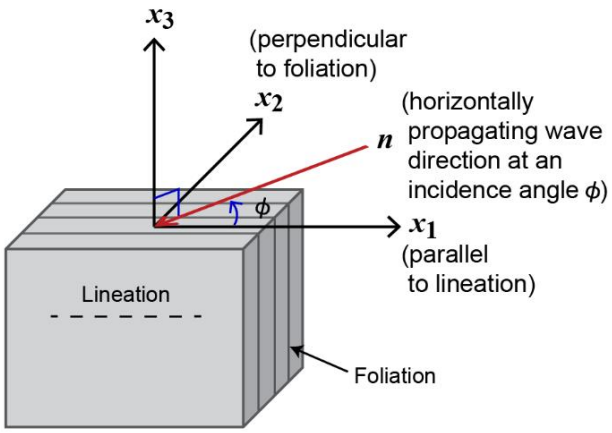

Figure 4.4 TESA toolbox and reference frame. (a) TESA toolbox interface. Note the reference frame of the *x*1-*x*2-*x*3 axes. (b) Seismic wave speed analysis after computing homogenized elastic properties in TESA. 3D wave speeds can be plotted as equal-area projections or spheres. (c) Coordinate system in TESA and the analyzed samples with vertical foliation and horizontal lineation. This study calculates 2D wave velocities in the *x*1-*x*2 plane as a function of the incidence angle ϕ.

4.5.2. Data Acquisition and Post-Processing

Thin sections of the two natural samples from the QF and schist host rocks (Figure 4.3) were cut perpendicular to the local foliation and parallel to the local stretching lineation, which are sub-parallel to the lithologic contact/shear-zone core. They were polished with colloidal silica suspension for >2 hours before applying a thin carbon coat. EBSD patterns of the two samples were collected using a Tescan Vega II scanning electron microscope equipped with an EDAX-TSL EBSD system at the University of Maine, USA. Working conditions were 20 kV acceleration voltage, 70° sample tilt, and 25 mm working distance. EDAX-TSL OIM Data Collection 5.31 software was used to index EBSD patterns on square grids with step size of 5 μm and 2 μm for relatively coarse-grained QF and fine-grained schist samples, respectively.

EBSD data were post-processed with EDAX-TSL OIM Analysis 5.31 software to produce clean EBSD maps for the purpose of numerical analysis, following the procedure suggested in Johnson et al. (2021a). They were reindexed to accurately identify phases using Hough peaks and chemistry, and to eliminate minor accessory phases (<5 modal%). Non- and poorly indexed pixels (<confidence index of 0.02) were replaced with well-indexed neighboring pixels. The well-indexed pixels are 86% and 61% of the EBSD maps for the QF and schist rocks, respectively. In order to produce perfectly bonded grain boundaries and uniform crystallographic orientation within a grain domain required for calculation of elastic properties using a finite element mesh, empty pixels (e.g., grain boundaries or eliminated minor phases) were filled with neighboring phases, twins in quartz and plagioclase were removed, and all pixels within a grain (with an internal misorientation <10°) were replaced by the average orientation for the grain. Finally, partially mis-indexed biotite and muscovite were manually corrected using a pseudosymmetry cleanup routine, comparing EBSD maps and photomicrographs.

4.5.3. Calculation of Elastic and Seismic Properties

To quantitatively determine bulk stiffness tensors and seismic wave velocities from the cleaned EBSD maps, the Euler angles, pixel coordinates and phase information were used in the TESA (Thermo-Elastic and Seismic Analysis) numerical toolbox featuring a MATLAB-based graphical user interface

(Figure 4.4a; Vel et al., 2016; Cook et al., 2018; Johnson et al., 2021a). The TESA toolbox was developed by Cook et al. (2018) to investigate seismic anisotropy of rocks, but also calculates grain-scale mechanical and thermal stresses and thermal conductivity for polyphase aggregates. The software is based on the asymptotic expansion homogenization (AEH) method in conjunction with the finite element method that is useful for accurately calculating the 3D homogenized elastic properties and computing seismic wave velocities in heterogeneous materials (Naus-Thijssen et al., 2011b; Vel et al., 2016; Almqvist and Mainprice, 2017; Cyprych et al., 2017). The AEH method captures the heterogeneous grain-scale stress and strain distributions in a polycrystalline sample by accounting for elastic interactions between the grains (Vel et al., 2016). Since 2D EBSD maps were used for the 3D homogenized elastic properties, it is assumed that the 2D microstructures (e.g., distributions and boundaries of grains) are projected in the third dimension (perpendicular to the microstructural image). Assuming that the modal mineralogy and crystallographic orientations are approximately maintained at the analysis scale in the third dimension, projection of the microstructure into the third dimension should provide results for seismic wave speeds accurate enough for our purposes. The homogenized stiffness tensors were computed using the elastic properties of trigonal α-quartz (Ohno et al., 2006), triclinic plagioclase (An25; Brown et al., 2016), monoclinic phlogopite (Chheda et al., 2014) for biotite, and monoclinic muscovite (Vaughan and Guggenheim, 1986). We note that biotite stiffness published by Aleksandrove and Ryzhova (1961) was not used because it assumes hexagonal symmetry. In the remainder of the paper when we refer to elastic properties of biotite, we use the elastic properties of phlogopite from Chheda et al. (2014). All four minerals are elastically anisotropic, and their single-crystal seismic properties are presented in Figure 4.5.

After homogenization analysis, we plot 3D wave velocities (V) using equal-area, upper-hemisphere projection (Figure 4.4b) and compute seismic anisotropy (in percentage) by $A = 100 \times (V_{\max} - V_{\min})/\big(0.5 \times (V_{\max} + V_{\min})\big)$. Using homogenized stiffness tensors, bulk densities, and the Christoffel equations (Christoffel, 1877), we calculate and plot 2D velocities of the compressional wave (*P* wave) and two shear waves (*SH* and *SV* waves depending on polarization direction; see Figure 4.6) for

incidence angles (azimuth ϕ) between 0° and 180° with 1° interval in the horizontal plane (*x*1-*x*2 plane in Figure 4.4c). These velocities are used to investigate contrasts in the velocities of different seismic waves, as a proxy for elastic contrast. In an anisotropic medium, *P* and *S* waves generally have quasi-compressional (qV_P) and quasi-shear (qV_{SH} and qV_{SV}) wave velocities since particle motion is neither exactly parallel nor perpendicular to the symmetry axis for most angles of incidence (e.g., Auld, 1990; Winterstein, 1990). Note that qV_{SH} and qV_{SV} (and thus their seismic anisotropies) can vary depending on the selected reference frame. The seismic velocity contrast (in percentage) between two rocks at a particular incidence angle is calculated as $100 \times |V_{\mathrm{rock1}} - V_{\mathrm{rock2}}| / \left(0.5 \times (V_{\mathrm{rock1}} + V_{\mathrm{rock2}})\right)$. The synthetic microstructures were similarly analyzed for elastic and seismic properties using the TESA toolbox. In anisotropic media, shear waves can also be classified into faster and slower *S* waves (*S1* and *S2*, respectively), independent of reference frame. For more complete datasets of seismic properties, we also plot 3D *S1*- and *S2*-wave velocities (qV_{S1} and qV_{S2}) and *S*-wave anisotropy percentage $AV_S = 100 \times (V_{S1} - V_{S2}) / \left(0.5 \times (V_{S1} + V_{S2})\right)$ for all the natural and synthetic rocks.

The TESA toolbox can use classical analytical homogenization methods such as Voigt (Voigt, 1928), Reuss (Reuss, 1929), and Voigt-Reuss-Hill (hereafter called "Hill"; Hill, 1952) averages that do not account for elastic interactions between the constituent grains. For comparison with AEH results, we plot 2D and 3D wave velocities via Voigt, Reuss, and Hill techniques of the natural and synthetic QF and schist host rocks of the SCSZ and discuss them in the text (Section 4.7.3).

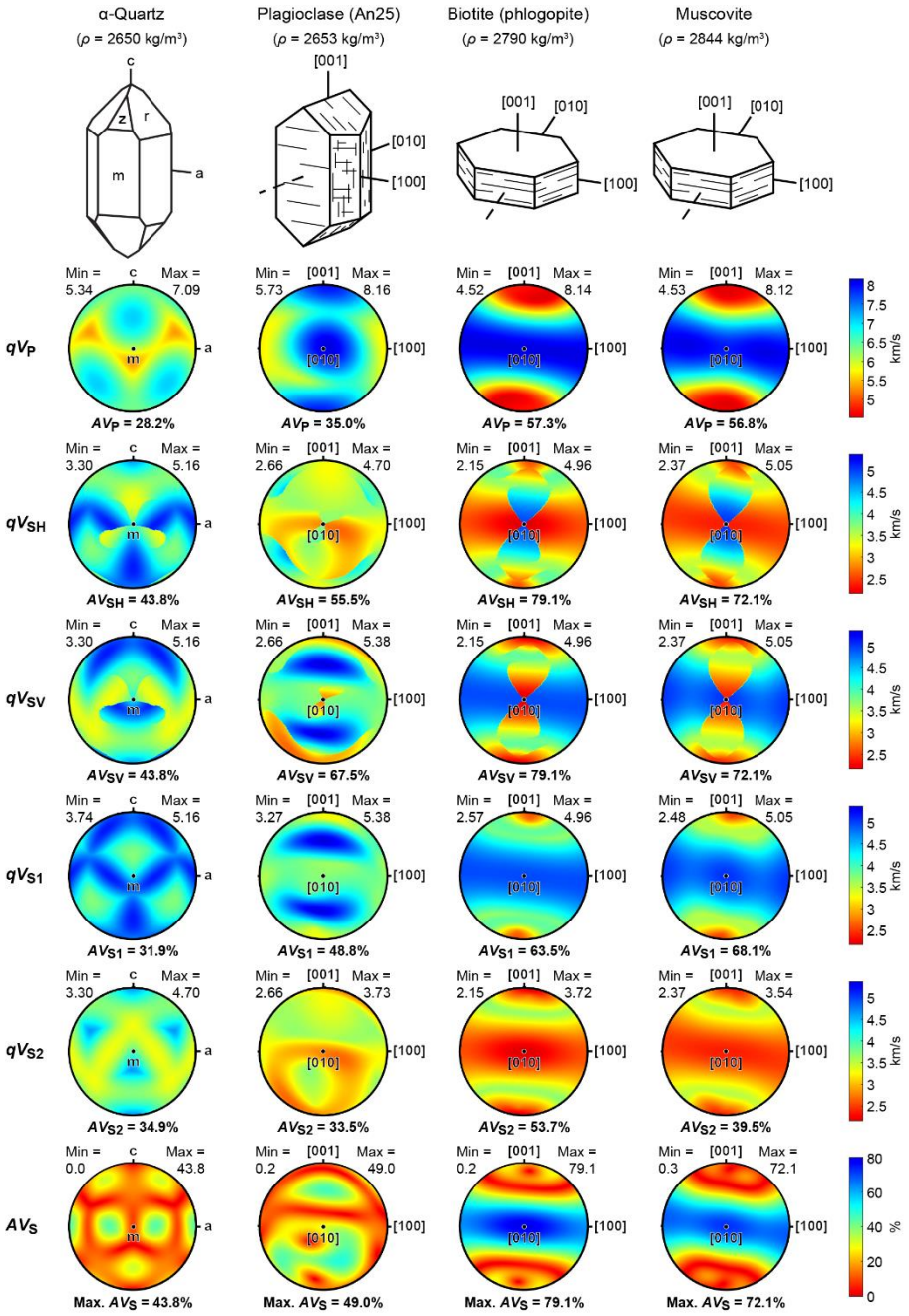

Figure 4.5 *P*-, *SH*-, *SV*-, *S1*- and *S2*-wave velocities (denoted by qV_P, qV_{SH}, qV_{SV}, qV_{S1} and qV_{S2}, respectively) and *S*-wave anisotropy percentage (AV_S) plotted as equal-area, upper hemisphere projections for single crystals of quartz, plagioclase (An25), phlogopite for biotite, and muscovite used in the present study. In this reference frame for single crystal velocities, the horizontal polarization for *SH*-wave is parallel to the a-c plane in quartz and the [100]-[001] plane in plagioclase, biotite and muscovite. Note that qV_{SH} and qV_{SV} (and thus their seismic anisotropies) can vary depending on the selected reference frame. 3D velocities of quartz, plagioclase, phlogopite and muscovite show trigonal, triclinic, monoclinic and monoclinic symmetry, respectively, being computed using the elastic properties of Ohno et al. (2006), Brown et al. (2016), Chheda et al. (2014) and Vaughan and Guggenheim (1986), and the densities of 2650, 2653, 2790 and 2844 kg/m^3. Seismic anisotropy (*AV*) for each seismic velocity is calculated from the difference between the maximum and minimum velocities divided by their average.

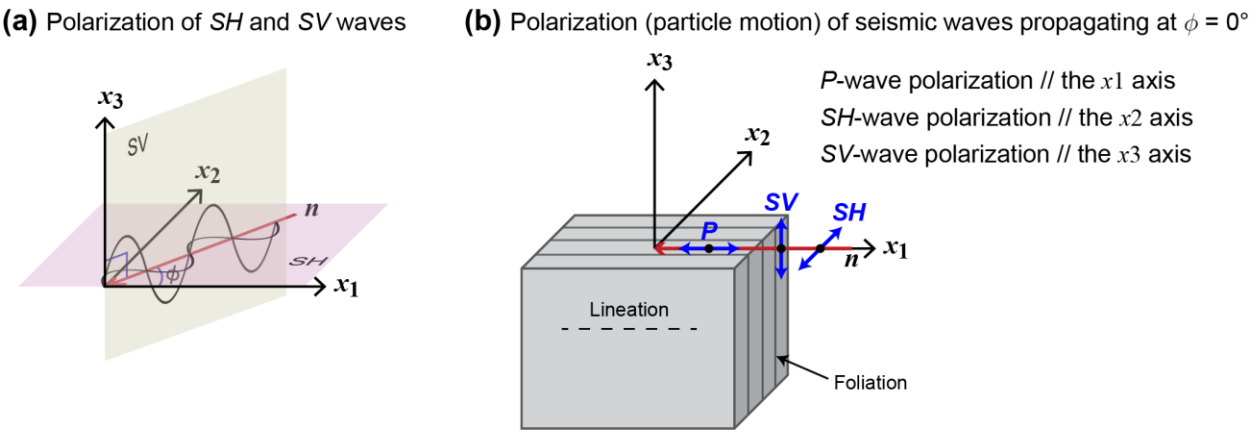

Figure 4.6 Illustration of polarization of seismic waves. (a) Polarization of the *SH* and *SV* waves horizontally propagating at an incidence angle ϕ. The *SH*-wave polarization is parallel to the *x*1-*x*2 plane. The *SV*-wave polarization direction lies in the planes that are parallel to the *x*3 axis. (b) Particle motion (polarization) of *P*, *SH* and *SV* waves horizontally propagating at ϕ = 0° (parallel to the foliation and lineation). The compressional *P* wave has particle motion parallel to the propagation direction (the *x*1 axis). Two shear waves show polarization perpendicular to the propagation direction. The *SH* wave has particle motion parallel to the *x*2 direction (perpendicular to the foliation). The *SV* wave has particle motion parallel to the *x*3 direction (perpendicular to the horizontal *x*1-*x*2 plane). ***n***, wave propagation direction.

4.6. Results

4.6.1. Microstructures of the Quartzofeldspathic (QF) and Schist Units

Two natural rock samples from the QF (sample BB6) and schist (sample 35) units are composed primarily of quartz, plagioclase, biotite and muscovite, with minor garnet (Figure 4.3). In the selected regions for EBSD analysis (Figure 4.7a), quartz and plagioclase show coarse grains up to millimeter scale in the QF sample (averaging 101.1 and 121.9 μm, respectively) but relatively fine grains in the mica-rich schist (averaging 24.6 and 32.1 μm, respectively). In the QF rock with relatively low mica content (13.9 modal%), biotite has large grain size (average 84.6 μm) compared to the schist and exhibits a preferred orientation of its basal (001) planes sub-parallel to the shear-zone core or foliation (the *x*1-*x*3 plane) although biotite layering anastomoses around plagioclase grains (Figures 4.3a, 4.7a and 4.9a). Muscovite comprises a very small portion (0.5 modal%) of the QF rock (Figure 4.7a). Owing to their large grain size, quartz and plagioclase in the QF rock show similar degrees of crystallographic preferred orientation to biotite (Figure 4.9a). In the schist with high mica content (70.5 modal%), both biotite and muscovite grain

sizes are relatively small (averaging 29.0 and 20.9 μm, respectively), and show strong preferred orientations of their basal (001) planes parallel to the foliation, whereas quartz and plagioclase have relatively weak crystallographic preferred orientations (Figures 4.7a and 4.9b). The total number (N) of grains analyzed by EBSD is 625 for the QF rock and 2623 for the schist. The number of grains for each mineral is as follows: N_{quartz} = 261, $N_{plagioclase}$ = 114, $N_{biotite}$ = 203, and $N_{muscovite}$ = 47 for the QF rock; N_{quartz} = 335, $N_{plagioclase}$ = 147, $N_{biotite}$ = 282, and $N_{muscovite}$ = 1859 for the schist.

4.6.2. Wave Velocities and Contrasts for the Natural QF Rock and Schist

4.6.2.1. *P* Wave

The 2D quasi-compressional wave velocities (qV_P) of the QF rock and schist in the horizontal $x1$-$x2$ plane are plotted as a function of azimuth ϕ in Figure 4.7b, using the homogenized stiffness tensors and densities computed by the TESA toolbox. qV_P at ϕ = 0° (or 180°) and ϕ = 90°, hereafter referred to as $qV_P(0°)$ and $qV_P(90°)$, represent a compressional wave velocity propagating, respectively, parallel and perpendicular to the strike of the SCSZ (the $x1$ direction). The QF rock with low mica content shows only a small variation in qV_P and thus low *P*-wave anisotropy in the $x1$-$x2$ plane (Figure 4.7b; see Table 4.1). In contrast, the schist with high mica content shows significant *P*-wave anisotropy in the $x1$-$x2$ plane. The schist qV_P showing the highest value at ϕ = 3° decreases with increasing ϕ and reaches its minimum value at ϕ = 96°, and its maximum difference is more than 2 km/s (Figure 4.7b; Table 4.1). Unlike the QF rock, the qV_P curve for the schist in the $x1$-$x2$ plane is approximately symmetrical with respect to ϕ = ~90° (Figure 4.7b). In the SCSZ-parallel direction, $qV_P(0°)$ of the schist is faster than that of the QF rock, whereas in the SCSZ-perpendicular direction, the schist shows slower $qV_P(90°)$ than the QF rock (Figure 4.7b).

Since the QF rock and schist show different degrees of seismic anisotropy in the $x1$-$x2$ plane, the *P*-wave velocity contrast between the two rocks varies with azimuth ϕ (Figure 4.7c). The qV_P contrast in the SCSZ ranges from 0% at the velocity crossovers to 17.6%, and the more compliant rock type (QF or

schist) based on qV_P is also changed with ϕ (Figure 4.7c). The SCSZ-parallel and perpendicular qV_P contrasts at $\phi = 0°$ and $\phi = 90°$, respectively, are 11.9% (more compliant QF) and 16.2% (more compliant schist).

The 3D qV_P for the QF and schist rocks is plotted in Figure 4.7d. Both rocks show minimum qV_P sub-perpendicular to the $x1$-$x3$ plane (foliation), but maximum and high qV_P in the QF rock is concentrated sub-parallel to the $x3$ direction, whereas the schist exhibits maximum and high qV_P along the foliation, displaying nearly hexagonal symmetry of *P*-wave velocity (Figure 4.7d). The *P*-wave seismic anisotropy of the schist (37.9%) is more than twice that of the QF rock (15.3%) owing to the abundant mica with strong crystallographic preferred orientation (Figures 4.7d and 4.9b).

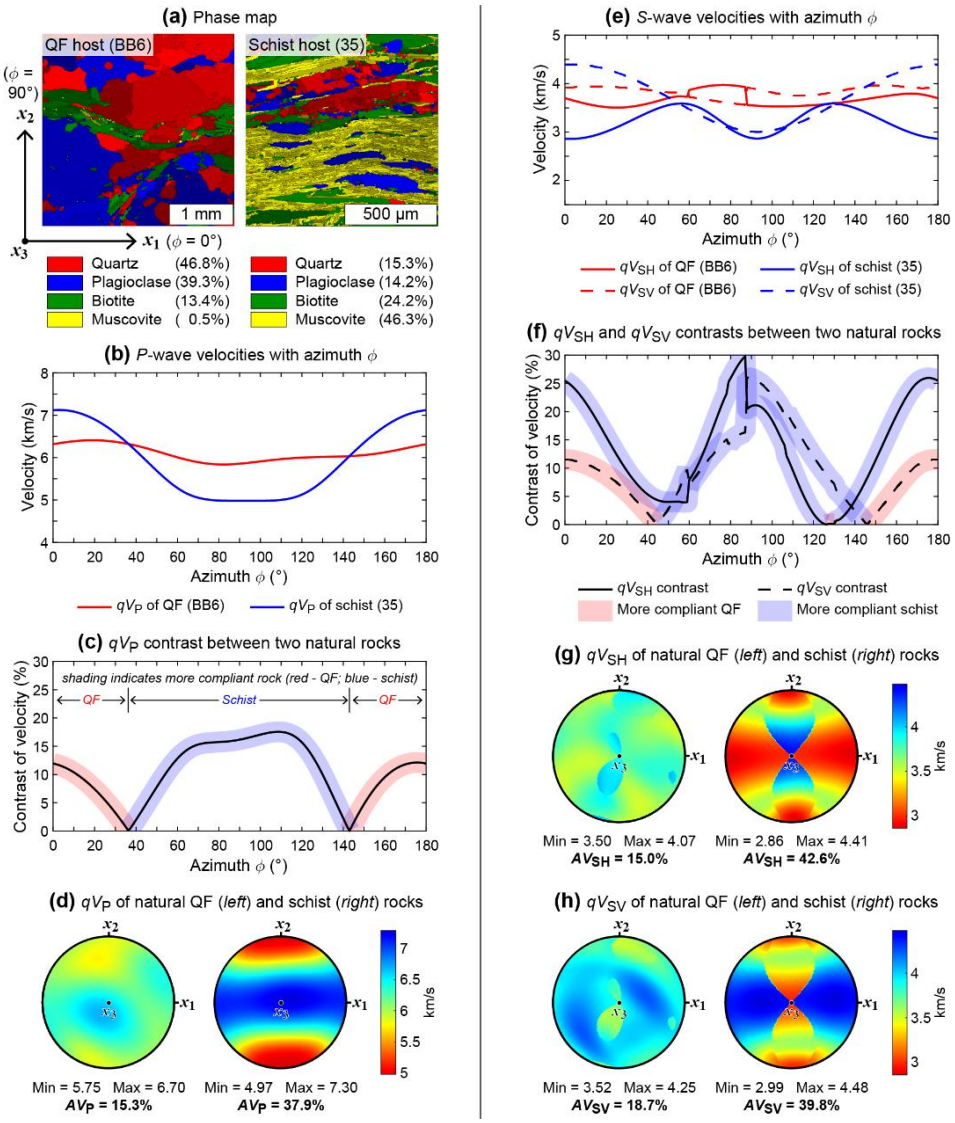

Figure 4.7 Phase maps, *P*- (qV_P) and *S*-wave velocities (qV_{SH} and qV_{SV}), and velocity contrasts for the quartzofeldspathic (QF) and schist host rocks of the Sandhill Corner shear zone. The velocities were computed using the AEH method. The compressional *P* wave has particle motion parallel to the propagation direction; the *SH*-wave polarization orientation is parallel to the horizontal *x*1-*x*2 plane; the *SV*-wave polarization orientation lies in the vertical planes that are parallel to the *x*3 axis (see Figure 4.6). (a) Phase maps of the analyzed QF (sample BB6) and schist (sample 35) host rocks by EBSD with lower (13.9 modal%) and higher (70.5 modal%) mica contents, respectively. Different shades of colors indicate different grains. See Figure 4.3 for analysis location. The coordinate system and azimuth ϕ (wave incidence angle) are also shown. (b) 2D qV_P for each rock plotted against azimuth ϕ from 0° to 180° in the *x*1-*x*2 plane. (c) qV_P contrast between the QF and schist rocks plotted against azimuth ϕ, calculated from (b). Shading indicates more compliant rock with lower velocity (red – QF; blue – schist). (d) 3D qV_P and its seismic anisotropy (AV_P) for each rock. (e) 2D qV_{SH} and qV_{SV} for each rock plotted against azimuth ϕ from 0° to 180° in the *x*1-*x*2 plane. (f) qV_{SH} and qV_{SV} contrasts between the QF and schist rocks plotted against azimuth ϕ, calculated from (e). (g) 3D qV_{SH} and its seismic anisotropy (AV_{SH}) for each rock. (h) 3D qV_{SV} and its seismic anisotropy (AV_{SV}) for each rock. 3D wave velocities in (d), (g) and (h) are presented in equal-area, upper hemisphere projection and with the same color limits for comparison. See Figure 4.8 for 3D *S1*- and *S2*-wave velocities (qV_{S1} and qV_{S2}) and *S*-wave anisotropy percentage (AV_S).

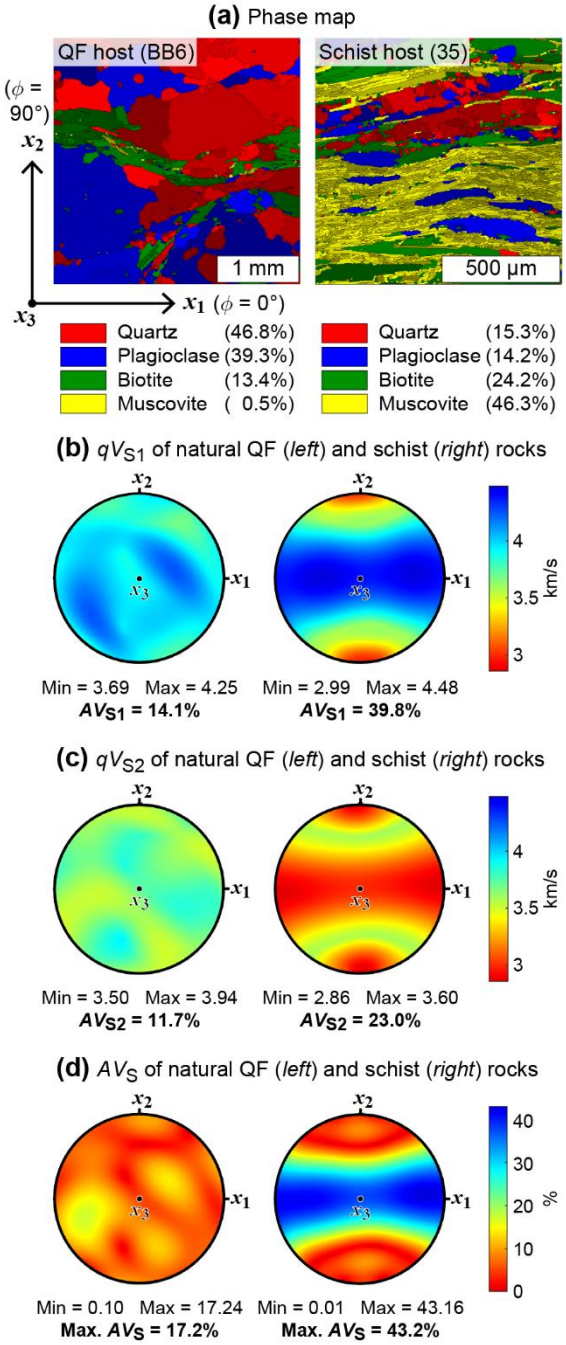

Figure 4.8 Phase maps, *S1*- and *S2*-wave velocities (qV_{S1} and qV_{S2}), and *S*-wave anisotropy percentage (AV_S) for the quartzofeldspathic (QF) and schist host rocks of the Sandhill Corner shear zone. (a) Phase maps of the natural QF (sample BB6) and schist (sample 35) host rocks. From Figure 4.7a. (b) 3D qV_{S1} and its seismic anisotropy (AV_{S1}) for each natural rock. (c) 3D qV_{S2} and its seismic anisotropy (AV_{S2}) for each natural rock. (d) 3D AV_S and its maximum anisotropy (max. AV_S) for each natural rock. (b), (c) and (d) are computed using the AEH method and presented in equal-area, upper hemisphere projection and with the same color limits for comparison.

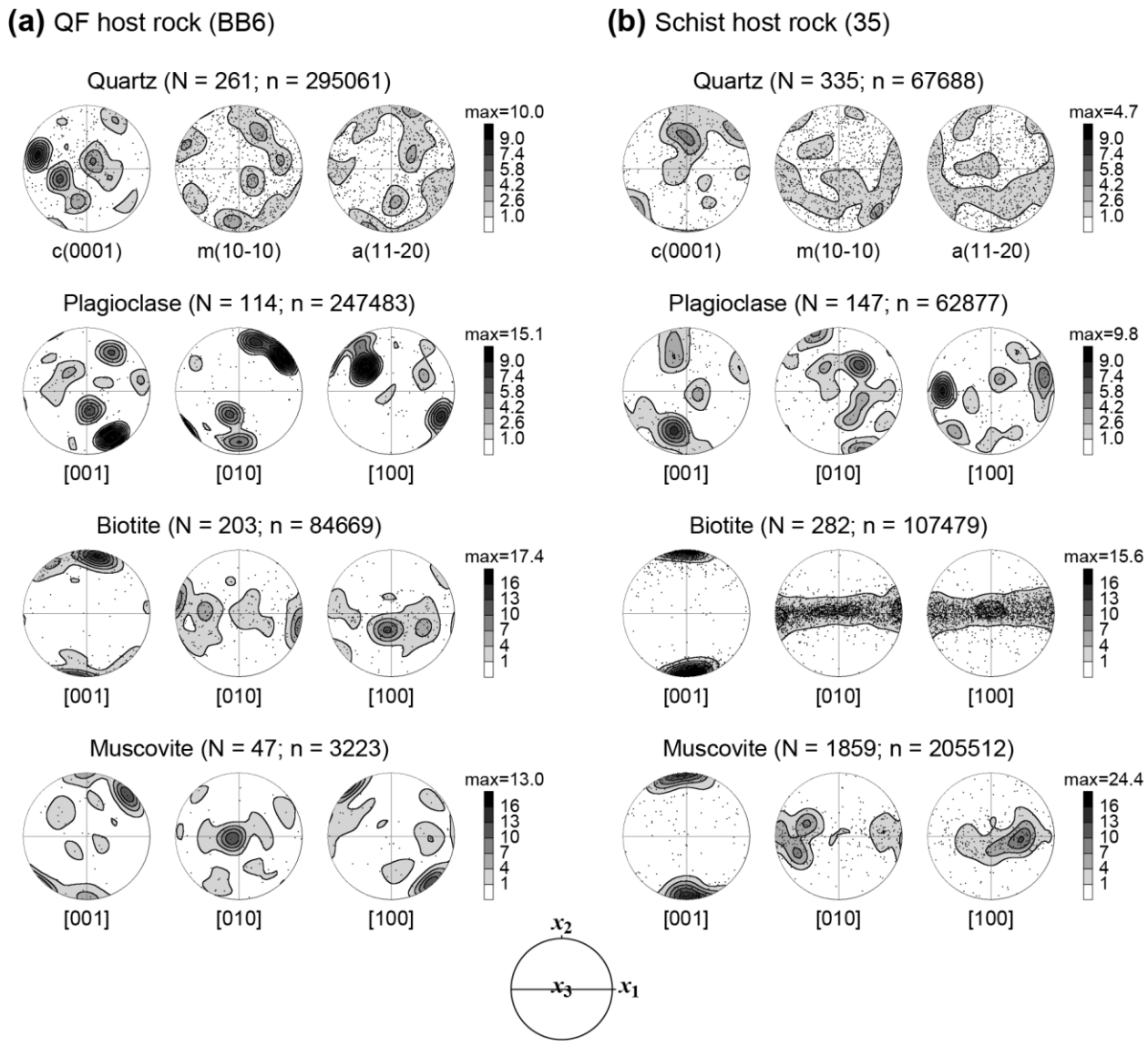

Figure 4.9 Crystallographic orientations of the natural rocks at all the EBSD analysis points (pixels) plotted as equal-area, upper hemisphere projections (not one-point-per-grain plots) and contoured as multiples of uniform distribution using smoothing parameters with series rank of 10 and Gaussian half-width of 10°. Thus, the contoured pole figures show area-weighted effect, which helps interpret seismic properties of the rocks. (a) Crystallographic orientations of quartz, plagioclase, biotite and muscovite in the QF host rock (sample BB6). (b) Crystallographic orientations of quartz, plagioclase, biotite and muscovite in the schist host rock (sample 35). The reference frame (*x*1-*x*2-*x*3) is displayed at the bottom; the numbers of grains (N) and analysis points (n) are also presented next to each mineral name. Note that the basal (001) planes of biotite and muscovite in the mica-rich schist are subparallel to the foliation (the *x*1-*x*3 plane).

4.6.2.2. *S* Waves

The 2D quasi-shear wave velocities with horizontal (qV_{SH}) and vertical (qV_{SV}) polarization of the QF and schist rocks are plotted as a function of azimuth ϕ in Figure 4.7e. The mica-poor QF rock shows only small variations in qV_{SH} and qV_{SV}, whereas the two *S* waves of the mica-rich schist have much larger seismic anisotropies in the *x*1-*x*2 plane (Figure 4.7e; see Table 4.1). In the schist, the slowest 2D qV_{SH} is present at ϕ = 3° with polarization sub-perpendicular to the foliation, and the fastest 2D qV_{SH} is at ϕ = 130° with neither polarization nor propagation (sub-)perpendicular to the foliation (Figure 4.7e; Table 4.1). 2D qV_{SV} of the schist is fastest at ϕ = 3° with both polarization and propagation (sub-)parallel to the foliation and slowest at ϕ = 93° with propagation sub-perpendicular to the foliation, and its maximum difference is more than 1 km/s (Figure 4.7e; Table 4.1). Unlike the QF rock, the schist has approximately symmetrical qV_{SH} and qV_{SV} patterns in the *x*1-*x*2 plane with respect to ϕ = ~90° (Figure 4.7e). In the SCSZ-parallel direction, the schist shows faster qV_{SV}(0°) than the QF rock, whereas in the SCSZ-perpendicular direction, qV_{SV}(90°) of the schist is slower (Figure 4.7e). For qV_{SH} in the *x*1-*x*2 plane, the schist exhibits slower velocities than the QF rock at all azimuth angles except for ϕ = 126° to 130° where it is slightly faster than the QF rock (Figure 4.7e).

The seismic contrasts of *SH* and *SV* waves between the two rocks also varies with azimuth ϕ owing to different degrees of seismic anisotropy in the *x*1-*x*2 plane (Figure 4.7f). The qV_{SH} and qV_{SV} contrasts range from 0% to 29.8% and 26.0%, respectively. The qV_{SH} and qV_{SV} contrasts at ϕ = 0° are 25.5% (more compliant schist) and 11.5% (more compliant QF), respectively. At ϕ = 90°, the contrasts of qV_{SH} and qV_{SV} are 21.0% and 25.9%, respectively, the schist being more compliant for both *SH* and *SV* waves (Figure 4.7f). There are abrupt changes in qV_{SH} and qV_{SV} contrasts at ϕ = ~60° and especially ~90° in Figure 4.7f. They are caused by abrupt change ("crossover") of qV_{SH} for the QF rock to faster *S* wave at ϕ = ~60° and to slower *S* wave at ϕ = ~90° in Figure 4.7e (or abrupt change of qV_{SV} for the QF rock to slower *S* wave at ϕ = ~60° and to faster *S* wave at ϕ = ~90°). The two plots in Figures 4.7e and 4.7f show that, unlike elastically isotropic rocks, seismic wave velocities and their contrasts in anisotropic rocks depend on the incidence angle ϕ in the horizontal *x*1-*x*2 plane, and this will be discussed in Section 4.7.1.

The 3D qV_{SH} and qV_{SV} for the QF and schist rocks are plotted in Figures 4.7g and 4.7h where patterns of qV_{SH} and qV_{SV} in the mica-rich schist exhibit nearly hexagonal symmetry. In Figures 4.7g and 4.7h, the *SH*- and *SV*-wave seismic anisotropies of the mica-rich schist (42.6% and 39.8%, respectively) are more than twice those of the QF rock (15.0% and 18.7%, respectively).

4.6.3. Comparison With Synthetic Rock Samples

Owing to the complex microstructures and seismic velocity patterns of the natural rocks (especially the QF rock), two simplified synthetic microstructures with nearly identical modal mineral abundance to the natural rocks were generated to better understand the effect of modal mineralogy on wave velocities and seismic anisotropy. The synthetic QF and schist samples have mica (biotite and muscovite) contents of 14.1% and 70.6%, respectively (Figure 4.10a).

4.6.3.1. *P* Wave

Similar to the natural rocks, the 2D qV_P of the synthetic QF rock with low mica content shows small variation, whereas the synthetic schist with high mica content has significant qV_P variation more than 2 km/s in the horizontal $x1$-$x2$ plane (Figure 4.10b; see Table 4.1). For both synthetic rocks, the qV_P curves in the $x1$-$x2$ plane do not have minimum speeds in sub-perpendicular directions to the foliation close to ϕ = 90° (e.g., minimum at ϕ = 56° or 81°) while maximum velocities are shown in (sub-)parallel directions to the foliation close to ϕ = 0° or 180° (Figure 4.10b; Table 4.1). Owing to strong crystallographic preferred orientations in mica and weak preferred orientations in quartz and plagioclase (Figure 4.12), these 2D velocity features for synthetic rocks are similar to the 2D qV_P for monoclinic biotite or muscovite single crystals plotted in the [100]-[001] plane (Figure 4.13). Interestingly, the qV_P curve for the mica-rich synthetic schist in the $x1$-$x2$ plane is approximately symmetrical with respect to ϕ = ~90° presumably due to a combination of the monoclinic velocity curves for biotite and muscovite (Figures 4.10b and 4.13). As

with the natural rocks, the foliation-parallel $qV_P(0°)$ of the synthetic schist is faster than that of the synthetic QF rock, whereas in the foliation-perpendicular direction, the synthetic schist has slower $qV_P(90°)$ than the synthetic QF rock (Figure 4.10b).

The seismic contrast of *P* wave between the two synthetic rocks varies with azimuth ϕ owing to different degrees of their seismic anisotropies in the $x1$-$x2$ plane (Figure 4.10c), with values ranging from 0% to 18.6%. The foliation-parallel and perpendicular qV_P contrasts at $\phi = 0°$ and $\phi = 90°$ are 13.5% (more compliant synthetic QF) and 18.6% (more compliant synthetic schist), respectively (Figure 4.10c).

The 3D qV_P for the synthetic QF rock shows much simpler velocity pattern than the natural QF rock (Figure 4.10d), close to monoclinic symmetry of biotite in Figure 4.5. This simpler pattern reflects the random crystallographic orientations of synthetic quartz and plagioclase grains unlike the natural QF rock (Figure 4.12a). However, both natural and synthetic QF rocks show similar minimum and maximum qV_P and thus similar *P*-wave seismic anisotropies (15.3% and 12.0%, respectively; Figures 4.7d and 4.10d). The mica-rich synthetic schist displays approximately hexagonal symmetry of qV_P similar to the natural schist, considering maximum and high qV_P along the foliation owing to strong preferred orientation of the basal (001) planes of biotite and muscovite parallel to the foliation (Figures 4.10d and 4.12b). As in the natural rocks, Figure 4.10d shows the *P*-wave seismic anisotropy of the mica-rich synthetic schist (40.5%) is much higher than that of the synthetic QF rock (12.0%). The *P*-wave velocity comparison between the natural and synthetic rocks indicates that mica content and its crystallographic orientation are important factors in determining seismic velocities and anisotropy compared to the other minerals (quartz and plagioclase) because biotite and muscovite have much higher seismic anisotropies than quartz and plagioclase (Figure 4.5).

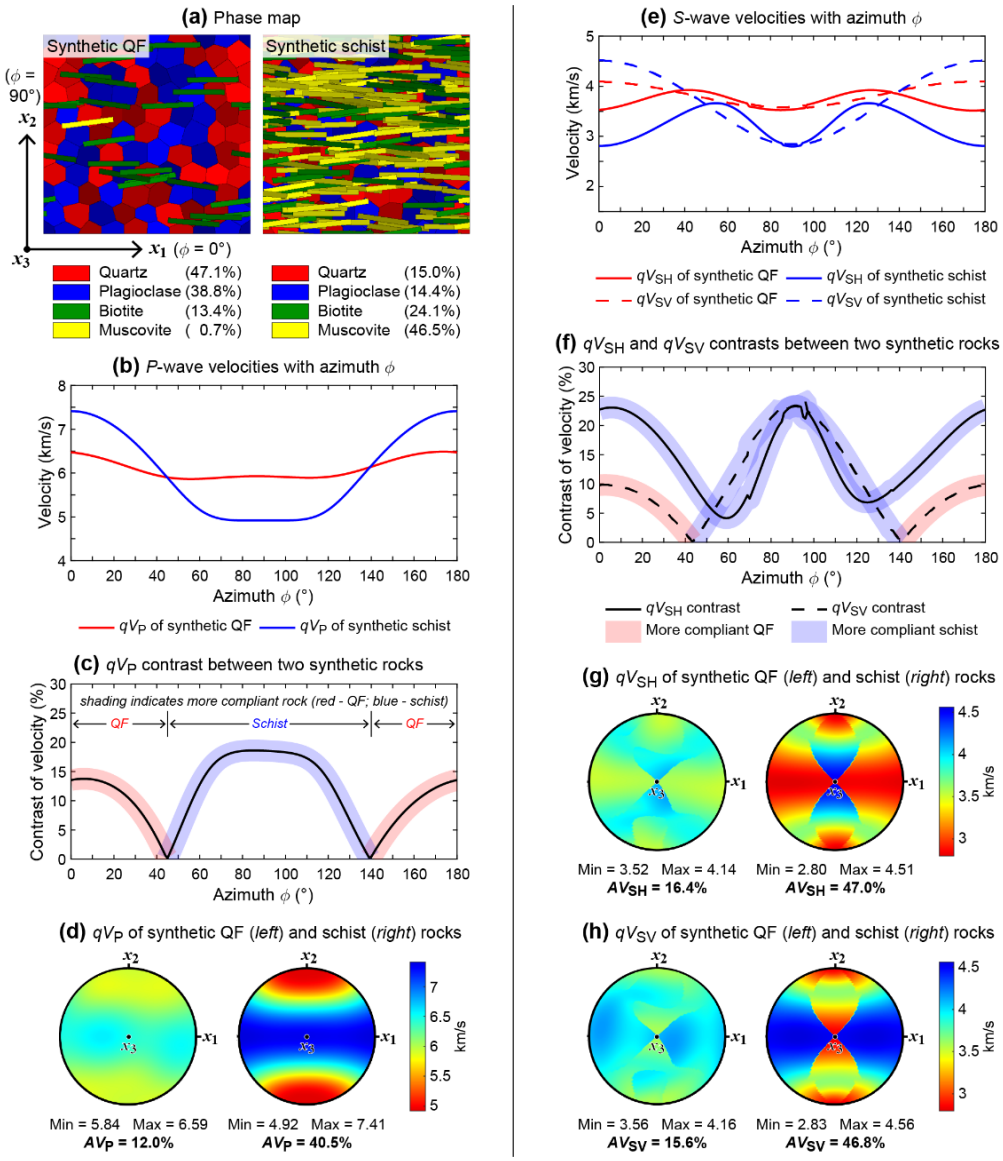

Figure 4.10 Phase maps, *P*- (qV_P) and *S*-wave velocities (qV_{SH} and qV_{SV}), and velocity contrasts for synthetic rock samples with the same mica contents as the natural quartzofeldspathic (QF) and schist host rocks of the Sandhill Corner shear zone. The velocities were computed using the AEH method. (a) Phase maps of the synthetic QF and schist rocks with lower (14.1 modal%) and higher (70.6 modal%) mica contents, respectively. Mica grains show a preferred orientation, but quartz and plagioclase grains are randomly oriented. The coordinate system and azimuth ϕ (wave incidence angle) are also presented. (b) 2D qV_P for each synthetic rock plotted against azimuth ϕ from 0° to 180° in the $x1$-$x2$ plane. (c) qV_P contrast between the synthetic QF and schist rocks plotted against azimuth ϕ, calculated from (b). Shading indicates more compliant rock with lower velocity (red – QF; blue – schist). (d) 3D qV_P and its seismic anisotropy (AV_P) for each synthetic rock. (e) 2D qV_{SH} and qV_{SV} for each synthetic rock plotted against azimuth ϕ from 0° to 180° in the $x1$-$x2$ plane. (f) qV_{SH} and qV_{SV} contrasts between the synthetic QF and schist rocks plotted against azimuth ϕ, calculated from (e). (g) 3D qV_{SH} and its seismic anisotropy (AV_{SH}) for each synthetic rock. (h) 3D qV_{SV} and its seismic anisotropy (AV_{SV}) for each synthetic rock. 3D wave velocities in (d), (g) and (h) are presented in equal-area, upper hemisphere projection and with the same color limits for comparison. See Figure 4.11 for 3D *S1*- and *S2*-wave velocities (qV_{S1} and qV_{S2}) and *S*-wave anisotropy percentage (AV_S).

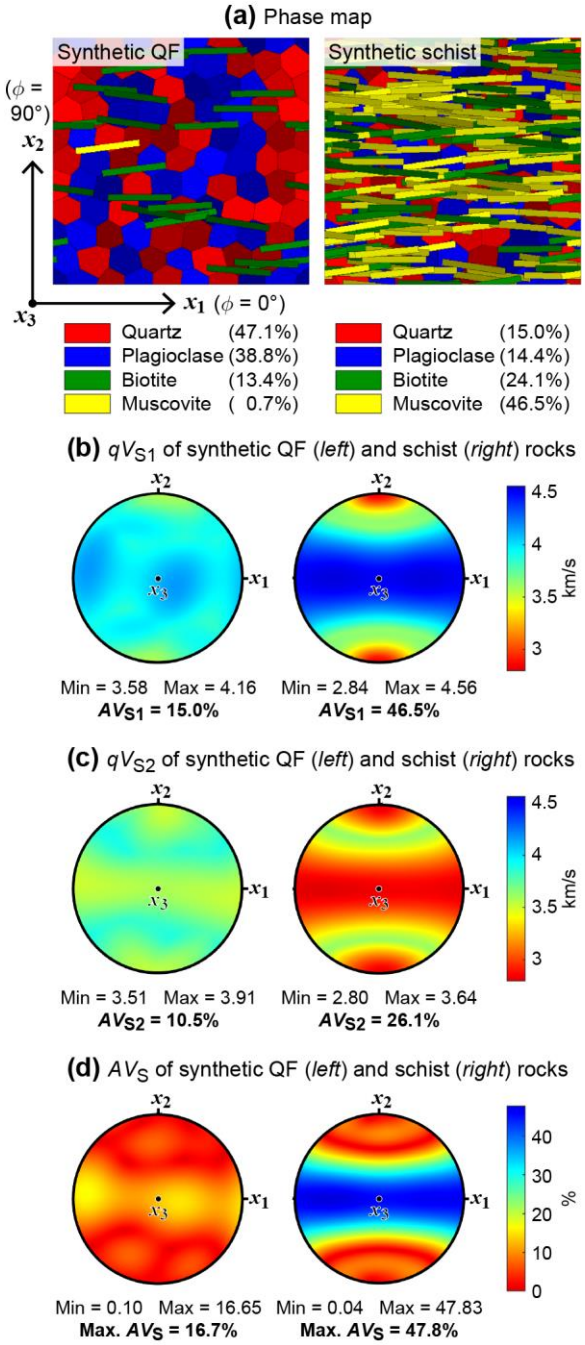

Figure 4.11 Phase maps, *S1*- and *S2*-wave velocities (qV_{S1} and qV_{S2}), and *S*-wave anisotropy percentage (AV_S) for synthetic rock samples with the same mica contents as the natural quartzofeldspathic (QF) and schist host rocks of the Sandhill Corner shear zone. (a) Phase maps of the synthetic QF and schist rocks. From Figure 4.10a. (b) 3D qV_{S1} and its seismic anisotropy (AV_{S1}) for each synthetic rock. (c) 3D qV_{S2} and its seismic anisotropy (AV_{S2}) for each synthetic rock. (d) 3D AV_S and its maximum anisotropy (max. AV_S) for each synthetic rock. (b), (c) and (d) are computed using the AEH method and presented in equal-area, upper hemisphere projection and with the same color limits for comparison.

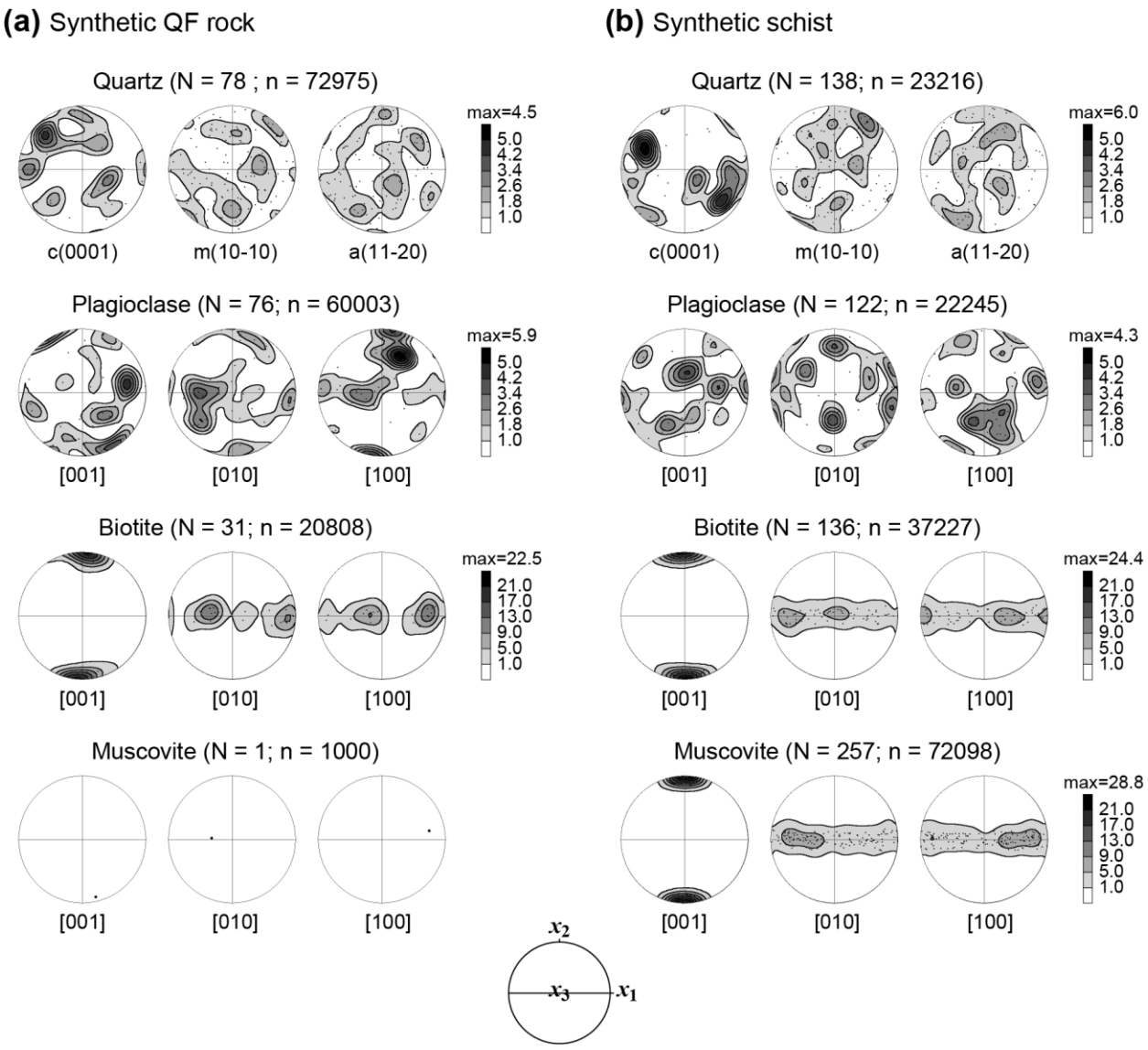

Figure 4.12 Crystallographic orientations of the synthetic rocks at all the pixels plotted as equal-area, upper hemisphere projections and contoured as multiples of uniform distribution using smoothing parameters with series rank of 10 and Gaussian half-width of 10°. (a) Crystallographic orientations of quartz, plagioclase and biotite in the synthetic QF rock. Muscovite is plotted using discrete pole figure because the synthetic QF rock has only one grain of muscovite. (b) Crystallographic orientations of quartz, plagioclase, biotite and muscovite in the synthetic schist. The reference frame (*x*1-*x*2-*x*3) is displayed at the bottom; the numbers of grains (N) and analysis points (n) are also presented next to each mineral name. Note that the basal (001) planes of micas in both synthetic rocks are subparallel to the foliation (the *x*1-*x*3 plane), and the other minerals (quartz and plagioclase) show very weak crystallographic preferred orientations compared to biotite.

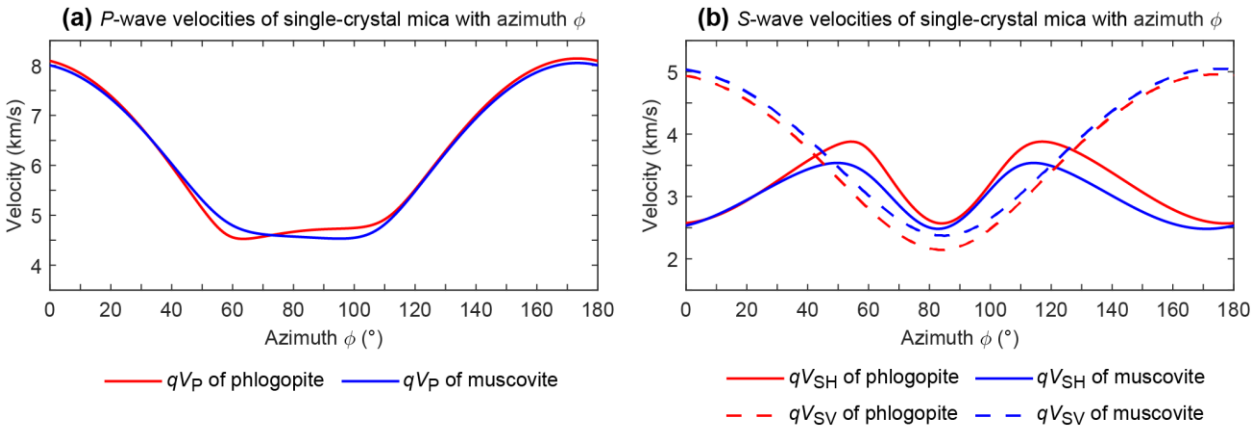

(c) Maximum and minimum seismic velocities of phlogopite and muscovite in (a) and (b)

	P wave		*SH* wave		*SV* wave	
	Max (at ϕ)	Min (at ϕ)	Max (at ϕ)	Min (at ϕ)	Max (at ϕ)	Min (at ϕ)
Phlogopite	8.141 km/s (ϕ = 173°)	4.526 km/s (ϕ = 64°)	3.880 km/s (ϕ = 117°)	2.568 km/s (ϕ = 84°)	4.956 km/s (ϕ = 174°)	2.148 km/s (ϕ = 84°)
			3.880 km/s (ϕ = 54°)[a]	2.569 km/s (ϕ = 177°)[b]		
Muscovite	8.051 km/s (ϕ = 173°)	4.531 km/s (ϕ = 95°)	3.539 km/s (ϕ = 114°)	2.481 km/s (ϕ = 171°)	5.048 km/s (ϕ = 175°)	2.373 km/s (ϕ = 85°)
			3.538 km/s (ϕ = 50°)[a]	2.481 km/s (ϕ = 83°)[b]		

[a]Another ϕ and velocity showing a maximum compared to the surrounding azimuth angles.
[b]Another ϕ and velocity showing a minimum compared to the surrounding azimuth angles.

Figure 4.13 2D seismic velocities for single crystals of biotite (phlogopite) and muscovite used in the present study. See Figure 4.5 for full 3D seismic velocities. (a) *P*-wave velocities (qV_P) of mica in the [100]-[001] plane. (b) *SH*- and *SV*-wave velocities (qV_{SH} and qV_{SV}) of mica in the [100]-[001] plane. If we consider [100] and [001] of mica as $x1$ and $x2$ axes, respectively, then this plot can be viewed as the 2D velocity plots used for rocks with azimuth ϕ from 0° to 180° in the $x1$-$x2$ plane. The 2D seismic velocities in the [100]-[001] plane is not perfectly symmetrical with respect to ϕ = 90° since 3D seismic velocities of phlogopite and muscovite show monoclinic symmetry (Figure 4.5). (c) Maximum and minimum velocities in (a) and (b) and their azimuth ϕ. *P* wave in both phlogopite and muscovite show a maximum velocity when propagating sub-parallel to the basal (001) plane (ϕ = 173°). The minimum qV_P is present at ϕ = 64° for phlogopite and 95° for muscovite. *SV* wave in phlogopite and muscovite have a minimum velocity at ϕ = 84° and 85°, respectively, due to sub-perpendicular propagation to the basal (001) plane and a maximum velocity at ϕ = 174° or 175°, respectively, because both propagation and polarization directions are sub-parallel to the basal (001) plane. *SH* wave exhibits minimum (or lower) velocities with sub-perpendicular propagation or polarization to the basal (001) plane (ϕ = 84° or 177° for phlogopite; ϕ = 171° or 83° for muscovite). On the other hand, maximum (or higher) qV_{SH} in phlogopite and muscovite is present at an angle where either its propagation or polarization direction is away from the basal (001) plane, and therefore the maximum qV_{SH} in the [100]-[001] plane is much lower than the maximum qV_{SV}.

4.6.3.2. *S* Waves

Similar to the natural rocks, 2D qV_{SH} and qV_{SV} of the synthetic mica-rich schist show much larger variations than the synthetic mica-poor QF rock in the $x1$-$x2$ plane (Figure 4.10e; see Table 4.1). For the synthetic QF and schist rocks, the slowest 2D qV_{SH} are present at ϕ = 174° and 90°, respectively, owing to its polarization or propagation (sub-)perpendicular to the foliation, and the fastest 2D qV_{SH} are present at ϕ = 42° and 55° with neither polarization nor propagation (sub-)perpendicular to the foliation (Figure 4.10e; Table 4.1). For qV_{SV} in the $x1$-$x2$ plane, as both polarization and propagation directions are (sub-)parallel to the foliation, the synthetic QF and schist rocks have maximum speeds at ϕ = 177° and 0°, respectively, and minimum speeds are present at ϕ = 97° and 95° with propagation sub-perpendicular to the foliation (Figure 4.10e; Table 4.1). These 2D velocity features for synthetic rocks are similar to the 2D qV_{SH} and qV_{SV} for monoclinic single-crystal biotite or muscovite plotted in the [100]-[001] plane (Figure 4.13), but the *S*-wave velocity curves for the mica-rich synthetic schist in the $x1$-$x2$ plane are approximately symmetrical with respect to ϕ = 90° presumably due to a combination of the monoclinic velocity curves for biotite and muscovite (Figure 4.10e). In the foliation-parallel direction, the synthetic schist shows faster $qV_{SV}(0°)$ than the synthetic QF rock, whereas in the foliation-perpendicular direction, $qV_{SV}(90°)$ of the synthetic schist is slower (Figure 4.10e). For qV_{SH} in the $x1$-$x2$ plane, the synthetic schist exhibits slower velocities than the synthetic QF rock at all azimuth angles (Figure 4.10e).

The seismic contrasts of *SH* and *SV* waves between the two synthetic rocks show similar variations with azimuth ϕ to the natural rocks (Figures 4.7f and 4.10f). The qV_{SH} contrast is between 4.1% and 23.4%, and the qV_{SV} contrast ranges from 0% to 24.4% (Figure 4.10f). The qV_{SH} and qV_{SV} contrasts at ϕ = 0° are 22.7% (more compliant synthetic schist) and 9.8% (more compliant synthetic QF), respectively. At ϕ = 90°, the contrasts of qV_{SH} and qV_{SV} are 23.3% and 23.2%, respectively, the synthetic schist being more compliant for both *SH* and *SV* waves (Figure 4.10f).

Unlike the complicated velocity patterns of the natural QF rock, the 3D qV_{SH} and qV_{SV} patterns for the synthetic QF rock is similar to the monoclinic symmetry velocity patterns of single-crystal biotite, but its seismic anisotropies (16.4% for qV_{SH} and 15.6% for qV_{SV}) are comparable to the natural QF rock (Figures

4.5, 4.10g and 4.10h). The mica-rich synthetic schist shows nearly hexagonal symmetry of qV_{SH} and qV_{SV} similar to the natural schist and has much higher seismic anisotropies (47.0% for qV_{SH} and 46.8% for qV_{SV}) than the mica-poor synthetic QF rock (Figures 4.10g and 4.10h).

Table 4.1 Maximum and minimum seismic velocities and their differences for the natural and synthetic rocks in the *x*1-*x*2 plane, computed using the AEH method.

	Seismic velocity (km/s)								
	P wave			*SH* wave			*SV* wave		
Rock sample	Max (at ϕ[a])	Min (at ϕ)	Diff[b]	Max (at ϕ)	Min (at ϕ)	Diff	Max (at ϕ)	Min (at ϕ)	Diff
Natural QF[c] (BB6)	6.408 (ϕ = 19°)	5.838 (ϕ = 82°)	0.570	3.971 (ϕ = 76°)	3.505 (ϕ = 25°)	0.467	3.964 (ϕ = 153°)	3.562 (ϕ = 87°)	0.403
Natural Schist (35)	7.124 (ϕ = 3°)	4.980 (ϕ = 96°)	2.144	3.598 (ϕ = 130°)	2.859 (ϕ = 3°)	0.739	4.397 (ϕ = 3°)	3.004 (ϕ = 93°)	1.393
Synthetic QF	6.488 (ϕ = 174°)	5.863 (ϕ = 56°)	0.625	3.924 (ϕ = 42°)	3.515 (ϕ = 174°)	0.409	4.095 (ϕ = 177°)	3.570 (ϕ = 97°)	0.525
Synthetic Schist	7.413 (ϕ = 0° or 180°)	4.918 (ϕ = 81°)	2.495	3.663 (ϕ = 55°)	2.798 (ϕ = 90°)	0.865	4.514 (ϕ = 0° or 180°)	2.827 (ϕ = 95°)	1.687

Note: 2D seismic velocities at all azimuth ϕ for the natural and synthetic rocks are plotted in Figures 4.7 and 4.10, respectively.

[a]Azimuth ϕ is the incidence angle of waves with respect to the *x*1 direction in the horizontal *x*1-*x*2 plane. For example, the *x*1 and *x*2 directions are ϕ = 0° and 90°, respectively. See Figure 4.4c for the coordinate system.

[b]Difference (Diff) = maximum velocity − minimum velocity.

[c]QF = quartzofeldspathic rock.

4.7. Discussion

4.7.1. Determination of Elastic Contrast Between the Anisotropic Rocks

The effective damage zone around the SCSZ reveals asymmetric distribution being wider (~207 m) in the QF rocks and narrower (~53 m) in the schist, with similarly asymmetric distribution of pulverized zones of ~63 m and ~5 m in the QF and schist units, respectively (Figure 4.2d; B. R. Song et al., 2020). Asymmetric damage is commonly observed around bimaterial strike-slip faults separating rocks with different elastic properties (e.g., Dor et al., 2006a, 2006b, 2008; Mitchell et al., 2011; Rempe et al., 2013). Based on numerical rupture-propagation studies, the contrast in rock material properties across a fault leads to bimaterial coupling, which results in wrinkle-like pulse ruptures with unilateral rupture directivity in the slip direction of the more compliant side, and therefore produces asymmetry of ground motion and damage distribution due to the directivity effect (e.g., Weertman, 1980; Andrews and Ben-Zion, 1997; Ben-Zion, 2001; Ben-Zion and Huang, 2002; Shi and Ben-Zion, 2006; Ampuero and Ben-Zion, 2008; Dalguer and Day, 2009; Erickson and Day, 2016; Xu and Ben-Zion, 2017). Thus, determining elastic properties and wave-speed contrasts across the fault appears to be an integral component of understanding the rupture directivity and its related effects.

Owing to the difficulty of incorporating elastic anisotropy, numerical studies of rupture propagation typically treat rocks as elastically isotropic (Figure 4.1; e.g., Andrews and Ben-Zion, 1997; Harris and Day, 1997; Cochard and Rice, 2000; Shi and Ben-Zion, 2006; Brietzke et al., 2007; Ampuero and Ben-Zion, 2008; Erickson and Day, 2016; Xu and Ben-Zion, 2017). However, earthquake ruptures in natural faults typically occur in rocks with at least moderate elastic anisotropy, partly caused by rock fabrics and associated crystallographic preferred orientation developed during deformation and associated metamorphism (e.g., Jefferies et al., 2006; Christensen and Okaya, 2007; Li et al., 2014b; Audet, 2015). In contrast to elastically isotropic rocks, anisotropic rocks show directional dependence of seismic wave velocities and thus velocity contrasts. For example, in the SCSZ-parallel direction at $\phi = 0°$, the QF rock is more compliant for qV_P or qV_{SV} but the schist is more compliant for qV_{SH}. In contrast, the schist is more compliant for all three waves in the SCSZ-perpendicular direction at $\phi = 90°$ (Figures 4.7c and 4.7f). In this

section, we discuss which elastic contrast between the two anisotropic rocks may be the most diagnostic for evaluating the potential for rupture directivity. Since it is difficult to visualize anisotropic elastic properties (e.g., stiffness tensor), we use seismic wave velocities and their contrasts as a proxy for elastic contrast.

In vertical strike-slip faults, small earthquakes generally propagate in two directions as a mixture of in-plane (mode II) and anti-plane (mode III) ruptures (e.g., Harris and Day, 2005). In contrast, for moderate and large strike-slip earthquakes (e.g., >M6.5), fault ruptures initiate with a mixture of mode II and III propagation, but after saturating the seismogenic zone, their subsequent propagation is predominantly lateral in mode II (e.g., Ben-Zion, 2006). Moreover, only mode II ruptures in strike-slip faults have been shown to exhibit the bimaterial coupling of shear slip and normal stress, generating the preferentially propagating wrinkle-like pulse (Ben-Zion and Andrews, 1998). The SCSZ is a vertical strike-slip fault which, based on the common occurrence of pseudotachylyte, experienced large earthquakes (Price et al., 2012; W. J. Song et al., 2020). Thus, in the present study, we consider 2D in-plane shear ruptures, horizontally propagating along the strike of the fault/shear zone and limit our discussion to wave velocities in the horizontal $x1$-$x2$ plane. The SCSZ system in this study is exhumed from middle crustal depths corresponding to temperatures of 400–500 °C (W. J. Song et al., 2020). Thus, we can apply the theoretical and numerical studies to the coseismic off-fault damage without considering the effect of Earth's free surface.

For a subshear rupture in bimaterial strike-slip faults, differential fault-normal particle motion near the rupture tip is key to the bimaterial coupling effect, and the contrast that governs the strength of the bimaterial effects is that of the *S*-wave velocities (Figures 4.1b and 4.1c; e.g., Somerville et al., 1997; Ben-Zion and Andrews, 1998; Ben-Zion, 2001). The fault-normal particle motion (parallel to the $x2$ axis) at the rupture tip for a subshear rupture is found only in the *SH* wave propagating parallel to the SCSZ-parallel slip direction at $\phi = 0°$ (Figure 4.6b). We therefore disregard the *P* wave as well as the *SV* wave at $\phi = 0°$ because their particle motions are parallel to the vertical fault/shear zone (Figure 4.6b).

The velocity contrast for the *SH* wave between the natural QF and schist rocks at $\phi = 0°$ is 25.5%, and the schist is more compliant (Figure 4.7f). In Section 4.7.2, by analogy with the model of rupture dynamics for bimaterial faults in elastically isotropic media described above, we consider the *SH* wave as diagnostic in the SCSZ and discuss preferred rupture propagation in the slip direction of the more compliant schist and greater damage-zone width in the less compliant QF rock (Figures 4.1b and 4.1e). Below we discuss subshear and supershear rupture models assuming that the *SH* wave in our anisotropic rocks can substitute for the *S*-wave in isotropic rocks.

4.7.2. Comparison With Previous Isotropic Bimaterial Models

4.7.2.1. Subshear Rupture Model

In subshear rupture models of a bimaterial interface (fault) separating two elastically isotropic dissimilar materials, the presence of elastic contrast across the interface causes mismatch in seismic wave velocities and produces head waves that propagate along the fault and radiate to the more compliant medium (Ben-Zion, 1989, 1990). Thus, in addition to slower *P*- and *S*-wave fronts, two different head wave fronts (*P*-to-*P* between faster and slower *P* waves, and *S*-to-*S* between faster and slower *S* waves) propagate on the more compliant side (Figure 4.1b; e.g., Ben-Zion, 2001). Numerical results of Andrews and Ben-Zion (1997) and Ben-Zion and Andrews (1998) showed that the *S*-to-*S* head wave contributes to normal stress transition from compression during the buildup of the head wave to tension after arrival of the slower *S* wave, which allows pulse-like slip to occur at the rupture front. Therefore, wrinkle-like pulse ruptures are governed by the contrast of *S* wave velocities across the interface.

In those models, even though the up-down symmetry across the interface is lost, the *P*- and *S*-wave fronts remain circular in both stiff and compliant sides due to elastically isotropic media (Figure 4.1b). In contrast, seismic wave speed varies with propagation direction in anisotropic materials, resulting in non-spherical wave fronts. In addition, the shear wave in anisotropic media splits into two quasi-shear waves

with different polarizations and velocities (e.g., qV_{SH} and qV_{SV}) and their polarizations are approximately orthogonal (e.g., Figure 4.6a), whereas no shear-wave splitting is observed in isotropic materials. Therefore, additional complexity arises in a bimaterial interface between anisotropic materials.

Figure 4.14 plots *P*-, *SH*- and *SV*-wave velocities in polar coordinates for the natural and synthetic rocks of the SCSZ, in which the QF rock is placed in the upper side (ϕ = 0° to 180°) and the schist in the lower side (ϕ = 180° to 360°). The lithologic contact or shear-zone core lies along the horizontal axis (ϕ = 0° or 180°), which is parallel to the fault/shear zone slip direction. Since the synthetic rocks have the same modal mineralogy and mica preferred orientation as the natural rocks, any differences in wave velocity patterns or wave fronts in Figure 4.14 between the synthetic and natural rocks are caused by other factors such as crystallographic orientations of quartz and plagioclase. Due to different degree of anisotropy in each rock, wave fronts in the QF and schist rocks show different variations, and therefore varying velocity contrasts are expected depending on propagation direction. For example, both natural and synthetic QF rocks with relatively weak anisotropy have sub-circular wave fronts, whereas both schists with strong anisotropy have non-circular wave fronts (Figure 4.14). In the schists, the *P* and *SV* waves are faster in the fault-parallel direction and slower in the fault-normal direction than those in the QF rocks (Figure 4.14). Since the *SH*-wave velocity pattern in the mica-rich schists with planar foliation is similar to single-crystal mica, their *SH* waves are slower than the QF rocks in all (for the synthetic rocks) or most (for the natural rocks) propagation directions including the fault-parallel and normal directions, indicating more compliant schists at most values of ϕ (Figures 4.7f, 4.10f and 4.14).

If we apply the numerical results of Andrews and Ben-Zion (1997) and Ben-Zion and Andrews (1998) in isotropic media to our velocity analysis, the contrast between *SH*-wave velocities across the SCSZ contact would govern the bimaterial effect that can lead to strongly asymmetric fault-normal particle motions and produce preferentially propagating wrinkle-like pulses. The *SV* wave with vertical polarization is not likely to facilitate bimaterial coupling and related effects. When considering a propagation direction parallel to the fault, at the rupture tip, rapid transition of normal stress and fault-normal motion from an *S*-to-*S* head wave to a slower *SH* wave of the schist would allow the pulse to propagate in the slip direction

of the more compliant schist and hence to preferentially produce off-fault damage in the stiffer QF rock with the faster *SH* wave (Figure 4.14a). With repeated ruptures (e.g., Doan and d'Hour, 2012; Aben et al., 2016), we might expect a strongly asymmetric damage zone that is wider in the QF rocks, consistent with the asymmetric distribution of damage observed across the SCSZ (Figure 4.2d).

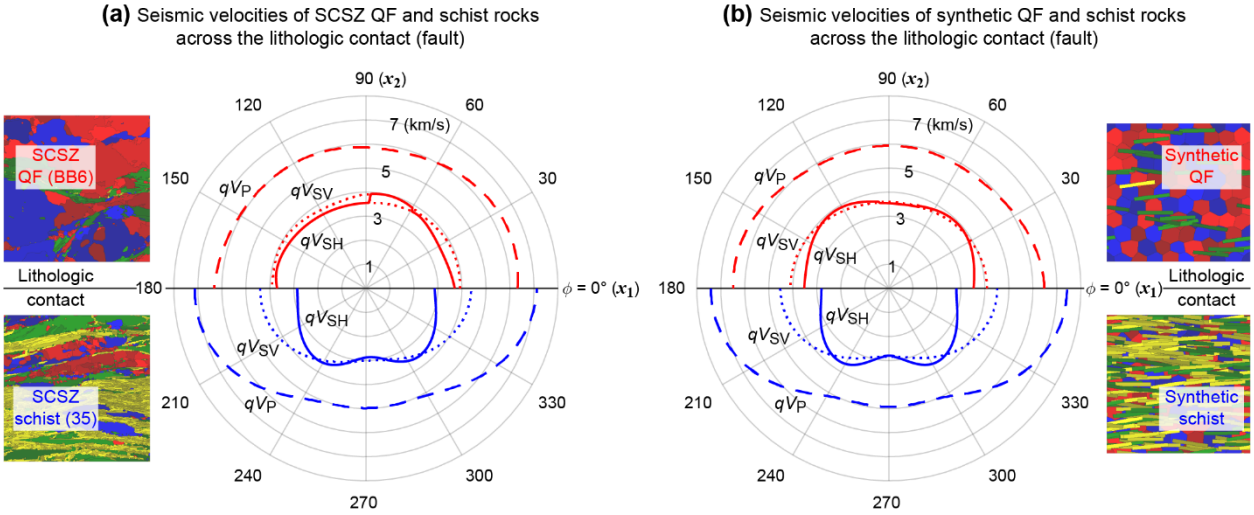

Figure 4.14 Polar plots of 2D seismic velocities (qV_P, qV_{SH} and qV_{SV}) in the $x1$-$x2$ plane for quartzofeldspathic (QF; upper half) and schist (lower half) rocks. The velocities were computed using the AEH method. (a) Natural QF and schist host rocks of the Sandhill Corner shear zone (SCSZ). (b) Synthetic QF and schist rocks. These are the same as the velocity graphs plotted in rectangular coordinates (Figures 4.7b, 4.7e, 4.10b and 4.10e), but these plots in polar coordinates can be considered as plan view of seismic waves at a unit time for QF and schist rocks across the lithologic contact (fault), highlighting how velocity changes with direction in an anisotropic medium.

4.7.2.2. Supershear Rupture Model

Most ruptures propagate at velocities below the Rayleigh wave speed, or ~92% of the shear wave speed (Craggs, 1960; Freund, 1990), and as noted above, asymmetric rock damage around the SCSZ is consistent with material contrast across the shear zone and preferred propagation of subshear ruptures. However, theoretical and numerical studies (e.g., Burridge, 1973; Andrews, 1976; Das and Aki, 1977; Freund, 1990; Broberg, 1994, 1995; Gao et al., 2001; Shi et al., 2008; Liu et al., 2014) and laboratory experiments (e.g., Rosakis et al., 1999; Xia et al., 2004; Passelègue et al., 2013) demonstrate that rupture speed can exceed the shear wave speed and even reach the compressional wave speed. There is also growing

evidence of these "supershear" earthquakes observed from large strike-slip faults in nature (e.g., Archuleta, 1984; Bouchon et al. 2001; Bouchon and Vallee 2003; Dunham and Archuleta, 2004; Wang and Mori, 2012; Yue et al., 2013; Socquet et al., 2019). In addition, experimental work suggests that subshear rupture might not produce high enough strain rates at sufficient distance to explain the width of pulverization around natural faults (e.g., Aben et al., 2017a; Xu and Ben-Zion, 2017; Griffith et al., 2018). For these reasons, supershear rupture has been considered as a possible mechanism for rock pulverization well off the main slip surface (Doan and Gary, 2009; Yuan et al., 2011) and such *S* shock waves are thought to have caused high strain rates at distance of up to several kilometers from the fault core (Bhat et al., 2007).

A supershear rupture along a bimaterial fault in elastically isotropic material preferentially propagates to the negative direction (e.g., Ranjith and Rice, 2001; Xia et al., 2005; Shlomai et al., 2020a). Theoretical analysis of Ranjith and Rice (2001), for example, predicted that supershear ruptures with speeds close to a *P*-wave velocity of a more compliant material can propagate only in the negative direction. Xia et al. (2005) and Shlomai et al. (2020a) experimentally observed supershear rupture along the negative direction at velocities approaching and exceeding the slower *P*-wave speed. Thus, if we assume a supershear rupture along the elastically anisotropic SCSZ and speculate that the *SH* wave with fault-parallel propagation is still important in determining material contrast and rupture directivity, then rupture would be more likely to propagate in the slip direction of the stiffer QF rocks, which is the opposite direction of preferred subshear rupture propagation. As a result, a wider damage zone would occur in the more compliant schist side, which is the opposite of what we observe in the SCSZ.

Alternatively, in numerical investigations, Shi and Ben-Zion (2006) observed supershear transitions in both directions along an isotropic bimaterial interface with velocities close to the *P*-wave speed of the more compliant material in the negative direction and close to the *P*-wave speed of the stiffer material in the positive direction. If this supershear rupture propagation produces off-fault damage, the resulting damage zones are likely to distribute symmetrically on both sides of the fault (Xu and Ben-Zion, 2017), which is inconsistent with our observation of asymmetric damage distribution. A possible explanation is that multiple bilateral supershear ruptures without a preferred-propagation direction have

occurred, but that the asymmetric damage distribution may be caused by the different rock types (QF and schist) rather than rupture directivity. For example, Aben et al. (2017b) proposed that more compliant rocks on one side of the fault would respond differently to similar dynamic loading from stiffer rocks on the opposite side, leading to asymmetric damage. Their experimental results showed that layered anisotropic sandstone was not pulverized during dynamic loading. An open question regarding further experimental work is whether the strong anisotropy of the SCSZ schist might have a mitigating effect on damage, resulting in the asymmetric damage in the SCSZ. In addition, supershear ruptures along anisotropic bimaterial interfaces have not yet been explored numerically, so the relationship between supershear rupture directivity and damage distribution remains an open question.

4.7.3. Comparison With Other Homogenization Methods

Since the AEH homogenization method (Vel et al., 2016) considers not only modal mineralogy and crystallographic orientations but also the relative positions and elastic interactions of the constituent grains, it calculates the non-uniform stress and strain distributions in polycrystalline rocks, achieving an accurate determination of the bulk elastic properties (Naus-Thijssen et al., 2011a, 2011b; Vel et al., 2016; Almqvist and Mainprice, 2017; Cyprych et al., 2017). We compare the AEH results of the natural and synthetic QF and schist rocks with three analytical homogenization techniques: Voigt, Reuss, and Hill averages. The Voigt average assumes a constant strain field throughout the material (Voigt, 1928) and shows theoretical maximum elastic moduli and wave speeds. On the other hand, the Reuss average assumes a constant stress field throughout the material (Reuss, 1929) and provides theoretical minimum elastic moduli and wave speeds. The Hill average is an arithmetic mean of the Voigt and Reuss bounds (Hill, 1952) and is commonly used to estimate bulk elastic properties of polycrystals.

In the comparison plots with Voigt, Reuss, and Hill averages for the natural and synthetic rocks (Figures 4.15–4.19), 2D seismic velocities (qV_P, qV_{SH} and qV_{SV}) plotted in the $x1$-$x2$ plane by the AEH method lie between the Voigt and Reuss bounds and are very close to the Hill average except where the *S*-wave crossovers occur for the natural QF rock (Figure 4.15). Similarly, 3D seismic velocities (qV_P, qV_{SH}

and qV_{SV}) using the AEH method are close to the Hill average, and the difference of seismic anisotropy between the AEH and Hill estimates is less than 3.1% for qV_P and 4.4% and 3.4% for qV_{SH} and qV_{SV}, respectively (Figures 4.16 and 4.18). Despite some differences in seismic velocities and anisotropies among the four homogenization techniques, they do not affect our interpretation of rupture directivity and damage asymmetry based on the AEH method. The velocity contrast plots in the $x1$-$x2$ plane for the natural and synthetic rocks are very similar to each other regardless of the homogenization methods, and especially in the SCSZ-parallel slip direction at $\phi = 0°$ where the difference of velocity contrast among the homogenization techniques is less than ~1.6% for *P* wave and ~3.9% for *S* waves (Figures 4.15 and 4.17).

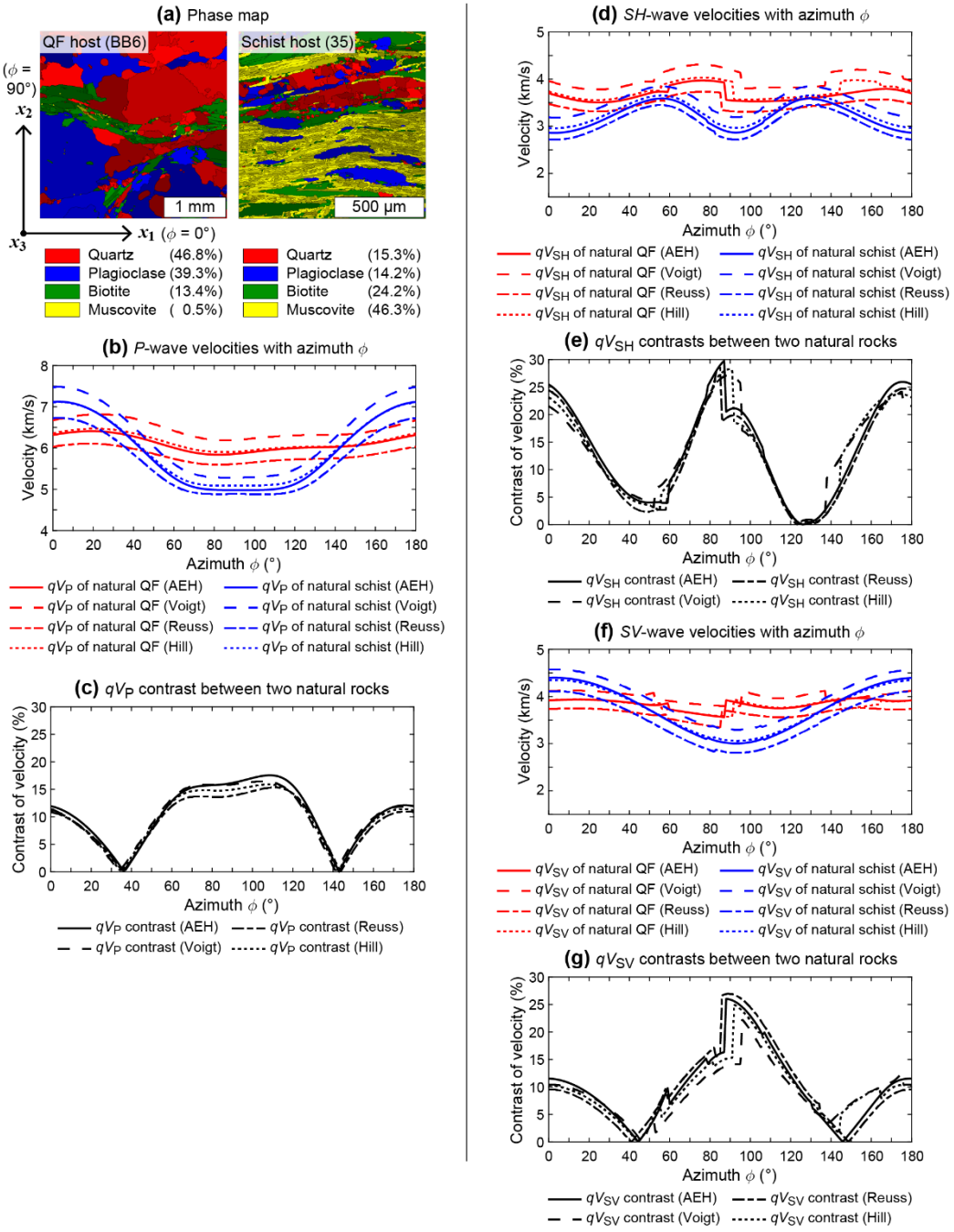

Figure 4.15 Comparison of the AEH results with Voigt, Reuss, and Hill averages for 2D seismic velocities and velocity contrasts in the quartzofeldspathic (QF) and schist host rocks of the Sandhill Corner shear zone. Velocities and their contrasts are plotted against azimuth ϕ from 0° to 180° in the $x1$-$x2$ plane. (a) Phase maps of the natural QF (sample BB6) and schist (sample 35) host rocks. From Figure 4.7a. (b) 2D *P*-wave velocities (qV_P) for each natural rock, calculated by the four homogenization techniques. (c) qV_P contrasts between the natural QF and schist rocks, calculated from (b). (d) 2D *SH*-wave velocities (qV_{SH}) for each natural rock, calculated by the four homogenization techniques. (e) qV_{SH} contrasts between the natural QF and schist rocks calculated from (d). (f) 2D *SV*-wave velocities (qV_{SV}) for each natural rock, calculated by the four homogenization techniques. (g) qV_{SV} contrasts between the natural QF and schist rocks, calculated from (f).

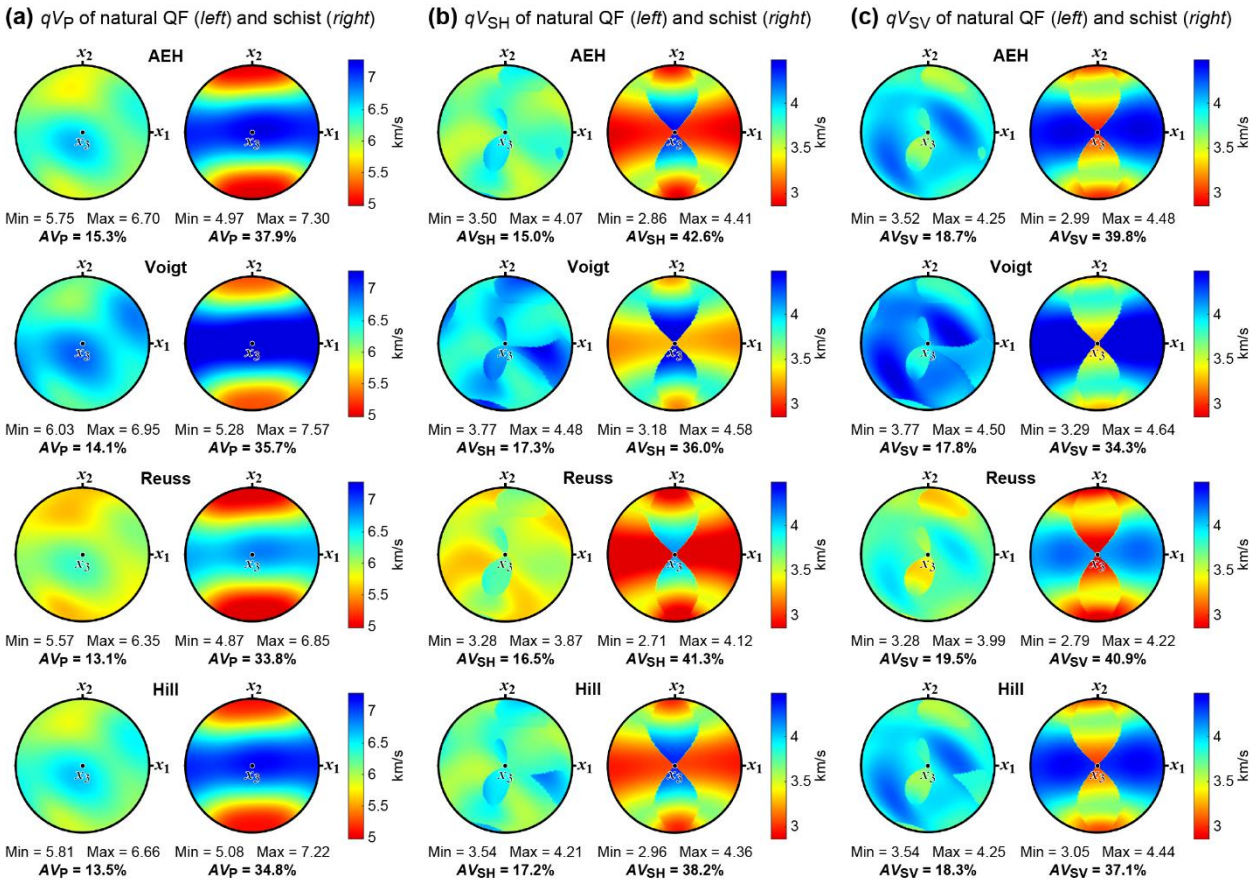

Figure 4.16 Comparison of the AEH results with Voigt, Reuss, and Hill averages for 3D seismic velocities and anisotropies in the quartzofeldspathic (QF) and schist host rocks of the Sandhill Corner shear zone. Velocities are presented in equal-area, upper hemisphere projection and with the same color limits for comparison. (a) 3D *P*-wave velocities (qV_P) and their seismic anisotropies (AV_P) for each natural rock, calculated by the four homogenization techniques. (b) 3D *SH*-wave velocities (qV_{SH}) and their seismic anisotropies (AV_{SH}) for each natural rock, calculated by the four homogenization techniques. (c) 3D *SV*-wave velocities (qV_{SV}) and their seismic anisotropies (AV_{SV}) for each natural rock, calculated by the four homogenization techniques. See Figure 4.15a for the coordinate system and the phase map of each natural rock.

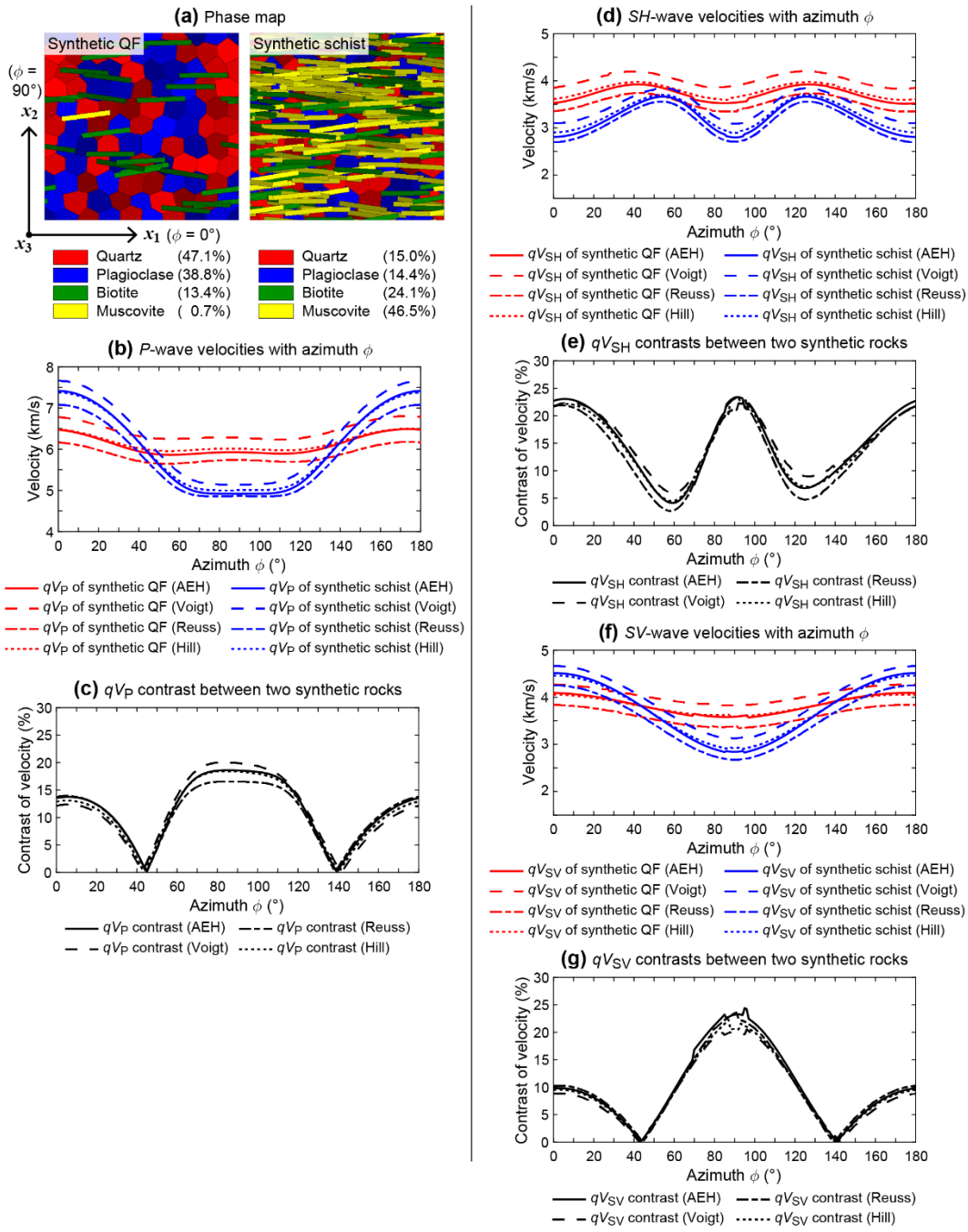

Figure 4.17 Comparison of the AEH results with Voigt, Reuss, and Hill averages for 2D seismic velocities and velocity contrasts in synthetic rock samples with the same mica contents as the natural quartzofeldspathic (QF) and schist host rocks of the Sandhill Corner shear zone. Velocities and their contrasts are plotted against azimuth ϕ from 0° to 180° in the *x*1-*x*2 plane. (a) Phase maps of the synthetic QF and schist rocks. From Figure 4.10a. (b) 2D *P*-wave velocities (qV_P) for each synthetic rock, calculated by the four homogenization techniques. (c) qV_P contrasts between the synthetic QF and schist rocks, calculated from (b). (d) 2D *SH*-wave velocities (qV_{SH}) for each synthetic rock, calculated by the four homogenization techniques. (e) qV_{SH} contrasts between the synthetic QF and schist rocks, calculated from (d). (f) 2D *SV*-wave velocities (qV_{SV}) for each synthetic rock, calculated by the four homogenization techniques. (g) qV_{SV} contrasts between the synthetic QF and schist rocks, calculated from (f).

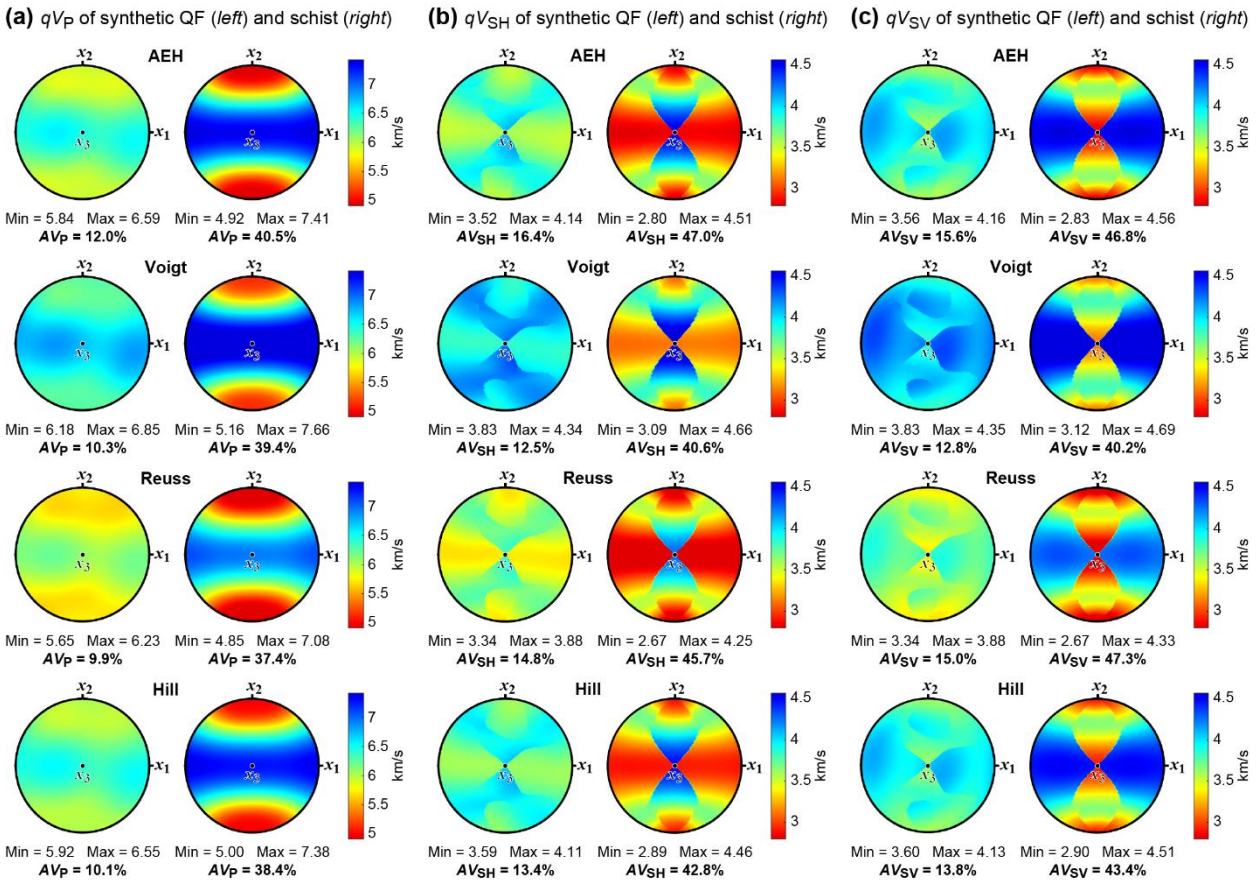

Figure 4.18 Comparison of the AEH results with Voigt, Reuss, and Hill averages for 3D seismic velocities and anisotropies in synthetic rock samples with the same mica contents as the natural quartzofeldspathic (QF) and schist host rocks of the Sandhill Corner shear zone. Velocities are presented in equal-area, upper hemisphere projection and with the same color limits for comparison. (a) 3D *P*-wave velocities (qV_P) and their seismic anisotropies (AV_P) for each synthetic rock, calculated by the four homogenization techniques. (b) 3D *SH*-wave velocities (qV_{SH}) and their seismic anisotropies (AV_{SH}) for each synthetic rock, calculated by the four homogenization techniques. (c) 3D *SV*-wave velocities (qV_{SV}) and their seismic anisotropies (AV_{SV}) for each synthetic rock, calculated by the four homogenization techniques. See Figure 4.17a for the coordinate system and the phase map of each synthetic rock.

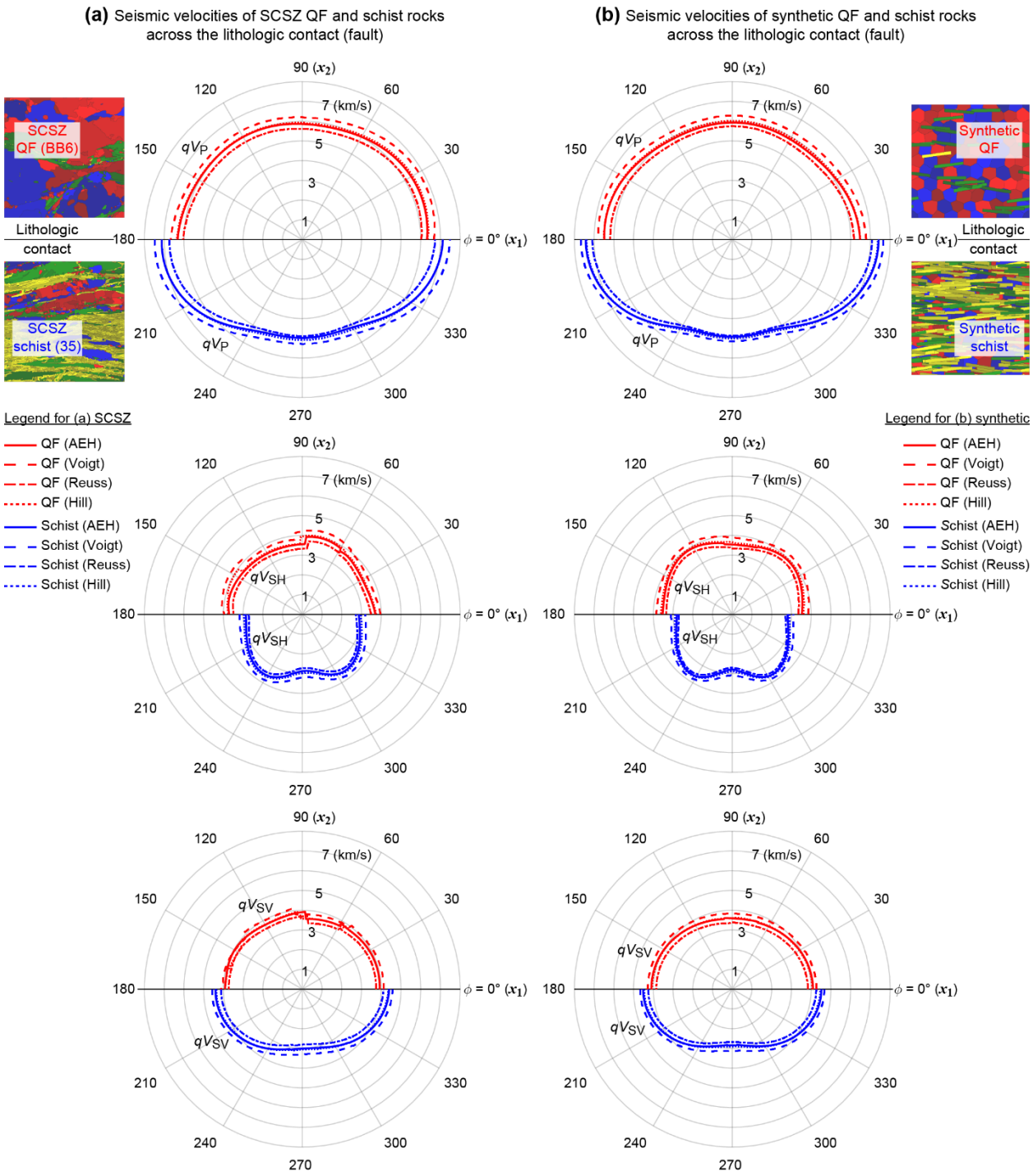

Figure 4.19 Comparison of the AEH results with Voigt, Reuss, and Hill averages for 2D seismic velocities in the *x*1-*x*2 plane of *P* wave (qV_P; *top*), *SH* wave (qV_{SH}; *middle*), and *SV* wave (qV_{SV}; *bottom*) plotted in polar coordinates. (a) Natural quartzofeldspathic (QF; upper half of each panel) and schist (lower half of each panel) host rocks of the Sandhill Corner shear zone (SCSZ). (b) Synthetic QF (upper half of each panel) and schist (lower half of each panel) rocks. These are the same as the velocity graphs plotted in rectangular coordinates (Figures 4.15b, 4.15d, 4.15f, 4.17b, 4.17d and 4.17f), but these plots in polar coordinates can be considered as plan view of seismic waves at a unit time for QF and schist rocks across the lithologic contact (fault), highlighting how velocity changes with direction in an anisotropic medium.

4.7.4. Effect of Mica Content on Seismic Velocity Contrast

The role of mica in seismic anisotropy has been relatively well studied because mica is recognized as a major contributor to observed seismic anisotropy in middle crustal settings owing to its high anisotropy and the common development of preferred shape and crystallographic orientation (e.g., Christensen, 1965; Barruol and Mainprice, 1993; Shapiro et al., 2004; Lloyd et al., 2009; Dempsey et al., 2011; Ward et al., 2012; Kästner et al., 2021). However, we are not aware of studies that have explored the relationship between mica content and seismic velocity contrast, so here we employ synthetic microstructures to explore this relationship and compare our results to published velocity data from natural rocks with varying mica content.

4.7.4.1. Sensitivity Analysis of Varying Mica Content

To explore the role of mica content on seismic velocity contrast, we generate eleven synthetic microstructures with modal% mica ranging from 0% to 100% in 10% intervals using the technique described in Section 4.5.1 (Figures 4.20 and 4.21). In the synthetic microstructures, we use three types of relative proportions of biotite (Bt) and muscovite (Ms): (1) 100% biotite, (2) Bt:Ms = 50:50, and (3) 100% muscovite. The remaining mineralogy has 50:50 relative proportions of quartz and plagioclase in all the cases. As expected, the variations of 2D seismic velocities in the $x1$-$x2$ plane increase with increasing modal percentage of aligned mica (Figure 4.20b). Similarly, 3D seismic anisotropies of *P* and *S* waves (AV_P and AV_{SH} shown in Figure 4.20c) increase with mica modal percentage, which is consistent with previous work (e.g., Christensen, 1965; Dempsey et al., 2011; Ward et al., 2012; Almqvist et al., 2021; Han and Jung, 2021; Kästner et al., 2021). We calculate velocity contrasts of these synthetic microstructures relative to the synthetic QF rock at $\phi = 0°$. As $qV_{SH}(0°)$ decreases with increasing mica content (Figure 4.20b), the contrast of $qV_{SH}(0°)$ increases up to 33.9% for 100 modal% biotite (Figure 4.20d). The synthetic rocks with mica content greater than the synthetic QF rock (>14.1 modal%) are more compliant than the QF rock based on *SH*-wave velocity (Figure 4.20d). This might allow us to predict that if a rock has a higher modal percentage of preferentially oriented mica and higher anisotropy on one side of a mature bimaterial fault,

then that rock is more compliant, the positive direction becomes the preferred rupture direction, and the fault would show asymmetric damage. This prediction may be valid given that rocks adjacent to large continental strike-slip faults such as the San Andreas fault generally have foliations oriented sub-parallel to the sub-vertical slip surface (e.g., Schulz and Evans, 2000).

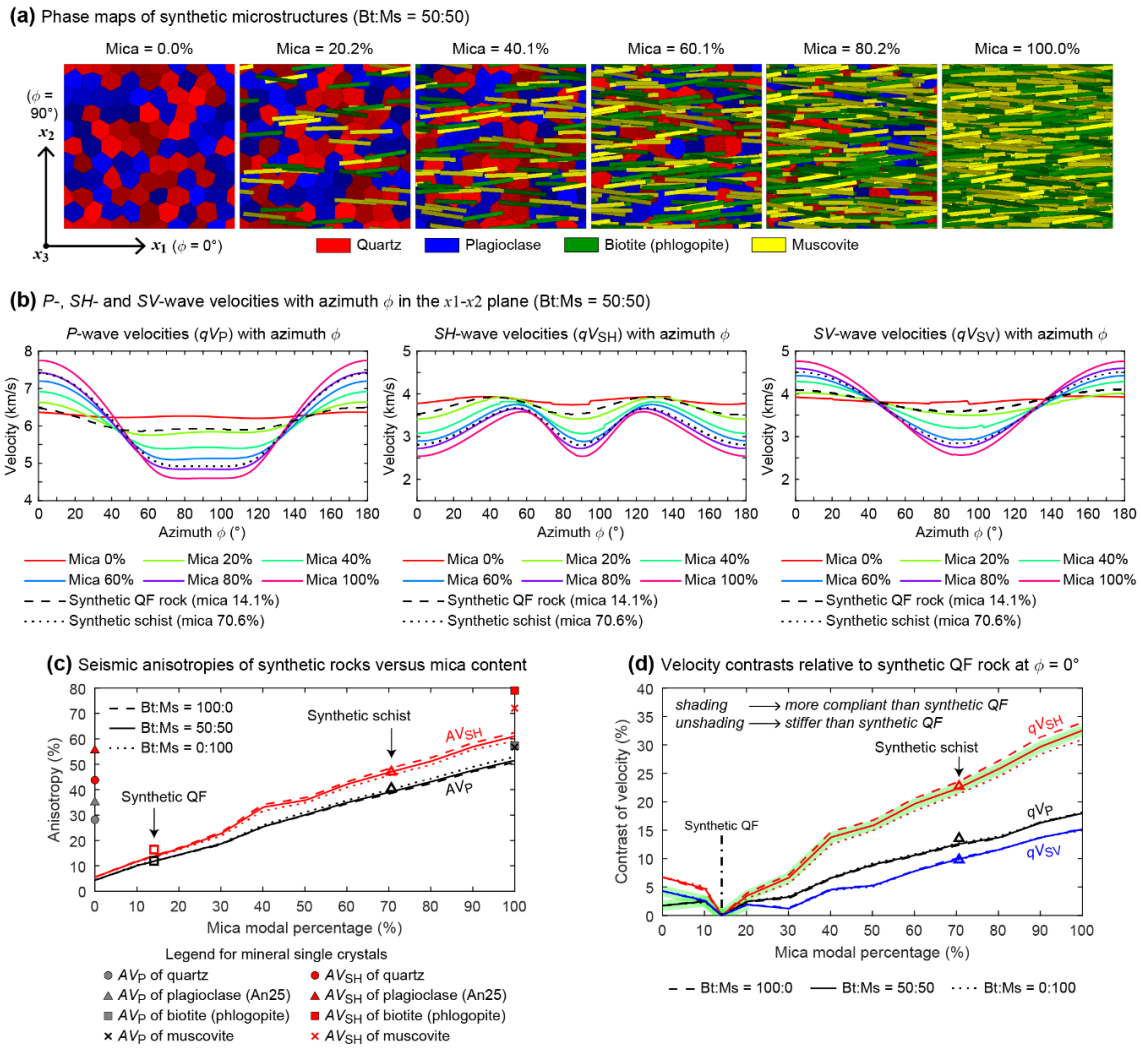

Figure 4.20 Effect of mica content, in synthetic rocks, on seismic velocity, anisotropy, and velocity contrast relative to the synthetic quartzofeldspathic (QF) rock. The velocities and anisotropies were computed using the AEH method. (a) Phase maps of selected synthetic microstructures with mica contents from 0% to 100% in 20% intervals. See Figure 4.21a for the full dataset (10% intervals). Each phase map with mica has the same ratio of biotite and muscovite (Bt:Ms = 50:50). The coordinate system and phase color information are also shown. (b) 2D seismic velocities of *P*, *SH* and *SV* waves for each synthetic microstructure in (a) plotted against azimuth ϕ (wave incidence angle) from 0° to 180° in the $x1$-$x2$ plane. See Figure 4.21b for the full dataset (10% intervals). The velocities for the synthetic QF (black dashed line) and schist (black dotted line) rocks are also plotted. (c) Seismic anisotropies of *P* and *SH* waves (AV_P and AV_{SH}, respectively) for the full dataset of synthetic microstructures, plotted against mica content. *SV*-wave seismic anisotropy is similar to AV_{SH} (see Figure 4.21a). Open squares and triangles indicate the synthetic QF and schist rocks, respectively (Figures 4.10d and 4.10g). Seismic anisotropies for single crystals of quartz, plagioclase, biotite (phlogopite) and muscovite are also plotted. (d) Velocity contrasts at ϕ = 0° for the full dataset of synthetic microstructures relative to the synthetic QF rock plotted against mica content. Open triangles indicate the synthetic schist (Figures 4.10c and 4.10f). Shading indicates the mica-modal ranges of more compliant rocks with lower velocities than the synthetic QF rock at ϕ = 0°. In (c) and (d), three types of results are plotted where relative modal percentages of biotite and muscovite are 100:0 (dashed line), 50:50 (solid line), and 0:100 (dotted line). See Figure 4.22 for 3D *S1*- and *S2*-wave velocities (qV_{S1} and qV_{S2}) and seismic anisotropies (AV_{S1} and AV_{S2}), and *S*-wave anisotropy percentage (AV_S).

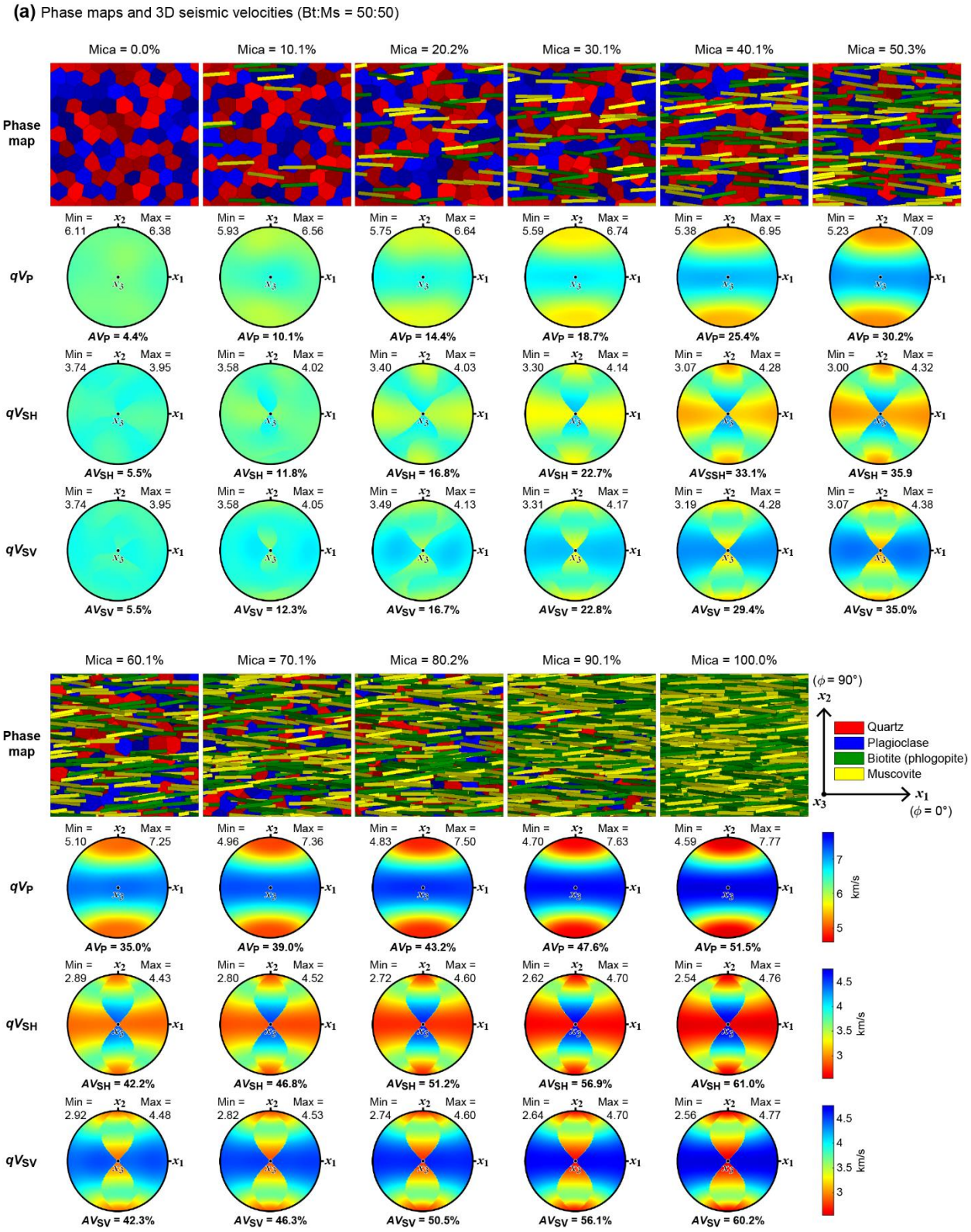

Figure 4.21 (see the next page for the caption)

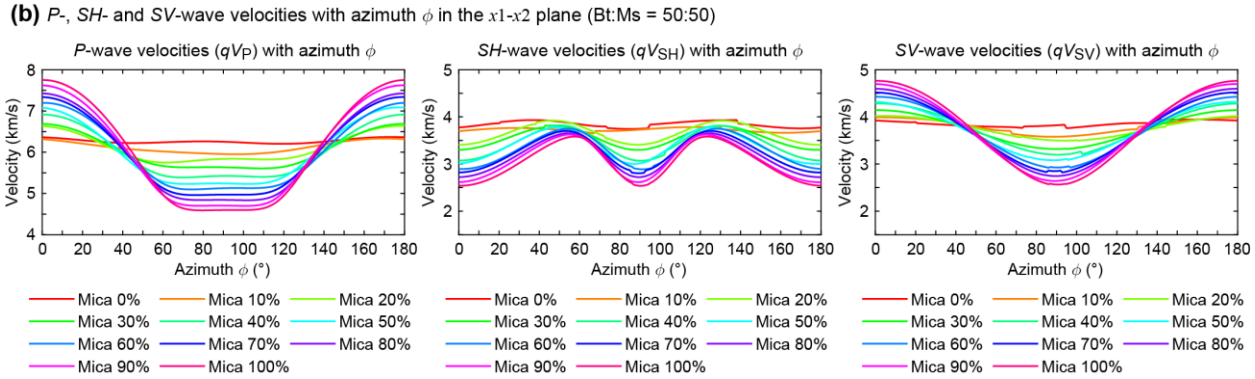

Figure 4.21 Effect of mica content, in synthetic rocks, on seismic velocities computed using the AEH method. (a) Phase maps and 3D seismic velocities of synthetic microstructures with mica contents from 0% to 100% in 10% intervals. Each phase map with mica has the same ratio of biotite and muscovite (Bt:Ms = 50:50). The coordinate system and phase color information are shown next to the phase map with 100% mica. *P*-, *SH*- and *SV*-wave velocities (qV_P, qV_{SH} and qV_{SV}, respectively) are presented in equal-area, upper hemisphere projection and with the same color limits for comparison. Seismic anisotropy (AV_P, AV_{SH} and AV_{SV}, respectively) for qV_P, qV_{SH} and qV_{SV} of each case is also displayed below each 3D seismic velocity plot. (b) 2D seismic velocities of *P*, *SH* and *SV* waves for each synthetic microstructure in (a) plotted with azimuth ϕ from 0° to 180° in the *x*1-*x*2 plane. See Figure 4.22 for *S1*- and *S2*-wave velocities (qV_{S1} and qV_{S2}, respectively) and *S*-wave anisotropy percentage (AV_S).

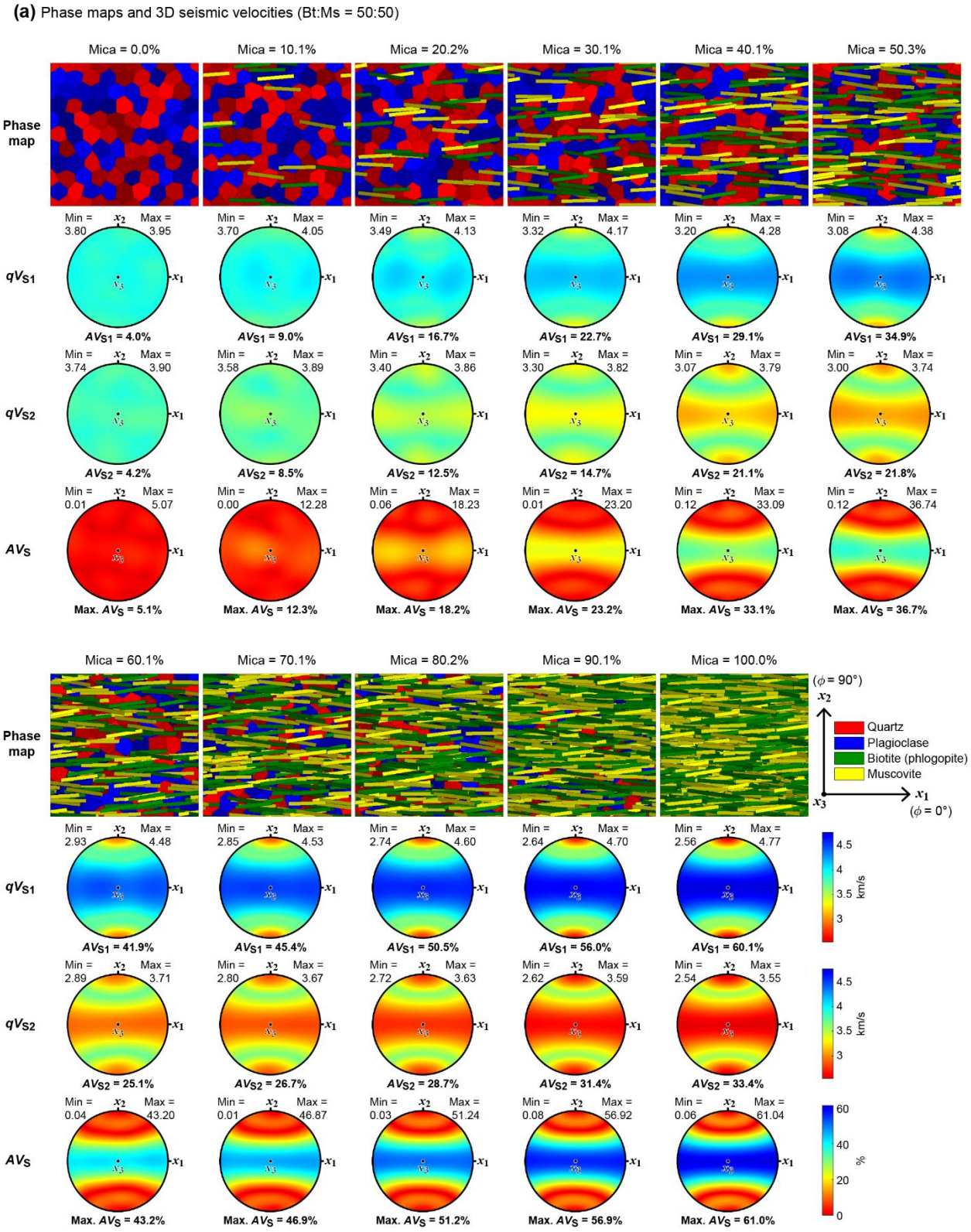

Figure 4.22 (see the next page for the caption)

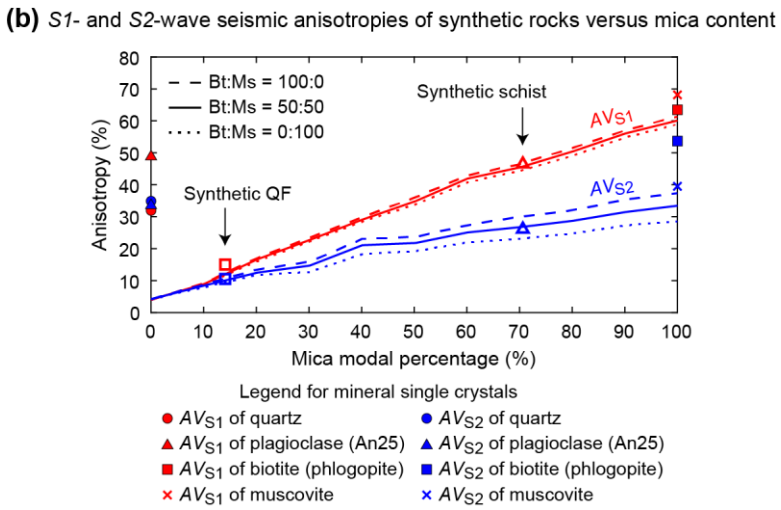

Figure 4.22 Effect of mica content, in synthetic rocks, on seismic velocities computed using the AEH method. (a) Phase maps and 3D seismic velocities of synthetic microstructures with mica contents from 0% to 100% in 10% intervals. Each phase map with mica has the same ratio of biotite and muscovite (Bt:Ms = 50:50). The coordinate system and phase color information are shown next to the phase map with 100% mica. *S1*- and *S2*-wave velocities (qV_{S1} and qV_{S2}, respectively) and *S*-wave anisotropy percentage (AV_S) are presented in equal-area, upper hemisphere projection and with the same color limits for comparison. Seismic anisotropy (AV_{S1} and AV_{S2}, respectively) for qV_{S1} and qV_{S2}, and maximum *S*-wave anisotropy (max. AV_S) of each case are also displayed below each 3D seismic property plot. (b) Seismic anisotropies of *S1* and *S2* waves (AV_{S1} and AV_{S2}, respectively) of synthetic microstructures, plotted against mica content. Open squares and triangles indicate the synthetic QF and schist rocks, respectively. Seismic anisotropies for single crystals of quartz, plagioclase, biotite (phlogopite) and muscovite are also plotted.

4.7.4.2. Comparison With Other Natural Rocks

To compare our sensitivity results with natural rocks, we used 206 rock samples from the literature for analysis of *P*-wave anisotropy (AV_P) and $qV_{SH}(0°)$ contrast in the direction parallel to the foliation and fault trace (see Tables 4.2 and 4.3 for details). Felsic to intermediate rocks with varying mica content (igneous rocks, quartzite, mylonite, gneiss, and schist) are considered since they are commonly observed in the middle crust and have the same minerals as the SCSZ rocks, consisting of quartz, feldspars, biotite and muscovite as major components (>95 modal%). Figure 4.23a compares AV_P of our natural SCSZ QF and schist rocks with those from the literature, overlaid on the synthetic AV_P for reference. Of the literature data, seismic properties of 185 rock samples were obtained by laboratory wave-speed measurements up to 1 GPa confining pressure (Birch, 1960; Christensen, 1965, 1966; Manghnani et al., 1974; Jones and Nur, 1984; McDonough and Fountain, 1988, 1993; Chroston and Brooks, 1989; Burke and Fountain, 1990; Fountain et al., 1990; Kern and Wenk, 1990; Burke, 1991; Burlini and Fountain, 1993; Ji et al., 1993, 1997a, 2007, 2015; Ji and Salisbury, 1993; Long, 1994; Mooney and Christensen, 1994; Rey et al., 1994; Salisbury and Fountain, 1994; Kern et al., 1996, 1999, 2001, 2008, 2009; Long and Salisbury, 1996; Godfrey et al., 2000; Khazanehdari et al., 2000; Hurich et al., 2001; Mazzoli et al., 2002; Cholach et al., 2005; Punturo et al., 2005; Cirrincione et al., 2010; Wenning et al., 2016; Bazargan et al., 2021). At room temperature, the velocity–pressure relations display a steep, non-linear increase of velocity with increasing confining pressure at low pressures (generally <100–300 MPa) due to progressive closure of microfractures, and then a gentle, nearly-linear increase of velocity with pressure at higher pressures related to intrinsic rock properties (e.g., Birch, 1960; Christensen, 1965; Kern and Wenk, 1990; Burlini and Fountain, 1993; Kern et al., 2008, 2009; Ji et al., 2015). The microfracture closure pressure (Pc), above which velocities increase linearly, is dependent on rock type and shape of pores and microfractures (e.g., Walsh, 1965). For taking intrinsic seismic properties of the rocks and comparison with EBSD analysis of the SCSZ samples and the other 21 rocks (Lloyd et al., 2009; Naus-Thijssen et al., 2011a; Ji et al., 2015; Watling, 2017; Kästner et al., 2021), we obtained the pressure derivative (dV/dP) and the velocity intercept V_0 at zero pressure by making and extrapolating a linear regression fit to the high-pressure part of each velocity–pressure curve above Pc

(e.g., Burlini and Fountain, 1993; Khazanehdari et al., 2000; Kern et al., 2001; Ji et al., 2007; Almqvist and Mainprice, 2017; Kästner et al., 2021). This relationship in the linear regime is described by $V(\mathrm{P}) = V_0 + (\mathrm{d}V/\mathrm{dP})\mathrm{P}$. The V_0 is used to calculate *P*-wave seismic anisotropies of the literature rock samples via the equation in Section 4.5.3. Generally, the 208 natural rock samples including the SCSZ rocks show increase in AV_P with increasing mica content (Figure 4.23a). However, most of them lie below the synthetic AV_P curve (Figure 4.23a), presumably owing to microstructural differences from the synthetic microstructures, including the following.

1. Mica shape and crystallographic preferred orientation. The synthetic microstructures were generated using mica grains with ±10° deviation angle of the basal (001) planes with respect to both the *x*1 (direction parallel to the foliation and lineation) and *x*3 (direction parallel to the foliation and perpendicular to the lineation) axes. These mica grain orientations are similar to those of the SCSZ rocks with strong foliation. If other natural rocks have weaker foliation than the synthetic microstructures by, for example, crenulation cleavage in schist (e.g., Naus-Thijssen et al., 2011a), or show more than one planar structure such as S-C structure in mylonite and gneiss (e.g., Lloyd et al., 2009), then their AV_P would be effectively lower than the synthetic rocks for the same mica content. In contrast, if rocks have stronger foliation defined by mica grains with a lower deviation angle than the synthetic microstructures, their AV_P would be higher (e.g., Naus-Thijssen et al., 2011b). Most published petrophysical wave-speed studies do not provide photomicrographs of microstructures, so the strength of mica preferred orientation is unknown.
2. Quartz and feldspar crystallographic preferred orientation. A strong crystallographic preferred orientation of quart or feldspar can increase or decrease the AV_P caused by mica especially in rocks with low mica content, and this effect would be strongly dependent on the orientation of quartz and feldspar relative to one another and mica (e.g., Ward et al., 2012). Assuming natural rocks have the same mica preferred orientation as the synthetic microstructures, the discrepancy

in AV_P between the natural and synthetic rocks could be explained by the quartz and feldspar crystallographic preferred orientation, noting that quartz and feldspar are randomly oriented in the synthetic microstructures.

3. Minor accessory minerals. The felsic to intermediate natural rocks used in this study consist of the major components (quartz, feldspars, biotite and muscovite) with >95 modal% in total. Minor accessory minerals with <5 modal% such as chlorite, epidote, garnet, carbonates, apatite, and opaque minerals can have a minor effect (increase or decrease) on seismic wave speeds and therefore seismic anisotropies of the rocks, particularly those with low mica content.
4. Microfractures, pores and other defects that affect petrophysical wave-speed measurements. The synthetic microstructures and EBSD analysis do not contain microdefects such as microfractures and pores. Although most microdefects are closed at confining pressures greater than 100–400 MPa (e.g., Birch, 1960; Christensen, 1965; Kern and Wenk, 1990; Burlini and Fountain, 1993; Kern et al., 2008, 2009; Ji et al., 2015), a few microfractures and pores might survive depending on their shapes and the temperatures of deformation (e.g., Bazargan et al., 2021; Johnson et al., 2021b; Meyer et al., 2021). In addition, if bulk stiffness via EBSD analysis is computed by analytical homogenization methods such as Hill average, grain boundaries can be considered as microdefects that affect petrophysical wave-speed measurements, which might result in a small difference between EBSD-derived and petrophysical AV_P for the same mica content.

In addition to the four causes above, for the data obtained by EBSD analysis, AV_P can depend on single-crystal elastic properties and homogenization scheme used in computation of bulk stiffness.

Of the 206 published data, 50 samples that have *S*-wave velocity data (V_0) and the information of rock-fabric orientation are used for the calculation of qV_{SH} contrast (Christensen, 1966; Burlini and Fountain, 1993; Ji and Salisbury, 1993; Salisbury and Fountain, 1994; Kern et al., 1996, 1999, 2001, 2008, 2009; Long and Salisbury, 1996; Godfrey et al., 2000; Punturo et al., 2005; Cirrincione et al., 2010; Naus-Thijssen et al., 2011a; Ji et al., 2015; Bazargan et al., 2021). Figure 4.23b shows qV_{SH} contrast of 50 natural

rock samples from the literature and the SCSZ schist relative to the natural SCSZ QF rock at $\phi = 0°$, overlaid on the synthetic $qV_{SH}(0°)$ contrasts relative to the natural QF rock for reference. The rocks with greater mica content than the SCSZ QF rock show a general increase in $qV_{SH}(0°)$ contrast and are more compliant than the SCSZ QF rock, broadly consistent with the prediction from our synthetic rock analyses (Figure 4.23b; e.g., Bazargan et al., 2021). We note a positive correlation between seismic anisotropy (e.g., AV_P and AV_{SH}) and velocity contrast of $qV_{SH}(0°)$ in the direction parallel to the foliation or fault trace, and higher compliance with increasing modal% mica (Figures 4.20 and 4.23). These results suggest that regardless of rock type, the modal proportion of highly anisotropic minerals (e.g., mica) is an important factor in seismic anisotropy and seismic/elastic contrast that impacts the rupture directivity of strike-slip bimaterial faults.

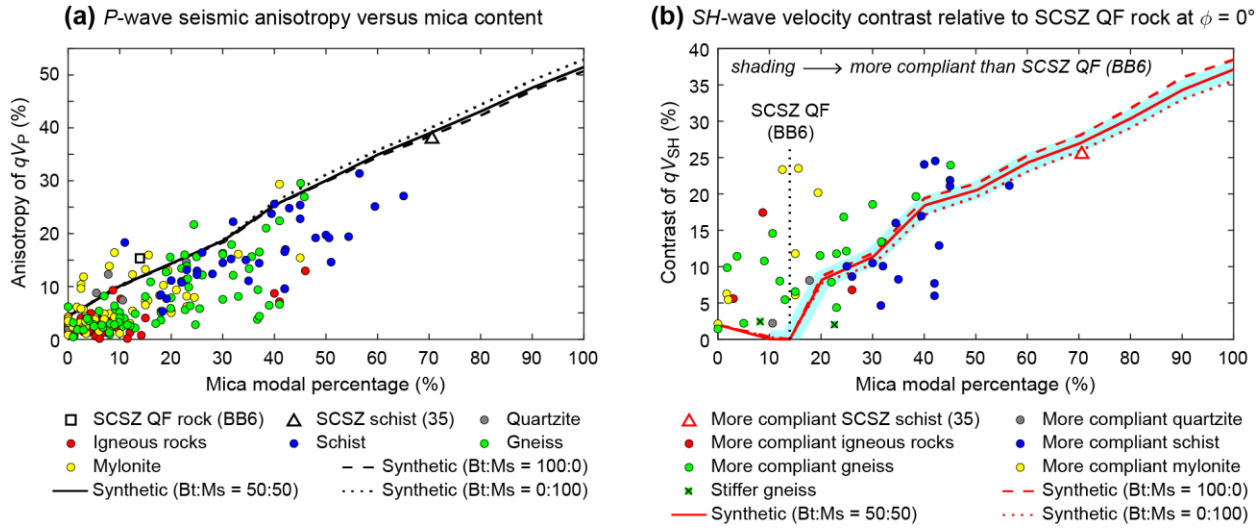

Figure 4.23 Comparison of seismic anisotropy and velocity contrast for natural rocks from the literature, obtained by petrophysical wave-speed measurements and EBSD analysis (see Tables 4.2 and 4.3 for details). Common felsic to intermediate rocks in the middle crust with different mica content are compared (schist, gneiss, mylonite, quartzite, and igneous rocks), in which quartz, feldspars, biotite and muscovite comprise >~95 modal%. (a) 3D *P*-wave seismic anisotropy (AV_P) for 208 rock samples (2 from the present study and 206 from the literature), plotted against mica content. Open black square and triangle indicate the quartzofeldspathic (QF) and schist host rocks of the Sandhill Corner shear zone (SCSZ), respectively. AV_P of synthetic rocks (black lines) from Figure 4.20c are overlaid for reference. AV_P of the natural rocks show a general increase with more mica content, similar to the synthetic rocks. (b) *SH*-wave velocity (qV_{SH}) contrast at ϕ = 0° for 51 rock samples (1 from the present study and 50 from the literature) relative to the natural SCSZ QF host rock (sample BB6), plotted against mica content. Open red triangle indicates the SCSZ schist host rock (sample 35). qV_{SH} contrasts of synthetic rocks (red lines) relative to the natural SCSZ QF rock are calculated and overlaid for reference. qV_{SH} contrasts of the natural rocks relative to the SCSZ QF host rock show a general increase with lower and higher mica content than the SCSZ QF host rock, similar to the synthetic rocks. The rocks with more mica content than the SCSZ QF host rock (13.9 modal%) tend to be more compliant for qV_{SH} at ϕ = 0°, which is also generally consistent with the synthetic rocks (shading).

4.7.5. Effects of Preexisting Damage and Mylonitization on Rupture Propagation and Asymmetric Damage

The SCSZ core is surrounded by ~260-m-wide asymmetric effective damage zones composed of fractured rocks (Figure 4.2d). Damage zones in the upper crust appear seismically as a low-velocity zone with reduction in elastic stiffness relative to the intact host rocks (e.g., Li and Vernon, 2001; Cochran et al., 2009; Lewis and Ben-Zion, 2010). The damage zone observed in the SCSZ has evolved through multiple seismic cycles based on deformed pseudotachylyte and multiple sets of dynamic microfractures in minerals such as feldspars (Price et al., 2012; B. R. Song et al., 2020; Johnson et al., 2021b). Therefore, accumulated microfractures produced during multiple earthquakes may potentially have caused significant reduction in stiffness of the more damaged QF rock, leading to changes in the material contrast across the shear zone. However, at middle crustal depths, healing/sealing processes in damaged rocks during post- and interseismic periods (e.g., Johnson et al., 2021b) and closure of microfractures under high confining pressure may facilitate nearly complete recovery of elastic stiffness (e.g., Li et al., 2006; Wu et al., 2009; Meyer et al., 2021; Lu and Ben-Zion, 2022). Thus, the long-term effect of damage on rupture dynamics in faults/shear zones at depth remains an open question.

In the present study, we used the SCSZ host rocks for elastic property measurements because we are interested in the early development and evolution of asymmetric damage. However, the rocks juxtaposed across the SCSZ are intensely deformed mylonite/ultramylonite and highly sheared schist. Such deformation can affect the intensity and pattern of seismic anisotropy and hence elastic contrast if it changes the strength of mica crystallographic preferred orientation, operates certain slip systems in minerals such as basal <a>, rhomb <a> or prism <a> slip in quartz (e.g., Mainprice and Casey, 1990; McDonough and Fountain, 1993; Ward et al., 2012; Ji et al., 2015; Han and Jung, 2021), and develops structures such as S-C fabrics, crenulations and folds (e.g., Lloyd et al., 2009; Naus-Thijssenet al., 2011a). For example, during long-term tectonic deformation, mylonitization typically generates a strong macroscopic foliation, which may increase seismic anisotropy owing to transition to C-type fabric from S-C fabric during deformation (e.g., Kern and Wenk, 1990; Lloyd et al., 2009). On the other hand, mylonite with a strong foliation might

have low seismic anisotropy compared to other rock types with the same mica content (e.g., Jones and Nur, 1982) if relatively strong crystallographic orientations of quartz and/or feldspar in mylonites mute seismic anisotropy generated by mica preferred orientation (e.g., Ward et al., 2012). In addition, the seismic properties of mylonites might be influenced by mixing of matrix phases during mylonitization and by change in deformation mechanism to grain-size-sensitive creep caused by progressive grain size reduction. Analysis of the fine-grained SCSZ mylonite requires laboratory wave-speed measurements and is left for future work.

4.8. Chapter Conclusions

We calculated the bulk elastic properties and seismic wave velocities of two elastically anisotropic rocks (quartzofeldspathic rock and mica-rich schist) from either side of the SCSZ to investigate the effect of elastic contrast in anisotropic bimaterial strike-slip faults on preferentially propagating wrinkle-like pulse ruptures and asymmetric damage. Our results suggest that if micaceous foliation is well-developed parallel to a bimaterial fault in anisotropic rocks, for a pure mode II rupture along the fault, the elastic contrast most relevant to the rupture directivity and asymmetric damage is governed by the *SH* waves that propagate parallel to the fault with fault-normal polarization.

The damage zone across the SCSZ exhibits strongly asymmetric distribution with a much wider damage zone on the QF rock side in which the velocity of fault-parallel *SH* wave is higher. This damage asymmetry agrees with modeling predictions of a subshear rupture along an isotropic bimaterial interface (e.g., Ben-Zion and Shi, 2005; Xu and Ben-Zion, 2017) and field observations of bimaterial faults (e.g., Dor et al., 2006a, 2006b, 2008; Mitchell et al., 2011; Rempe et al., 2013) showing damage primarily on the side of the fault with higher seismic velocity. Thus, velocity contrast of the *SH* waves across bimaterial interfaces separating elastically anisotropic rocks appears to provide results that are consistent with numerical modeling results for bimaterial interfaces separating elastically isotropic rocks.

The intensity of contrast in *SH*-wave velocities between two rocks is strongly associated with orientation and proportion of preferentially aligned mica. Regardless of rock type, if a rock on one side of a bimaterial fault has a larger modal% of mica with fault-parallel preferred orientation, then that rock is likely to have higher anisotropy and slower *SH* wave propagating parallel to the fault. In locations where mica constitutes an important modal fraction of the rocks, details of its distribution and orientation may be necessary for more precise determination of elastic contrasts and a better understanding of local rupture directivity and asymmetric damage in elastically anisotropic bimaterial rupture.

4.9. Chapter Acknowledgments

This research was funded by National Science Foundation grants EAR-0820946, EAR-1347087, EAR-1727090 and EAR-2150831. B. R. Song was partially supported by a Michael J. Eckardt Dissertation Fellowship from the University of Maine. We thank Yehuda Ben-Zion for helpful discussion, and Mohsen Bazargan and Katsuyoshi Michibayashi for providing their datasets of seismic properties. We thank the Editor Douglas Schmitt, the Associate Editor Bjarne Almqvist, the reviewer Haemyeong Jung, and one anonymous reviewer for their constructive comments that improved the manuscript.

4.10. Chapter Data Availability Statement

Data used to produce Figure 4.2d are available in B. R. Song et al. (2020). All the other data including homogenized stiffness tensors of the natural and synthetic rocks used in the present study are available at Figshare via https://doi.org/10.6084/m9.figshare.19776145.

Table 4.2 Comparison with the literature for qV_P seismic anisotropy.

Category	Sample	Lithology*	Reference	Method	Quartz (modal%)	Feldspars (modal%)	**Mica (modal%)**	[// x1] V_{P0} at 0 MPa (km/s)	[// x1] dV_P/dP (10^{-4} km s^{-1} MPa^{-1})	[// x2] V_{P0} at 0 MPa (km/s)	[// x2] dV_P/dP (10^{-4} km s^{-1} MPa^{-1})	[// x3] V_{P0} at 0 MPa (km/s)	[// x3] dV_P/dP (10^{-4} km s^{-1} MPa^{-1})	**AV_{P0} at 0 MPa (%)**
This Study	BB6	QF Rock	This study	EBSD	46.80	39.26	**13.94**							**15.32**
This Study	35	Schist	This study	EBSD	15.26	14.18	**70.56**							**37.88**
Quartzite	IV-91	Quartzite (Metapsammite)	Burlini & Fountain (1993)	Petrophysical	74.21	7.89	**17.76**	6.15	4.04	5.76	4.11	6.26	2.73	**8.32**
Quartzite	IV-92	Quartzite (Metapsammite)	Burlini & Fountain (1993)	Petrophysical	70.06	6.51	**22.93**	6.41	2.93	5.57	5.43	6.45	2.54	**14.64**
Quartzite	IV-93	Quartzite (Metapsammite)	Burlini & Fountain (1993)	Petrophysical	68.84	22.9	**7.79**	6.73	4.84	5.95	3.18	6.48	3.51	**12.30**
Quartzite	Quartzite	Quartzite	Christensen (1965)	Petrophysical	95.6	1.1	**0.1**	6.086	1.95	6.204	1.3	6.097	1.9	**1.92**
Quartzite	Feldspathic Mica Quartzite	Feldspathic Mica Quartzite	Christensen (1965) for VP; Christensen (1966) for VS	Petrophysical	68.9	20.2	**10.6**	6.362	1.9	5.907	2.65	6.204	2.3	**7.42**
Quartzite	664-2	Metasandstone	Kästner et al. (2021)	EBSD	73	25	**2**							**5.76**
Quartzite	RM-19	Quartzite	McDonough & Fountain (1993)	Petrophysical	90.5	4	**5.5**	5.9917	2.5	5.79	3	6.3217	3.5	**8.78**
Igneous	Westerly	Granite	Birch (1960)	Petrophysical	27.5	66.8	**4.5**	6.0929	2.6071	5.9257	1.9643	6.0357	1.9643	**2.78**
Igneous	Stone Mt	Granite	Birch (1960)	Petrophysical	26	70	**4**	6.2571	1.6429	6.18	1.75	6.1543	2.7857	**1.66**
Igneous	Chelmsford	Granite	Birch (1960)	Petrophysical	31	62	**5**	6.2043	1.7857	6.0714	2.4286	6.1529	2.1071	**2.17**
Igneous	Porterville	Quartz Monzonite	Birch (1960)	Petrophysical	34	60	**4**	6.1729	2.1071	6.09	2.25	6.1157	2.9643	**1.35**
Igneous	Hyderabad-B	Granite	Birch (1960)	Petrophysical	28	68	**0**	6.4729	2.1071	6.2614	1.6786			**3.32**
Igneous	Barre	Granite	Birch (1960)	Petrophysical	26	62	**12**	6.2086	2.0714	6.1271	2.1429	6.1814	2.4286	**1.32**
Igneous	Sacred Heart	Granite	Birch (1960)	Petrophysical	26	68	**3**	6.3414	1.6786	6.1457	1.9643	6.3086	1.8214	**3.13**
Igneous	Hyderabad-A	Granite	Birch (1960)	Petrophysical	30	66	**0**	6.4971	1.6429	6.3886	1.8214	6.4286	1.8214	**1.68**
Igneous	Sylmar	Albitite	Birch (1960)	Petrophysical	0	98	**0**	6.73	1	6.5614	1.4286	6.6157	1.4643	**2.54**
Igneous	Butt	Granodiorite	Birch (1960)	Petrophysical	27	63	**7**	6.3986	1.8214	6.3143	2.2857	6.3157	2.4643	**1.33**
Igneous	IV-44	Granite	Burke & Fountain (1990)	Petrophysical	45	48	**7**	6.2	3	6.368	2.6	6.123	3.6	**3.92**
Igneous	34	Pluton	Cholach et al. (2005)	Petrophysical	34.9	52	**8.2**	6.46	3	6.18	3			**4.43**
Igneous	VOLC-A	Pluton	Cholach et al. (2005)	Petrophysical	27.3	64.8	**6.7**	5.75	3	5.5	4	5.73	2	**4.44**

Table 4.2 (Continued)

Category	Sample	Lithology*	Reference	Method	Quartz (modal%)	Feldspars (modal%)	**Mica (modal%)**	[// x1] V_{P0} at 0 MPa (km/s)	[// x1] dV_P/dP (10^{-4} km s^{-1} MPa^{-1})	[// x2] V_{P0} at 0 MPa (km/s)	[// x2] dV_P/dP (10^{-4} km s^{-1} MPa^{-1})	[// x3] V_{P0} at 0 MPa (km/s)	[// x3] dV_P/dP (10^{-4} km s^{-1} MPa^{-1})	**AV_{P0} at 0 MPa (%)**
Igneous	93-17	Pluton	Cholach et al. (2005)	Petrophysical	33.4	17.4	**46**	6.38	2	5.63	4	6.41	3	**12.96**
Igneous	L15	Monzonite / Diorite	Chroston & Brooks (1989)	Petrophysical	17	77	**4**			6.4217	3.5	6.5233	4	**1.57**
Igneous	L26	Tonalite	Chroston & Brooks (1989)	Petrophysical	21	59	**20**	5.9983	10.5	5.9783	2.5	6.3117	3.5	**5.43**
Igneous	L27	Tonalite	Chroston & Brooks (1989)	Petrophysical	12	46	**41**	6.2583	4.5	5.83	8	6.26	2	**7.11**
Igneous	H7	Granodiorite	Chroston & Brooks (1989)	Petrophysical	30	30	**40**	6.275	6.5	5.7517	7.5	6.0817	9.5	**8.70**
Igneous	H18	Granite	Chroston & Brooks (1989)	Petrophysical	44	48	**4**	6.2	5	6.0067	6	5.9767	7	**3.67**
Igneous	KZ-19	Granite	Fountain et al. (1990)	Petrophysical	27.4	63.6	**5.3**	6.5067	2.25	6.4667	3.25	6.4767	2.75	**0.62**
Igneous	KZ-35	Tonalite	Fountain et al. (1990)	Petrophysical	29.5	69	**0**	6.4133	2.5	6.2333	3	6.3267	2.5	**2.85**
Igneous	ai99b	Granite	Hurich et al. (2001)	Petrophysical	41	56	**0**	6.07	1.5	6.12	1.5	6.16	0.5	**1.47**
Igneous	ai117	Intermediate Rock	Hurich et al. (2001)	Petrophysical	41	53.7	**0**	6.12	1.5	5.98	2	6.04	2	**2.31**
Igneous	D95-13	Granite	Kern et al. (1999)	Petrophysical	20	77	**3**	5.8467	3.5	5.7933	5.5	5.8767	3.5	**1.43**
Igneous	OKU 1658	Meta-Pegmatoid (Pegmatitic Granite)	Kern et al. (2009)	Petrophysical	32.2	58.1	**8.7**	6.28	2	6.05	4	6.64	0	**9.30**
Igneous	S53	Granite	Khazanehdari et al. (2000)	Petrophysical	50	44	**6**	6.098	5	5.98	5.6	6.132	4.6	**2.51**
Igneous	B-9	Granite	Long (1994)	Petrophysical	43.9	51.1	**4.4**	6.22	2.5	6	2	6.2267	2.25	**3.71**
Igneous	B-10	Granite	Long (1994)	Petrophysical	20.5	72.5	**5.9**	6.2833	0.75	6.2	2	6.15	2.25	**2.14**
Igneous	B-18	Granite	Long (1994)	Petrophysical	38.4	60.1	**1.2**	6.08	2.5	6.1233	0.75	6.0867	2.25	**0.71**
Igneous	B-24	Granite	Long (1994)	Petrophysical	81.3	6.6	**10.2**	6.24	2.25	6.0067	2.25	5.78	2	**7.65**
Igneous	B-28	Granite	Long (1994)	Petrophysical	31.4	63.4	**2.5**	6.2167	3.5	6.2533	2	6.4733	2	**4.04**
Igneous	B-33	Granite	Long (1994)	Petrophysical	50.8	43	**3.5**	6.0867	2.75	6.02	2.5	6.2633	2	**3.96**
Igneous	B-43	Granite	Long (1994)	Petrophysical	40.8	57	**0.4**	6.25	2.5	6.12	2.5	6.2167	1.75	**2.10**
Igneous	B-44	Granodiorite	Long (1994)	Petrophysical	31.8	62	**6.1**	6.1667	2.5	6.1767	2.25			**0.16**

Table 4.2 (Continued)

Category	Sample	Lithology*	Reference	Method	Quartz (modal%)	Feldspars (modal%)	**Mica (modal%)**	[// x1] V_{P0} at 0 MPa (km/s)	[// x1] dV_P/dP (10^{-4} km s^{-1} MPa^{-1})	[// x2] V_{P0} at 0 MPa (km/s)	[// x2] dV_P/dP (10^{-4} km s^{-1} MPa^{-1})	[// x3] V_{P0} at 0 MPa (km/s)	[// x3] dV_P/dP (10^{-4} km s^{-1} MPa^{-1})	**AV_{P0} at 0 MPa (%)**
Igneous	B-46	Granite	Long (1994)	Petrophysical	20.7	64.9	**9.3**	6.0167	2.25	6.1467	2.25	6.1567	1.75	**2.30**
Igneous	B-49	Granite	Long (1994)	Petrophysical	30	67.6	**1.6**	5.9467	1.75	6.0867	1.25	6.1233	2.25	**2.93**
Igneous	B-58	Granite	Long (1994)	Petrophysical	20.3	74.4	**4.4**	6.0433	4.75	5.7533	4.75	5.8667	5	**4.92**
Igneous	B-60	Granite	Long (1994)	Petrophysical	25.4	73.3	**0.9**	6.1833	3.5	6.12	1.75	6.0733	3	**1.79**
Igneous	B-62	Granodiorite	Long (1994)	Petrophysical	25.2	65.8	**7.3**	5.9167	2.75	6.02	2.5			**1.73**
Igneous	B-66	Granite	Long (1994)	Petrophysical	20.2	69.3	**6.6**	6.1767	3	5.9767	3.5	6.1967	3	**3.61**
Igneous	B-79	Granodiorite	Long (1994)	Petrophysical	38.6	55.9	**5.3**	6.2667	2.25	6.14	2.5			**2.04**
Igneous	1	Granulated Anorthosite	Manghnani et al. (1974)	Petrophysical	0	100	**0**	6.6652	2.115	6.8207	2.165	6.8028	1.51	**2.31**
Igneous	9-6	Tonalite	Mazzoli et al. (2002)	Petrophysical	33.9	46.4	**14.2**	6.11	5.1	6.092	4.7	6.063	8.9	**0.77**
Igneous	RM-16	Quartz Monzonite	McDonough & Fountain (1993)	Petrophysical	11.5	77	**11.5**	6.08	3	6.09	2	6.0817	3.5	**0.16**
Igneous	RM-33	Tonalitic Pegmatite	McDonough & Fountain (1993)	Petrophysical	27.5	57.5	**15**	6.4733	3	6.2167	4	6.2817	3.5	**4.04**
Igneous	ct11	Pegmatitic Rock	Punturo et al. (2005)	Petrophysical	44	28	**26**	5.978	5.8	5.29	13.5	5.69	7.5	**12.21**
Schist	IV-82	Schist (Metapelite)	Burlini & Fountain (1993)	Petrophysical	37.88	19.34	**39.44**	7.39	3.11	5.82	3.52	6.56	3.02	**23.77**
Schist	IV-83	Schist (Metapelite)	Burlini & Fountain (1993)	Petrophysical	24.54	32.77	**42.14**	6.3	6.31	5.38	5.17	6.38	2.18	**17.01**
Schist	IV-85	Schist (Metapelite)	Burlini & Fountain (1993)	Petrophysical	48.88	15.12	**34.48**	6.52	5.51	5.61	5	6.47	3.4	**15.00**
Schist	IV-86	Schist (Metapelite)	Burlini & Fountain (1993)	Petrophysical	49.19	12.64	**37.06**	6.32	3.92	5.47	5.54	6.13	4.7	**14.42**
Schist	IV-87	Schist (Metapelite)	Burlini & Fountain (1993)	Petrophysical	42.52	23.83	**31.6**	6.58	3.43	5.65	5.1	6.26	4.41	**15.21**
Schist	IV-88	Schist (Metapelite)	Burlini & Fountain (1993)	Petrophysical	31.03	3.46	**65.06**	7.12	5.48	5.42	6.86	6.91	4.01	**27.11**
Schist	IV-90	Schist (Metapelite)	Burlini & Fountain (1993)	Petrophysical	39.05	17.06	**42.89**	6.75	4.11	5.26	6.79	6.54	3.37	**24.81**
Schist	5	Schist (Metasediment)	Cholach et al. (2005)	Petrophysical	40.2	40.3	**19.1**	6.35	2	5.88	2			**7.69**
Schist	7	Schist (Metasediment)	Cholach et al. (2005)	Petrophysical	24.8	51.7	**18.3**	6.57	1	6.23	1	6.54	2	**5.31**

Table 4.2 (Continued)

Category	Sample	Lithology*	Reference	Method	Quartz (modal%)	Feldspars (modal%)	**Mica (modal%)**	[// x1] V_{P0} at 0 MPa (km/s)	[// x1] dV_P/dP (10^{-4} km s^{-1} MPa^{-1})	[// x2] V_{P0} at 0 MPa (km/s)	[// x2] dV_P/dP (10^{-4} km s^{-1} MPa^{-1})	[// x3] V_{P0} at 0 MPa (km/s)	[// x3] dV_P/dP (10^{-4} km s^{-1} MPa^{-1})	**AV_{P0} at 0 MPa (%)**
Schist	11b	Schist (Metasediment)	Cholach et al. (2005)	Petrophysical	24.4	52.5	**23**	6.32	3	5.54	8	5.69	7	**13.15**
Schist	S8	Mica Schist	Chroston & Brooks (1989)	Petrophysical	50	0	**50**	6.7	0	5.4967	10.5	6.56	3	**19.73**
Schist	A-1	Schist (Haast)	Godfrey et al. (2000)	Petrophysical	65	7	**25**	6.5147	1.085	5.7223	1.605	6.4512	0.96	**12.95**
Schist	A-12	Schist (Haast)	Godfrey et al. (2000)	Petrophysical	25	37	**35**	6.5182	1.05	5.8346	1.74	6.2579	1.445	**11.07**
Schist	A-18	Schist (Haast)	Godfrey et al. (2000)	Petrophysical	50	16	**30**	6.7106	1.31	5.8048	2.6	6.4707	1.515	**14.47**
Schist	A-35	Schist (Haast)	Godfrey et al. (2000)	Petrophysical	49	7	**42**	6.8128	1.01	5.77	1.83	6.2765	1.275	**16.58**
Schist	TA-80	Schist (Coldfoot)	Godfrey et al. (2000)	Petrophysical	38	16	**42**	6.3305	1.125	5.7656	1.97	6.3472	0.86	**9.60**
Schist	GLG119	Schist	Ji et al. (2015)	EBSD	33	46	**20**							**11.13**
Schist	GLG132J	Schist	Ji et al. (2015)	EBSD	60	14	**26**							**16.42**
Schist	GLG257	Qz-Bt Schist	Ji et al. (2015)	EBSD	60	0	**40**							**25.60**
Schist	GLG258	Qz-Bt Schist	Ji et al. (2015)	Petrophysical	55	0	**45**	6.2898	2.4667	5.0025	3.47	6.0292	3.4267	**22.80**
Schist	GLG258	Qz-Bt Schist	Ji et al. (2015)	EBSD	55	0	**45**							**25.39**
Schist	YN1389	Qz-Bt-Ms Schist	Ji et al. (2015)	EBSD	67	0	**32**							**22.24**
Schist	P5	Qz-Bt Schist	Ji et al. (2015)	Petrophysical	75	0	**22**	6.42	3.2533	5.7635	4.2467	6.1668	3.5	**10.78**
Schist	S382	Qz-Bt Schist	Ji et al. (2015)	Petrophysical	80	0	**18**	6.17	3.2533	5.6702	3.5	6.023	3	**8.44**
Schist	S19	Qz-Bt Schist	Ji et al. (2015)	Petrophysical	62	13	**25**	6.396	2.7567	5.6591	2.5	5.9291	1.5	**12.23**
Schist	S3530	Qz-Fsp-Bt Schist	Ji et al. (2015)	Petrophysical	40	49	**11**	7.0335	2.2467	5.8532	2.7533	6.4168	2.2467	**18.32**
Schist	S1132.1	Qz-Fsp-Bt Schist	Ji et al. (2015)	Petrophysical	35	37	**28**	5.976	2.7567	5.2791	3.5	5.876	2.756	**12.38**
Schist	569-2	Mica Schist	Kästner et al. (2021)	EBSD	16	33	**51**							**14.61**
Schist	Map A	Schist (Planar Foliation)	Naus-Thijssen et al. (2011)	EBSD	30.4	13.1	**56.5**							**31.37**
Schist	CD05	Mafic Schist	Watling (2017)	EBSD	31.2	6.5	**59.5**							**25.13**
Schist	CD09	Felsic Schist	Watling (2017)	EBSD	31.3	10.3	**54.4**							**19.42**
Schist	CD14	Felsic Schist	Watling (2017)	EBSD	33.8	14.5	**50.6**							**19.19**

Table 4.2 (Continued)

Category	Sample	Lithology*	Reference	Method	Quartz (modal%)	Feldspars (modal%)	**Mica (modal%)**	[// x1] V_{P0} at 0 MPa (km/s)	[// x1] dV_P/dP (10^{-4} km s^{-1} MPa^{-1})	[// x2] V_{P0} at 0 MPa (km/s)	[// x2] dV_P/dP (10^{-4} km s^{-1} MPa^{-1})	[// x3] V_{P0} at 0 MPa (km/s)	[// x3] dV_P/dP (10^{-4} km s^{-1} MPa^{-1})	**AV_{P0} at 0 MPa (%)**
Schist	C691-1	Grt-bearing Mica Schist	Wenning et al. (2016)	Petrophysical	2	48	**48**	6.42		5.51		6.68		**19.20**
Gneiss	309	Qz-Fsp Gneiss	Bazargan et al. (2021)	Petrophysical	50	50	**0**	6.1032	2.029	5.8538	2.3121	6.2267	1.5332	**6.17**
Gneiss	Bethlehem	Granodiorite Gneiss	Birch (1960)	Petrophysical	20	60	**18**	6.2229	2.1071	5.9129	2.6071	6.0486	2.5714	**5.11**
Gneiss	GFTZ-26	Orthogneiss	Burke (1991)	Petrophysical	20	67.2	**10.9**	6.329	2.3	6.082	1.9	6.103	4.1	**3.98**
Gneiss	GFTZ-30	Paragneiss	Burke (1991)	Petrophysical	30.1	32.6	**35.1**	6.669	2.3	5.833	0.6	6.368	1.6	**13.37**
Gneiss	GFTZ-41	Paragneiss	Burke (1991)	Petrophysical	31.1	40.7	**22.7**	6.394	1.3	6.046	0.7	6.334	1.3	**5.59**
Gneiss	GFTZ-49	Paragneiss	Burke (1991)	Petrophysical	65.8	24.1	**9.2**	6.041	0.7	5.974	1.3	6.321	0.7	**5.64**
Gneiss	GFTZ-55	Paragneiss	Burke (1991)	Petrophysical	23.9	37.5	**36.7**	5.952	2.4	6.001	0.7	6.181	1.7	**3.77**
Gneiss	GFTZ-91	Paragneiss	Burke (1991)	Petrophysical	26.7	46.6	**23.7**	6.517	0.9	6.116	1.7	6.304	1.3	**6.35**
Gneiss	IV-21	Paragneiss (Kinzigite)	Burke & Fountain (1990)	Petrophysical	33	31	**32**	6.2459	3.7353	5.5319	4.9412	6.2316	3.0294	**12.12**
Gneiss	IV-33	Orthogneiss	Burke & Fountain (1990)	Petrophysical	51	31	**18**	5.983	4.6	5.813	6.6	6.028	4.6	**3.63**
Gneiss	IV-37	Paragneiss	Burke & Fountain (1990)	Petrophysical	74	6	**20**	6.238	2.6	5.766	3.7	5.993	3.6	**7.86**
Gneiss	IV-38	Paragneiss	Burke & Fountain (1990)	Petrophysical	43	26	**26**	6.258	4.6	5.541	4.7	6.239	4.3	**12.15**
Gneiss	IV-41	Paragneiss	Burke & Fountain (1990)	Petrophysical	81	5	**10**	6.226	3.7	5.915	3	6.159	3.3	**5.12**
Gneiss	IV-42	Paragneiss	Burke & Fountain (1990)	Petrophysical	57	28	**13**	6.015	4	5.975	5	6.105	4	**2.15**
Gneiss	IV-43	Paragneiss	Burke & Fountain (1990)	Petrophysical	55	3	**41**	5.943	2.6	5.562	4.9	5.915	5	**6.62**
Gneiss	IV-52	Paragneiss	Burke & Fountain (1990)	Petrophysical	62	5	**30**	6.436	3.7	6.065	4	6.542	2.9	**7.57**
Gneiss	IV-53	Paragneiss	Burke & Fountain (1990)	Petrophysical	51	13	**33**	6.199	4.3	5.715	3	6.061	3.7	**8.12**
Gneiss	IV-55	Orthogneiss	Burke & Fountain (1990)	Petrophysical	67	16	**17**	5.853	5.6	5.68	5	5.813	5.6	**3.00**
Gneiss	Gneiss 1	Gneiss	Christensen (1965)	Petrophysical	32	61.4	**6.7**	6.143	2.35	6.065	2.25	6.204	2.05	**2.27**

Table 4.2 (Continued)

Category	Sample	Lithology*	Reference	Method	Quartz (modal%)	Feldspars (modal%)	**Mica (modal%)**	[// x1] V_{P0} at 0 MPa (km/s)	[// x1] dV_P/dP (10^{-4} km s^{-1} MPa^{-1})	[// x2] V_{P0} at 0 MPa (km/s)	[// x2] dV_P/dP (10^{-4} km s^{-1} MPa^{-1})	[// x3] V_{P0} at 0 MPa (km/s)	[// x3] dV_P/dP (10^{-4} km s^{-1} MPa^{-1})	**AV_{P0} at 0 MPa (%)**
Gneiss	Gneiss 2	Gneiss	Christensen (1965) for VP; Christensen (1966) for VS	Petrophysical	22.1	67.4	**10.6**	6.113	2.85	5.986	2.7	6.137	2.15	**2.49**
Gneiss	Gneiss 6	Gneiss	Christensen (1965) for VP; Christensen (1966) for VS	Petrophysical	39.4	31.9	**24.9**	6.387	2.65	5.462	5.4	6.323	3.1	**15.61**
Gneiss	F10	Monzonitic Gneiss	Chroston & Brooks (1989)	Petrophysical	16	78	**6**			6.1417	2.5	5.8217	4.5	**5.35**
Gneiss	KZ-4	Tonalite Gneiss (Bt-Pl-Qz Gneiss)	Fountain et al. (1990) for VP; Salisbury & Fountain (1994) for VS	Petrophysical	33.2	56.6	**8.2**	6.4333	2.5	6.2467	3.25	6.3967	2.75	**2.94**
Gneiss	KZ-5	Tonalite Gneiss (Bt-Pl-Qz Gneiss)	Fountain et al. (1990)	Petrophysical	27.3	60.4	**8.1**	6.4533	3.5	6.3933	3.75	6.43	3.5	**0.93**
Gneiss	KZ-17	Paragneiss (Bt-Pl-Qz Gneiss)	Fountain et al. (1990) for VP; Salisbury & Fountain (1994) for VS	Petrophysical	42.5	18.2	**38.4**	6.57	4.25	5.32	6.5	6.2233	5.5	**21.03**
Gneiss	KZ-27	Granodiorite Gneiss	Fountain et al. (1990)	Petrophysical	41.5	48.5	**8**	6.39	2.5	6.38	2.75	6.4633	2.5	**1.30**
Gneiss	KZ-36	Tonalite Gneiss (Bt-Pl-Qz Gneiss)	Fountain et al. (1990)	Petrophysical	23	64	**9**	6.5633	2.5	6.16	3.5	6.35	3.25	**6.34**
Gneiss	KZ-37	Tonalite Gneiss (Bt-Pl-Qz Gneiss)	Fountain et al. (1990)	Petrophysical	29	59.5	**6.5**	6.46	3.25	6.2867	2.5	6.3233	3	**2.72**
Gneiss	KZ-38b	Tonalite Gneiss (Qz Diorite gneiss)	Fountain et al. (1990) for VP; Salisbury & Fountain (1994) for VS	Petrophysical	16.5	77	**5**	6.43	2.75	6.26	2.25	6.4367	3.25	**2.78**
Gneiss	B1578R14P18t	Bt-Ms-Pl-Kfs Orthogneiss	Ji et al. (2007)	Petrophysical	25	65	**7**	6.452	1.855	5.944	1.527			**8.20**
Gneiss	B2184R88P4s	Bt-Hbl-Pl-Kfs Paragneiss	Ji et al. (2007)	Petrophysical	40	55	**4**	5.954	1.739	6.17	1.264			**3.56**

Table 4.2 (Continued)

Category	Sample	Lithology*	Reference	Method	Quartz (modal%)	Feldspars (modal%)	**Mica (modal%)**	[// x1] V_{P0} at 0 MPa (km/s)	[// x1] dV_P/dP (10^{-4} km s^{-1} MPa^{-1})	[// x2] V_{P0} at 0 MPa (km/s)	[// x2] dV_P/dP (10^{-4} km s^{-1} MPa^{-1})	[// x3] V_{P0} at 0 MPa (km/s)	[// x3] dV_P/dP (10^{-4} km s^{-1} MPa^{-1})	**AV_{P0} at 0 MPa (%)**
Gneiss	GLG14	Granitic Gneiss	Ji et al. (2015)	Petrophysical	28	68	**3.7**	5.5145	3.13	5.3065	3.8467	5.5205	3.87	**3.95**
Gneiss	GLG97-2	Granitic Gneiss	Ji et al. (2015)	Petrophysical	34	64	**1.8**	5.4946	3.25	5.4426	3.9467	5.3948	4.5233	**1.83**
Gneiss	GLG134	Dioritic Gneiss	Ji et al. (2015)	EBSD	20	50	**30**							**16.30**
Gneiss	593-4	Paragneiss	Kästner et al. (2021)	EBSD	38	19	**42**							**9.54**
Gneiss	WSZ1	Gneiss? (Metarhyolite)	Kern et al. (1996)	Petrophysical	40	39	**22**	5.8867	4.75	5.2733	9.5	5.6	7.25	**10.99**
Gneiss	BT2	Trondhjemitic Gneiss	Kern et al. (1996)	Petrophysical	34	52	**13**	6.0467	4	5.76	5.75	6.0333	3.75	**4.86**
Gneiss	D95-16	Tonalitic Gneiss	Kern et al. (1999)	Petrophysical	13	71	**12**	6.0533	3.75	5.9	6.25	6.0333	4.75	**2.56**
Gneiss	38098S	Bt Gneiss	Kern et al. (2001)	Petrophysical	23	47	**30**	6.45	4.5	5.49	5	6.27	3.5	**16.08**
Gneiss	PP358	Bt-Pl Gneiss	Kern et al. (2001)	Petrophysical	32	43	**23**	6.53	1	5.8267	3.5	6.06	1.75	**11.38**
Gneiss	PP363	Bt-Pl Gneiss	Kern et al. (2001)	Petrophysical	26	49	**23**	6.4667	2	5.63	3.75	6.24	2	**13.83**
Gneiss	OKU 578	Bt Gneiss	Kern et al. (2009)	Petrophysical	34.1	19.9	**45.1**	6.748	1.7	5.012	6.4	5.972	2.7	**29.52**
Gneiss	OKU 676	Bt Gneiss	Kern et al. (2009)	Petrophysical	42.3	37	**19.8**	6.47	1	5.536	3	6.22	1	**15.56**
Gneiss	OKU 818	Bt Gneiss	Kern et al. (2008, 2009)	Petrophysical	39.9	37.4	**22.6**	6.47	1.4	5.512	4.2	5.886	2	**15.99**
Gneiss	OKU 1093	Bt Gneiss	Kern et al. (2009)	Petrophysical	29.2	39	**31.7**	6.588	1.8	5.504	3.9	5.97	3.5	**17.93**
Gneiss	OKU 1844	Bt Gneiss	Kern et al. (2009)	Petrophysical	36.6	38.1	**24.4**	6.566	1.2	5.28	6.3	6.256	1.7	**21.71**
Gneiss	S11	Gneiss	Khazanehdari et al. (2000)	Petrophysical	38	42	**19**	6.398	4	5.632	4.4	5.968	5.8	**12.73**
Gneiss	S59	Gneiss	Khazanehdari et al. (2000)	Petrophysical	31	25	**39**	5.888	5	5.602	5.6	5.974	3.6	**6.43**
Gneiss	S123	Orthogneiss	Khazanehdari et al. (2000)	Petrophysical	45	45	**10**	5.946	5.4	5.71	4			**4.05**
Gneiss	Whole Sample	Gneiss (Nanga Parbat)	Lloyd et al. (2009)	EBSD	35.2	44.9	**19.9**							**5.88**

Table 4.2 (Continued)

Category	Sample	Lithology*	Reference	Method	Quartz (modal%)	Feldspars (modal%)	**Mica (modal%)**	[// x1] V_{P0} at 0 MPa (km/s)	[// x1] dV_P/dP (10^{-4} km s^{-1} MPa^{-1})	[// x2] V_{P0} at 0 MPa (km/s)	[// x2] dV_P/dP (10^{-4} km s^{-1} MPa^{-1})	[// x3] V_{P0} at 0 MPa (km/s)	[// x3] dV_P/dP (10^{-4} km s^{-1} MPa^{-1})	**AV_{P0} at 0 MPa (%)**
Gneiss	C-Type Fabric	Gneiss (Nanga Parbat; C-Fabric)	Lloyd et al. (2009)	EBSD	32.3	30.6	**37.1**							**16.52**
Gneiss	S-Type Fabric	Gneiss (Nanga Parbat; S-Fabric)	Lloyd et al. (2009)	EBSD	25.1	51.7	**23.2**							**11.46**
Gneiss	B-26	Paragneiss	Long (1994) for VP; Long & Salisbury (1996) for VS	Petrophysical	5	79.9	**15**	6.4233	3.5	5.9233	4.5	6.15	2	**8.10**
Gneiss	B-30	Paragneiss	Long (1994)	Petrophysical	0.5	59.9	**37.1**	6.3867	2.25	6.1133	1.5	6.13	3.75	**4.37**
Gneiss	3	Migmatitic Bt-Qz-Fsp Gneiss	Manghnani et al. (1974)	Petrophysical	49.8	40.2	**9.8**	6.4971	1.895	6.2905	1.925	6.4296	2.245	**3.23**
Gneiss	3-10	Paragneiss	Mazzoli et al. (2002)	Petrophysical	44.8	7.1	**45.8**	6.93	6.5	5.284	4.9	6.112	5.1	**26.95**
Gneiss	25-5	Aplitic Gneiss	Mazzoli et al. (2002)	Petrophysical	65.7	8.6	**24.7**	5.898	5.6	5.736	4.7	5.806	5.6	**2.78**
Gneiss	23-9	Paragneiss	Mazzoli et al. (2002)	Petrophysical	61	2.3	**35.6**	6.389	3.2	5.462	4.8	6.071	7.8	**15.64**
Gneiss	KD-7	Tonalitic Qz-Pl-Bt Gneiss	McDonough & Fountain (1988)	Petrophysical	26	66	**3**	5.9617	3.5	6.07	2	6.03	3	**1.80**
Gneiss	RM-15	Quartzofeldspathic Gneiss	McDonough & Fountain (1993)	Petrophysical	32.5	56	**11.5**	6.1033	3	5.9383	4.5	6.0833	5	**2.74**
Gneiss	RM-17	Bt-Pl-Qz Gneiss	McDonough & Fountain (1993)	Petrophysical	49	35	**16**	6.455	4.5	5.79	3	6.0033	4	**10.86**
Gneiss	RM-37	Quartzofeldspathic Gneiss	McDonough & Fountain (1993)	Petrophysical	9	64.5	**25.5**	6.5817	3.5	6.31	4	6.21	4	**5.81**
Gneiss	K-8	Granitic Gneiss	Mooney & Christensen (1994)	Petrophysical	21	74	**5**	6.1638	2.585	6.1848	2.685	6.3184	1.68	**2.48**
Gneiss	K-14	Granitic Gneiss	Mooney & Christensen (1994)	Petrophysical	22	75	**1**	6.084	1.875	6.1117	1.74	6.0882	1.94	**0.45**
Gneiss	K-15	Granitic Gneiss	Mooney & Christensen (1994)	Petrophysical	25	74	**1**	6.1411	2.92	6.0059	2.305	5.9492	1.89	**3.17**

Table 4.2 (Continued)

Category	Sample	Lithology*	Reference	Method	Quartz (modal%)	Feldspars (modal%)	**Mica (modal%)**	[// x1] V_{P0} at 0 MPa (km/s)	[// x1] dV_P/dP (10^{-4} km s^{-1} MPa^{-1})	[// x2] V_{P0} at 0 MPa (km/s)	[// x2] dV_P/dP (10^{-4} km s^{-1} MPa^{-1})	[// x3] V_{P0} at 0 MPa (km/s)	[// x3] dV_P/dP (10^{-4} km s^{-1} MPa^{-1})	**AV_{P0} at 0 MPa (%)**
Gneiss	ct20	Paragneiss	Punturo et al. (2005)	Petrophysical	42	16	**41**	6.55	2	5.23	6	6.04	2.5	**22.41**
Gneiss	ct30	Augen Gneiss	Punturo et al. (2005)	Petrophysical	35	54	**9**	5.33	12	5.47	8.5	5.32	13	**2.78**
Gneiss	CD19	Felsic Gneiss	Watling (2017)	EBSD	23.2	53.5	**23.4**							**9.87**
Gneiss	CD21	Felsic Gneiss	Watling (2017)	EBSD	25.1	38.1	**36.8**							**9.38**
Gneiss	CD22	Felsic Gneiss	Watling (2017)	EBSD	42.8	35.2	**22**							**13.42**
Mylonite	GFTZ-64	Mylonite (Orthogneiss)	Burke (1991)	Petrophysical	28.1	64.9	**2.3**	6.058	2.6	6.141	1.7	6.25	1	**3.12**
Mylonite	GFTZ-66	Mylonite (Orthogneiss)	Burke (1991)	Petrophysical	27.7	63.2	**5.2**	6.275	2	6.042	2.4	6.25	1	**3.78**
Mylonite	GFTZ-73	Mylonite (Orthogneiss)	Burke (1991)	Petrophysical	29.4	66.4	**0.9**	6.245	2	6.154	1.3	6.099	0.3	**2.37**
Mylonite	GFTZ-77	Mylonite (Orthogneiss)	Burke (1991)	Petrophysical	28.7	62.6	**6**	6.254	1.3	6.244	1.3	6.341	0.7	**1.54**
Mylonite	M13	Mylonite (Least Deformed Leucogneiss)	Cirrincione et al. (2010)	Petrophysical	34.5	49.7	**12.5**	5.4383	10.5	4.81	16	5.3917	11.5	**12.26**
Mylonite	M8	Mylonite (Less Deformed Leucogneiss)	Cirrincione et al. (2010)	Petrophysical	36.7	42.7	**15.6**	5.4097	11	4.65	18	5.4567	11	**15.96**
Mylonite	M3	Mylonite (More Deformed Leucogneiss)	Cirrincione et al. (2010)	Petrophysical	34.8	43.4	**19.4**	5.5303	9.9	4.896	15.6	5.5755	9.55	**12.98**
Mylonite	M4	Mylonite (Most Deformed Leucogneiss)	Cirrincione et al. (2010)	Petrophysical	37.9	59.2	**1.7**	5.545	10.5	5.23	15	5.56	10	**6.12**
Mylonite	M201	Diatexitic Ultramylonite	Ji et al. (1993) for VP; Ji & Salisbury (1993) for VS	Petrophysical	46.1	51.5	**0**	5.971	1.7	6.104	1.3	6.23	2	**4.25**
Mylonite	R88	Diatexitic Ultramylonite	Ji et al. (1993)	Petrophysical	48.8	45.5	**2.9**	6.111	1.7	6.154	1.3	6.253	1.6	**2.30**
Mylonite	M248B	Granitic Mylonite	Ji et al. (1993)	Petrophysical	29	66.4	**3.4**	6.157	1.4	6.15	1	6.299	1.3	**2.39**
Mylonite	MT-1	Granitic Mylonite	Ji et al. (1997)	Petrophysical	44.5	44.5	**8**	6.094	3.5	5.804	3.4	6.02	2.2	**4.87**
Mylonite	MT-2	Quartzitic Mylonite	Ji et al. (1997)	Petrophysical	90	9	**0**	5.722	2.5	5.908	2.7	5.746	3.2	**3.20**

Table 4.2 (Continued)

Category	Sample	Lithology*	Reference	Method	Quartz (modal%)	Feldspars (modal%)	**Mica (modal%)**	[// x1] V_{P0} at 0 MPa (km/s)	[// x1] dV_P/dP (10^{-4} km s^{-1} MPa^{-1})	[// x2] V_{P0} at 0 MPa (km/s)	[// x2] dV_P/dP (10^{-4} km s^{-1} MPa^{-1})	[// x3] V_{P0} at 0 MPa (km/s)	[// x3] dV_P/dP (10^{-4} km s^{-1} MPa^{-1})	**AV_{P0} at 0 MPa (%)**
Mylonite	MT-4	Quartzitic Mylonite	Ji et al. (1997)	Petrophysical	77	19	**0**	6.244	2.4	6.006	2.8	6.144	2.3	**3.89**
Mylonite	MT-5	Granitic Mylonite	Ji et al. (1997)	Petrophysical	50	50	**0**	5.88	2	5.831	2.7	5.86	2	**0.84**
Mylonite	GLG102	Felsic Mylonite	Ji et al. (2015)	EBSD	42.8	53.2	**3.4**							**3.41**
Mylonite	GLG133	Dioritic Mylonite	Ji et al. (2015)	Petrophysical	50	33	**15**	5.9195	3.7367	5.6525	2.8567	6.0757	3.0767	**7.22**
Mylonite	GLG133	Dioritic Mylonite	Ji et al. (2015)	EBSD	50	33	**15**							**13.23**
Mylonite	WP 6	Mylonite	Jones & Nur (1984)	Petrophysical	35	20	**45**	5.8747	2.9252	5.0333	5.7477	5.5655	3.8318	**15.43**
Mylonite	WJ 8	Mylonite	Jones & Nur (1984)	Petrophysical	55	4	**41**	6.311	2.1636	4.6954	5.9533	6.1479	1.6729	**29.36**
Mylonite	PC92	Mylonite (Phyllonite)	Kern & Wenk (1990)	Petrophysical	25	62	**9**	6.1341	3.3214	5.2034	8.0357	6.0498	4.1786	**16.42**
Mylonite	18679S	Mylonitized Orthophyre	Kern et al. (2001)	Petrophysical	43	55	**2**	6.1233	3.5	6.0733	5.75	6.19	2.5	**1.90**
Mylonite	KD-4	Mylonite (Tonalitic Qz-Pl-Bt Gneiss)	McDonough & Fountain (1988)	Petrophysical	60	30	**10**	6.15	2	6.08	2			**1.14**
Mylonite	KD-5	Blastomylonite (Quartzite)	McDonough & Fountain (1988)	Petrophysical	96	1.5	**2.5**	5.94	2	5.76	2	6.39	3	**10.37**
Mylonite	KD-9	Blastomylonite (Quartzite)	McDonough & Fountain (1988)	Petrophysical	94.5	2.5	**3**	6.08	3	5.65	3	6.36	3	**11.82**
Mylonite	KD-11	Mylonite (Granodioritic Qz-Pl-Kfs Gneiss)	McDonough & Fountain (1988)	Petrophysical	29	67.5	**3.5**	6.33	2	6.28	2	6.35	3	**1.11**
Mylonite	KD-12	Blastomylonite (Quartzite)	McDonough & Fountain (1988)	Petrophysical	88.5	3	**8**	5.99	2	5.6317	3.5	6.47	2	**13.85**
Mylonite	KD-13	Blastomylonite (Tonalitic Qz-Pl-Bt Gneiss)	McDonough & Fountain (1988)	Petrophysical	60	24	**15.5**	6.03	2	5.89	3	6.34	3	**7.36**
Mylonite	KD-14	Blastomylonite (Quartzite)	McDonough & Fountain (1988)	Petrophysical	92.5	5	**2.5**	5.9717	3.5	5.75	2	6.3317	3.5	**9.63**
Mylonite	KD-25	Mylonite (Foliated Granite)	McDonough & Fountain (1988)	Petrophysical	32	62.5	**4**	6.09	2	5.8717	3.5	6.02	3	**3.65**
Mylonite	KD-28	Mylonite (Tonalitic Pl-Qz-Bt Gneiss)	McDonough & Fountain (1988)	Petrophysical	26	66.5	**7**	6.34	3	6.04	3	6.3017	3.5	**4.85**
Mylonite	RM-1	Mylonite (Quartzite)	McDonough & Fountain (1993)	Petrophysical	85	4.5	**10.5**	5.8733	4	5.8917	4.5	6.0517	3.5	**2.99**

Table 4.2 (Continued)

Category	Sample	Lithology*	Reference	Method	Quartz (modal%)	Feldspars (modal%)	**Mica (modal%)**	[// x1] V_{P0} at 0 MPa (km/s)	[// x1] dV_P/dP (10^{-4} km s^{-1} MPa^{-1})	[// x2] V_{P0} at 0 MPa (km/s)	[// x2] dV_P/dP (10^{-4} km s^{-1} MPa^{-1})	[// x3] V_{P0} at 0 MPa (km/s)	[// x3] dV_P/dP (10^{-4} km s^{-1} MPa^{-1})	**AV_{P0} at 0 MPa (%)**
Mylonite	RM-5	Mylonite (Quartzite)	McDonough & Fountain (1993)	Petrophysical	86	1.5	**12.5**	5.9083	2.5	5.84	4	6.1633	3	**5.39**
Mylonite	RM-6	Mylonite (Bt-Qz-Pl Gneiss)	McDonough & Fountain (1993)	Petrophysical	28	49	**23**	6.0883	6.5	5.7217	5.5	6.0683	4.5	**6.21**
Mylonite	RM-7	Mylonite (Micaceous Quartzite)	McDonough & Fountain (1993)	Petrophysical	79.5	5.5	**15**	6.0217	2.5	5.9217	3.5	6.32	3	**6.51**
Mylonite	RM-8	Mylonite (Quartzite)	McDonough & Fountain (1993)	Petrophysical	97	0	**3**	5.85	3	6.1917	2.5	6.15	2	**5.68**
Mylonite	RM-9	Mylonite (Quartzite)	McDonough & Fountain (1993)	Petrophysical	94.5	3	**2.5**	5.86	2	6.1517	2.5	6.21	2	**5.80**
Mylonite	RM-10	Mylonite (Quartzofeldspathic Gneiss)	McDonough & Fountain (1993)	Petrophysical	54.5	41.5	**4**	6.13	3	5.99	3	6.2317	2.5	**3.96**
Mylonite	RM-11	Mylonite (Quartzofeldspathic Gneiss)	McDonough & Fountain (1993)	Petrophysical	35.5	56.5	**8**	5.99	4	6.0233	5	6.0917	3.5	**1.68**
Mylonite	RM-12	Mylonite (Quartzofeldspathic Gneiss)	McDonough & Fountain (1993)	Petrophysical	34	53.5	**12**	5.95	5	5.9517	3.5	6.1333	4	**3.03**
Mylonite	RM-22	Mylonite (Tonalitic Pegmatite)	McDonough & Fountain (1993)	Petrophysical	36	64	**0**	6.2217	2.5	6.4417	3.5	6.27	3	**3.47**
Mylonite	RM-24	Mylonite (Quartzofeldspathic Gneiss)	McDonough & Fountain (1993)	Petrophysical	37.5	55.5	**7**	6.1117	3.5	5.95	4	6.1817	3.5	**3.82**
Mylonite	RM-25	Mylonite (Qz-Bt-Pl Schist)	McDonough & Fountain (1993)	Petrophysical	13.5	62	**24.5**	6.1217	3.5	5.655	4.5	5.9733	4	**7.93**
Mylonite	RM-28	Mylonite (Tonalite)	McDonough & Fountain (1993)	Petrophysical	25	66	**9**	5.9617	4.5	5.765	4.5	6.0133	4	**4.22**
Mylonite	RM-29	Mylonite (Pl-Bt-Qz Schist)	McDonough & Fountain (1993)	Petrophysical	68.5	13	**18.5**	5.93	2	5.6317	3.5	6.24	3	**10.25**
Mylonite	RM-30	Mylonite (Bt-Qz-Pl Schist)	McDonough & Fountain (1993)	Petrophysical	33.5	43.5	**23**	5.7933	3	5.75	4	6.24	3	**8.17**
Mylonite	Domain I	Mylonite (Least Strained Leucogranite)	Rey et al. (1994)	Petrophysical	32	50	**18**	5.64		5.348		5.404		**5.31**

Table 4.2 (Continued)

Category	Sample	Lithology*	Reference	Method	Quartz (modal%)	Feldspars (modal%)	**Mica (modal%)**	[// x1] V_{P0} at 0 MPa (km/s)	[// x1] dV_P/dP (10^{-4} km s^{-1} MPa^{-1})	[// x2] V_{P0} at 0 MPa (km/s)	[// x2] dV_P/dP (10^{-4} km s^{-1} MPa^{-1})	[// x3] V_{P0} at 0 MPa (km/s)	[// x3] dV_P/dP (10^{-4} km s^{-1} MPa^{-1})	**AV_{P0} at 0 MPa (%)**
Mylonite	Domain II	Mylonite (Less Strained Leucogranite)	Rey et al. (1994)	Petrophysical	34	46	**20**	**5.591**		5.317		5.44		**5.02**
Mylonite	Domain III	Mylonite (More Strained Leucogranite)	Rey et al. (1994)	Petrophysical	37	42	**21**	**5.61**		5.109		5.218		**9.35**
Mylonite	Domain IV	Mylonite (Most Strained Leucogranite)	Rey et al. (1994)	Petrophysical		65.8	**33**	**5.703**		4.852		5.525		**16.13**

*Mineral abbreviations: Bt, biotite; Fsp, Feldspar; Grt, garnet; Hbl, hornblende; Kfs, K-feldspar; Ms, muscovite; Pl, plagioclase; Qz, quartz.

Table 4.3 Comparison with the literature for qV_{SH} contrast relative to the SCSZ QF rock (BB6) at $\phi = 0°$.

Category	Sample	Lithology*	Reference	Method	Quartz (modal%)	Feldspars (modal%)	**Mica (modal%)**	[// x1] V_{SH0} at 0 MPa (km/s)	[// x1] dV_{SH}/dP (10^{-4} km s^{-1} MPa^{-1})	**V_{SH} Contrast at $f = 0°$, Relative to Natural QF (%)**	More Compliant V_{SH} Contrast than Natural QF?
This Study	BB6	QF Rock	This study	EBSD	46.80	39.26	**13.94**	3.6983		**0**	
This Study	35	Schist	This study	EBSD	15.26	14.18	**70.56**	2.8629		**25.46**	Yes
Quartzite	IV-91	Quartzite (Metapsammite)	Burlini & Fountain (1993)	Petrophysical	74.21	7.89	**17.76**	3.41	1.49	**8.11**	Yes
Quartzite	Feldspathic Mica Quartzite	Feldspathic Mica Quartzite	Christensen (1965) for VP; Christensen (1966) for VS	Petrophysical	68.9	20.2	**10.6**	3.617	1.15	**2.22**	Yes
Igneous	D95-13	Granite	Kern et al. (1999)	Petrophysical	20	77	**3**	3.4967	1.125	**5.60**	Yes
Igneous	OKU 1658	Meta-Pegmatoid (Pegmatitic Granite)	Kern et al. (2009)	Petrophysical	32.2	58.1	**8.7**	3.105	1	**17.44**	Yes
Igneous	ct11	Pegmatitic Rock	Punturo et al. (2005)	Petrophysical	44	28	**26**	3.455	3.75	**6.80**	Yes
Schist	IV-82	Schist (Metapelite)	Burlini & Fountain (1993)	Petrophysical	37.88	19.34	**39.44**	3.12	2.22	**16.96**	Yes
Schist	IV-83	Schist (Metapelite)	Burlini & Fountain (1993)	Petrophysical	24.54	32.77	**42.14**	2.89	3.24	**24.54**	Yes
Schist	IV-85	Schist (Metapelite)	Burlini & Fountain (1993)	Petrophysical	48.88	15.12	**34.48**	3.15	3.65	**16.01**	Yes
Schist	IV-87	Schist (Metapelite)	Burlini & Fountain (1993)	Petrophysical	42.52	23.83	**31.6**	3.53	2.54	**4.66**	Yes
Schist	IV-90	Schist (Metapelite)	Burlini & Fountain (1993)	Petrophysical	39.05	17.06	**42.89**	3.25	1.24	**12.90**	Yes
Schist	A-1	Schist (Haast)	Godfrey et al. (2000)	Petrophysical	65	7	**25**	3.3446	0.61	**10.04**	Yes
Schist	A-12	Schist (Haast)	Godfrey et al. (2000)	Petrophysical	25	37	**35**	3.405	0.56	**8.26**	Yes
Schist	A-18	Schist (Haast)	Godfrey et al. (2000)	Petrophysical	50	16	**30**	3.3296	1.17	**10.49**	Yes
Schist	A-35	Schist (Haast)	Godfrey et al. (2000)	Petrophysical	49	7	**42**	3.483	0.46	**6.00**	Yes
Schist	TA-80	Schist (Coldfoot)	Godfrey et al. (2000)	Petrophysical	38	16	**42**	3.4243	0.405	**7.69**	Yes
Schist	GLG132J	Schist	Ji et al. (2015)	EBSD	60	14	**26**	3.3919		**8.64**	Yes

Table 4.3 (Continued)

Category	Sample	Lithology*	Reference	Method	Quartz (modal%)	Feldspars (modal%)	**Mica (modal%)**	[// x1] V_{SH0} at 0 MPa (km/s)	[// x1] dV_{SH}/dP (10^{-4} km s^{-1} MPa^{-1})	**V_{SH} Contrast at f = 0°, Relative to Natural QF (%)**	More Compliant V_{SH} Contrast than Natural QF?
Schist	GLG257	Qz-Bt Schist	Ji et al. (2015)	EBSD	60	0	**40**	2.9040		**24.06**	Yes
Schist	GLG258	Qz-Bt Schist	Ji et al. (2015)	Petrophysical	55	0	**45**	2.9687	3.15	**21.89**	Yes
Schist	GLG258	Qz-Bt Schist	Ji et al. (2015)	EBSD	55	0	**45**	2.9933		**21.07**	Yes
Schist	YN1389	Qz-Bt-Ms Schist	Ji et al. (2015)	EBSD	67	0	**32**	3.3436		**10.07**	Yes
Schist	Map A	Schist (Planar Foliation)	Naus-Thijssen et al. (2011)	EBSD	30.4	13.1	**56.5**	2.9910		**21.15**	Yes
Gneiss	309	Qz-Fsp Gneiss	Bazargan et al. (2021)	Petrophysical	50	50	**0**	3.6452	-0.1291	**1.45**	Yes
Gneiss	Gneiss 2	Gneiss	Christensen (1965) for VP; Christensen (1966) for VS	Petrophysical	22.1	67.4	**10.6**	3.196	2.95	**14.57**	Yes
Gneiss	Gneiss 6	Gneiss	Christensen (1965) for VP; Christensen (1966) for VS	Petrophysical	39.4	31.9	**24.9**	3.275	2	**12.14**	Yes
Gneiss	KZ-4	Tonalite Gneiss (Bt-Pl-Qz Gneiss)	Fountain et al. (1990) for VP; Salisbury & Fountain (1994) for VS	Petrophysical	33.2	56.6	**8.2**	3.79	0.5	**2.45**	No
Gneiss	KZ-17	Paragneiss (Bt-Pl-Qz Gneiss)	Fountain et al. (1990) for VP; Salisbury & Fountain (1994) for VS	Petrophysical	42.5	18.2	**38.4**	3.0367	1.5	**19.65**	Yes
Gneiss	KZ-38b	Tonalite Gneiss (Qz Diorite gneiss)	Fountain et al. (1990) for VP; Salisbury & Fountain (1994) for VS	Petrophysical	16.5	77	**5**	3.617	1.15	**2.22**	Yes
Gneiss	GLG14	Granitic Gneiss	Ji et al. (2015)	Petrophysical	28	68	**3.7**	3.2984	3.0133	**11.43**	Yes
Gneiss	GLG97-2	Granitic Gneiss	Ji et al. (2015)	Petrophysical	34	64	**1.8**	3.3506	2.05	**9.87**	Yes

Table 4.3 (Continued)

Category	Sample	Lithology*	Reference	Method	Quartz (modal%)	Feldspars (modal%)	**Mica (modal%)**	[// x1] V_{SH0} at 0 MPa (km/s)	[// x1] dV_{SH}/dP (10^{-4} km s^{-1} MPa^{-1})	**V_{SH} Contrast at f = 0°, Relative to Natural QF (%)**	More Compliant V_{SH} Contrast than Natural QF?
Gneiss	WSZ1	Gneiss? (Metarhyolite)	Kern et al. (1996)	Petrophysical	40	39	**22**	3.4183	2.75	**7.87**	Yes
Gneiss	BT2	Trondhjemitic Gneiss	Kern et al. (1996)	Petrophysical	34	52	**13**	3.5017	1.875	**5.46**	Yes
Gneiss	D95-16	Tonalitic Gneiss	Kern et al. (1999)	Petrophysical	13	71	**12**	3.4133	1.75	**8.02**	Yes
Gneiss	38098S	Bt Gneiss	Kern et al. (2001)	Petrophysical	23	47	**30**	3.07	3	**18.57**	Yes
Gneiss	PP358	Bt-Pl Gneiss	Kern et al. (2001)	Petrophysical	32	43	**23**	3.54	0.25	**4.37**	Yes
Gneiss	PP363	Bt-Pl Gneiss	Kern et al. (2001)	Petrophysical	26	49	**23**	3.2867	1.25	**11.79**	Yes
Gneiss	OKU 578	Bt Gneiss	Kern et al. (2009)	Petrophysical	34.1	19.9	**45.1**	2.907	2	**23.96**	Yes
Gneiss	OKU 676	Bt Gneiss	Kern et al. (2009)	Petrophysical	42.3	37	**19.8**	3.295	0.6	**11.53**	Yes
Gneiss	OKU 818	Bt Gneiss	Kern et al. (2008, 2009)	Petrophysical	39.9	37.4	**22.6**	3.774	0.7	**2.03**	No
Gneiss	OKU 1093	Bt Gneiss	Kern et al. (2009)	Petrophysical	29.2	39	**31.7**	3.233	1	**13.43**	Yes
Gneiss	OKU 1844	Bt Gneiss	Kern et al. (2009)	Petrophysical	36.6	38.1	**24.4**	3.124	0.9	**16.84**	Yes
Gneiss	B-26	Paragneiss	Long (1994) for VP; Long & Salisbury (1996) for VS	Petrophysical	5	79.9	**15**	3.4633	1.25	**6.56**	Yes
Gneiss	ct30	Augen Gneiss	Punturo et al. (2005)	Petrophysical	35	54	**9**	3.32	5.25	**10.78**	Yes
Mylonite	M13	Mylonite (Least Deformed Leucogneiss)	Cirrincione et al. (2010)	Petrophysical	34.5	49.7	**12.5**	2.925	9	**23.35**	Yes
Mylonite	M8	Mylonite (Less Deformed Leucogneiss)	Cirrincione et al. (2010)	Petrophysical	36.7	42.7	**15.6**	2.92	9	**23.52**	Yes

Table 4.3 (Continued)

Category	Sample	Lithology*	Reference	Method	Quartz (modal%)	Feldspars (modal%)	**Mica (modal%)**	[// x1] V_{SH0} at 0 MPa (km/s)	[// x1] dV_{SH}/dP (10^{-4} km s^{-1} MPa^{-1})	**V_{SH} Contrast at f = 0°, Relative to Natural QF (%)**	More Compliant V_{SH} Contrast than Natural QF?
Mylonite	M3	Mylonite (More Deformed Leucogneiss)	Cirrincione et al. (2010)	Petrophysical	34.8	43.4	**19.4**	3.0208	7.75	**20.17**	Yes
Mylonite	M4	Mylonite (Most Deformed Leucogneiss)	Cirrincione et al. (2010)	Petrophysical	37.9	59.2	**1.7**	3.4735	3.35	**6.27**	Yes
Mylonite	M201	Diatexitic Ultramylonite	Ji et al. (1993) for VP; Ji & Salisbury (1993) for VS	Petrophysical	46.1	51.5	**0**	3.62	1	**2.14**	Yes
Mylonite	GLG133	Dioritic Mylonite	Ji et al. (2015)	Petrophysical	50	33	**15**	3.4792	4.6367	**6.11**	Yes
Mylonite	GLG133	Dioritic Mylonite	Ji et al. (2015)	EBSD	50	33	**15**	3.2868		**11.78**	Yes
Mylonite	18679S	Mylonitized Orthophyre	Kern et al. (2001)	Petrophysical	43	55	**2**	3.5017	1.875	**5.46**	Yes

*Mineral abbreviations: Bt, biotite; Fsp, Feldspar; Ms, muscovite; Pl, plagioclase; Qz, quartz.

CHAPTER 5

CONCLUSIONS AND FUTURE WORK

5.1. Conclusions

5.1.1. Damage Zones at the Base of Continental, Seismogenic Strike-Slip Faults

There has been a long debate regarding the spatial extent of coseismic damage zones associated with strike-slip faults. For example, field, laboratory, and numerical investigations have suggested that the width of these damage zone decreases with depth, diminishing significantly at depths of ~5–10 km or less (e.g., Ben-Zion and Shi, 2005; Yuan et al., 2011; Aben et al., 2017a). On the other hand, recent analysis of low-magnitude seismicity and high-resolution seismic imaging estimated damage zones down to depths of ~20 km in, for example, New Zealand (e.g., Li et al., 2014a) and southern California, USA (e.g., Cochran et al., 2009; Ben-Zion and Zaliapin, 2019). This leads to the questions about (1) the occurrence of strong coseismic damage at the base of the seismogenic zone and (2) the width of the resulting damage zones at that depth. My results in Chapter 2 support the conclusion that the width of coseismic damage zones around mature strike-slip faults can reach tens to hundreds of meters near the base of the seismogenic zone.

The spatial distribution (width and depth) of off-fault damage zones is fundamentally important because they affect transient and long-term changes in fluid flow (e.g., Mitchell and Faulkner, 2008), heat transport (e.g., Morton et al., 2012), and overall fault rock rheology (e.g., Handy et al., 2007). As fracturing and fragmentation create a conduit-like system to migrate hydrothermal fluid, damage zones with high permeability tends to have higher fluid storage which may diffuse pore pressure and lead to fluid-rock interaction, mineral dissolution and precipitation, and alteration to weak minerals. As healing and mineral-filling occur, damage zones may act as a barrier to flow and pore pressure diffusion, leading to pore pressure buildup. Therefore, stress redistribution, chemical reaction, and changes in rock mineralogy and rheology within damage zones depend on the evolution of permeability structure, which can be significantly modified by damage distribution.

5.1.2. Microstructures of Pulverized Rocks at Frictional to Viscous Transition (FVT) depths

Highly fractured and fragmented rocks with grains down to the micron scale have been documented around large continental strike-slip faults at the surface (e.g., Dor et al., 2006b; Rockwell et al., 2009; Mitchell et al., 2011; Rempe et al., 2013; Muto et al., 2015). The fragments in these so-called pulverized rocks are characterized by no or little relative rotation, thus preserving the original crystal shapes of the parent minerals. They are generally attributed to dynamic earthquake ruptures, and thus considered as valuable indicators for determining if fault slip is seismic or aseismic. However, at FVT depths, coseismically pulverized rocks tend to experience some degree of shearing during post- and interseismic periods because of viscous flow of the surrounding ductile matrix. This difference raises some fundamental questions:

(1) what are the microstructural characteristics of highly fractured and pulverized rocks in coseismic damage zones at FVT depths?

(2) how do they compare to those formed at the surface along continental strike-slip faults?

(3) can fragment size statistics of fragmented minerals like garnet be used to distinguish between dynamic and quasi-static damage?

In Chapter 3, I compared two fragmented rocks: dynamically pulverized rock from the seismogenic SCSZ and quasi-statically sheared rock from the tectonic PPHSZ. Both rocks show increase in *D*-value related to viscous shear deformation. However, the dynamically deformed rocks have *D*-values in range between 1.5 and 3 whereas the tectonically deformed rocks have *D*-values smaller than 1.5. My results imply that fragmented minerals at FVT depths can still be used as indicators of coseismic damage to determine whether they are pulverized or quasi-statically deformed, irrespective of the degree of shearing. The boundary of $D \sim 1.5$ is also consistent with the transition to dynamic loading found in explosive fragmentation.

5.1.3. Bimaterial Faults Separating Two Different Anisotropic Rocks

According to the subshear rupture model along elastically isotropic, strike-slip bimaterial faults, coupling between shear slip and normal stress causes wrinkle-like pulse ruptures preferentially propagating in the slip direction of the more compliant material, resulting in asymmetric damage distribution (e.g., Weertman, 1980; Andrews and Ben-Zion, 1997; Ben-Zion, 2001; Ben-Zion and Huang, 2002; Shi and Ben-Zion, 2006; Ampuero and Ben-Zion, 2008; Dalguer and Day, 2009; Erickson and Day, 2016; Xu and Ben-Zion, 2017). Given that most fault rocks are elastically and therefore seismically anisotropic, I consider these questions about anisotropic bimaterial faults:

(1) what is the best way to describe the elastic contrast of anisotropic rocks across a bimaterial fault that allows comparison with theory and numerical experiments aimed at elastically isotropic bimaterial interfaces?

(2) how does asymmetric damage around an anisotropic bimaterial fault relate to elastic contrast and rupture directivity?

In Chapter 4, using two elastically anisotropic rocks from either side of the SCSZ, I concluded that the horizontal shear wave (*SH* wave) that propagates parallel to the fault with fault-normal polarization is the governing measure of the elastic contrast for anisotropic bimaterial strike-slip faults. The relationship among velocity contrast of the *SH* waves, rupture directivity, and asymmetric development of damage in the anisotropic bimaterial faults agrees with modeling predictions from isotropic bimaterial faults.

At middle crustal depths, seismic anisotropy of rocks is strongly associated with orientation and proportion of preferentially aligned mineral phases such as mica and amphibole. Thus, it may be necessary to investigate details of distribution and orientation of these mineral phases to predict anisotropic elastic properties and evaluate the contribution of seismic anisotropy on rupture directivity.

5.2. Directions for Future Research

5.2.1. Combined Microstructural-Minerochemical Analysis

As I addressed in conclusion above (Section 5.1.1), the spatial distribution (width and depth) of damage zones affects the transient and long-term evolution of permeability structure, likely resulting in fluid-rock interaction, mineral dissolution and precipitation, and alteration to weak minerals. Combined microstructural and minerochemical analysis on microfracture-filling materials (e.g., quartz, calcite, and chlorite) and secondary hydrous minerals such as epidote replacing microfracture-filling materials may provide clues for the cyclic interaction between earthquake-induced damage and hydrothermal fluids during seismic cycles.

5.2.2. Particle Size Distribution (PSD) Analysis Using Different Mineral Phases

For the rock fragmentation problem, the PSD was measured from only garnet grains. Although garnet is a common mineral, it is rare in quartzofeldspathic rocks: for example, garnet is not common in the QF rocks (less than 5%) of the SCSZ while it is a main component of the L-tectonite of PPHSZ. According to Blenkinsop (1991), PSD depends on mineral types. Thus, the question remains as to whether predicted fragment size distributions for garnet are valid for phases such as quartz and feldspar. Quartz deforms both brittley and viscously depending on strain rate at middle crustal depths, so microfractures and fragmentations induced by brittle deformation can be overprinted by viscous deformation microstructures (e.g., grain boundary migration and recrystallization). However, feldspar can preserve brittle microstructures at depths corresponding to temperatures less than ~500 °C. Fracture-healing and sealing in quartz and feldspar also makes PSD analysis challenging owing to low CL image resolution and EBSD detection limits on low strain samples, but to better clarify the transition between quasi-static and dynamic fragmentation, future work may focus on ways to combine differences in PSDs of garnet and feldspar.

5.2.3. PSD Analysis of Garnet Grains in Experimentally Deformed Rocks

Regarding fragmentation of natural rocks such as the SCSZ rocks, dynamically deformed garnet grains are likely to experience multiple seismic events, and then the PSDs may reflect multiple stages of fragmentation. To investigate how multiple fragmentation events affect PSD, physical experiments may resolve it by comparing single and multiple events. In addition, PSD analysis of garnet grains in experimentally deformed rocks might provide insight into different stages of fragmentation including volumetric and secondary surficial fragmentation.

5.2.4. Damage Distribution and Rupture Directivity Along Multiple Transects of the SCSZ

In this study, the internal structure of damage zones of the SCSZ was investigated across only one transect of the SCSZ. Estimating width of pulverized rocks and quantitatively determining elastic contrast across multiple transects of the SCSZ may show along-strike variation of damage and possibly damage asymmetry, which would impact our assessment of preferred rupture propagation. According to Ben-Zion and Zaliapin (2019), the damage zones are more continuous at depths of 10–15 km while they reveal heterogeneous patchy or diffused distributions near surface. However, the patchy distribution may be an indicator of dynamic pulverization (Ostermeijer et al., 2022). The methods developed in my dissertation may be used to assess whether highly damaged and pulverized rocks will be continuously or discontinuously distributed near the base of the seismogenic zone.

5.2.5. Damage Distribution and Rupture Directivity from Different Region of the NFS

Rocks in the study area of this dissertation are deformed at FVT depths corresponding to temperature of ~400–500 °C where the shear zone has mutually overprinting pseudotachylyte and mylonite. Undeformed pseudotachylyte is observed along the southeast flank of the NFS in Cape Elizabeth of southern coastal Maine, indicating the fault zone was active at a shallower ~7–8 km depth corresponding to temperature of 250–300 °C (Swanson, 2006). Comparison between two well-known pseudotachylyte-bearing strike-slip faults exhumed from different depths will allow us to test the validity of the methods and

conclusions in this study. In addition, when compared to damage zones around an active strike-slip fault near the surface, it will provide useful data to constrain spatial distributions of coseismic off-fault damage at three different depths between the surface and the base of the seismogenic zone.

5.2.6. Elastic and Seismic Properties Within the Mature Damage Zone Adjacent to the Shear Zone Core

I used two representative host-rock samples to calculate elastic properties across the bimaterial shear zone because I wanted to obtain elastic properties representing initial or early states of bimaterial contact in development of the shear zone. I also assumed that protomylonite, mylonite and ultramylonite have a similar mineralogy to their host rock with only varying minor accessory minerals. However, with increasing maturity of the shear zone, highly damaged and pulverized rocks adjacent to the shear zone core may have undergone multiple stages of fluid-rock interaction, leading to changes in rock mineralogy to weak minerals and increase in compliance. The greater compliance of QF rock adjacent to the shear zone may affect elastic contrast of the bimaterial shear zone. Due to the small grain size, I did not assess the elastic properties of the highly strained mylonitic/ultramylonitic rocks and sheared schist adjacent to the shear zone core. I was unable to measure crystallographic information of the very fine grain size of mica and other minerals because our in-house SEM/EBSD system at the University of Maine does not use a field emission source. In future, using the FE-SEM, mylonite samples with very fine mica down to submicron size can be analyzed. In addition to this method, it would also be possible to determine stiffness tensors across the shear zone using laboratory petrophysical techniques. Finally, a high-resolution active-source seismological study would also shed light on the elastic properties across the shear zone.

5.2.7. Damage Distribution and Rupture Directivity for Transpressional/Transtensional Faults

My dissertation focuses on vertical strike-slip faults where the movement of two blocks mostly occurs horizontally. However, more than 80% of plate boundary faults are transpressional or transtensional faults where motion along the faults is obliquely convergent or divergent. Methods used in my dissertation

can be extended to non-vertical transpressional/transtensional faults such as the Alpine fault in the South Island of New Zealand. The Alpine fault is a transpressional fault system where an oblique continental collision occurs between the Australian and Pacific plates. Both the SCSZ and the Alpine fault show dextral strike-slip deformation, but the dips of the two faults differ; for example, the central section of the Alpine fault dips ~50°SE (Sibson et al., 1981) while the SCSZ has sub-vertical dip. The central and South Westland sections of the Alpine fault separate quartzofeldspathic gneiss (northwestern foot wall side) and schist (southeastern hanging wall side), allowing us to examine (1) off-fault damage distribution using PSDs of fragmented garnet and possibly other minerals and (2) relationships among elastic contrast of the anisotropic rocks across a fault, rupture directivity, and off-fault damage asymmetry. Dextral-reverse fault motion on the central section of the Alpine fault changes to dextral-normal (transtensional) fault motion on the South Westland section of the Alpine fault (Barth et al., 2013). Thus, the effect of the geometric variations on rupture directivity can be investigated. However, it should be noted that asymmetric damage surrounding an oblique-slip fault can also result from interaction of a dipping fault with the Earth's surface with absence of elastic contrast (Ma, 2009).

5.2.8. Numerical Study of an Anisotropic Bimaterial Interface

Many numerical studies of dynamic ruptures have shown that the elastic contrast of bimaterial faults leads to preferred rupture propagation and asymmetric off-fault damage (e.g., Andrews & Ben-Zion, 1997; Shi & Ben-Zion, 2006; Ampuero & Ben-Zion, 2008; Dalguer & Day, 2009; Erickson & Day, 2016; Xu & Ben-Zion, 2017). However, these models assume that materials surrounding the interface are elastically isotropic. Direct comparison between the results in my dissertation and numerical studies using elastically anisotropic bimaterial interfaces could be a focus of future work.

REFERENCES

Aben, F.M., Brantut, N., Mitchell, T.M., 2020. Off-fault damage characterization during and after experimental quasi-static and dynamic rupture in crustal rock from laboratory P wave tomography and microstructures. Journal of Geophysical Research: Solid Earth 125(8), e2020JB019860. https://doi.org/10.1029/2020JB019860

Aben, F.M., Doan, M.-L., Gratier, J.-P., Renard, F., 2017a. Coseismic damage generation and pulverization in fault zones. In: Thomas, M.Y., Mitchell, T.M., Bhat, H.S. (Eds.), Fault zone dynamic processes: Evolution of fault properties during seismic rupture, Geophysical Monograph Series, vol. 227. American Geophysical Union, pp. 47–80. https://doi.org/10.1002/9781119156895.ch4

Aben, F.M., Doan, M.-L., Gratier, J.-P., Renard, F., 2017b. High strain rate deformation of porous sandstone and the asymmetry of earthquake damage in shallow fault zones. Earth and Planetary Science Letters 463, 81–91. https://doi.org/10.1016/j.epsl.2017.01.016

Aben, F.M., Doan, M.-L., Mitchell, T. M., Toussaint, R., Reuschlé, T., Fondriest, M., Gratier, J.-P., Renard, F., 2016. Dynamic fracturing by successive coseismic loadings leads to pulverization in active fault zones. Journal of Geophysical Research: Solid Earth 121(4), 2338–2360. https://doi.org/10.1002/2015JB012542

Abercrombie, R.E., Rice, J.R., 2005. Can observations of earthquake scaling constrain slip weakening? Geophysical Journal International 162(2), 406–424. https://doi.org/10.1111/j.1365-246X.2005.02579.x

Acosta, M., Passelègue, F.X., Schubnel, A., Violay, M., 2018. Dynamic weakening during earthquakes controlled by fluid thermodynamics. Nature Communications 9, 3074. https://doi.org/10.1038/s41467-018-05603-9

Adams, G.G., 1995. Self-excited oscillations of two elastic half-spaces sliding with a constant coefficient of friction. Journal of Applied Mechanics 62(4), 867–872. https://doi.org/10.1115/1.2896013

Adda-Bedia, M., Ben Amar, M., 2003. Self-sustained slip pulses of finite size between dissimilar materials. Journal of the Mechanics and Physics of Solids 51(10), 1849–1861. https://doi.org/10.1016/S0022-5096(03)00068-1

Aki, K., 1979. Characterization of barriers on an earthquake fault. Journal of Geophysical Research: Solid Earth 84(B11), 6140–6148. https://doi.org/10.1029/JB084iB11p06140

Albertini, G., Kammer, D.S., 2017. Off-fault heterogeneities promote supershear transition of dynamic mode II cracks. Journal of Geophysical Research: Solid Earth 122(8), 6625–6641. https://doi.org/10.1002/2017JB014301

Aleksandrov, K.S., Ryzhova, T.V., 1961. Elastic properties of rock-forming minerals II: Layered silicates. Bulletin of the Academy of Sciences of the U.S.S.R., Geophysics Series (English Translation) 9(12), 1165–1168.

Allam, A.A., Ben-Zion, Y., Peng, Z., 2014. Seismic imaging of a bimaterial interface along the Hayward fault, CA, with fault zone head waves and direct P arrivals. Pure and Applied Geophysics 171(11), 2993–3011. https://doi.org/10.1007/s00024-014-0784-0

Allam, A.A., Kroll, K.A., Milliner, C.W.D., Richards-Dinger, K.B., 2019. Effects of fault roughness on coseismic slip and earthquake locations. Journal of Geophysical Research: Solid Earth 124(11), 11336–11349. https://doi.org/10.1029/2018JB016216

Allen, J. L., Shaw, C. A., 2013. Seismogenic fault-zone processes and heterogeneity recorded by pseudotachylyte: New insights from the Homestake shear zone, Colorado. In: Abbott, L.D., Hancock, G.S. (Eds.), Classic concepts and new directions: exploring 125 years of GSA discoveries in the rocky mountain region, Geological Society of America Field Guide, vol. 33. Geological Society of America, pp. 165–183. https://doi.org/10.1130/2013.0033(05)

Almqvist, B.S.G., Cyprych, D., Piazolo, S., 2021. Seismic anisotropy of mid crustal orogenic nappes and their bounding structures: An example from the Middle Allochthon (Seve Nappe) of the Central Scandinavian Caledonides. Tectonophysics 819, 229045. https://doi.org/10.1016/j.tecto.2021.229045

Almqvist, B.S.G., Mainprice, D., 2017. Seismic properties and anisotropy of the continental crust: Predictions based on mineral texture and rock microstructure. Reviews of Geophysics 55(2), 367–433. https://doi.org/10.1002/2016RG000552

Ampuero, J.P., Ben-Zion, Y., 2008. Cracks, pulses and macroscopic asymmetry of dynamic rupture on a bimaterial interface with velocity-weakening friction. Geophysical Journal International 173(2), 674–692. https://doi.org/10.1111/j.1365-246X.2008.03736.x

Ampuero, J. P., Mao, X., 2017. Upper limit on damage zone thickness controlled by seismogenic depth. In: Thomas, M.Y., Mitchell, T.M., Bhat, H.S. (Eds.), Fault zone dynamic processes: Evolution of fault properties during seismic rupture, Geophysical Monograph Series, vol. 227. American Geophysical Union, pp. 243–253. https://doi.org/10.1002/9781119156895.ch13

An, L.-J., Sammis, C., 1994. Particle size distribution of cataclastic fault materials from southern California: a 3-D study. Pure and Applied Geophysics 143(1–3), 203–227.

Anders, M.H., Wiltschko, D.V, 1994. Microfracturing, paleostress and the growth of faults. Journal of Structural Geology 16(6), 795–815. https://doi.org/10.1016/0191-8141(94)90146-5

Anderson, E.K., Song, W.J., Johnson, S.E., Cruz-Uribe, A.M., 2021. Mica kink-band geometry as an indicator of coseismic dynamic loading. Earth and Planetary Science Letters 567, 117000. https://doi.org/10.1016/j.epsl.2021.117000

Andrews, D.J., 1976. Rupture velocity of plane strain shear cracks. Journal of Geophysical Research: Solid Earth and Planets 81(32), 5679–5687. https://doi.org/10.1029/JB081i032p05679

Andrews, D.J., 2005. Rupture dynamics with energy loss outside the slip zone. Journal of Geophysical Research: Solid Earth 110(B1), B01307. https://doi.org/10.1029/2004JB003191.

Andrews, D.J., 2010. Ground motion hazard from supershear rupture. Tectonophysics 493(3–4), 216–221. https://doi.org/10.1016/j.tecto.2010.02.003

Andrews, D.J., Ben-Zion, Y., 1997. Wrinkle-like slip pulse on a fault between different materials. Journal of Geophysical Research: Solid Earth 102(B1), 553–571. https://doi.org/10.1029/96JB02856

Archuleta, R.J., 1984. A faulting model for the 1979 Imperial Valley earthquake. Journal of Geophysical Research: Solid Earth 89(B6), 4559–4585. https://doi.org/10.1029/JB089iB06p04559

Audet, P., 2015. Layered crustal anisotropy around the San Andreas Fault near Parkfield, California. Journal of Geophysical Research: Solid Earth 120(5), 3527–3543. https://doi.org/10.1002/2014JB011821

Auld, B.A., 1990. Acoustic fields and waves in solids: Volume I (2nd edn). Krieger Publishing Company.

Austrheim, H., Dunkel, K.G., Plümper, O., Ildefonse, B., Liu, Y., Jamtveit, B., 2017. Fragmentation of wall rock garnets during deep crustal earthquakes. Science Advances 3(2), e1602067. https://doi.org/10.1126/sciadv.1602067

Badge, M.N., Petroš, V., 2005. Fatigue properties of intact sandstone samples subjected to dynamic uniaxial cyclical loading. International Journal of Rock Mechanics and Mining Sciences 42(2), 237–250. https://doi.org/10.1016/j.ijrmms.2004.08.008

Babuška, V., Cara, M., 1991. Seismic anisotropy in the Earth. Kluwer Academic Publishers. https://doi.org/10.1007/978-94-011-3600-6

Balsamo, F., Storti, F., 2011. Size-dependent comminution, tectonic mixing, and sealing behavior of a "structurally oversimplified" fault zone in poorly lithified sands: evidence for a coseismic rupture? Geological Society of America Bulletin 123(3–4), 601–619. https://doi.org/10.1130/B30099.1

Barber, T., Griffith, W.A., 2017. Experimental constraints on dynamic fragmentation as a dissipative process during seismic slip. Philosophical Transactions of the Royal Society A 375(2103), 20160002. https://doi.org/10.1098/rsta.2016.0002

Barnett, W., 2004. Subsidence breccias in kimberlite pipes—An application of fractal analysis. Lithos 76(1–4), 299–316. https://doi.org/10.1016/j.lithos.2004.03.019

Barruol, G., Mainprice, D., 1993. A quantitative evaluation of the contribution of crustal rocks to the shear-wave splitting of teleseismic SKS waves. Physics of the Earth and Planetary Interiors 78(3–4), 281–300. https://doi.org/10.1016/0031-9201(93)90161-2

Barth, N.C., Boulton, C., Carpenter, B.M., Batt, G.E., Toy, V.G., 2013. Slip localization on the southern Alpine Fault, New Zealand. Tectonics 32(3), 620–640. https://doi.org/10.1002/tect.20041

Barth, N.C., Toy, V.G., Langridge, R.M., Norris, R.J., 2012. Scale dependence of oblique plate-boundary partitioning: New insights from LiDAR, central Alpine fault, New Zealand. Lithosphere 4(5), 435–448. https://doi.org/10.1130/L201.1

Bazargan, M., Motra, H.B., Almqvist, B.S.G., Piazolo, S., Hieronymus, C., 2021. Pressure, temperature and lithological dependence of seismic and magnetic susceptibility anisotropy in amphibolites and gneisses from the central Scandinavian Caledonides. Tectonophysics 820, 229113. https://doi.org/10.1016/j.tecto.2021.229113

Beeler, N., Kilgore, B., McGarr, A., Fletcher, J., Evans, J., Baker, S. R., (2012). Observed source parameters for dynamic rupture with non-uniform initial stress and relatively high fracture energy. Journal of Structural Geology, 38, 77–89. https://doi.org/10.1016/j.jsg.2011.11.013

Beeler, N.M., Di Toro, G., Nielsen, S., 2016. Earthquake source properties from pseudotachylite. Bulletin of the Seismological Society of America 106(6), 2764–2776. https://doi.org/10.1785/0120150344

Bennett, J.G., 1936. Broken coal. Journal of the Institute of Fuel 10, 22-39.

Ben-Zion, Y., 1989. The response of two joined quarter spaces to SH line sources located at the material discontinuity interface. Geophysical Journal International 98(2), 213–222. https://doi.org/10.1111/j.1365-246X.1989.tb03346.x

Ben-Zion, Y., 1990. The response of two half spaces to point dislocations at the material interface. Geophysical Journal International 101(3), 507–528. https://doi.org/10.1111/j.1365-246X.1990.tb05567.x

Ben-Zion, Y., 2001. Dynamic ruptures in recent models of earthquake faults. Journal of the Mechanics and Physics of Solids 49(9), 2209–2244. https://doi.org/10.1016/S0022-5096(01)00036-9

Ben-Zion, Y., 2006. Comment on "The wrinkle-like slip pulse is not important in earthquake dynamics" by D. J. Andrews and R. A. Harris. Geophysical Research Letters 33(6), L06310. https://doi.org/10.1029/2005GL025372

Ben-Zion, Y., Ampuero, J.-P., 2009. Seismic radiation from regions sustaining material damage. Geophysical Journal International 178(3), 1351–1356. https://doi.org/10.1111/j.1365-246X.2009.04285.x

Ben-Zion, Y., Andrews, D.J., 1998. Properties and implications of dynamic rupture along a material interface. Bulletin of the Seismological Society of America 88(4), 1085–1094.

Ben-Zion, Y., Huang, Y., 2002. Dynamic rupture on an interface between a compliant fault zone layer and a stiffer surrounding solid. Journal of Geophysical Research: Solid Earth 107(B2), 2042. https://doi.org/10.1029/2001JB000254

Ben-Zion, Y., Rice, J. R., 1997. Dynamic simulations of slip on a smooth fault in an elastic solid. Journal of Geophysical Research: Solid Earth 102(B8), 17771–17784. https://doi.org/10.1029/97JB01341

Ben-Zion, Y., Sammis, C.G., 2003. Characterization of fault zones. Pure and Applied Geophysics 160(3), 677–715. https://doi.org/10.1007/pl00012554

Ben-Zion, Y., Sammis, C.G., 2013. Shear heating during distributed fracturing and pulverization of rocks. Geology 41(2), 139–142. https://doi.org/10.1130/G33665.1

Ben-Zion, Y., Shi, Z., 2005. Dynamic rupture on a material interface with spontaneous generation of plastic strain in the bulk. Earth and Planetary Science Letters 236(1–2), 486–496. https://doi.org/10.1016/j.epsl.2005.03.025

Ben-Zion, Y., Vernon, F.L., Ozakin, Y., Zigone, D., Ross, Z. E., Meng, H., White, M., Reyes, J., Hollis, D., Barklage, M., 2015. Basic data features and results from a spatially dense seismic array on the San Jacinto fault zone. Geophysical Journal International 202(1), 370–380. https://doi.org/10.1093/gji/ggv142

Ben-Zion, Y., Zaliapin, I., 2019. Spatial variations of rock damage production by earthquakes in southern California. Earth and Planetary Science Letters 512, 184–193. https://doi.org/10.1016/j.epsl.2019.02.006

Bernard, P., Baumont, D., 2005. Shear Mach wave characterization for kinematic fault rupture models with constant supershear rupture velocity. Geophysical Journal International 162(2), 431–447. https://doi.org/10.1111/j.1365-246X.2005.02611.x

Bernard, P., Herrero, A., Berge, C., 1996. Modeling directivity of heterogeneous earthquake ruptures. Bulletin of the Seismological Society of America 86(4), 1149–1160.

Bertero, V.V., Mahin, S.A., Herrera, R.A., 1978. Aseismic design implications of near-fault San Fernando earthquake records. Earthquake Engineering and Structural Dynamics 6(1), 31–42. https://doi.org/10.1002/eqe.4290060105

Bestmann, M., Pennacchioni, G., Frank, G., Göken, M., de Wall, H., 2011. Pseudotachylyte in muscovite-bearing quartzite: Coseismic friction-induced melting and plastic deformation of quartz. Journal of Structural Geology 33(2), 169–186. https://doi.org/10.1016/j.jsg.2010.10.009

Bestmann, M., Pennacchioni, G., Nielsen, S., Göken, M., de Wall, H., 2012. Deformation and ultrafine dynamic recrystallization of quartz in pseudotachylyte-bearing brittle faults: A matter of a few seconds. Journal of Structural Geology 38, 21–38. https://doi.org/10.1016/j.jsg.2011.10.001

Bhat, H.S., Dmowska, R., King, G.C.P., Klinger, Y., Rice, J.R., 2007. Off-fault damage patterns due to supershear ruptures with application to the 2001 M_w 8.1 Kokoxili (Kunlun) Tibet earthquake. Journal of Geophysical Research: Solid Earth 112(B6), B06301. https://doi.org/10.1029/2006JB004425

Bhat, H.S., Rosakis, A. J., Sammis, C.G., 2012. A micromechanics based constitutive model for brittle failure at high strain rates. Journal of Applied Mechanics 79(3), 031016. https://doi.org/10.1115/1.4005897

Biegel, R.L., Sammis, C.G., Dieterich, J.H., 1989. The frictional properties of a simulated gouge having a fractal particle distribution. Journal of Structural Geology 11(7), 827–846. https://doi.org/10.1016/0191-8141(89)90101-6

Billi, A., Storti, F., 2004. Fractal distribution of particle size in carbonate cataclastic rocks from the core of a regional strike-slip fault zone. Tectonophysics 384(1–4), 115–128. https://doi.org/10.1016/j.tecto.2004.03.015

Birch, F., 1960. The velocity of compressional waves in rocks to 10 kilobars, Part 1. Journal of Geophysical Research 65(4), 1083–1102. https://doi.org/10.1029/JZ065i004p01083

Bistacchi, A., Massironi, M. Menegon, L., 2010. Three-dimensional characterization of a crustal-scale fault zone: the Pusteria and Sprechenstein fault system (Eastern Alps). Journal of Structural Geology 32(12), 2022–2041. https://doi.org/10.1016/j.jsg.2010.06.003

Bjørk, T.E., Austrheim, M.H., 2009. Quantifying granular material and deformation: Advantages of combining grain size, shape, and mineral phase recognition analysis. Journal of Structural Geology 31(7), 637–653. https://doi.org/10.1016/j.jsg.2009.03.020

Blenkinsop, T.G., 1991. Cataclasis and processes of particle size reduction. Pure and Applied Geophysics 136, 59–86. https://doi.org/10.1007/BF00878888

Boatwright, J., Boore, D.M., 1982. Analysis of the ground accelerations radiated by the 1980 Livermore Valley earthquakes for directivity and dynamic source characteristics. Bulletin of the Seismological Society of America 72(6A), 1843–1865.

Boese, C.M., Townend, J., Smith, E.G.C., Stern, T., 2012. Microseismicity and stress in the vicinity of the Alpine Fault, central Southern Alps, New Zealand. Journal of Geophysical Research: Solid Earth 117, B02302. https://doi.org/10.1029/2011JB008460

Bouchon, M., Bouin, M.P., Karabulut, H., Toksöz, M.N., Dietrich, M., Rosakis, A.J., 2001. How fast is rupture during an earthquake? New insights from the 1999 Turkey earthquakes. Geophysical Research Letters 28(14), 2723–2726. https://doi.org/10.1029/2001GL013112

Bouchon, M., Vallée, M., 2003. Observation of long supershear rupture during the magnitude 8.1 Kunlunshan earthquake. Science 301(5634), 824–826. https://doi.org/10.1126/science.1086832

Botvina, L.R., 2011. Dynamic fragmentation criterion that reflects the effect of the composition and mechanical properties of a material and loading conditions. Russian Metallurgy (Metally) 2011(10), 973–980. https://doi.org/10.1134/S0036029511100016

Brantley, S.L., Evans, B., Hickman, S.H., Crerar, D.A., 1990. Healing of microcracks in quartz: Implications for fluid flow. Geology 18(2), 136–139. https://doi.org/10.1130/0091-7613(1990)018<0136:HOMIQI>2.3.CO;2

Brantut, N., Han, R., Shimamoto, T., Findling, N., Schubnel, A., 2011. Fast slip with inhibited temperature rise due to mineral dehydration: Evidence from experiments on gypsum. Geology 39(1), 59–62. https://doi.org/10.1130/G31424.1

Brantut, N., Platt, J.D., 2017. Dynamic weakening and the depth dependence of earthquake faulting. In: Thomas, M.Y., Mitchell, T.M., Bhat, H.S. (Eds.), Fault zone dynamic processes: Evolution of fault properties during seismic rupture, Geophysical Monograph Series, vol. 227. American Geophysical Union. pp. 171–194. https://doi.org/10.1002/9781119156895.ch9

Brantut, N., Viesca, R.C., 2017. The fracture energy of ruptures driven by flash heating. Geophysical Research Letters 44(13), 6718–6725. https://doi.org/10.1002/2017GL074110

Braunagel, M.J., Griffith, W.A., 2019. The effect of dynamic stress cycling on the compressive strength of rocks. Geophysical Research Letters 46(12), 6479–6486. https://doi.org/10.1029/2019GL082723

Bray, J.D., Rodriguez-Marek, A., Gillie, J.L., 2009. Design ground motions near active faults. Bulletin of the New Zealand Society for Earthquake Engineering 42(1), 1–8. https://doi.org/10.5459/bnzsee.42.1.1-8

Brener, E.A., Weikamp, M., Spatschek, R., Bar-Sinai, Y., Bouchbinder, E., 2016. Dynamic instabilities of frictional sliding at a bimaterial interface. Journal of the Mechanics and Physics of Solids 89, 149–173. https://doi.org/10.1016/j.jmps.2016.01.009

Brietzke, G.B., Cochard, A., Igel, H., 2007. Dynamic rupture along bimaterial interfaces in 3D. Geophysical Research Letters 34(11), L11305. https://doi.org/10.1029/2007GL029908

Brietzke, G.B., Cochard, A., Igel, H., 2009. Importance of bimaterial interfaces for earthquake dynamics and strong ground motion. Geophysical Journal International 178(2), 921–938. https://doi.org/10.1111/j.1365-246X.2009.04209.x

Broberg, K.B., 1994. Intersonic bilateral slip. Geophysical Journal International 119(3), 706–714. https://doi.org/10.1111/j.1365-246X.1994.tb04010.x

Broberg, K.B., 1995. Intersonic mode II crack expansion. Archives of Mechanics 47(5), 859–871.

Brodsky, E.E., Gilchrist, J.J., Sagy, A., Collettini, C., 2011. Faults smooth gradually as a function of slip. Earth and Planetary Science Letters 302(1–2), 185–193. https://doi.org/10.1016/j.epsl.2010.12.010

Brodsky, E.E., Mori, J.J., Anderson, L., Chester, F.M., Conin, M., Dunham, E.M., Eguchi, N., Fulton, P.M., Hino, R., Hirose, T., Ikari, M.J., Ishikawa, T., Jeppson, T., Kano,Y., Kirkpatrick, J., Kodaira, S., Lin, W., Nakamura, Y., Rabinowitz, H.S., Regalla, C., Remitti, F., Rowe, C., Saffer, D.M., Saito, S., Sample, J., Sanada, Y., Savage, H.M., Sun, T., Toczko, S., Ujiie, K., Wolfson-Schwehr, M., Yang, T., 2020. The state of stress on the fault before, during, and after a major earthquake. Annual Review of Earth and Planetary Sciences 48, 49–74. https://doi.org/10.1146/annurev-earth-053018-060507

Brown, J.M., Angel, R.J., Ross, N.L., 2016. Elasticity of plagioclase feldspars. Journal of Geophysical Research: Solid Earth 121(2), 663–675. https://doi.org/10.1002/2015JB012736

Bruhat, L., Fang, Z., Dunham, E.M., 2016. Rupture complexity and the supershear transition on rough faults. Journal of Geophysical Research: Solid Earth 121(1), 210–224. https://doi.org/10.1002/2015JB012512

Brune, J.N., 1970. Tectonic stress and the spectra of seismic shear waves from earthquakes. Journal of Geophysical Research: Solid Earth 75(26), 4997–5009. https://doi.org/10.1029/JB075i026p04997

Brune, J.N., 2001. Fault-normal dynamic unloading and loading: An explanation for “non-gouge” rock powder and lack of fault-parallel shear bands along the San Andreas fault. EOS Transactions American Geophysical Union, 82(47), Fall Meeting Supplement, Abstract S22B-0655.

Brune, J.N., Brown, S., Johnson, P.A., 1993. Rupture mechanism and interface separation in foam rubber models of earthquakes: a possible solution to the heat flow paradox and the paradox of large overthrusts. Tectonophysics 218(1–3), 59–67. https://doi.org/10.1016/0040-1951(93)90259-M

Buhl, E., Kowitz, A., Elbeshausen, D., Sommer, F., Dresen, G., Poelchau, M.H., Reimold, W.U., Schmitt, R.T., Kenkmann, T., 2013. Particle size distribution and strain rate attenuation in hypervelocity impact and shock recovery experiments. Journal of Structural Geology 56, 20–33. https://doi.org/10.1016/j.jsg.2013.08.007

Burke, M.M., 1991. Reflectivity of highly deformed terranes based on laboratory and in situ velocity measurements from the Grenville Front Tectonic Zone, central Ontario, Canada (Doctoral dissertation). Dalhousie University. Retrieved from http://hdl.handle.net/10222/55211

Burke, M.M., Fountain, D.M., 1990. Seismic properties of rocks from an exposure of extended continental crust—New laboratory measurements from the Ivrea Zone. Tectonophysics 182(1–2), 119–146. https://doi.org/10.1016/0040-1951(90)90346-A

Burlini, L., Fountain, D.M., 1993. Seismic anisotropy of metapelites from the Ivrea-Verbano zone and Serie dei Laghi (northern Italy). Physics of the Earth and Planetary Interiors 78(3), 301–317. https://doi.org/10.1016/0031-9201(93)90162-3

Burridge, R., 1973. Admissible speeds for plane-strain self-similar shear dracks with friction but lacking cohesion. Geophysical Journal of the Royal Astronomical Society 35(4), 439–455. https://doi.org/10.1111/j.1365-246X.1973.tb00608.x

Camacho, G.T., Ortiz, M., 1996. Computational modelling of impact damage in brittle materials. International Journal of Solids and Structures 33(20–22), 2899–2938. https://doi.org/10.1016/0020-7683(95)00255-3

Campbell, L.R., Menegon, L., Fagereng, Å., Pennacchioni, G., 2020. Earthquake nucleation in the lower crust by local stress amplification. Nature Communications 11, 1322. https://doi.org/10.1038/s41467-020-15150-x

Capaccioni, F., Cerroni, P., Coradini, M., Di Martino, M., Farinella, P., Flamini, E., Martelli, G., Paolicchi, P., Smith P.N., Woodward, A., Zappala, V., 1986. Asteroidal catastrophic collisions simulated by hypervelocity impact experiments. Icarus 66(3), 487–514. https://doi.org/10.1016/0019-1035(86)90087-4

Carpinteri, A., Pugno, N., 2002. A fractal comminution approach to evaluate the drilling energy dissipation. International Journal for Numerical and Analytical Methods in Geomechanics 26(5), 499–513. https://doi.org/10.1002/nag.209

Champion, C., Liel, A., 2012. The effect of near-fault directivity on building seismic collapse risk. Earthquake Engineering and Structural Dynamics 41(10), 1391–1409. https://doi.org/10.1002/eqe.1188

Cheng, Y., Wang, X, Zhan, Z., Ben-Zion, Y., 2021. Isotropic source components of events in the 2019 Ridgecrest, California, earthquake sequence. Geophysical Research Letters 48(18), e2021GL094515. https://doi.org/10.1029/2021GL094515

Chester, F.M., Chester, J.S., 1998. Ultracataclasite structure and friction processes of the Punchbowl fault, San Andreas system, California. Tectonophysics 295(1–2), 199–221. https://doi.org/10.1016/S0040-1951(98)00121-8

Chester, F.M., Chester, J.S., 2000. Stress and deformation along wavy frictional faults. Journal of Geophysical Research: Solid Earth 105(B10), 23421–23430. https://doi.org/10.1029/2000JB900241

Chester, F.M., Chester, J.S., Kirschner, D.L., Schulz, S.E., Evans, J.P., 2004. Structure of large-displacement, strike-slip fault zones in the brittle continental crust. In: Karner, G.D., Taylor, B., Driscoll, N.W., Kohlsted, D.L. (Eds.), Rheology and deformation of the lithosphere at continental margins. Columbia University Press, pp. 223–260. https://doi.org/10.7312/karn12738.12

Chester, J.S., Chester, F.M., Kronenberg, A.K., 2005. Fracture surface energy of the Punchbowl fault, San Andreas system. Nature 437(7055), 133–136. https://doi.org/10.1038/nature03942

Chheda, T.D., Mookherjee, M., Mainprice, D., dos Santos, A.M., Molaison, J.J., Chantel, J., Manthilake, G., Bassett, W.A., 2014. Structure and elasticity of phlogopite under compression: Geophysical implications. Physics of the Earth and Planetary Interiors 233, 1–12. https://doi.org/10.1016/j.pepi.2014.05.004

Ching, E.S.C., Lui, S.L., Xia, K.-Q., 2000. Energy dependence of impact fragmentation of long glass rods. Physica A: Statistical Mechanics and Its Applications 287(1–2), 83–90. https://doi.org/10.1016/S0378-4371(00)00446-5

Cholach, P.Y., Molyneux, J.B., Schmitt, D.R., 2005. Flin Flon Belt seismic anisotropy: Elastic symmetry, heterogeneity, and shear-wave splitting. Canadian Journal of Earth Sciences 42(4), 533–554. https://doi.org/10.1139/E04-094

Christensen, N.I., 1965. Compressional wave velocities in metamorphic rocks at pressures to 10 kilobars. Journal of Geophysical Research 70(24), 6147–6164. https://doi.org/10.1029/JZ070I024P06147

Christensen, N.I., 1966. Shear wave velocities in metamorphic rocks at pressures to 10 kilobars. Journal of Geophysical Research 71(14), 3549–3556. https://doi.org/10.1029/JZ071i014p03549

Christensen, N.I., Mooney, W.D., 1995. Seismic velocity structure and composition of the continental crust: A global view. Journal of Geophysical Research: Solid Earth 100(B6), 9761–9788. https://doi.org/10.1029/95JB00259

Christensen, N.I., Okaya, D.A., 2007. Compressional and shear wave velocities in South Island, New Zealand rocks and their application to the interpretation of seismological models of the New Zealand crust. In: Okaya, D., Stern, T., Davey, F. (Eds.), A continental plate boundary: Tectonics at South Island, New Zealand, Geophysical Monograph Series, vol. 175. American Geophysical Union, pp. 123–155. https://doi.org/10.1029/175GM08

Christoffel, E.B., 1877. Ueber die Fortpflanzung von Stössen durch elastische feste Körper. Annali Di Matematica Pura Ed Applicata 8, 193–243. https://doi.org/10.1007/bf02420789

Chroston, P.N., Brooks, S.G., 1989. Lower crustal seismic velocities from Lofoten-Vesterålen, North Norway. Tectonophysics 157(4), 251–269. https://doi.org/10.1016/0040-1951(89)90143-1

Cirrincione, R., Fazio, E., Heilbronner, R., Kern, H., Mengel, K., Ortolano, G., Pezzino, A., Punturo, R., 2010. Microstructure and elastic anisotropy of naturally deformed leucogneiss from a shear zone in Montalto (southern Calabria, Italy). Geological Society, London, Special Publications 332, 49–68. https://doi.org/10.1144/SP332.4

Clark, C., Schmidt Mumm, A., Collins, A.S., 2006. A coupled micro- and macrostructural approach to the analysis of fluid induced brecciation, Curnamona Province, South Australia. Journal of Structural Geology 28(5), 745–761. https://doi.org/10.1016/j.jsg.2006.01.005

Cocco, M., Tinti, E., 2008. Scale dependence in the dynamics of earthquake propagation: Evidence from seismological and geological observations. Earth and Planetary Science Letters 273(1–2), 123–131. https://doi.org/10.1016/j.epsl.2008.06.025

Cocco, M., Spudich, P., Tinti, E., 2006. On the mechanical work absorbed on faults during earthquake ruptures. In: Abercrombie, R., McGarr, A., Di Toro, G., Kanamori, H. (Eds.), Earthquakes: radiated energy and the physics of faulting, Geophysical Monograph Series, vol. 170. American Geophysical Union, pp. 237–254. https://doi.org/10.1029/170GM24

Cochard, A., Rice, J.R., 2000. Fault rupture between dissimilar materials: Ill-posedness, regularization, and slip-pulse response. Journal of Geophysical Research: Solid Earth 105(B11), 25891–25907. https://doi.org/10.1029/2000jb900230

Cochran, E.S., Li, Y.-G., Shearer, P.M., Barbot, S., Fialko, Y., Vidale, J.E., 2009. Seismic and geodetic evidence for extensive, long-lived fault damage zones. Geology 37(4), 315–318. https://doi.org/10.1130/G25306A.1

Cowan, D.S., 1999. Do faults preserve a record of seismic slip? A field geologist's opinion. Journal of Structural Geology 21(8–9), 995–1001. https://doi.org/10.1016/S0191-8141(99)00046-2

Cook, A.C., Vel, S.S., Johnson, S.E., Gerbi, C.C., Song, W.J., 2018. ThermoElastic and Seismic Analysis (TESA) toolbox for polycrystalline materials. Retrieved from https://umaine.edu/mecheng/vel/software/tesa_toolbox/

Craggs, J.W., 1960. On the propagation of a crack in an elastic-brittle material. Journal of the Mechanics and Physics of Solids 8(1), 66–75. https://doi.org/10.1016/0022-5096(60)90006-5

Crum, S.V., 1990. Fractal concepts applied to bench-blast fragmentation. In: Hustrulid, W., Johnson, G.A. (Eds.), Rock Mechanics Contributions and Challenges: Proceedings of the 31st U.S. Symposium. CRC Press, pp. 913–919. https://doi.org/10.1201/9781003078944-136

Cui, L., An, L., Gong, W., 2006. Effects of process parameters on the comminution capability of high pressure water jet mill. International Journal of Mineral Processing 81(2), 113–121. https://doi.org/10.1016/j.minpro.2006.07.005

Cyprych, D., Piazolo, S., Almqvist, B.S.G., 2017. Seismic anisotropy from compositional banding in granulites from the deep magmatic arc of Fiordland, New Zealand. Earth and Planetary Science Letters 477, 156–167. https://doi.org/10.1016/j.epsl.2017.08.017

Dalguer, L.A., Day, S.M., 2009. Asymmetric rupture of large aspect-ratio faults at bimaterial interface in 3D. Geophysical Research Letters 36(23), L23307. https://doi.org/10.1029/2009GL040303

Dalguer, L.A., Irikura, K., Riera, J.D., 2003. Simulation of tensile crack generation by three-dimensional dynamic shear rupture propagation during an earthquake. Journal of Geophysical Research: Solid Earth 108(B3), ESE 3-1-ESE 3-20. https://doi.org/10.1029/2001jb001738

Danesi, S., Bannister, S., Morelli, A., 2007. Repeating earthquakes from rupture of an asperity under an Antarctic outlet glacier. Earth and Planetary Science Letters 253(1–2), 151–158. https://doi.org/10.1016/j.epsl.2006.10.023

Das, S., Aki, K., 1977. A numerical study of two-dimensional spontaneous rupture propagation. Geophysical Journal of the Royal Astronomical Society 50(3), 643–668. https://doi.org/10.1111/j.1365-246X.1977.tb01339.x

Davis, G.H., Reynolds, S.J., Kluth, C.F., 2011. Structural geology of rocks and regions (3rd. Edn). John Wiley & Sons, Inc.

Davies, T. R. H., McSaveney, M. J., Reznichenko, N. V., (2019). What happens to fracture energy in brittle fracture? Revisiting the Griffith assumption. Solid Earth, 10(4), 1385–1395. https://doi.org/10.5194/se-10-1385-2019

Davies, T.R.H., McSaveney, M.J., Reznichenko, N.V., 2021. Corrigendum to “What happens to fracture energy in brittle fracture? Revisiting the Griffith assumption” published in Solid Earth, 10, 1385–1395, 2019. Solid Earth. https://doi.org/10.5194/se-10-1385-2019-corrigendum

Davydova, M., Uvarov, S., Chudinov, V., 2014. Scaling law of quasi brittle fragmentation. Procedia Materials Science 3, 580–585. https://doi.org/10.1016/j.mspro.2014.06.096

Dellino, P., Liotino, G., 2002. The fractal and multifractal dimension of volcanic ash particles contour: a test study on the utility and volcanological relevance. Journal of Volcanological and Geothermal Research 113(1–2), 1–18. https://doi.org/10.1016/S0377-0273(01)00247-5

DeMets, C., Gordon, R.G., Argus, D.F., Stein, S., 1990. Current plate motions. Geophyscal Journal International 101(2), 425–478. https://doi.org/10.1111/j.1365-246X.1990.tb06579.x

DeMets, C., Gordon, R.G., Argus, D., Stein, S., 1994. Effect of recent revisions to the geomagnetic reversal time scale on estimates of current plate motion. Geophyiscal Research Letters 21(20), 2191-2194. https://doi.org/10.1029/94GL02118

Dempsey, E.D., Prior, D.J., Mariani, E., Toy, V.G., Tatham, D.J., 2011. Mica-controlled anisotropy within mid-to-upper crustal mylonites: An EBSD study of mica fabrics in the Alpine Fault Zone, New Zealand. Geological Society, London, Special Publications 360, 33–47. https://doi.org/10.1144/SP360.3

Dieterich, J.H., Smith, D.E., 2009. Nonplanar faults: Mechanics of slip and off-fault damage. Pure and Applied Geophysics 166(10–11), 1799–1815. https://doi.org/10.1007/s00024-009-0517-y

Di Toro, G., Hirose, T., Nielsen, S., Pennacchioni, G., Shimamoto, T., 2006. Natural and experimental evidence of melt lubrication of faults during earthquakes. Science 311(5761), 647–649. https://doi.org/10.1126/science.1121012

Di Toro, G., Nielsen, S., Pennacchioni, G., 2005. Earthquake rupture dynamics frozen in exhumed ancient faults. Nature 436(7053), 1009–1012. https://doi.org/10.1038/nature03910

Di Toro, G., Pennacchioni, G., Nielsen, S., 2009. Pseudotachylytes and earthquake source mechanics. In: Fukuyama, E. (Ed.), Fault-zone properties and earthquake rupture dynamics, International Geophysics Series, vol. 94. Academic Press, pp. 87–133. https://doi.org/10.1016/S0074-6142(08)00005-3

Doan, M.-L., Billi, A., 2011. High strain rate damage of Carrara marble. Geophysical Research Letters 38(19), L19302. https://doi.org/10.1029/2011GL049169

Doan, M.-L., d'Hour, V., 2012. Effect of initial damage on rock pulverization along faults. Journal of Structural Geology 45, 113–124. https://doi.org/10.1016/j.jsg.2012.05.006

Doan, M.-L., Gary, G., 2009. Rock pulverization at high strain rate near the San Andreas fault. Nature Geoscience 2(10), 709–712. https://doi.org/10.1038/ngeo640

Doll, W.E., Domoracki, W.J., Costain, J.K., Çoruh, C., Ludman, A., Hopeck, J.T., 1996. Seismic reflection evidence for the evolution of a transcurrent fault system: The Norumbega fault zone, Maine. Geology, 24(3), 251–254. https://doi.org/10.1130/0091-7613(1996)024<0251:SREFTE>2.3.CO;2

Donnison, J.R., Sugden, R.A., 1984. The distribution of asteroid diameters. Monthly Notices of the Royal Astronomical Society 210(3), 673–682. https://doi.org/10.1093/mnras/210.3.673

Dor, O., Ben-Zion, Y., Rockwell, T.K., Brune, J., 2006a. Pulverized rocks in the Mojave section of the San Andreas Fault Zone. Earth and Planetary Science Letters 245(3–4), 642–654. https://doi.org/10.1016/j.epsl.2006.03.034

Dor, O., Chester, J.S., Ben-Zion, Y., Brune, J.N., Rockwell, T.K., 2009. Characterization of damage in sandstones along the Mojave section of the San Andreas Fault: implications for the shallow extent of damage generation. Pure and Applied Geophysics 166(10–11), 1747–1773. https://doi.org/10.1007/s00024-009-0516-z

Dor, O., Rockwell, T.K., Ben-Zion, Y., 2006b. Geological observations of damage asymmetry in the structure of the San Jacinto, San Andreas and Punchbowl faults in southern California: A possible indicator for preferred rupture propagation direction. Pure and Applied Geophysics 163(2–3), 301–349. https://doi.org/10.1007/s00024-005-0023-9

Dor, O., Yildirim, C., Rockwell, T.K., Ben-Zion, Y., Emre, O., Sisk, M., Duman, T.Y., 2008. Geological and geomorphologic asymmetry across the rupture zones of the 1943 and 1944 earthquakes on the North Anatolian Fault: Possible signals for preferred earthquake propagation direction. Geophysical Journal International 173(2), 483–504. https://doi.org/10.1111/j.1365-246X.2008.03709.x

Dresen, G., Kwaitek, G., Goebel, T. Ben-Zion, Y., 2020. Seismic and aseismic preparatory processes before large stick–slip failure. Pure and Applied Geophysics 177, 5741–5760. https://doi.org/10.1007/s00024-020-02605-x

Drugan, W.J., 2001. Dynamic fragmentation of brittle materials: analytical mechanics-based models. Journal of the Mechanics and Physics of Solids 49(6), 1181–1208. https://doi.org/10.1016/S0022-5096(01)00002-3

Dunham, E.M., 2007. Conditions governing the occurrence of supershear ruptures under slip-weakening friction. Journal of Geophysical Research: Solid Earth 112, B07302. https://doi.org/10.1029/2006JB004717

Dunham, E.M., Archuleta, R.J., 2004. Evidence for a supershear transient during the 2002 Denali fault earthquake. Bulletin of the Seismological Society of America 94(6B), S256–S268. https://doi.org/10.1785/0120040616

Dunham, E.M., Belanger, D., Cong, L., Kozdon, J. E., 2011. Earthquake ruptures with strongly rate-weakening friction and off-fault plasticity, part 2: nonplanar faults. Bulletin of the Seismological Society of America 101(5), 2308–2322. https://doi.org/10.1785/0120100076

Edwards, M.A., Ratschbacher, L., 2005. Seismic and aseismic weakening effects in transtension: field and microstructural observations on the mechanics and architecture of a large fault zone in SE Tibet. Geological Society, London, Special Publications 245, 109–141. https://doi.org/10.1144/GSL.SP.2005.245.01.06

Engelder, J.T., 1974. Cataclasis and the generation of fault gouge. Geological Society of America Bulletin 85(10), 1515–1522. http://dx.doi.org/10.1130/0016-7606(1974)85<1515:CATGOF>2.0.CO;2

Enlow, R.L., Koons, P.O., 1998. Critical wedges in three dimensions: Analytical expressions from Mohr-Coulomb constrained perturbation analysis. Journal of Geophysical Research: Solid Earth.103(B3), 4897-4914. https://doi.org/10.1029/97JB03209

Erickson, B.A., Day, S.M., 2016. Bimaterial effects in an earthquake cycle model using rate-and-state friction. Journal of Geophysical Research: Solid Earth 121(4), 2480–2506. https://doi.org/10.1002/2015JB012470

Farris, D.W., Paterson, S.R., 2007. Contamination of silicic magmas and fractal fragmentation of xenoliths in Paleocene plutons on Kodiak Island, Alaska. The Canadian Mineralogist 45(1), 107–129. https://doi.org/10.2113/gscanmin.45.1.107

Fineberg, J., Gross, S.P., Marder, M., Swinney, H.L., 1992. Instability in the propagation of fast cracks. Physical Review B 45(10), 5146–5154. https://doi.org/10.1103/PhysRevB.45.5146

Fineberg, J., Marder, M., 1999. Instability in dynamic fracture. Physics Reports 313(1–2), 1–108. https://doi.org/10.1016/S0370-1573(98)00085-4

FLAC^{3D} (Fast Lagrangian Analysis of Continua in 3 Dimensions) User's Guide 2014. Version 5.1. Minneapolis, Minnesota: Itasca Consulting Group Inc.

Fondriest, M., Smith, S.A.F., Di Toro, G., Zampieri, D., Mittempergher, S., 2012. Fault zone structure and seismic slip localization in dolostones, an example from the Southern Alps, Italy. Journal of Structural Geology 45, 52–67. https://doi.org/10.1016/j.jsg.2012.06.014

Fountain, D.M., Salisbury, M.H., Percival, J., 1990. Seismic structure of the continental crust based on rock velocity measurements from the Kapuskasing Uplift. Journal of Geophysical Research: Solid Earth 95(B2), 1167–1186. https://doi.org/10.1029/JB095iB02p01167

Freund, L.B., 1990. Dynamic fracture mechanics. Cambridge University Press. https://doi.org/10.1017/CBO9780511546761

Friedman, M. 1963. Petrofabric analysis of experimentally deformed calcite-cemented sandstones. The Journal of Geology 71(1), 12–37. https://www.jstor.org/stable/30069361

Fujiwara, A., Kamimoto, G., Tsukamoto, A., 1977. Destruction of basaltic bodies by high-velocity impact. Icarus 31(2), 277–288. https://doi.org/10.1016/0019-1035(77)90038-0

Fulton, P.M., Brodsky, E.E., Kano, Y., Mori, J., Chester, F., Ishikawa, T., Harris, R.N., Lin, W. Eguchi, N., Toczko, S., Expedition 343, 343T, and KR13-08 Scientists, 2013. Low coseismic friction on the Tohoku-Oki fault determined from temperature measurements. Science 342(6163), 1214–1217. https://doi.org/10.1126/science.1243641

Gao, H., Huang, Y., Abraham, F.F., 2001. Continuum and atomistic studies of intersonic crack propagation. Journal of the Mechanics and Physics of Solids 49(9), 2113–2132. https://doi.org/10.1016/S0022-5096(01)00032-1

Genç, Ö., Ergün, L., Benzer, H., 2004. Single particle impact breakage characterization of materials by drop weight testing. Physicochemical Problems of Mineral Processing 38(1), 241–255.

Ghaffari, H.O., Griffith, W.A., Barber, T.J., 2019. Energy delocalization during dynamic rock fragmentation. Geophysical Journal International 217(2), 1034–1046. https://doi.org/10.1093/gji/ggz064

Gilvarry, J.J., 1961. Fracture of brittle solids. I. Distribution function for fragment size in single fracture (theoretical). Journal of Applied Physics vol. 32, p. 391–399. https://doi.org/10.1063/1.1736016

Glenn, L.A., Chudnovsky, A., 198). Strain-energy effects on dynamic fragmentation. Journal of Applied Physics 59(4), 1379–1380. https://doi.org/10.1063/1.336532

Godfrey, N.J., Christensen, N.I., Okaya, D.A., 2000. Anisotropy of schists: Contribution of crustal anisotropy to active source seismic experiments and shear wave splitting observations. Journal of Geophysical Research: Solid Earth 105(B12), 27991–28007. https://doi.org/10.1029/2000JB900286

Goebel, T.H.W., Candela, T., Sammis, C.G., Becker, T.W., Dresen, G., Schorlemmer, D., 2014. Seismic event distributions and off-fault damage during frictional sliding of saw-cut surfaces with pre-defined roughness. Geophysical Journal International,196(1), 612–625. https://doi.org/10.1093/gji/ggt401

Goldsby, D.L., Tullis, T.E., 2011. Flash heating leads to low frictional strength of crustal rocks at earthquake slip rates. Science 334(6053), 216–218. https://doi.org/10.1126/science.1207902

Goldstein, A., Hepburn, J.C., 1999. Possible correlations of the Norumbega fault system with faults in southeastern New England. In: Ludman, A., West, D.P., Jr. (Eds.), Norumbega fault system of the northern Appalachians, Geological Society of American Special Paper, vol. 331. Geological Society of America, pp. 73–83. https://doi.org/10.1130/0-8137-2331-0.73

Grady, D.E., 1982. Local inertial effects in dynamic fragmentation. Journal of Applied Physics 53(1), 322–325. https://doi.org/10.1063/1.329934

Grady, D.E., 1988. The spall strength of condensed matter. Journal of the Mechanics and Physics of Solids 36(3), 353–384. https://doi.org/10.1016/0022-5096(88)90015-4

Grady, D.E., 2006. Fragmentation of Rings and Shells. Springer. https://doi.org/10.1007/b138675

Grady, D.E., 2009. Dynamic fragmentation of solids. In: Horie, Y. (Ed.), Shock wave science and technology reference library, vol. 3. Springer, pp. 169–275. https://doi.org/10.1007/978-3-540-77080-0_4

Grady, D.E., 2010. Length scales and size distributions in dynamic fragmentation. International Journal of Fracture, 163(1–2), 85–99. https://doi.org/10.1007/s10704-009-9418-4

Grady, D.E., 2017. Physics of shock and impact: Volume 1. IOP Publishing. https://doi.org/10.1088/978-0-7503-1254-7

Grady, D.E., Kipp, M.E., 1987. Dynamic rock fragmentation. In: Atkinson, K. (Ed.), Fracture mechanics of rock. Academic Press, pp. 429–475.

Green II, H.W., Shi, F., Bozhilov, K., Xia, G., Reches, Z., 2015. Phase transformation and nanometric flow cause extreme weakening during fault slip. Nature Geoscience 8, 484–489. https://doi.org/10.1038/ngeo2436

Griffith, W.A., Nielsen, S., Di Toro, G., Smith, S.A.F., 2010. Rough faults, distributed weakening, and off-fault deformation. Journal of Geophyical Research: Solid Earth 115, B08409, https://doi.org/10.1029/2009JB006925

Griffith, W.A., Rosakis, A., Pollard, D.D., Ko, C.W., 2009. Dynamic rupture experiments elucidate tensile crack development during propagating earthquake ruptures. Geology 37(9), 795–798. https://doi.org/10.1130/G30064A.1

Griffith, W.A., St. Julien, R.C., Ghaffari, H.O., Barber, T.J., 2018. A tensile origin for fault rock pulverization. Journal of Geophysical Research: Solid Earth 123(8), 7055–7073. https://doi.org/10.1029/2018JB015786

Grover, T.W., Fernandes, L.C., 2003. Bedrock geology of the Weeks Mills quadrangle, Maine: Maine Geological Survey, Open-File Map 03-49, color map, scale 1:24000. Maine Geological Survey Maps 31. Retrieved from https://digitalmaine.com/mgs_maps/31

Guatteri, M., Spudich, P., Beroza, G. C., 2001. Inferring rate and state friction parameters from a rupture model of the 1995 Hyogo-ken Nanbu (Kobe) Japan earthquake. Journal of Geophysical Research: Solid Earth 106(B11), 26511–26521. https://doi.org/10.1029/2001JB000294

Hadizadeh, J., Johnson, W.K., 2003. Estimating local strain due to comminution in experimental cataclastic textures. Journal of Structural Geology 25(11), 1973–1979. https://doi.org/10.1016/S0191-8141(03)00016-6

Hagan, J.T., 1981. Impossibility of fragmenting small particles: brittle—ductile transition. Journal of Materials Science 16, 2909–2911. https://doi.org/10.1007/BF02402857

Hall, J.F., Heaton, T.H., Halling, M.W., Wald, D.J., 1995. Near-source ground motion and its effects on flexible buildings. Earthquake Spectra 11(4), 569–605. https://doi.org/10.1193/1.1585828

Han, S., Jung, H., 2021. Deformation microstructures of phyllite in Gunsan, Korea, and implications for seismic anisotropy in continental crust. Minerals 11(3), 294. https://doi.org/10.3390/min11030294

Handy, M.R., Hirth, G., Bürgmann, R., 2007. Continental fault ftructure and rheology from the frictional-to-viscous transition downward. In: Handy, M.R., Hirth, G., Hovius, N. (Eds.), Tectonic faults: Agents of change on a dynamic Earth. The MIT Press, pp. 139–182. https://doi.org/10.7551/mitpress/6703.003.0008

Hanks, T.C., Kanamori, H., 1979. A moment magnitude scale. Journal of Geophysical Research: Solid Earth 84(B5), 2348–2350. https://doi.org/10.1029/JB084iB05p02348

Hanson, C.R., Norris, R.J., Cooper, A.F., 1990. Regional fracture-patterns east of the Alpine Fault between the Fox and Franz Josef Glaciers, Westland, New Zealand. New Zealand Journal of Geology and Geophysics 33(4), 617–622. https://doi.org/10.1080/00288306.1990.10421379

Harper, C.A., 2001. Handbook of Ceramics, Glasses and Diamonds. McGraw-Hill Professional.

Harris, R.A., Day, S.M., 1997. Effects of a low-velocity zone on a dynamic rupture. Bulletin of the Seismological Society of America 87(5), 1267–1280.

Harris, R.A., Day, S.M., 2005. Material contrast does not predict earthquake rupture propagation direction. Geophysical Research Letters 32(23), L23301. https://doi.org/10.1029/2005GL023941

Hawemann, F., Mancktelow, N., Wex, S., Pennacchioni, G., Camacho, A., 2019. Fracturing and crystal plastic behaviour of garnet under seismic stress in the dry lower continental crust (Musgrave Ranges, Central Australia). Solid Earth 10(5), 1635–1649. https://doi.org/10.5194/se-10-1635-2019

Hearmon, R.F.S., 1979. The elastic constants of crystals and other anisotropic materials. In: Hellwege, K.-H., Hellwege, A.M. (Eds.), Landolt-Börnstein tables, group III, vol. 11. Springer-Verlag, pp. 1–244.

Heaton, T.H., 1990. Evidence for and implications of self-healing pulses of slip in earthquake rupture. Physics of the Earth and Planetary Interiors 64(1), 1–20. https://doi.org/10.1016/0031-9201(90)90002-F

Heidrick, T.L., Titley, S.R., 1982. Fracture and dike patterns in Laramide plutons and their structural and tectonic implications. In: Titley, S.R. (Eds.), Advances in geology of the porphyry copper deposits, southwestern United States. University of Arizona Press, pp. 73–92.

Heilbronner, R., Keulen, N., 2006. Grain size and grain shape analysis of fault rocks. Tectonophysics 427(1–4), 199–216. http://dx.doi.org/10.1016/j.tecto.2006.05.020

Hill, R., 1952. The elastic behaviour of a crystalline aggregate, Proceedings of the Physical Society Section A 65(5), 349–354. https://doi.org/10.1088/0370-1298/65/5/307

Hirose, T., Shimamoto, T., 2005. Growth of molten zone as a mechanism of slip weakening of simulated faults in gabbro during frictional melting. Journal of Geophysical Research: Solid Earth 110, B05202. https://doi.org/10.1029/2004JB003207

Hoek, E. Martin, C.D., 2014. Fracture initiation and propagation in intact rock – a review. Journal of Rock Mechanics and Geotechnical Engineering 6(4), 287–300. https://doi.org/10.1016/j.jrmge.2014.06.001

Hogan, J.D., Rogers, R.J., Spray, J.G., Boonsue, S., 2012. Dynamic fragmentation of granite for impact energies of 6–28J. Engineering Fracture Mechanics 79, 103–125. https://doi.org/10.1016/j.engfracmech.2011.10.006

Hogan, J.D., Farbaniec, L., Shaeffer, M., Ramesh, K.T., 2015. The effects of microstructure and confinement on the compressive fragmentation of an advanced ceramic. Journal of the American Ceramic Society 98(3), 902–912. https://doi.org/10.1111/jace.13353

Hogan, J.D., Farbaniec, L., Daphalapurkar, N., Ramesh, K.T., 2016. On compressive brittle fragmentation. Journal of the American Ceramic Society 99(6), 2159–2169. https://doi.org/10.1111/jace.14171

Hossain, M.D.S., Kruhl, J.H., 2015. Fractal geometry-based quantification of shock-induced rock fragmentation in and around an impact crater. Pure and Applied Geophysics 172, 2009–2023. https://doi.org/10.1007/s00024-014-0922-8

Hou, T.-x., Xu, Q., Zhou, J.-w., 2015. Size distribution, morphology and fractal characteristics of brittle rock fragmentations by the impact loading effect. Acta Mechanica 226, 3623–3637. https://doi.org/10.1007/s00707-015-1409-0

Howarth, J.D., Fitzsimons, S.J., Norris, R.J., Jacobsen, G.E., 2012. Lake sediments record cycles of sediment flux driven by large earthquakes on the Alpine fault, New Zealand. Geology 40(12), 1091–1094. https://doi.org/10.1130/G33486.1

Howarth, J.D., Fitzsimons, S.J., Norris, R.J., Langridge, R., Vandergoes, M.J., 2016. A 2000 yr rupture history for the Alpine fault derived from Lake Ellery, South Island, New Zealand. Geological Society of America Bulletin 128(3–4), 627–643. https://doi.org/10.1130/B31300.1

Huang, Y., Ampuero, J.-P., Helmberger, D.V, 2014a. Earthquake ruptures modulated by waves in damaged fault zones. Journal of Geophysical Research: Solid Earth 119(4), 3133–3154. https://doi.org/10.1002/2013JB010724

Huang, Y., Ampuero, J.-P., Helmberger, D.V., 2016. The potential for supershear earthquakes in damaged fault zones – theory and observations. Earth and Planetary Science Letters 433, 109–115. https://doi.org/10.1016/j.epsl.2015.10.046

Huang, Y., Ampuero, J.-P., Kanamori, H., 2014b. Slip-weakening models of the 2011 Tohoku-Oki earthquake and constraints on stress drop and fracture energy. Pure and Applied Geophysics 171(10), 2555–2568. https://doi.org/10.1007/s00024-013-0718-2

Hubbard, M.S., 1999. Norumbega fault zone: Part of an orogen-parallel strike-slip system, northern Appalachians. In: Ludman, A., West, D.P., Jr. (Eds.), Norumbega fault system of the northern Appalachians, Geological Society of America Special Paper, vol. 331. Geological Society of America, pp. 155–165. https://doi.org/10.1130/0-8137-2331-0.155

Humphreys, F.J., 2001. Grain and subgrain characterisation by electron backscatter diffraction. Journal of Materials Science 36, 3833–3854.

Hurich, C.A., Deemer, S.J., Indares, A., Salisbury, M., 2001. Compositional and metamorphic controls on velocity and reflectivity in the continental crust: An example from the Grenville Province of eastern Québec. Journal of Geophysical Research: Solid Earth 106(B1), 665–682. https://doi.org/10.1029/2000JB900244

Husseini, M. I., Jovanovich, D.B., Randall, M.J., Freund, L.B., 1975. The fracture energy of earthquakes. Geophysical Journal International 43(2), 367–385. https://doi.org/10.1111/j.1365-246X.1975.tb00640.x

Hussey, A.M., II, 1988. Lithotectonic stratigraphy, deformation, plutonism, and metamorphism, greater Casco Bay region, southwestern Maine. In: Tucker, R.D., Marvinney, R.G. (Eds.), Studies in Maine geology: Volume 1—structure and stratigraphy. Maine Geological Survey, pp. 17–34. http://digitalmaine.com/mgs_publications/47

Hussey, A.M., II, Bothner, W.A., Thomson, J.A., 1986. Geological comparisons across the Norumbega Fault Zone, southwestern Maine. In: Newburg, D.W. (Ed.), Guidebook for field trips in southwestern Maine: New England Intercollegiate Geological Conference, pp. 53–78. https://scholars.unh.edu/neigc_trips/390

Ide, S., 2003. Fracture surface energy of natural earthquakes from the viewpoint of seismic observations. Bulletin Earthquake Research Institute 78(1), 59–65.

Incel, S., Schubnel, A., Renner, J., John, T., Labrousse, L., Hilairet, N., Freeman, H., Wang, Y., Renard, F., Jamtveit, B., 2019. Experimental evidence for wall-rock pulverization during dynamic rupture at ultra-high pressure conditions. Earth and Planetary Science Letters 528, 115832. https://doi.org/10.1016/j.epsl.2019.115832

Ishii, T., Matsushita, M., 1992. Fragmentation of long thin glass rods. Journal of the Physical Society of Japan 61(10), 3474–3477. https://doi.org/10.1143/JPSJ.61.3474

Jamtveit, B., Petley-Ragan, A., Incel, S., Dunkel, K.G., Aupart, C., Austrheim, H., Corfu, F., Menegon, L., Renard, F., 2019. The effects of earthquakes and fluids on the metamorphism of the lower continental crust. Journal of Geophysical Research: Solid Earth 124(8), 7725–7755. https://doi.org/10.1029/2018JB016461

Jébrak, M., 1997. Hydrothermal breccias in vein-type ore deposits: A review of mechanisms, morphology and size distribution. Ore Geology Reviews 12(3), 111–134. https://doi.org/10.1016/S0169-1368(97)00009-7

Jefferies, S.P., Holdsworth, R.E., Wibberley, C.A.J., Shimamoto, T., Spiers, C.J., Niemeijer, A.R., Lloyd, G.E., 2006. The nature and importance of phyllonite development in crustal-scale fault cores: An example from the Median Tectonic Line, Japan. Journal of Structural Geology 28(2), 220–235. https://doi.org/10.1016/j.jsg.2005.10.008

Ji, C., Helmberger, D.V, Wald, D.J., Ma, K.-F., 2003. Slip history and dynamic implications of the 1999 Chi-Chi, Taiwan, earthquake. Journal of Geophysical Research: Solid Earth 108(B9), 2412. https://doi.org/10.1029/2002JB001764

Ji, S., Long, C., Martignole, J., Salisbury, M.H., 1997a. Seismic reflectivity of a finely layered, granulite-facies ductile shear zone in the southern Grenville Province (Quebec). Tectonophysics 279(1–4), 113–133. https://doi.org/10.1016/S0040-1951(97)00133-9

Ji, S., Salisbury, M.H., 1993. Shear-wave velocities, anisotropy and splitting in high-grade mylonites. Tectonophysics 221(3–4), 453–473. https://doi.org/10.1016/0040-1951(93)90173-H

Ji, S., Salisbury, M.H., Hanmer, S., 1993. Petrofabric, P-wave anisotropy and seismic reflectivity of high-grade tectonites. Tectonophysics 222(2), 195–226. https://doi.org/10.1016/0040-1951(93)90049-P

Ji, S., Shao, T., Michibayashi, K., Oya, S., Satsukawa, T., Wang, Q., Zhao, W., Salisbury, M.H., 2015. Magnitude and symmetry of seismic anisotropy in mica- and amphibole-bearing metamorphic rocks and implications for tectonic interpretation of seismic data from the southeast Tibetan Plateau. Journal of Geophysical Research: Solid Earth 120(9), 6404–6430. https://doi.org/10.1002/2015JB012209

Ji, S., Wang, Q., Marcotte, D., Salisbury, M.H., Xu, Z., 2007. P wave velocities, anisotropy and hysteresis in ultrahigh-pressure metamorphic rocks as a function of confining pressure. Journal of Geophysical Research: Solid Earth 112(B9), B09204. https://doi.org/10.1029/2006JB004867

Ji, S., Zhao, P., Saruwatari, K., 1997b. Fracturing of garnet crystals in anisotropic metamorphic rocks during uplift. Journal of Structural Geology 19(5), 603–620. https://doi.org/10.1016/S0191-8141(97)00006-0

Jiang, F., Speziale, S., Duffy, T. S., 2004. Single-crystal elasticity of grossular- and almandine-rich garnets to 11 GPa by Brillouin scattering. Journal of Geophysical Research: Solid Earth 109(B10), B10210. https://doi.org/10.1029/2004JB003081

Jiang, W., Cheng, X., Xiong, Z., Ma, Z., Ali, T., Cai, H., Zhang, J., 2019. Static and dynamic mechanical properties of Yttrium Aluminum Garnet (YAG). Ceramics International 45(9), 12256–12263. https://doi.org/10.1016/j.ceramint.2019.03.136

Johnson, A.M., Fleming, R.W., Cruikshank, K.M., 1994. Shear zones formed along long, straight traces of fault zones during the 28 June 1992 Landers, California, earthquake. Bulletin of the Seismological Society of America 84(3), 499–510.

Johnson, S.E., 2015. Microstructural evidence for repeated cycles of coseismic damage and viscous flow at the frictional to viscous transition in an ancient strike-slip fault. In: Mukherjee, S. (Ed.), Atlas of structural geology. Elsevier, pp. 141–142.

Johnson, S.E., Lenferink, H.J., Price, N.A., Marsh, J.H., Koons, P.O., West, D.P., Jr., Beane, R., 2009. Clast-based kinematic vorticity gauges: The effects of slip at matrix/clast interfaces. Journal of Structural Geology 31(11), 1322–1339. https://doi.org/10.1016/j.jsg.2009.07.008

Johnson, S.E., Song, W.J., Cook, A.C., Vel, S.S., Gerbi, C.C., 2021a. The quartz α↔β phase transition: Does it drive damage and reaction in continental crust? Earth and Planetary Science Letters 553, 116622. https://doi.org/10.1016/j.epsl.2020.116622

Johnson, S.E., Song, W.J., Vel, S.S., Song, B.R., Gerbi, C.C., 2021b. Energy partitioning, dynamic fragmentation, and off-fault damage in the earthquake source volume. Journal of Geophysical Research: Solid Earth 126(11), e2021JB022616. https://doi.org/10.1029/2021JB022616

Jones, T.D., Nur, A., 1982. Seismic velocity and anisotropy in mylonites and the reflectivity of deep crustal fault zones. Geology 10(5), 260–263. https://doi.org/10.1130/0091-7613(1982)10<260:SVAAIM>2.0.CO;2

Jones, T.D., Nur, A., 1984. The nature of seismic reflections from deep crustal fault zones. Journal of Geophysical Research: Solid Earth 89(B5), 3153–3171. https://doi.org/10.1029/JB089iB05p03153

Julian, B.R., Miller, A.D., Foulger, G.R., 1998. Non-double-couple earthquakes 1. Theory. Reviews of Geophysics 36(4), 525–549. https://doi.org/10.1029/98RG00716

Kalkan, E., Kunnath, S.K., 2006. Effects of fling step and forward directivity on seismic response of buildings. Earthquake Spectra 22(2), 367–390. https://doi.org/10.1193/1.2192560

Kaminski, E., Jaupart, C., 1998. The size distribution of pyroclasts and the fragmentation sequence in explosive volcanic eruptions. Journal of Geophysical Research: Solid Earth 103(B12), 29759–29779. https://doi.org/10.1029/98JB02795

Kanamori, H., 1994. Mechanics of earthquakes. Annual Review of Earth and Planetary Sciences 22(1), 207–237. https://doi.org/10.1146/annurev.earth.22.1.207

Kanamori, H., Brodsky, E. E., 2004. The physics of earthquakes. Reports on Progress in Physics 67(8), 1429–1496. https://doi.org/10.1088/0034-4885/67/8/R03

Kanamori, H., Rivera, L., 2006. Energy partitioning during an earthquake. In: Abercrombie, R., McGarr, A., Di Toro, G., Kanamori, H. (Eds.), Earthquakes: radiated energy and the physics of faulting, Geophysical Monograph Series, vol. 170. American Geophysical Union, pp. 3–13. https://doi.org/10.1029/170GM22

Kästner, F., Pierdominici, S., Zappone, A., Morales, L.F.G., Schleicher, A.M., Wilke, F.D.H., Berndt, C., 2021. Cross-scale seismic anisotropy analysis in metamorphic rocks from the COSC-1 borehole in the Scandinavian Caledonides. Journal of Geophysical Research: Solid Earth 126(5), e2020JB021154. https://doi.org/10.1029/2020JB021154

Kern, H., Gao, S., Jin, Z., Popp, T., Jin, S., 1999. Petrophysical studies on rocks from the Dabie ultrahigh-pressure (UHP) metamorphic belt, Central China: Implications for the composition and delamination of the lower crust. Tectonophysics 301(3–4), 191–215. https://doi.org/10.1016/S0040-1951(98)00268-6

Kern, H., Gao, S., Liu, Q.-S., 1996. Seismic properties and densities of middle and lower crustal rocks exposed along the North China Geoscience Transect. Earth and Planetary Science Letters 139(3–4), 439–455. https://doi.org/10.1016/0012-821X(95)00240-D

Kern, H., Ivankina, T.I., Nikitin, A.N., Lokajíček, T., Pros, Z., 2008. The effect of oriented microcracks and crystallographic and shape preferred orientation on bulk elastic anisotropy of a foliated biotite gneiss from Outokumpu. Tectonophysics 457(3–4), 143–149. https://doi.org/10.1016/j.tecto.2008.06.015

Kern, H., Mengel, K., Strauss, K.W., Ivankina, T.I., Nikitin, A.N., Kukkonen, I.T., 2009. Elastic wave velocities, chemistry and modal mineralogy of crustal rocks sampled by the Outokumpu scientific drill hole: Evidence from lab measurements and modeling. Physics of the Earth and Planetary Interiors 175(3–4), 151–166. https://doi.org/10.1016/j.pepi.2009.03.009

Kern, H., Popp, T., Gorbatsevich, F., Zharikov, A., Lobanov, K.V, Smirnov, Y.P., 2001. Pressure and temperature dependence of V_P and V_S in rocks from the superdeep well and from surface analogues at Kola and the nature of velocity anisotropy. Tectonophysics 338(2), 113–134. https://doi.org/10.1016/S0040-1951(01)00128-7

Kern, H., Wenk, H.-R., 1990. Fabric-related velocity anisotropy and shear wave splitting in rocks from the Santa Rosa Mylonite Zone, California. Journal of Geophysical Research: Solid Earth 95(B7), 11213–11223. https://doi.org/10.1029/JB095iB07p11213

Keulen, N., Heilbronner, R., Stünitz, H., Boullier, A.-M., Ito, H., 2007. Grain size distributions of fault rocks: A comparison between experimentally and naturally deformed granitoids. Journal of Structural Geology 29(8), 1282–1300. https://doi.org/10.1016/j.jsg.2007.04.003

Keulen, N., Stünitz, H., Heilbronner, R., 2008. Healing microstructures of experimental and natural fault gouge. Journal of Geophysical Research: Solid Earth 113, B06205. https://doi.org/10.1029/2007JB005039

Key, W.R.O., Schultz, R.A., 2011. Fault formation in porous sedimentary rocks at high strain rates: first results from the Upheaval Dome impact structure, Utah, USA. Geological Society of America Bulletin 123(5–6), 1161–1170. https://doi.org/10.1130/B30087.1

Khazanehdari, J., Rutter, E.H., Brodie, K.H., 2000. High-pressure-high-temperature seismic velocity structure of the midcrustal and lower crustal rocks of the Ivrea-Verbano zone and Serie dei Laghi, NW Italy. Journal of Geophysical Research: Solid Earth 105(B6), 13843–13858. https://doi.org/10.1029/2000JB900025

Kolzenburg, S., Russell, J. K., Kennedy, L.A., 2013. Energetics of glass fragmentation: Experiments on synthetic and natural glasses. Geochemistry, Geophysics, Geosystems 14(11), 4936–4951. https://doi.org/10.1002/2013GC004819

Koons, P.O., 1987. Some thermal and mechanical consequences of rapid uplift: an example from the Southern Alps, New Zealand. Earth and Planetary Science Letters 86(2–4), 307–319. https://doi.org/10.1016/0012-821X(87)90228-7

Koons, P.O., 1994. Three-dimensional critical wedges: tectonics and topography in oblique collisional orogens. Journal of Geophysical Research: Solid Earth 99(B6), 12301–12315. https://doi.org/10.1029/94JB00611

Koons P.O., Kirby E., 2007. Topography, Denudation, and Deformation. The Role of Surface Processes in Fault Evolution. In: Handy, M.R., Hirth, G., Hovius, N. (Eds.), Tectonic faults: Agents of change on a dynamic Earth. The MIT Press, pp. 205–230. https://doi.org/10.7551/mitpress/6703.003.0010

Koons P.O., Norris R.J., Craw D., Cooper A.F., 2003. Influence of exhumation of the structural evolution of transpressional plate boundaries: An example from the Southern Alps, New Zealand. Geology 31(1), 3–6. https://doi.org/10.1130/0091-7613(2003)031<0003:IOEOTS>2.0.CO;2

Koons, P.O., Upton, P., Barker, A.D., 2012. The influence of mechanical properties on the link between tectonic and topographic evolution. Geomorphology 29(1), 168–180. https://doi.org/10.1016/j.geomorph.2010.11.012

Kostrov, B.V., Das, S., 1988. Principles of earthquake source mechanics. Cambridge University Press.

Kostrov, V.V., 1974. Seismic moment and energy of earthquakes, and seismic flow of rock. Izvestiya, Physics of the Solid Earth 10(1), 23–40.

Kozdon, J.E., Dunham, E.M., 2013. Rupture to the trench: Dynamic rupture simulations of the 11 March 2011 Tohoku earthquake. Bulletin of the Seismological Society of America 103(2B), 1275–1289. https://doi.org/10.1785/0120120136

Kueppers, U., Perugini, D., Dingwell, D.B., 2006. “Explosive energy” during volcanic eruptions from fractal analysis of pyroclasts. Earth and Planetary Science Letters 248(3–4), 800–807. https://doi.org/10.1016/j.epsl.2006.06.033

Lachenbruch, A.H., McGarr, A., 1990. Stress and heat flow. In: Wallace, R.E. (Ed.), The San Andreas fault system, California. U.S. Geological Survey Professional Paper 1515, pp. 261–277.

Lambert, V., Lapusta, N., 2020. Rupture-dependent breakdown energy in fault models with thermo-hydro-mechanical processes. Solid Earth 11(6), 2283–2302. https://doi.org/10.5194/se-11-2283-2020

Lan, H., Chen, J., Macciotta, R., 2019. Universal confined tensile strength of intact rock. Scientific Reports 9, 6170. https://doi.org/10.1038/s41598-019-42698-6

Lancieri, M., Madariaga, R., Bonilla, F., 2012. Spectral scaling of the aftershocks of the Tocopilla 2007 earthquake in northern Chile. Geophysical Journal International 189(1), 469–480. https://doi.org/10.1111/j.1365-246X.2011.05327.x

Lange, M.A., Ahrens, T.J., Boslough, M.B., 1984. Impact cratering and spall failure of gabbro. Icarus 58(3), 383–395. https://doi.org/10.1016/0019-1035(84)90084-8

Langridge, R.M., Ries, W.F., Farrier, T., Barth, N.C., Khajavi, N., De Pascale, G.P., 2014. Developing sub 5-m LiDAR DEMs for forested sections of the Alpine and Hope faults, South Island, New Zealand: Implications for structural interpretations. Journal of Structural Geology 64, 53–66. https://doi.org/10.1016/j.jsg.2013.11.007

Langridge, R.M., Ries, W.F., Litchfield, N.J., Villamor, P., Van Dissen, R.J., Barrell, D.J.A., Rattenbury, M.S., Heron, D.W., Haubrock, S., Townsend, D.B., Lee, J.M., Berryman, K.R., Nicol, A., Cox, S.C., Stirling, M.W., 2016. The New Zealand Active Faults Database. New Zealand Journal of Geology and Geophysics 59(1), 86–96. https://doi.org/10.1080/00288306.2015.1112818

Levy, S., Molinari, J. F., 2010. Dynamic fragmentation of ceramics, signature of defects and scaling of fragment sizes. Journal of the Mechanics and Physics of Solids 58(1), 12–26. https://doi.org/10.1016/j.jmps.2009.09.002

Lewis, M.A., Ben-Zion, Y., 2010. Diversity of fault zone damage and trapping structures in the Parkfield section of the San Andreas Fault from comprehensive analysis of near fault seismograms. Geophysical Journal International 183(3), 1579–1595. https://doi.org/10.1111/j.1365-246X.2010.04816.x

Li, V.C., 1987. Mechanics of shear rupture applied to earthquake zones. In: Atkinson, B.K. (Ed.), Fracture mechanics of Rock. Academic Press, pp. 351–428. https://doi.org/10.1016/B978-0-12-066266-1.50014-4

Li, X., Yao, W., Wang, C., 2021. The influence of multiple dynamic loading on fragmentation characteristics in dynamic compression tests. Rock Mechanics and Rock Engineering 54, 1583–1596. https://doi.org/10.1007/s00603-020-02324-8

Li, Y.-G., Chen, P., Cochran, E.S., Vidale, J.E., Burdette, T., 2006. Seismic evidence for rock damage and healing on the San Andreas fault associated with the 2004 M 6.0 Parkfield earthquake. Bulletin of the Seismological Society of America 96(4B), S349–S363. https://doi.org/10.1785/0120050803

Li, Y.-G., De Pascale, G.P., Quigley, M.C., Gravley, D.M., 2014a. Fault damage zones of the M7.1 Darfield and M6.3 Christchurch earthquakes characterized by fault-zone trapped waves. Tectonophysics 618, 79–101. https://doi.org/10.1016/j.tecto.2014.01.029

Li, Y.-G., Vernon, F.L., 2001. Characterization of the San Jacinto fault zone near Anza, California, by fault zone trapped waves. Journal of Geophysical Research: Solid Earth 106(B12), 30671–30688. https://doi.org/10.1029/2000JB000107

Li, Z., Zhang, H., Peng, Z., 2014b. Structure-controlled seismic anisotropy along the Karadere-Düzce branch of the North Anatolian Fault revealed by shear-wave splitting tomography. Earth and Planetary Science Letters 391, 319–326. https://doi.org/10.1016/j.epsl.2014.01.046

Lienau, C.C., 1936. Random fracture of a brittle solid. Journal of the Franklin Institute 221(5), 673–686. https://doi.org/10.1016/S0016-0032(36)91108-0

Lin, A., Yamashita, K., 2013. Spatial variations in damage zone width along strike-slip faults: An example from active faults in southwest Japan. Journal of Structural Geology 57, 1–15. https://doi.org/10.1016/j.jsg.2013.10.006

Liu, C., Bizzarri, A., Das, S., 2014. Progression of spontaneous in-plane shear faults from sub-Rayleigh to compressional wave rupture speeds. Journal of Geophysical Research: Solid Earth 119(11), 8331–8345. https://doi.org/10.1002/2014JB011187

Liu, K., Zhao, J., 2021. Progressive damage behaviours of triaxially confined rocks under multiple dynamic loads. Rock Mechanics and Rock Engineering 54, 3327-3358. https://doi.org/10.1007/s00603-021-02408-z

Lloyd, G.E., Butler, R.W.H., Casey, M., Mainprice, D., 2009. Mica, deformation fabrics and the seismic properties of the continental crust. Earth and Planetary Science Letters 288(1–2), 320–328. https://doi.org/10.1016/j.epsl.2009.09.035

Lockner, D.A., Okubo, P.G., 1983. Measurements of frictional heating in granite. Journal of Geophysical Research: Solid Earth 88(B5), 4313– 4320. https://doi.org/10.1029/JB088iB05p04313

Lockner, D.A., Walsh, J.B., Byerlee, J.D., 1977. Changes in seismic velocity and attenuation during deformation of granite. Journal of Geophysical Research: Solid Earth and Planets 82(33), 5374–5378. https://doi.org/10.1029/jb082i033p05374

Long, C., 1994. Seismic nature of middle continental crust: Comparison of laboratory velocity and LITHOPROBE seismic reflection and refraction data from the Britt Domain, southwestern Grenville Province, Canada (Doctoral dissertation). Dalhousie University. Retrieved from http://hdl.handle.net/10222/55018

Long, C., Salisbury, M.H., 1996. The velocity structure of the Britt Domain, southwestern Grenville Province, from laboratory and refraction experiments. Canadian Journal of Earth Sciences 33(5), 729–745. https://doi.org/10.1139/e96-056

Lu, Y., Ben-Zion, Y., 2022. Regional seismic velocity changes following the 2019 M_w7.1 Ridgecrest, California earthquake from autocorrelations and P/S converted waves. Geophysical Journal International 228(1), 620-630, https://doi.org/10.1093/gji/ggab350

Ludman, A., 1998. Evolution of a transcurrent fault system in shallow crustal metasedimentary rocks: The Norumbega fault zone, eastern Maine. Journal of Structural Geology 20(1), 93–107. https://doi.org/10.1016/S0191-8141(97)00094-1

Ludman, A., Lanzirotti, A., Lux, D., Wang, C., 1999. Constraints on timing and displacement of multistage shearing in the Norumbega fault system, eastern Maine. In: Ludman, A., West, D.P., Jr. (Eds.), Norumbega fault system of the northern Appalachians, Geological Society of American Special Paper, vol. 331. Geological Society of America, pp. 179–194. https://doi.org/10.1130/0-8137-2331-0.179

Ludman, A., West, D.P., Jr., 1999. Norumbega Fault System of the Northern Appalachians. Geological Society of America Special Paper 331. https://doi.org/https://doi.org/10.1130/SPE331

Ma, K.-F., Tanaka, H., Song, S.-R., Wang, C.-Y., Hung, J.-H., Tsai, Y.-B., Mori, J., Song, Y.-F., Yeh, E.-C., Soh, W., Sone, H., Kuo, L.-W., Wu, H.-Y., 2006. Slip zone and energetics of a large earthquake from the Taiwan Chelungpu-fault Drilling Project. Nature 444(7118), 473–476. https://doi.org/10.1038/nature05253

Ma, X., Elbanna, A.E., 2015. Effect of off-fault low-velocity elastic inclusions on supershear rupture dynamics. Geophysical Journal International 203(1), 664–677. https://doi.org/10.1093/gji/ggv302

Mainprice, D., Casey, M., 1990. The calculated seismic properties of quartz mylonites with typical fabrics: Relationship to kinematics and temperature. Geophysical Journal International 103(3), 599–608. https://doi.org/10.1111/J.1365-246X.1990.TB05674.X

Madariaga, R., 1977. High-frequency radiation from crack (stress drop) models of earthquake faulting. Geophysical Journal International 51(3), 625–651. https://doi.org/10.1111/j.1365-246X.1977.tb04211.x

Malagnini, L., Munafo', I., Cocco, M., Nielsen, S., Mayeda, K., Boschi, E., 2014. Gradual fault weakening with seismic slip: Inferences from the seismic sequences of L'Aquila, 2009, and Northridge, 1994. Pure and Applied Geophysics 171(10), 2709–2730. https://doi.org/10.1007/s00024-013-0752-0

Mandelbrot, B.B., 1982. The fractal geometry of nature. W. H. Freeman and Company.

Manghnani, M.H., Ramananantoandro, R., Clark, S.P., 1974. Compressional and shear wave velocities in granulite facies rocks and eclogites to 10 kbar. Journal of Geophysical Research: Solid Earth and Planets 79(35), 5427–5446. https://doi.org/10.1029/JB079i035p05427

Mardon, D., Kronenberg, A. K., Handin, J., Friedman, M., Russell, J. E., 1990. Mechanisms of fracture propagation in experimentally extended Sioux quartzite. Tectonophysics 182(3–4), 259–278. https://doi.org/10.1016/0040-1951(90)90167-7

Marone, C., Scholz, C., 1989. Particle-size distribution and microstructures within simulated gouge. Journal of Structural Geology 11(7), 799–814. https://doi.org/10.1016/0191-8141(89)90099-0

Matsui, T., Waza, T., Kani, K., Suzuki, S., 1982. Laboratory simulation of planetesimal collision. Journal of Geophysical Research: Solid Earth 87(B13), 10968–10982. https://doi.org/10.1029/JB087iB13p10968

Matsumoto, H., Yamanaka, C., Ikeya, M., 2001. ESR analysis of the Nojima fault gouge, Japan, from the DPRI 500 m borehole. Island Arc 10(3–4), 479–485. https://doi.org/10.1046/j.1440-1738.2001.00346.x

Mazzoli, C. , Sassi, R., Burlini, L., 2002. Experimental study of the seismic properties of the Eastern Alps (Italy) along the Aurina–Tures–Badia Valleys transect. Tectonophysics 354(3–4), 179–194. https://doi.org/10.1016/S0040-1951(02)00294-9

Mauldon, M., Dunne, W.M., Rohrbaugh Jr., M.B., 2001. Circular scanlines and circular windows: new tools for characterizing the geometry of fracture traces. Journal of Structural Geology 23(2–3), 247–258. http://dx.doi.org/10.1016/S0191-8141(00)00094-8

McCaffrey, R., 1992. Oblique plate convergence, slip vectors, and forearc deformation. Journal of Geophysical Research: Solid Earth 97(B6), 8905–8915. https://doi.org/10.1029/92JB00483

McCaffrey, R., 1996. Slip partitioning at convergent plate boundaries of SE Asia. Geological Society, London, Special Publications 106(1), 3–18. https://doi.org/10.1144/GSL.SP.1996.106.01.02

McDonough, D.T., Fountain, D.M., 1988. Reflection characteristics of a mylonite zone based on compressional wave velocities of rock samples. Geophysical Journal International 93(3), 547–558. https://doi.org/10.1111/j.1365-246X.1988.tb03880.x

McDonough, D.T., Fountain, D.M., 1993. P-wave anisotropy of mylonitic and infrastructural rocks from a Cordilleran core complex: The Ruby-East Humboldt Range, Nevada. Physics of the Earth and Planetary Interiors 78(3–4), 319–336. https://doi.org/10.1016/0031-9201(93)90163-4

McGarr, A., 1999. On relating apparent stress to the stress causing earthquake fault slip. Journal of Geophysical Research: Solid Earth 104(B2), 3003–3011. https://doi.org/10.1029/1998JB900083

McGarr, A., Spottiswoode, S.M., Gay, N.C., Ortlepp, W.D., 1979. Observations relevant to seismic driving stress, stress drop, and efficiency. Journal of Geophysical Research: Solid Earth 84(B5), 2251– 2261. https://doi.org/10.1029/JB084iB05p02251

Mckay, M.B., Erickson, B.A., Kozdon, J.E., 2019. A computational method for earthquake cycles within anisotropic media. Geophysical Journal International 219(2), 816–833. https://doi.org/10.1093/gji/ggz320

Meyer, G.G., Brantut, N., Mitchell, T.M., Meredith, P.G., Plümper, O., 2021. Time dependent mechanical crack closure as a potential rapid source of post-seismic wave speed recovery: Insights from experiments in Carrara marble. Journal of Geophysical Research: Solid Earth 126(4), e2020JB021301. https://doi.org/10.1029/2020JB021301

Milliner, C.W.D., Dolan, J.F., Hollingsworth, J., Leprince, S., Ayoub, F., Sammis, C. G., 2015. Quantifying near-field and off-fault deformation patterns of the 1992 Mw 7.3 Landers earthquake. Geochemistry, Geophysics, Geosystems 16(5), 1577–1598. https://doi.org/10.1002/2014GC005693

Mitchell, T.M., Ben-Zion, Y., Shimamoto, T., 2011. Pulverized fault rocks and damage asymmetry along the Arima-Takatsuki Tectonic Line, Japan. Earth and Planetary Science Letters 308(3–4), 284–297. https://doi.org/10.1016/j.epsl.2011.04.023

Mitchell, T.M., Faulkner, D.R., 2008. Experimental measurements of permeability evolution during triaxial compression of initially intact crystalline rocks and implications for fluid flow in fault zones. Journal of Geophysical Research: Solid Earth 113(B11), B11412. https://doi.org/10.1029/2008JB005588

Mitchell, T.M., Faulkner, D.R., 2012. Towards quantifying the matrix permeability of fault damage zones in low porosity rocks. Earth and Planetary Science Letters 339–340, 24–31. https://doi.org/10.1016/j.epsl.2012.05.014

Monzawa, N., Otsuki, K., 2003. Comminution and fluidization of granular fault materials: implications for fault slip behavior. Tectonophysics 367(1–2), 127–143. https://doi.org/10.1016/S0040-1951(03)00133-1

Mooney, W.D., Christensen, N.I., 1994. Composition of the crust beneath the Kenya rift. Tectonophysics 236(1–4), 391–408. https://doi.org/10.1016/0040-1951(94)90186-4

Morton, N., Girty, G.H., Rockwell, T.K., 2012. Fault zone architecture of the San Jacinto fault zone in Horse Canyon, southern California: A model for focused post-seismic fluid flow and heat transfer in the shallow crust. Earth and Planetary Science Letters 329–330, 71–83. https://doi.org/10.1016/j.epsl.2012.02.013

Muto, J., Nakatani, T., Nishikawa, O., Nagahama, H., 2015. Fractal particle size distribution of pulverized fault rocks as a function of distance from the fault core. Geophysical Research Letters 42(10), 3811–3819. https://doi.org/10.1002/2015GL064026

Nagahama, H., Yoshii, K., 1994. Scaling laws of fragmentation. In: Kruhl, J.H. (Ed.), Fractals and dynamic systems in geoscience. Springer, pp. 25–36. https://doi.org/10.1007/978-3-662-07304-9_2

Naus-Thijssen, F.M.J., Goupee, A.J., Johnson, S.E., Vel, S.S., Gerbi, C., 2011a. The influence of crenulation cleavage development on the bulk elastic and seismic properties of phyllosilicate-rich rocks. Earth and Planetary Science Letters 311(3–4), 212–224. https://doi.org/10.1016/j.epsl.2011.08.048

Naus-Thijssen, F.M.J., Goupee, A.J., Vel, S.S., Johnson, S.E., 2011b. The influence of microstructure on seismic wave speed anisotropy in the crust: Computational analysis of quartz-muscovite rocks. Geophysical Journal International 185(2), 609–621. https://doi.org/10.1111/j.1365-246X.2011.04978.x

Newberg, D.W., 1985. Bedrock Geology of the Palermo 7.5’ quadrangle, Maine: Maine Geological Survey, Open-File Report 85-84, 14 page report and map, scale 1:24000. Maine Geological Survey Maps 326. Retrieved from https://digitalmaine.com/mgs_maps/326/

Nielsen, S., Spagnuolo, E., Violay, M., Smith, S., Di Toro, G., Bistacchi, A., 2016. G: Fracture energy, friction and dissipation in earthquakes. Journal of Seismology 20(4), 1187–1205. https://doi.org/10.1007/s10950-016-9560-1

Noda, H., Lapusta, N., 2010. Three-dimensional earthquake sequence simulations with evolving temperature and pore pressure due to shear heating: Effect of heterogeneous hydraulic diffusivity. Journal of Geophysical Research: Solid Earth 115(11), B12314. https://doi.org/10.1029/2010JB007780

Norris, R.J., Cooper, A.F., 1995. Origin of small-scale segmentation and transpressional thrusting along the Alpine Fault, New Zealand. Geological Society of America Bulletin 107(2), 231–240. https://doi.org/10.1130/0016-7606(1995)107<0231:OOSSSA>2.3.CO;2

Norris, R.J., Cooper, A.F., 1997. Erosional control on the structural evolution of a transpressional thrust complex on the Alpine Fault, New Zealand. Journal of Structural Geology 19(10), 1323-1342. https://doi.org/10.1016/S0191-8141(97)00036-9

Norris, R.J., Cooper, A.F., 2007. The Alpine fault, New Zealand: Surface geology and field relationships. In: Okaya, D., Stern, T., Davey, F. (Eds.), A continental plate boundary: tectonics at South Island, New Zealand, Geophysical Monograph Series, vol. 175. American Geophysical Union, pp. 157–175. https://doi.org/10.1029/175GM09

Norris, R.J., Koons, P.O., Cooper, A.F., 1990. The obliquely-convergent plate boundary in the South Island of New Zealand: implications for ancient collision zones. Journal of Structural Geology 12(5–6), 715–725. https://doi.org/10.1016/0191-8141(90)90084-C

Ohno, I., Harada, K., Yoshitomi, C., 2006. Temperature variation of elastic constants of quartz across the α - β transition. Physics and Chemistry of Minerals 33(1), 1–9. https://doi.org/10.1007/s00269-005-0008-3

O'keefe, J.D., Ahrens, T.J., 1985. Impact and explosion crater ejecta, fragment size, and velocity. Icarus 62(2), 328–338. https://doi.org/10.1016/0019-1035(85)90128-9

Okubo, K., Bhat, H.S., Rougier, E., Marty, S., Schubnel, A., Lei, Z., Knight, E.E., Klinger, Y., 2019. Dynamics, radiation, and overall energy budget of earthquake rupture with coseismic off-fault damage. Journal of Geophysical Research: Solid Earth 124(11), 11771–11801. https://doi.org/10.1029/2019JB017304

Okubo, K., Rougier, E., Lei, Z., Bhat, H.S., 2020. Modeling earthquakes with off-fault damage using the combined finite-discrete element method. Computational Particle Mechanics 7, 1057–1072. https://doi.org/10.1007/s40571-020-00335-4

Olgaard, D.L., Brace, W.F., 1983. The microstructure of gouge from a mining-induced seismic shear zone. International Journal of Rock Mechanics and Mining Sciences & Geomechanics Abstracts 20(1), 11–19. https://doi.org/10.1016/0148-9062(83)91610-8

Ostermeijer, G.A., Aben, F.M., Mitchell, T.M., Rockwell, T.K., Rempe, M., Farrington, K., 2022. Evolution of co-seismic off-fault damage towards pulverisation. Earth and Planetary Science Letters 579, 117353. https://doi.org/10.1016/j.epsl.2021.117353

Ostermeijer, G.A., Mitchell, T.M., Aben, F.M., Dorsey, M.T., Browning, J., Rockwell, T.K., Fletcher, J.M., Ostermeijer, F., 2020. Damage zone heterogeneity on seismogenic faults in crystalline rock; a field study of the Borrego Fault, Baja California, Journal of Structural Geology 137, 104016. https://doi.org/10.1016/j.jsg.2020.104016

Pankiwskyj, K.A., 1996. Structure and stratigraphy across the Hackmatack Pond Fault, Kennebec and Waldo Counties, Maine: Maine Geological Survey, Open-File Report 96-2, 15 page report and 2 maps, scale 1:24000. Maine Geological Survey Maps 226. Retrieved from http://digitalmaine.com/mgs_maps/226

Papa, S., Pennacchioni, G., Angel, R.J., Faccenda, M., 2018. The fate of garnet during (deep-seated) coseismic frictional heating: The role of thermal shock. Geology 46(5), 471–474. https://doi.org/10.1130/G40077.1

Papa, S., Spagnuolo, E., Di Toro, G., Cavallo, A., Favero, M., Camacho, A., Pennacchioni, G., 2021. Selective clast survival in an experimentally-produced pseudotachylyte. Journal of Srtructural Geology 147, https://doi.org/10.1016/j.jsg.2021.104328

Parks, G.A., 1990. Surface energy and adsorption at mineral-water interfaces: an introduction. Reviews in Mineralogy and Geochemistry 23, 133–175.

Passelègue, F.X., Schubnel, A., Nielsen, S., Bhat, H.S., Madariaga, R., 2013. From sub-Rayleigh to supershear ruptures during stick-slip experiments on crustal rocks. Science 340(6137), 1208–1211. https://doi.org/10.1126/science.1235637

Perrin, C., Manighetti, I., Ampuero, J.-P., Cappa, F., Gaudemer, Y., 2016. Location of largest earthquake slip and fast rupture controlled by along-strike change in fault structural maturity due to fault growth. Journal of Geophysical Research: Solid Earth 121(5), 3666–3685. https://doi.org/10.1002/2015JB012671

Perrin, C., Waldhauser, F., Scholz, C.H., 2021. The shear deformation zone and the smoothing of faults with displacement. Journal of Geophysical Research: Solid Earth 126(5), e2020JB020447. https://doi.org/10.1029/2020JB020447

Perugini, D. Kueppers, L., 2012. Fractal analysis of experimentally generated pyroclasts: A tool for volcanic hazard assessment. Acta Geophysica 60(3), 682–698. https://doi.org/10.2478/s11600-012-0019-7

Perugini, D., Speziali, A., Caricchi,L., Kueppers, U., 2011. Application of fractal fragmentation theory to natural pyroclastic deposits: Insights into volcanic explosivity of the Valentano scoria cone (Italy). Journal of Volcanology and Geothermal Research 202(3–4), 200–210, https://doi.org/10.1016/j.jvolgeores.2011.02.008

Perugini, D., Valentini, L., Poli, G., 2007. Insights into magma chamber processes from the analysis of size distribution of enclaves in lava flows: A case study from Vulcano Island (Southern Italy). Journal of Volcanology and Geothermal Research 166(3–4), 193–203. https://doi.org/10.1016/j.jvolgeores.2007.07.017

Petley-Ragan, A., Ben-Zion, Y., Austrheim, H., Ildefonse, B., Renard, F., Jamtveit, B., 2019. Dynamic earthquake rupture in the lower crust. Science Advances 5(7), eaaw0913. https://doi.org/10.1126/sciadv.aaw0913

Petley-Ragan, A., Dunkel, K.G., Austrheim, H., Ildefonse, B., Jamtveit, B., 2018. Microstructural records of earthquakes in the lower crust and associated fluid-driven metamorphism in plagioclase-rich granulites. Journal of Geophysical Research: Solid Earth 123(5), 3729–3746. https://doi.org/10.1029/2017JB015348

Peyrat, S., Madariaga, R., Buforn, E., Campos, J., Asch, G., Vilotte, J. P., 2010. Kinematic rupture process of the 2007 Tocopilla earthquake and its main aftershocks from teleseismic and strong-motion data. Geophysical Journal International 182(3), 1411–1430. https://doi.org/10.1111/j.1365-246X.2010.04685.x

Phillips, N.J., Williams, R.T., 2021. To D or not to D? Re-evaluating particle-size distributions in natural and experimental fault rocks. Earth and Planetary Science Letters 553, 116635 https://doi.org/10.1016/j.epsl.2020.116635

Pickering, G., Bull, J.M., Sanderson, D.J., 1995. Sampling power-law distributions. Tectonophysics 248(1–2), 1–20. https://doi.org/10.1016/0040-1951(95)00030-Q

Pittarello, L., Di Toro, G., Bizzarri, A., Pennacchioni, G., Hadizadeh, J., Cocco, M., 2008. Energy partitioning during seismic slip in pseudotachylyte-bearing faults (Gole Larghe Fault, Adamello, Italy). Earth and Planetary Science Letters 269(1–2), 131–139. https://doi.org/10.1016/j.epsl.2008.01.052

Poliakov, A.N., Dmowska, R., Rice, J.R., 2002. Dynamic shear rupture interactions with fault bends and off-axis secondary faulting. Journal of Geophysical Research: Solid Earth 107(B11), 2295. https://doi.org/10.1029/2001JB000572.

Prasher, C.L., 1987. Crushing and grinding process handbook. Wiley.

Price, N.A., Johnson, S.E., Gerbi, C.C., West, D.P., Jr., 2012. Identifying deformed pseudotachylyte and its influence on the strength and evolution of a crustal shear zone at the base of the seismogenic zone. Tectonophysics 518–521, 63–83. https://doi.org/10.1016/j.tecto.2011.11.011

Price, N.A., Song, W.J., Johnson, S.E., Gerbi, C.C., Beane, R.J., West, D.P., Jr., 2016. Recrystallization fabrics of sheared quartz veins with a strong pre-existing crystallographic preferred orientation from a seismogenic shear zone. Tectonophysics 682, 214–236. https://doi.org/10.1016/j.tecto.2016.05.030

Punturo, R., Kern, H., Cirrincione, R., Mazzoleni, P., Pezzino, A., 2005. P- and S-wave velocities and densities in silicate and calcite rocks from the Peloritani Mountains, Sicily (Italy): The effect of pressure, temperature and the direction of wave propagation. Tectonophysics 409(1–4), 55–72. https://doi.org/10.1016/j.tecto.2005.08.006

Ramesh, K.T., Hogan, J.D., Kimberley, J., Stickle, A., 2015. A review of mechanisms and models for dynamic failure, strength, and fragmentation. Planetary and Space Science 107, 10–23. https://doi.org/10.1016/j.pss.2014.11.010

Rampal, P., Dansereau, V., Olason, E., Bouillon, S., Williams, T., Korosov, A., Samaké, A., 2019. On the multi-fractal scaling properties of sea ice deformation. Cryosphere 13(9), 2457–2474. https://doi.org/10.5194/tc-13-2457-2019

Ranjith, K., Rice, J.R., 2001. Slip dynamics at an interface between dissimilar materials. Journal of the Mechanics and Physics of Solids 49(2), 341–361. https://doi.org/10.1016/S0022-5096(00)00029-6

Reches, Z., Dewers, T.A., 2005. Gouge formation by dynamic pulverization during earthquake rupture. Earth and Planetary Science Letters 235(1–2), 361–374. https://doi.org/10.1016/j.epsl.2005.04.009

Redner, S., 1990. Fragmentation. In: Herrmann, H.J., Roux, S. (Eds.), Statistical models for the fracture of disordered media. Elsevier, pp. 321–348. https://doi.org/10.1016/B978-0-444-88551-7.50021-5

Rempe, M., Mitchell, T., Renner, J., Nippress, S., Ben-Zion, Y., Rockwell, T., 2013. Damage and seismic velocity structure of pulverized rocks near the San Andreas Fault. Journal of Geophysical Research: Solid Earth 118(6), 2813–2831. https://doi.org/10.1002/jgrb.50184

Reuss, A. (1929). Berechnung der Fließgrenze von Mischkristallen auf Grund der Plastizitätsbedingung für Einkristalle. Zeitschrift für Angewandte Mathematik und Mechanik 9(1), 49–58. https://doi.org/10.1002/zamm.19290090104

Rey, P.F., Fountain, D.M., Clement, W.P., 1994. P wave velocity across a noncoaxial ductile shear zone and its associated strain gradient: Consequences for upper crustal reflectivity. Journal of Geophysical Research: Solid Earth 99(B3), 4533–4548. https://doi.org/10.1029/93JB03105

Rice, J.R., 2006. Heating and weakening of faults during earthquake slip. Journal of Geophysical Research: Solid Earth 111, B05311, https://doi.org/10.1029/2005JB004006

Rice, J.R., Ben-Zion, Y., 1996. Slip complexity in earthquake fault models. Proceedings of the National Academy of Sciences 93(9), 3811–3818. https://doi.org/10.1073/pnas.93.9.3811

Rice, J.R., Lapusta, N., Ranjith, K., 2001. Rate and state dependent friction and the stability of sliding between elastically deformable solids. Journal of the Mechanics and Physics of Solids 49(9), 1865–1898. https://doi.org/10.1016/S0022-5096(01)00042-4

Rice, J.R., Sammis, C.G., Parsons, R., 2005. Off-fault secondary failure induced by a dynamic slip pulse. Bulletin of the Seismological Society of America 95(1). 109–134. https://doi.org/10.1785/0120030166.

Rockwell, T., Sisk, M., Girty, G., Dor, O., Wechsler, N., & Ben-Zion, Y., 2009. Chemical and physical characteristics of pulverized tejon lookout granite adjacent to the San Andreas and Garlock faults: Implications for earthquake physics. Pure and Applied Geophysics 166(10–11), 1725–1746. https://doi.org/10.1007/s00024-009-0514-1

Rosakis, A.J., Samudrala, O., Coker, D., 1999. Cracks faster than the shear wave speed. Science 284(5418), 1337–1340. https://doi.org/10.1126/science.284.5418.1337

Rosin, P., Rammler, E., 1933. The laws governing the fineness of powdered coal. Journal of the Institute of Fuel 7, 29–36.

Ross, Z.E., Hauksson, E., Ben-Zion, Y., 2017. Abundant off-fault seismicity and orthogonal structures in the San Jacinto fault zone. Science Advances 3(3), e1601946. https://doi.org/10.1126/sciadv.1601946

Rousell, D.H., Fedorowich, J.S., Dressler, B.O., 2003. Sudbury breccia (Canada): a product of the 1850 Ma Sudbury event and host to footwall Cu-Ni-PGE deposits. Earth-science Reviews 60(3–4), 147–174. http://dx.doi.org/10.1016/S0012-8252(02)00091-0

Rowe, C.D., Griffith, W.A., 2015. Do faults preserve a record of seismic slip: A second opinion. Journal of Structural Geology 78, 1–26. https://doi.org/10.1016/j.jsg.2015.06.006

Rowe, C.D., Ross, C., Swanson, M.T., Pollock, S., Backeberg, N.R., Barshi, N.A., Bate, C.E., Carruthers, S., Coulson, S., Dascher-Cousineau, K., Harrichhausen, N., Peña Castro, A.F., Nisbet, H., Rakoczy, P., Scibek, J. Smith, H., Tarling, M.S., Timofeev, A., Young, E., (2018). Geometric complexity of earthquake rupture surfaces preserved in pseudotachylyte networks. Journal of Geophysical Research: Solid Earth 123(9), 7998–8015. https://doi.org/10.1029/2018JB016192

Roy, S.G., Koons, P.O., Upton, P., Tucker, G.E., 2015. The influence of crustal strength fields on the patterns and rates of fluvial incision. Journal of Geophysical Research: Earth Surface 120(2), 275–299. https://doi.org/10.1002/2014JF003281

Roy, S.G., Koons, P.O., Upton, P., Tucker, G.E., 2016. Dynamic links among rock damage, erosion, and strain during orogenesis. Geology 44(7), 583–586. https://doi.org/10.1130/G37753.1

Roy, S.G., Johnson, S.E., Koons, P.O., Jin, Z., 2012. Fractal analysis and thermal-elastic modeling of a subvolcanic magmatic breccia: The role of post-fragmentation partial melting and thermal fracture in clast size distributions. Geochemistry, Geophysics, Geosystems 13(5), Q05009. https://doi.org/10.1029/2011GC004018

Sagy A., Brodsky E.E., 2009. Geometric and rheological asperities in an exposed fault zone. Journal of Geophysical Research: Solid Earth 114, B02301. https://doi.org/10.1029/2008jb005701

Sagy, A., Korngreen, D., 2012. Dynamic branched fractures in pulverized rocks from a deep borehole. Geology 40(9), 799–802. https://doi.org/10.1130/G33194.1

Sagy, A., Reches, Z., Roman, I., 2001. Dynamic fracturing: field and experimental observations. Journal of Structural Geology 23(8), 1223–1239. https://doi.org/10.1016/S0191-8141(00)00190-5

Salisbury, M.H., Fountain, D.M., 1994. The seismic velocity and Poisson's ratio structure of the Kapuskasing uplift from laboratory measurements. Canadian Journal of Earth Sciences 31(7), 1052–1063. https://doi.org/10.1139/e94-095

Sammis, C.G., Ben-Zion, Y., 2008. Mechanics of grain-size reduction in fault zones. Journal of Geophysical Research: Solid Earth 113, B02306. https://doi.org/10.1029/2006JB004892

Sammis, C.G., Biegel, R., 1989. Fractals, fault-gouge, and friction. Pure and Applied Geophysics 131, 255–271.

Sammis, C., King, G., Biegel, R., 1987. The kinematics of gouge deformation. Pure and Applied Geophysics 125(5), 777–812. https://doi.org/10.1007/BF00878033

Sammis, C.G., Osborne, R., Anderson, J., Banerdt, M., White, P., 1986. Selfsimilar cataclasis in the formation of gouge. Pure and Applied Geophysics 124, 53–78.

Scholz, C.H., 2019. The mechanics of earthquakes and faulting (3rd edn). Cambridge University Press. https://doi.org/10.1017/9781316681473

Scholz, C.H., Sawers, N.H., Yu, J.-Z., Anders, M.H., 1993. Fault growth and fault scaling laws: Preliminary results. Journal of Geophysical Research: Solid Earth 98(B12), 21,951-21,961. https://doi.org/10.1029/93JB01008

Schoutens, J.E., 1979. Nuclear geoplosics sourcebook: Volume IV, part II—empirical analysis of nuclear and high-explosive cratering and ejecta. Defense Nuclear Agency.

Schubnel, A., Fortin, J., Burlini, L., Gueguen, Y., 2005. Damage and recovery of calcite rocks deformed in the cataclastic regime. Geological Society, London, Special Publications 245, 203–221. https://doi.org/10.1144/GSL.SP.2005.245.01.10

Schuhmann, R., Jr., 1940. Principles of comminution, I. Size distribution and surface calculations. The American Institute of Mining, Metallurgical, and Petroleum Engineers (AIME) Technical Publication 1189, 1–11.

Schulz, S.E., Evans, J.P., 2000. Mesoscopic structure of the Punchbowl Fault, Southern California and the geologic and geophysical structure of active strike-slip faults. Journal of Structural Geology 22(7), 913–930. https://doi.org/10.1016/S0191-8141(00)00019-5

Shapiro, N.M., Ritzwoller, M.H., Molnar, P., Levin, V., 2004. Thinning and flow of Tibetan crust constrained by seismic anisotropy. Science 305(5681), 233–236.

Shao, S.-M., Zou, J.-C., 1996. Fractal research of gouge. Acta Seismologica Sinica 9, 485–491.

Sharon, E., Gross, S.P., Fineberg, J., 1996. Energy dissipation in dynamic fracture. Physical Review Letters, 76(12), 2117–2120. https://doi.org/10.1103/PhysRevLett.76.2117

Shi, Z., Ben-Zion, Y., 2006. Dynamic rupture on a bimaterial interface governed by slip-weakening friction. Geophysical Journal International 165(2), 469–484. https://doi.org/10.1111/j.1365-246X.2006.02853.x

Shi, Z., Ben-Zion, Y., Needleman, A., 2008. Properties of dynamic rupture and energy partition in a solid with a frictional interface. Journal of the Mechanics and Physics of Solids 56(1), 5–24. https://doi.org/10.1016/j.jmps.2007.04.006

Shi, Z., Day, S.M., 2013. Rupture dynamics and ground motion from 3-D rough-fault simulations. Journal of Geophysical Research: Solid Earth 118(3), 1122–1141. https://doi.org/10.1002/jgrb.50094

Shipton, Z.K., Evans, J.P., Abercrombie, R.E., Brodsky, E.E., 2006. The missing sinks: Slip localization in faults, damage zones, and the seismic energy budget. In: Abercrombie, R., McGarr, A., Di Toro, G., Kanamori, H. (Eds.), Earthquakes: radiated energy and the physics of faulting, Geophysical Monograph Series, vol. 170. American Geophysical Union, pp. 217–222. https://doi.org/10.1029/170GM22

Shlomai, H., Adda-Bedia, M., Arias, R.E., Fineberg, J., 2020a. Supershear frictional ruptures along bimaterial interfaces. Journal of Geophysical Research: Solid Earth 125(8), e2020JB019829. https://doi.org/10.1029/2020JB019829

Shlomai, H., Kammer, D.S., Adda-Bedia, M., Arias, R. E., Fineberg, J., 2021. Unstable cracks trigger asymptotic rupture modes in bimaterial friction. Journal of the Mechanics and Physics of Solids 149, 104330. https://doi.org/10.1016/j.jmps.2021.104330

Shlomai, H., Kammer, D. S., Adda-Bedia, M., Fineberg, J., 2020b. The onset of the frictional motion of dissimilar materials. Proceeds of the National Academy of Sciences, 117(24), 13379–13385. https://doi.org/10.1073/pnas.1916869117

Short, N.M., 1966. Effects of shock pressures from a nuclear explosion on mechanical and optical properties of granodiorite. Journal of Geophysical Research 71(4), 1195–1215. https://doi.org/10.1029/JZ071i004p01195

Sibson, R.H., 1973. Interactions between temperature and pore fluid pressure during earthquake faulting and a mechanism for partial or total stress relief. Nature Physical Science 243, 66–68. https://doi.org/10.1038/physci243066a0

Sibson, R.H., 1975. Generation of pseudotachylyte by ancient seismic faulting. Geophysical Journal of the Royal Astronomical Society 43(3), 775–794. https://doi.org/10.1111/j.1365-246X.1975.tb06195.x

Sibson, R.H., 1989. Earthquake faulting as a structural process. Journal of Structural Geology 11(1–2), 1–14. https://doi.org/10.1016/0191-8141(89)90032-1

Sibson, R.H., Toy, V.G., 2006. The habitat of fault-generated pseudotachylyte: presence vs. absence of friction-melt. In: Abercrombie, R., McGarr, A., Di Toro, G., Kanamori, H. (Eds.), Earthquakes: radiated energy and the physics of faulting, Geophysical Monograph Series, vol. 170. American Geophysical Union, pp. 153–166. https://doi.org/10.1029/170GM16

Sibson, R.H., White, S.H., Atkinson, B.K., 1981. Structure and distribution of fault rocks in the Alpine Fault Zone, New Zealand. Geological Society, London, Special Publications 9, 197–210. https://doi.org/10.1144/GSL.SP.1981.009.01.18

Sieh, K.E., 1978. Slip along the San Andreas fault associated with the great 1857 earthquake. Bulletin of the Seismological Society of America 68(5), 1421–1448. https://doi.org/10.1785/BSSA0680051421

Skemer, P., Katayama, I., Jiang, Z., Karato, S.-I., 2005. The misorientation index: Development of a new method for calculating the strength of lattice-preferred orientation. Tectonophysics 411(1–4), 157–167. https://doi.org/10.1016/j.tecto.2005.08.023

Sleep, N.H., 2019. Thermal weakening of asperity tips on fault planes at high sliding velocities. Geochemistry, Geophysics, Geosystems 20(2), 1164–1188. https://doi.org/10.1029/2018GC008062

Smith, S.A.F., Bistacchi, A., Mitchell, T.M., Mittempergher, S., Di Toro, G., 2013. The structure of an exhumed intraplate seismogenic fault in crystalline basement. Tectonophysics 599, 29–44. https://doi.org/10.1016/j.tecto.2013.03.031

Socquet, A., Hollingsworth, J., Pathier, E., Bouchon, M., 2019. Evidence of supershear during the 2018 magnitude 7.5 Palu earthquake from space geodesy. Nature Geoscience 12(3), 192–199. https://doi.org/10.1038/s41561-018-0296-0

Soda, Y., Okudaira, T., 2018. Microstructural evidence for the deep pulverization in a lower crustal meta-anorthosite. Terra Nova 30(6), 399–405. https://doi.org/10.1111/ter.12355

Somerville, P.G., Smith, N.F., Graves, R.W., Abrahamson, N.A., 1997. Modification of empirical strong ground motion attenuation relations to include the amplitude and duration effects of rupture directivity. Seismological Research Letters 68(1), 199–222. https://doi.org/10.1785/gssrl.68.1.199

Song, B.R., Johnson, S.E., Song, W.J., Gerbi, C.C., Yates, M.G., 2020. Coseismic damage runs deep in continental strike-slip faults. Earth and Planetary Science Letters 539, 116226. https://doi.org/10.1016/j.epsl.2020.116226

Song, W.J., Johnson, S.E., Gerbi, C.C., 2020. Quartz fluid inclusion abundance and off-fault damage in a deeply exhumed, strike-slip, seismogenic fault. Journal of Structural Geology 139, 104118. https://doi.org/10.1016/j.jsg.2020.104118

Spudich, P., Olsen, K.B., 2001. Fault zone amplified waves as a possible seismic hazard along the Calaveras fault in central California. Geophysical Research Letters 28(13), 2533–2536. https://doi.org/10.1029/2000GL011902

Storti, F., Billi, A., Salvini, F., 2003. Particle size distributions in natural carbonate fault rocks: insights for non-self-similar cataclasis. Earth and Planetary Science Letters 206(1–2), 173–186. https://doi.org/10.1016/S0012-821X(02)01077-4

Strassburger, E., Patel, P., McCauley, J.W., Kovalchick, C., Ramesh, K.T., Templeton, D.W., 2008. High-speed transmission shadowgraphic and dynamic photoelasticity study of stress wave and impact damage propagation in transparent materials and laminates using the edge-on impact (EOI) method. U.S. Army Research Laboratory.

Stünitz, H., Keulen, N., Hirose, T., Heilbronner, R., 2010. Grain size distribution and microstructures of experimentally sheared granitoid gouge at coseismic slip rates – Criteria to distinguish seismic and aseismic faults? Journal of Structural Geology 32(1), 59–69. https://doi.org/10.1016/j.jsg.2009.08.002

Sullivan, W.A., 2009. Kinematic significance of L tectonites in the footwall of a major terrane-bounding thrust fault, Klamath Mountains, California, USA. Journal of Structural Geology 31(10), 1197–1211. https://doi.org/10.1016/j.jsg.2009.06.016

Sullivan, W.A., Peterman, E.M., 2017. Pulverized granite at the brittle-ductile transition: An example from the Kellyland fault zone, eastern Maine, U.S.A. Journal of Structural Geology 101, 109–123. https://doi.org/10.1016/j.jsg.2017.07.002

Suteanu, C., Zugravescu, D., Munteanu, F., 2000. Fractal approach of structuring by fragmentation. Pure and Applied Geophysics 157(4), 539–557. https://doi.org/10.1007/PL00001106

Sutherland, R., Berryman, K., Norris, R., 2006. Quaternary slip rate and geomorphology of the Alpine fault: Implications for kinematics and seismic hazard in southwest New Zealand. Geological Society of America Bulletin 118(3-4), 464–474. https://doi.org/10.1130/B25627.1

Sutherland, R., Eberhart-Phillips, D., Harris, R.A., Stern, T., Beavan, J., Ellis, S., Henrys, S., Cox, S., Norris, R.J., Berryman, K.R., Townend, J., Bannister, S., Pettinga, J., Leitner, B., Wallace, L., Little, T. A., Cooper, A. F., Yetton, M., Stirling, M., 2007. Do great earthquakes occur on the Alpine Fault in the Central South Island, New Zealand? In: Okaya, D., Stern, T., Davey, F. (Eds.), A continental plate boundary: tectonics at South Island, New Zealand, Geophysical Monograph Series, vol. 175. American Geophysical Union, pp. 235–251. https://doi.org/10.1029/175GM12

Sutherland, R., Townend, J., Toy, V., Upton, P., Coussens, J., Allen, M., Baratin, L.-M., Barth, N.C., Becroft, L., Boese, C., Boles, A., Boulton, C., Broderick, N.G.R., Janku-Capova, L., Carpenter, B.M., Célérier, B., Chamberlain, C., Cooper, A., Coutts, A., Cox, S., Craw, L., Doan, M.-L., Eccles, J., Faulkner, D., Grieve, J., Grochowski, J., Gulley, A., Hartog, A., Howarth, J, Jacobs, K., Jeppson, T., Kato, N., Keys, S., Kirilova, M., Kometani, Y., Langridge, R., Lin, W., Little, T., Lukacs, A., Mallyon, D., Mariani, E., Massiot, C., Mathewson, L., Melosh, B., Menzies, C., Moore, J., Morales, L., Morgan, C., Mori, H., Niemeijer, A., Nishikawa, O., Prior, D., Sauer, K., Savage, M., Schleicher, A., Schmitt, D.R., Shigematsu, N., Taylor-Offord, S., Teagle, D., Tobin, H., Valdez, R., Weaver, K., Wiersberg, T., Williams, J., Woodman, N., Zimmer, M., 2017. Extreme hydrothermal conditions at an active plate-bounding fault. Nature 546, 137–140. https://doi.org/10.1038/nature22355

Swanson, M.T., 1992. Late Acadian-Alleghenian transpressional deformation: Evidence from asymmetric boudinage in the Casco Bay Area, coastal Maine. Journal of Structural Geology 14(3), 323–341. https://doi.org/10.1016/0191-8141(92)90090-J

Swanson, M.T., 2006. Pseudotachylyte-bearing strike-slip faults in mylonitic host rocks, Fort Foster Brittle Zone, Kittery, Maine. In: Abercrombie, R., McGarr, A., Di Toro, G., Kanamori, H. (Eds.), Earthquakes: Radiated energy and the physics of faulting, Geophysical Monograph Series, vol. 170. American Geophysical Union, pp. 167–179. https://doi.org/10.1029/170GM17

Swanson, M.T., Pollock, S.G., Hussey, A.M., II, 1986. The structural and stratigraphic development of the Casco Bay Group at Harpswell Neck, Maine. In: Newburg, D.W. (Ed.), Guidebook for field trips in southwestern Maine: New England Intercollegiate Geological Conference, pp. 350–370. https://scholars.unh.edu/neigc_trips/406

Taşdemir, A., 2009. Fractal evaluation of particle size distributions of chromites in different comminution environments. Minerals Engineering 22(2), 156–167. https://doi.org/10.1016/j.mineng.2008.06.002

Thomas, M.Y., Bhat, H.S., 2018. Dynamic evolution of off-fault medium during an earthquake: A micromechanics based model. Geophysical Journal International 214(2), 1267–1280. https://doi.org/10.1093/gji/ggy129

Thomas, M.Y., Bhat, H.S., Klinger, Y., 2017. Effect of brittle off-fault damage on earthquake rupture dynamics. In: Thomas, M.Y., Mitchell, T.M., Bhat, H.S. (Eds.), Fault zone dynamic processes: Evolution of fault properties during seismic rupture, Geophysical Monograph Series, vol. 227. American Geophysical Union, pp. 225–280. https://doi.org/10.1002/9781119156895.ch14

Thomson, R., 1993. Clyde Dam Engineering Geological Completion Report Volume 1: Text and Appendices. Institute of Geological and Nuclear Sciences science report 94/33.

Tinti, E., Spudich, P., Cocco, M., 2005. Earthquake fracture energy inferred from kinematic rupture models on extended faults. Journal of Geophysical Research: Solid Earth 110, B12303. https://doi.org/10.1029/2005JB003644

Tinti, E., Spudich, P., Cocco, M., 2008. Correction to “Earthquake fracture energy inferred from kinematic rupture models on extended faults.” Journal of Geophysical Research: Solid Earth 113, B07301. https://doi.org/10.1029/2008JB005829

Toy, V.G., Sutherland, R., Townend, J., Allen, M.J., Becroft, L., Boles, A., Boulton, C., Carpenter, B., Cooper, A., Cox, S.C, Daube, C., Faulkner, D.R., Halfpenny, A., Kato, N., Keys, S., Kirilova, M., Kometani, Y., Little, T., Mariani, E., Melosh, B., Menzies, C.D., Morales, L., Morgan, C., Mori, H., Niemeijer, A., Norris, R., Prior, D., Sauer, K., Schleicher, A., Shigematsu, N., Teagle, D.A.H., Tobin, H., Valdez, R., Williams, J., Yeo, S., Baratin, L.-M., Barth, N.C., Benson, A., Boese, C., Celerier, B., Chamberlain, C.J., Conze, R., Coussens, J., Craw, L., Doan, M.-L., Eccles, J.L., Grieve, J., Grochowski, J., Gulley, A., Howarth, J., Zamudio, K.D., Janku-Capova, L., Jeppson, T.N., Langridge, R.M., Mallyon, D., Marx, R., Massiot, C., Mathewson, L., Moore, J., Nishikawa, O., Pooley, B., Pyne, A., Savage, M.K., Schmitt, D., Taylor-Offord, S., Upton, P., Weaver, K.C., Wiersberg, T., Zimmer, M., 2017. Bedrock geology of DFDP-2B, central Alpine Fault, New Zealand. New Zealand Journal of Geology and Geophysics 60(4), 497–518. https://doi.org/10.1080/00288306.2017.1375533

Trepmann, C.A., Stöckhert, B., 2001. Mechanical twinning of jadeite – an indication of synseismic loading beneath the brittle–ductile transition. International Journal of Earth Sciences 90, 4–13. https://doi.org/10.1007/s005310000165

Trepmann, C.A., Stöckhert, B., 2002. Cataclastic deformation of garnet: A record of synseismic loading and postseismic creep. Journal of Structural Geology 24(11), 1845–1856. https://doi.org/10.1016/S0191-8141(02)00004-4

Trepmann, C.A., Stöckhert, B., 2003. Quartz microstructures developed during non-steady state plastic flow at rapidly decaying stress and strain rate. Journal of Structural Geology 25(12), 2035–2051. https://doi.org/10.1016/S0191-8141(03)00073-7

Trepmann, C.A., Stöckhert, B., Dorner, D., Moghadam, R.H., Küster, M., Röller, K., 2007. Simulating coseismic deformation of quartz in the middle crust and fabric evolution during postseismic stress relaxation — An experimental study. Tectonophysics 442(1–4), 83–104. https://doi.org/10.1016/j.tecto.2007.05.005

Tromans, D., Meech, J. A., 2002. Fracture toughness and surface energies of minerals: theoretical estimates for oxides, sulfides, silicates and halides. Minerals Engineereing 15(12), 1027–1041. https://doi.org/10.1016/S0892-6875(02)00213-3

Tsai, V.C., Hirth, G., 2020. Elastic impact consequences for high-frequency earthquake ground motion. Geophysical Research Letters, 47(5), e2019GL086302. https://doi.org/10.1029/2019GL086302

Turcotte, D.L., 1986. Fractals and fragmentation. Journal of Geophysical Research: Solid Earth 91(B2), 1921–1926. https://doi.org/10.1029/JB091iB02p01921

Turcotte, D.L., Schubert, G., 2014. Geodynamics (3rd edn). Cambridge University Press. https://doi.org/10.1017/CBO9780511843877

Uenishi, K., 2021. Overlooked mechanisms behind seismic damage. Physics Today 74(1), 34. https://doi.org/10.1063/PT.3.4655

Upton, P., Koons, P.O., 2007. Three-dimensional geodynamic framework for the Central Southern Alps, New Zealand: Integrating geology, geophysics and mechanical observations. In: Okaya, D., Stern, T., Davey, F. (Eds.), A continental plate boundary: tectonics at South Island, New Zealand, Geophysical Monograph Series, vol. 175. American Geophysical Union, pp. 253–270. https://doi.org/10.1029/175GM13

Upton, P., Koons, P.O., Craw, D., Henderson, C.M., Enlow, R., 2009. Along-strike differences in the Southern Alps of New Zealand: Consequences of inherited variation in rheology. Tectonics 28(2), TC2007. https://doi.org/10.1029/2008TC002353

Vallée, M., Landès, M., Shapiro, N.M., Klinger, Y., 2008. The 14 November 2001 Kokoxili (Tibet) earthquake: High-frequency seismic radiation originating from the transitions between sub-Rayleigh and supershear rupture velocity regimes. Journal of Geophysical Research: Solid Earth 113, B07305. https://doi.org/10.1029/2007JB005520

Vaughan, M.T., Guggenheim, S., 1986. Elasticity of muscovite and its relationship to crystal structure. Journal of Geophysical Research: Solid Earth 91(B5), 4657–4664. https://doi.org/10.1029/JB091iB05p04657

Vel, S.S., Cook, A.C., Johnson, S.E., Gerbi, C.C., 2016. Computational homogenization and micromechanical analysis of textured polycrystalline materials. Computer Methods in Applied Mechanics and Engineering 310, 749–779. https://doi.org/10.1016/j.cma.2016.07.037

Verberne, B.A., de Bresser, J.H.P., Niemeijer, A.R., Spiers, C.J., de Winter, D.A.M., Plümper, O., 2013. Nanocrystalline slip zones in calcite fault gouge show intense crystallographic preferred orientation: Crystal plasticity at sub-seismic slip rates at 18–150 °C. Geology 41(8), 863–866. https://doi.org/10.1130/G34279.1

Viesca, R.C., Garagash, D.I., 2015. Ubiquitous weakening of faults due to thermal pressurization. Nature Geoscience 8, 875–879. https://doi.org/10.1038/ngeo2554

Voigt, W., 1928. Lehrbuch der Kristallphysik. Teubners-Verlag.

Wald, D.J., 1996. Slip history of the 1995 Kobe, Japan, earthquake determined from strong motion, teleseismic, and geodetic data. Journal of Physics of the Earth 44(5), 489–503. https://doi.org/10.4294/jpe1952.44.489

Wallace, L.M., Beavan, J., McCaffrey, R., Berryman, K., Denys, P., 2007. Balancing the plate motion budget in the South Island, New Zealand using GPS, geological and seismological data. Geophysical Journal International 168(1), 332–352. https://doi.org/10.1111/j.1365-246X.2006.03183.x

Walsh, J.B., 1965. The effect of cracks on the compressibility of rock. Journal of Geophysical Research 70(2), 381–389. https://doi.org/10.1029/JZ070i002p00381

Wang, C., Ludman, A., 2004. Deformation conditions, kinematics, and displacement history of shallow crustal ductile shearing in the Norumbega fault system in the Northern Appalachians, eastern Maine. Tectonophysics 384(1–4), 129–148. https://doi.org/10.1016/j.tecto.2004.03.013

Wang, D., Mori, J., 2012. The 2010 Qinghai, China, earthquake: A moderate earthquake with supershear rupture. Bulletin of the Seismological Society of America 102(1), 301–308. https://doi.org/10.1785/0120110034

Ward, D., Mahan, K., Schulte-Pelkum, V., 2012. Roles of quartz and mica in seismic anisotropy of mylonites. Geophysical Journal International 190(2), 1123–1134. https://doi.org/10.1111/j.1365-246X.2012.05528.x

Watling, B., 2017. Seismic anisotropy as a function of mineralogy and rock type in Chester gneiss dome, southeast Vermont (Doctoral dissertation). Wayne State University. Retrieved from https://digitalcommons.wayne.edu/oa_theses/593

Wechsler, N., Allen, E.E., Rockwell, T.K., Girty, G., Chester, J.S., Ben-Zion, Y., 2011. Characterization of pulverized granitoids in a shallow core along the San Andreas fault, Littlerock, CA. Geophysical Journal International 186(2), 401–417. https://doi.org/10.1111/j.1365-246X.2011.05059.x

Wechsler, N., Rockwell, T. K., & Ben-Zion, Y., 2009. Application of high resolution DEM data to detect rock damage from geomorphic signals along the central San Jacinto Fault. Geomorphology 113(1–2), 82–96. https://doi.org/10.1016/j.geomorph.2009.06.007

Weertman, J., 1980. Unstable slippage across a fault that separates elastic media of different elastic constants. Journal of Geophysical Research: Solid Earth 85(B3), 1455–1461. https://doi.org/10.1029/JB085iB03p01455

Weertman, J., 2005. Slip event propagation direction in transition region of low surface slope. Annals of Glaciology 40(1), 43–46. https://doi.org/10.3189/172756405781813429

Wenk, H.-R., Johnson, L.R., Ratschbacher, L., 2000. Pseudotachylites in the Eastern Peninsular Ranges of California. Tectonophysics 321(2), 253–277. https://doi.org/10.1016/S0040-1951(00)00064-0

Wentworth, C.M., Zoback, M.D., 1989. The style of Late Cenozoic deformation at the eastern front of the California Coast Ranges. Tectonics 8(2), 237–246. https://doi.org/10.1029/TC008i002p00237

Wenning, Q.C., Almqvist, B.S.G., Hedin, P., Zappone, A., 2016. Seismic anisotropy in mid to lower orogenic crust: Insights from laboratory measurements of V_p and V_s in drill core from central Scandinavian Caledonides. Tectonophysics 692, 14–28. https://doi.org/10.1016/j.tecto.2016.07.002

West, D.P., Jr., 1999. Timing of displacements along the Norumbega fault system, south-central and south-coastal Maine. In: Ludman, A., West, D.P., Jr. (Eds.), Norumbega fault system of the northern Appalachians, Geological Society of America Special Paper, vol. 331. Geological Society of America, pp. 167–178. https://doi.org/10.1130/0-8137-2331-0.167

West, D.P., Jr., Hubbard, M.S., 1997. Progressive localization of deformation during exhumation of a major strike-slip shear zone: Norumbega fault zone, south-central Maine, USA. Tectonophysics 273(3–4), 185–201. https://doi.org/10.1016/S0040-1951(96)00306-X

West, D.P., Jr., Peterman, E.M., 2004. Bedrock geology of the Razorville quadrangle, Maine: Maine Geological Survey, Open-File Map 04-29, color map, scale 1:24000. Maine Geological Survey Maps 40. Retrieved from https://digitalmaine.com/mgs_maps/40

White, A.F., 1995. Chemical weathering rates of silicate minerals in soils. Reviews in Mineralogy and Geochemistry 31, 407–461.

White, A.F., Peterson, M.L,. 1990. Role of reactive-surface-area characterization in geochemical kinetic models. In: Melchior, D.C., Bassett, R.L. (Eds.), Chemical modeling of aqueous systems II, American Chemical Society Symposium Series, vol. 416. American Chemical Society, pp. 461–475. https://doi.org/10.1021/bk-1990-0416.ch035

Whitney, D.L., Broz, M., Cook, R.F., 2007. Hardness, toughness, and modulus of some common metamorphic minerals. American Mineralogist 92(2–3), 281–288. https://doi.org/10.2138/am.2007.2212

Wibberley, C.A., Shimamoto, T., 2005. Earthquake slip weakening and asperities explained by thermal pressurization. Nature 436, 689–692. https://doi.org/10.1038/nature03901

Wilson, J.E., Chester, J.S., Chester, F.E., 2003. Microfracture analysis of fault growth and wear processes, Punchbowl Fault, San Andreas system, California. Journal of Structural Geology 25(11), 1855–1873. https://doi.org/10.1016/S0191-8141(03)00036-1

Wilson, B., Dewers, T., Reches, Z., & Brune, J., 2005. Particle size and energetics of gouge from earthquake rupture zones. Nature 434(7034), 749–752. https://doi.org/10.1038/nature03433

Winterstein, D.F., 1990. Velocity anisotropy terminology for geophysicists. Geophysics 55(8), 1070–1088. https://doi.org/10.1190/1.1442919

Withers, K.B., Olsen, K.B., Day, S.M., Shi, Z., 2019. Ground motion and intraevent variability from 3D deterministic broadband (0–7.5 Hz) simulations along a nonplanar strike-slip fault. Bulletin of the Seismological Society of America 109(1), 229–250. https://doi.org/10.1785/0120180006

Wittel, F.K., Carmona, H.A., Kun, F., Herrmann, H.J., 2008. Mechanisms in impact fragmentation. International Journal of Fracture 154, 105–117. https://doi.org/10.1007/s10704-008-9267-6

Wright, J.E., Fahan, M.R., 1988. An expanded view of Jurassic orogenesis in the western United States Cordillera: Middle Jurassic (pre-Nevadan) regional metamorphism and thrust faulting within an active arc environment, Klamath Mountains, California. Geological Society of America Bulletin 100(6), 859–876. https://doi.org/10.1130/0016-7606(1988)100<0859:AEVOJO>2.3.CO;2

Wu, C., Peng, Z., Ben-Zion, Y., 2009. Non-linearity and temporal changes of fault zone site response associated with strong ground motion, Geophysical Journal International 176(1), 265–278, https://doi.org/10.1111/j.1365-246X.2008.04005.x

Xia, K., Nasseri, M.H.B., Mohanty, B., Lu, F., Chen, R., Luo, S.N., 2008. Effects of microstructures on dynamic compression of Barre granite. International Journal of Rock Mechanics and Mining Sciences 45(6), 879–887. https://doi.org/10.1016/j.ijrmms.2007.09.013

Xia, K., Rosakis, A.J., Kanamori, H., 2004. Laboratory earthquakes: The sub-Rayleigh-to-supershear rupture transition. Science 303(5665), 1859–1861. https://doi.org/10.1126/science.1094022

Xia, K., Rosakis, A.J., Kanamori, H., Rice, J.R., 2005. Laboratory earthquakes along inhomogeneous faults: Directionality and supershear. Science 308(5722), 681–684. https://doi.org/10.1126/science.1108193

Xu, S., Ben-Zion, Y., 2017. Theoretical constraints on dynamic pulverization of fault zone rocks. Geophysical Journal International 209(1), 282–296. https://doi.org/10.1093/gji/ggx033

Xu, S., Ben-Zion, Y., Ampuero, J.-P., 2012a. Properties of inelastic yielding zones generated by in-plane dynamic ruptures—I. Model description and basic results. Geophysical Journal International 191(3), 1325–1342. https://doi.org/10.1111/j.1365-246X.2012.05679.x

Xu, S., Ben-Zion, Y., Ampuero, J.-P., 2012b. Properties of inelastic yielding zones generated by in-plane dynamic ruptures—II. Detailed parameter-space study. Geophysical Journal International 191(3), 1343–1360. https://doi.org/10.1111/j.1365-246X.2012.05685.x

Yazdani, A., Nicknam, A., Dadras, E.Y., Eftekhari, S.N., 2017. Near-field probabilistic seismic hazard analysis of metropolitan Tehran using region-specific directivity models. Pure and Applied Geophysics 174(1), 117–132. https://doi.org/10.1007/s00024-016-1389-6

You, M., 2015. Strength criterion for rocks under compressive-tensile stresses and its application. Journal of Rock Mechanics and Geotechnical Engineering 7(4), 434–439. https://doi.org/10.1016/j.jrmge.2015.05.002

Yuan, F., Prakash, V., Tullis, T., 2011. Origin of pulverized rocks during earthquake fault rupture. Journal of Geophysical Research: Solid Earth 116(B6), B06309. https://doi.org/10.1029/2010JB007721

Yue, H., Lay, T., 2011. Inversion of high-rate (1 sps) GPS data for rupture process of the 11 March 2011 Tohoku earthquake (Mw 9.1). Geophysical Research Letters 38(7), L00G09. https://doi.org/10.1029/2011GL048700

Yue, H., Lay, T., Freymueller, J.T., Ding, K., Rivera, L., Ruppert, N.A., Koper, K.D., 2013. Supershear rupture of the 5 January 2013 Craig, Alaska (Mw 7.5) earthquake. Journal of Geophysical Research: Solid Earth 118(11), 5903–5919. https://doi.org/10.1002/2013JB010594

Zeeb, C., Gomez-Rivas, E., Bons, P.D., Virgo, S., Blum, P., 2013. Fracture network evaluation program (FraNEP): A software for analyzing 2D fracture trace-line maps. Computers & Geosciences 60, 11–22. http://dx.doi.org/10.1016/j.cageo.2013.04.027

Zhai, C., Li, C., Kunnath, S., Wen, W., 2018. An efficient algorithm for identifying pulse-like ground motions based on significant velocity half-cycles. Earthquake Engineering and Structural Dynamics 47(3), 757–771. https://doi.org/10.1002/eqe.2989

Zhang, Q.B., Zhao, J., 2014. A review of dynamic experimental techniques and mechanical behavior of rock materials. Rock Mechanics and Rock Engineering 47, 1411–1478. https://doi.org/10.1007/s00603-013-0463-y

Zhou, F., Molinari, J.-F., Ramesh, K.T., 2006a. Analysis of the brittle fragmentation of an expanding ring. Computational Materials Science 37(1–2), 74–85. https://doi.org/10.1016/j.commatsci.2005.12.017

Zhou, F., Molinari, J.-F., Ramesh, K.T., 2006b. Effects of material properties on the fragmentation of brittle materials. International Journal of Fracture 139(2), 169–196. https://doi.org/10.1007/s10704-006-7135-9

APPENDICES

APPENDIX A. A THREE-DIEMENSIONAL MODEL OF TOPOGRAPHY AND TECTONIC STRESSES WITH IMPLICATIONS FOR STRAIN PARTITIONING AND FAULT SEGMENTATION AROUND A TRANSPRESSIONAL FAULT

A.1. Appendix Abstract

High topographic relief in active transpressional mountain belts significantly influences dynamic and kinematic evolution of a deforming orogen, perturbing stress and strain patterns, which in turn can produce complex patterns of strain partitioning due to variations in rock rheology and boundary conditions. The Alpine Fault, New Zealand is an excellent natural laboratory to understand the relationship among the above factors. The central Alpine Fault in the upper 1–2 km is serially partitioned by the development of strike-slip fault and oblique thrust segments (1–10 km scale) displaying a zigzag geometry, and each segment also consists of several parallel faults (1 m–1 km scale), owing to topographic variations and oblique convergence between the Pacific and Australian plates. Using a 3D, strain-softening mechanical model, conditioned by a digital elevation model of the Franz-Whataroa region in the central Alpine Fault, we investigated the solution space that could reproduce the observed kinematics. The numerical sensitivity analyses include (1) rock strength (cohesion and friction angle) difference between the weak Alpine Fault and the strong surroundings, and (2) direction of the plate displacement (orthogonal to highly oblique convergence). To study the propagation, linkage, and interaction history of shallow faults with the deeper, through-going fault zone, we initially divided the brittle-frictional upper crust into two regions: an upper, 1–2 km thick region with no preexisting weakness, and a lower region where a dipping weak zone is constrained by seismic observations. In the presence of strain-softening upper crust, all oblique convergence models result in zigzag-like partitioning of strain into strike-slip and oblique thrust components along ridges and valleys at the range front, and include small-scale parallel partitioning.

A.2. Appendix Introduction

Strain partitioning and fault segmentation in transpressional mountain belts appears linked to stress perturbations controlled by oblique tectonic loading, topographically-induced stress, dynamic stress during fault rupture, and their heterogeneous interactions. Field-based studies alone cannot provide full information on the spatial and temporal variation of stress patterns and the relative impact of the controlling factors due to heterogeneity-induced complexity along with coupling between tectonic deformation and surface processes.

For this reason, kinematic and dynamic characteristics of 3-D deformation formed by strain partitioning in an obliquely convergent region such as the Southern Alps, New Zealand, is still poorly understood. In this study, we investigate the numerical solution for 3-D deformation to answer the following questions.

(1) How sensitive is strain partitioning and fault evolution to rock rheology and boundary conditions?

(2) How are the stress and strain distributions around a fault zone reflected in fault segmentation and how do they relate to the topography?

A.2.1. Obliquity along Plate Boundaries

The Alpine fault of New Zealand is an active transpressional (dextral-reverse sense) plate boundary between the Australian and Pacific plates. The ~39 mm/yr at 071° of relative plate motion (NUVEL-1A) in the central Alpine fault at 43.5°S and 170°E (DeMets et al., 1990) is partitioned into a fault parallel slip rate of ~23 mm/yr and normal slip rate of ~12 mm/yr (Sutherland et al., 2006). Figure A.1 shows three obliquities (orthogonal, oblique and highly oblique) used in the present study.

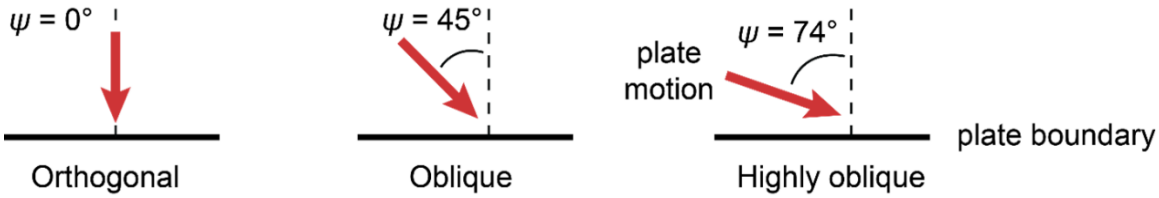

Figure A.1 Three obliquities used in the present study. Obliquity (ψ) is an angle between the plate motion vector and the normal to the plate boundary. The relative motion of two plates is generally oblique. To analyze linkage between obliquity and strain partitioning controlled by topography, we performed sensitivity tests using orthogonal (0°), oblique (45°), and highly oblique (74°, obliquity of Alpine fault) motions.

A.2.2. Strain Partitioning in the Alpine Fault, New Zealand

The central Alpine Fault in the upper 1–2 km is serially partitioned by the development of strike-slip and oblique thrust segments (1–10 km scale) displaying a zigzag geometry. Each segment also consists of several parallel faults (1 m to 1 km scale). Figure A.2 illustrates serial and parallel partitioning (Norris and Cooper 2007).

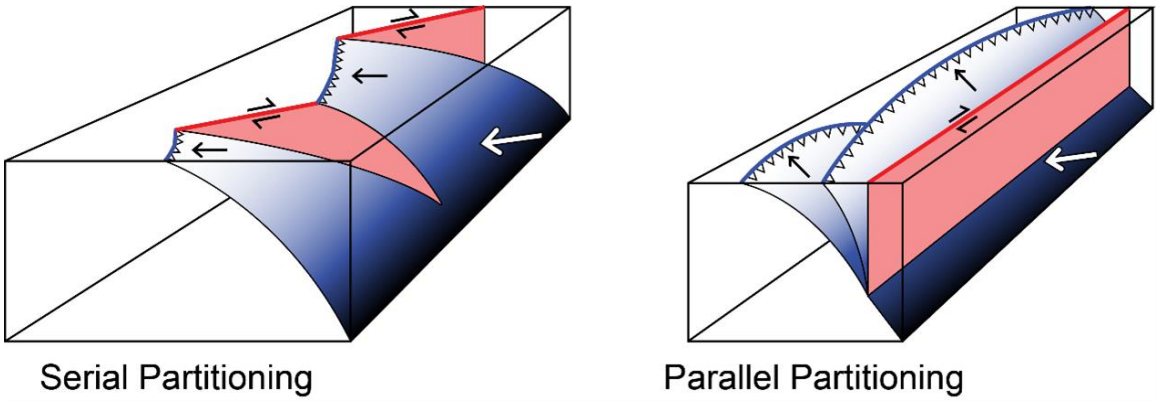

Figure A.2 Serial and parallel strain partitioning (Norris and Cooper, 2007).

A.3. Model Setup

The numerical model setup using strain-softening behavior of FLAC^{3D} is shown in Figure A.3. The Mohr-Coulomb plastic model in FLAC^{3D} allows simulating strain-hardening/softening behaviors (Itasca, 2012). This can be controlled by yielding parameters such as friction angle (ϕ), cohesion (c), dilation angle, and tensile strength, which are a function of plastic strain. In the model, we set up a softening behavior to reduce internal friction angle and cohesion when/where strain is higher than 0.03.

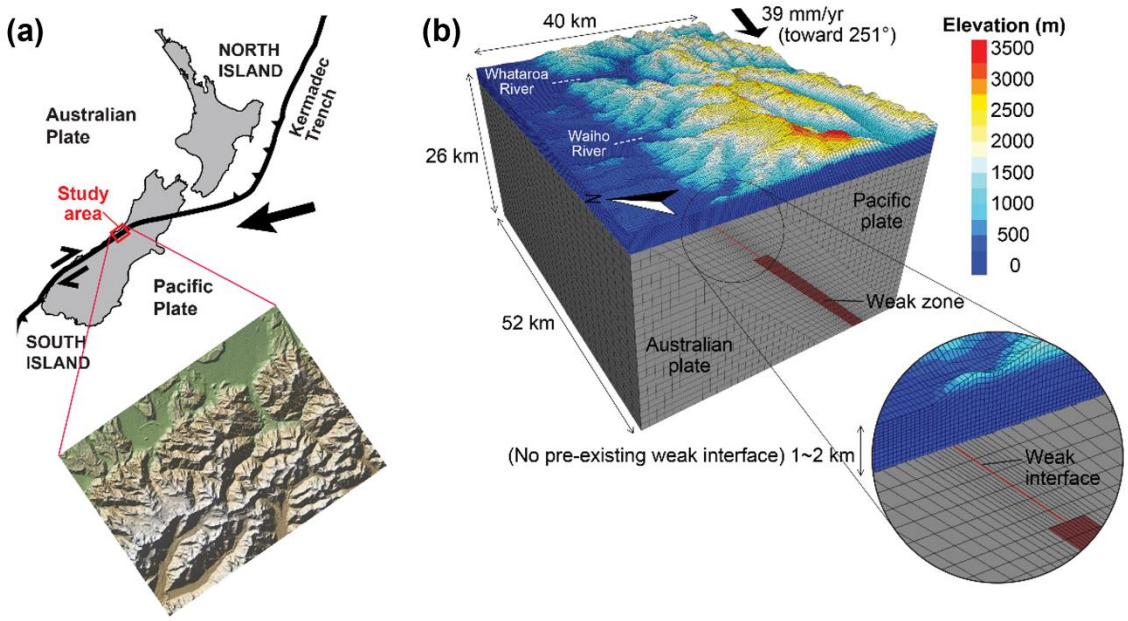

Figure A.3 Strain softening rheological model (FLAC^{3D}) of the Whataroa-Waiho region in the central Alpine fault. (a) A 200 m spaced digital elevation model of the study area. The red box in the map indicates the study area, Whataroa-Waiho region. (b) The Whataroa-Waiho region embedded into a model with dimensions of 200 km × 100 km × 26 km to minimize boundary effects. An upper, 1–2 km thick region has no preexisting weakness.

A.4. Strain Partitioning Sensitivity Analysis

Faults initiate from short segmentation, grow as echelon arrays, and become a localized fault zone by the segment linkage. The purpose of the numerical simulation is to explore the influence of topographic relief on strain partitioning and fault evolution during long-term tectonic process. We did two types of sensitivity tests: (1) direction of the plate displacement for different fault strength (Figure A.4); and (2) rock strength difference between the Alpine fault (ϕ_{ft} or c_{ft}) and the stronger surroundings ($\phi_{bedrock}$ or $c_{bedrock}$) for different preexisting fault depths (Figure A.5).

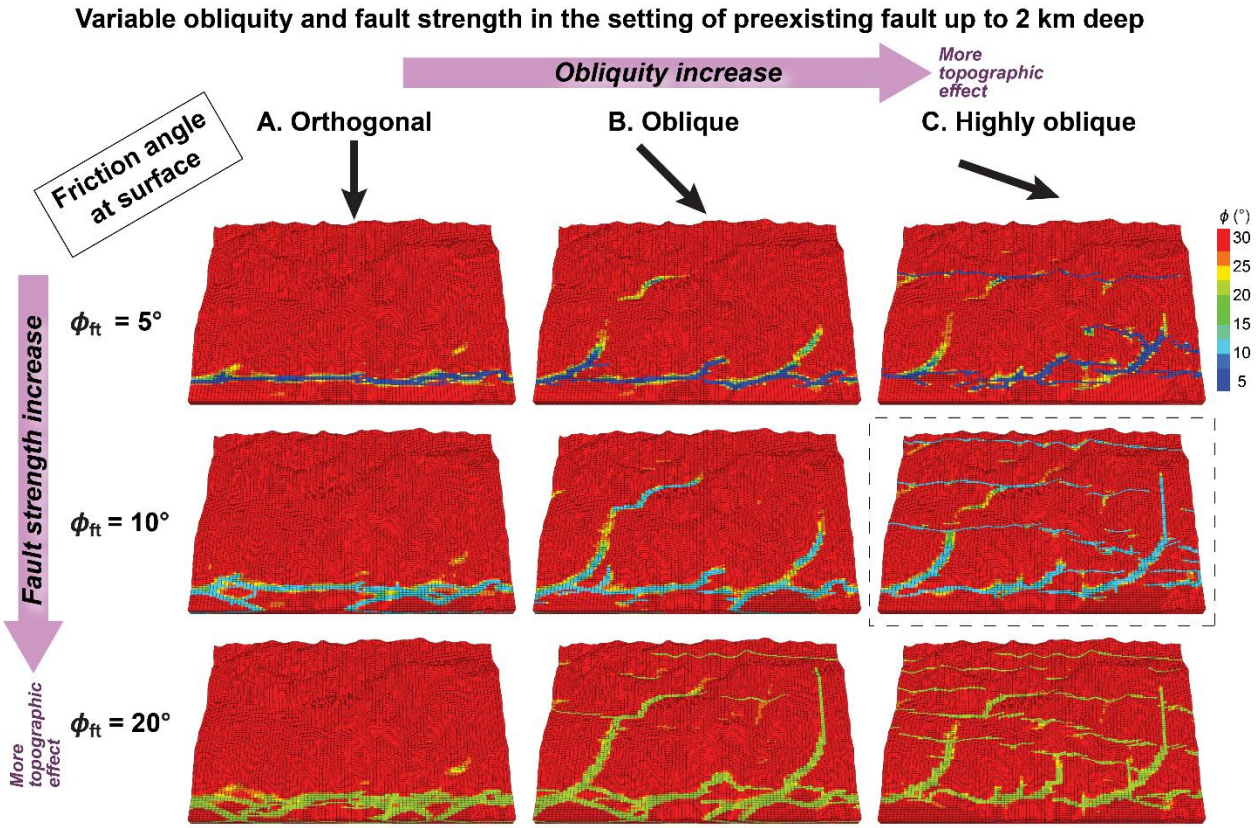

Figure A.4 The influence of obliquity and fault strength (friction angle, ϕ_{ft}) on strain partitioning. The obliquity of plate convergence increases from A to C. Greater magnitude of strain partitioning occurs within highly oblique models while strain is localized along discrete shear bands in orthogonal models. Note that even in orthogonal models, river valleys produce complex strain patterns. For a given convergence obliquity, the degree of strain partitioning is a function of the internal friction angle of fault. The initial parameters of each model are $\phi_{bedrock}$ = 30°, $c_{bedrock}$ = 20 MPa, and c_{ft} = 500 kPa.

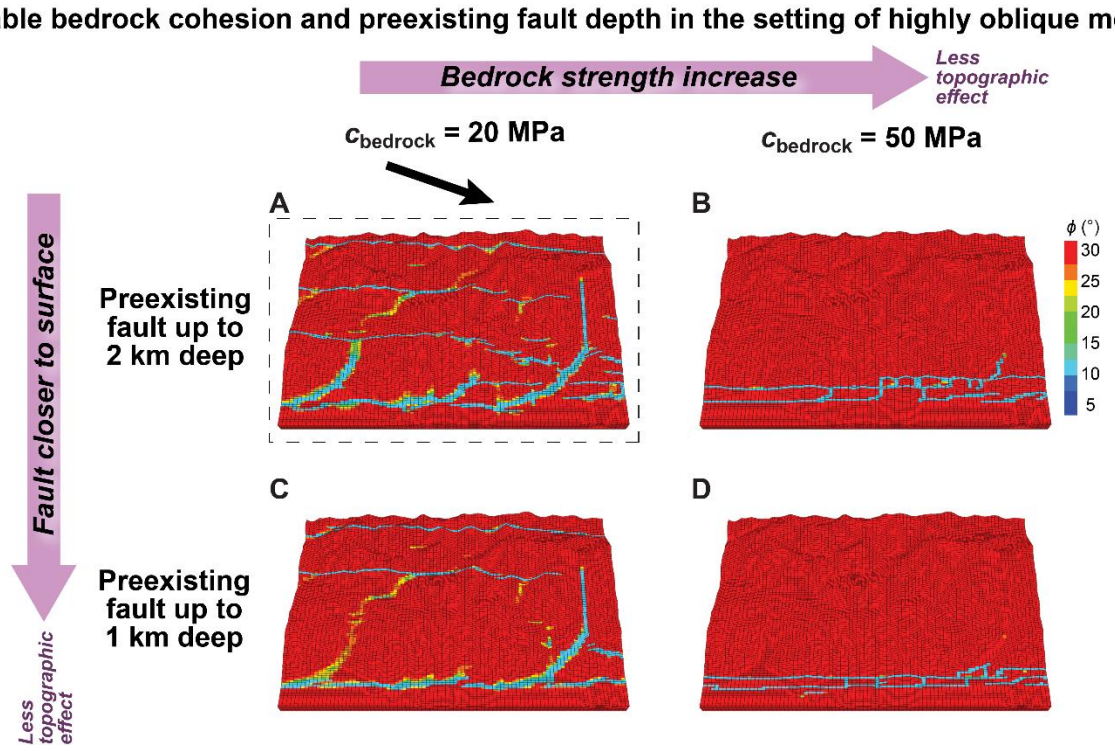

Figure A.5 The influence of bedrock strength (cohesion, $c_{bedrock}$) and preexisting fault depth on strain partitioning. A is the same model as the highly oblique model with ϕ_{ft} = 10° in Figure A.4 (dashed box). When bedrock cohesion (strength) is higher, strain is distinctly accommodated in the vicinity of the Alpine fault (B and D). Serial, zigzag-like, partitioning is unlikely to occur. Strain partitioning is more effective when preexisting weak zones are further below surface (see A and C). The initial parameters of each model are $\phi_{bedrock}$ = 30°, ϕ_{ft} = 10°, and c_{ft} = 500 kPa.

A.5. Stress State in Transpressional Mountain Belts

Using the model result of Figure A.4C when ϕ_{ft} = 10°, we analyzed the orientations of principle stresses and displacements to see possible fault type of each segment and compared them with reported field data in the range front area (Figure A.6).

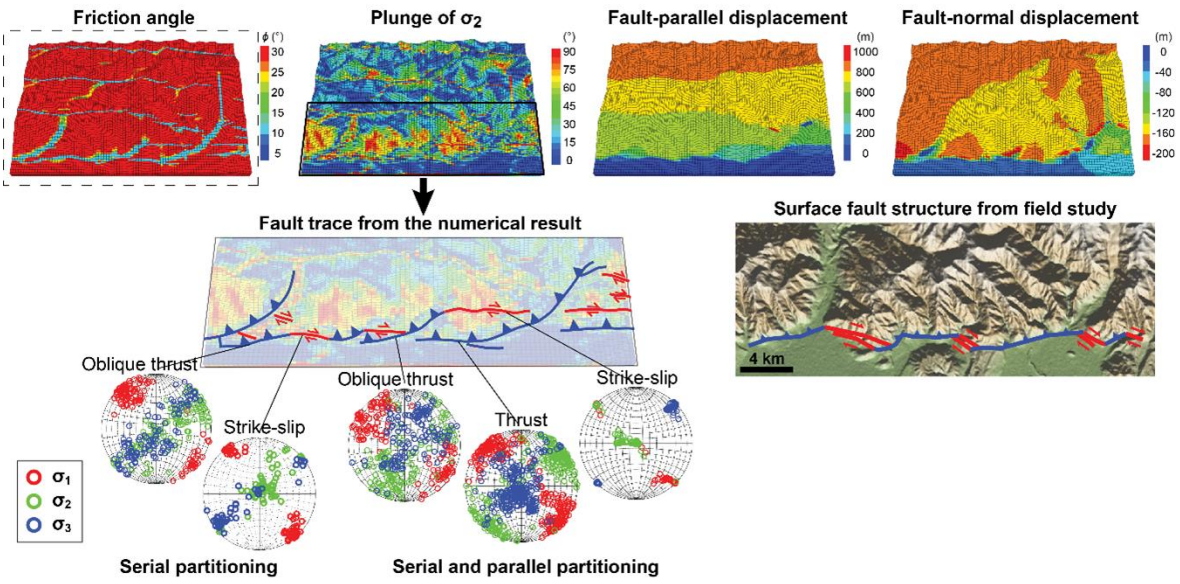

Figure A.6 Influence of topography on surficial fault failure by perturbing the ambient stress field. The fault trace from the σ_2 plunge map and the principal stress analyses indicates that the whole range front (35 km in length) is serially partitioned, and at smaller scales (1–7 km in length), parallel partitioning is partially shown. Although this result is generally consistent with the field study of the area (Barth et al., 2012), the difference between them probably resulted from lack of fluid (pore pressure) and surface (erosion) processes in our numerical models.

A.6. Appendix Conclusions and Future Study

Mutual influence between topography and oblique far-field tectonic stresses leads to strain partitioning and fault segmentation. When the strength ratio between the fault and surrounding rock is large (relatively weak fault vs. strong bedrock), both dip-slip and strike-slip displacements of deformation have entirely taken place along the preexisting weak zone. The results from this study suggest that the Alpine fault is a weak fault where strain localization occurs near the range front.

Topography (valley and ridge) affects surface fault geometries in all the convergent tectonic settings from orthogonal to highly oblique. To improve strain partitioning modeling, pore pressure and erosion parameters need to be considered (e.g., coupled to river incision model, etc.). In addition to the current quasi-static model, dynamic analysis is critical to understand stress perturbations and fault evolution during rupture.

APPENDIX B. TOPOGRAPHIC CONTROL ON SHALLOW FAULT STRUCTURE AND STRAIN PARTITIONING NEAR WHATAROA, NEW ZEALAND DEMONSTRATES WEAK ALPINE FAULT[3]

B.1. Appendix Abstract

It is notoriously difficult to characterise the strength and stress states of major plate boundaries. By taking advantage of the well-constrained stress contribution of topography adjacent to a segmented section of the Alpine fault, New Zealand, we have identified a mechanical mix that produces the distinct fault segmentation pattern seen in field observations. Slope-generated shear and normal stresses rotate the principal stresses relative to the regional tectonically derived stress state and under certain strength states influence the displacement pattern. Three-dimensional models show that the scale and form of the near- surface partitioning depend on both topographic relief and local fault strength relative to the bedrock. The models suggest the Alpine fault is weak to moderately weak relative to the bedrock and is a single structure to within c. 500 m of the surface, above which segmentation occurs. Adjacent to the Alpine fault, the stress state is highly variable. The intermediate principal stress, σ_2, is rotated from tectonically dominated, near-vertical beneath ridges to near-horizontal beneath large valleys. Individual segments along the Alpine Fault dominated by strike-slip faulting, oblique thrusting or thrusting, can be identified by extracting the topographic contribution to the stress state from numerical models.

B.2. Appendix Introduction

The Alpine fault, which extends along the western edge of the Southern Alps, is the most obvious manifestation of the Australian–Pacific plate boundary through the South Island (Figure B.1). It accommodates 65–75% of the total Australian–Pacific relative plate boundary movement, rupturing episodically in large magnitude earthquakes (M_w c. 8) and appears to be late in its seismic cycle (Sutherland

[3] The content of this chapter has been published in: Upton, P., Song, B.R, Koons, P.O., 2018, New Zealand Journal of Geology and Geophysics 61, 1–8, https://doi.org/10.1080/00288306.2017.1397706.

et al. 2007; Howarth et al. 2012, 2016). At scales of tens of kilometres, the Alpine fault appears to be a remarkably linear feature. Unlike at many oblique plate boundaries (Wentworth and Zoback 1989; McCaffrey 1992, 1996), it accommodates both fault-parallel and fault-normal components of deformation along a single structure through most of the frictional crust (Norris et al. 1990; Koons et al. 2003). Close to the surface, in the upper kilometre of the crust, the central Alpine fault becomes segmented (Norris and Cooper 1995, 1997; Barth et al. 2012; Langridge et al. 2014). When first mapping the central section, Norris and Cooper (1995, 1997) proposed 'serial partitioning' to explain their observations that northerly striking sections accommodate oblique thrusting, whereas more easterly striking sections are dominantly dextral strike-slip. This model was in contrast to the more common parallel partitioning where oblique motion is accommodated on parallel thrust and strike-slip faults (Wentworth and Zoback 1989; McCaffrey 1992, 1996). Norris and Cooper (1995) used sandbox models to propose that local stress field perturbations due to the steep range front with deeply incised river valleys promote serial partitioning. The acquisition of airborne light detection and ranging (LiDAR) data has refined these observations and highlighted more parallel partitioning along the fault (Barth et al. 2012; Langridge et al. 2014). Barth et al. (2012) suggest that the style of partitioning and fault segmentation is scale dependent. At the first order ($>10^6$ to 10^4 m) it is unpartitioned (Koons et al. 2003), at the second order (10^4 to 10^3 m) motion is serially partitioned in the upper c. 1–2 km and at a third order (10^3–10^0 m) it is parallel partitioned into fault wedges in the hanging wall.

Strain partitioning implies local perturbation of the stress state. Field-based studies and LiDAR cannot fully characterise the spatial variation of stress orientations; nor can they define the relative impact of controlling factors including topographic relief and fault strength. The purpose of this article is to use a fully 3D mechanical modelling system to quantify the constraints on strain partitioning and fault segmentation in the near-surface of the Alpine fault. Our focus is the Whataroa valley where recent drilling to nearly 1 km depth in an attempt to intersect the fault plane revealed unexpected complexity in the valley geometry and potentially the fault as well (Sutherland et al. 2017; Toy et al. 2017). We show that topographic relief, coupled with strain-dependent rheological evolution, perturbs the 3D stress state in the

top couple of kilometres, controlling where and how displacement on the Alpine fault is accommodated in the near-surface and we use this finding to estimate its frictional strength.

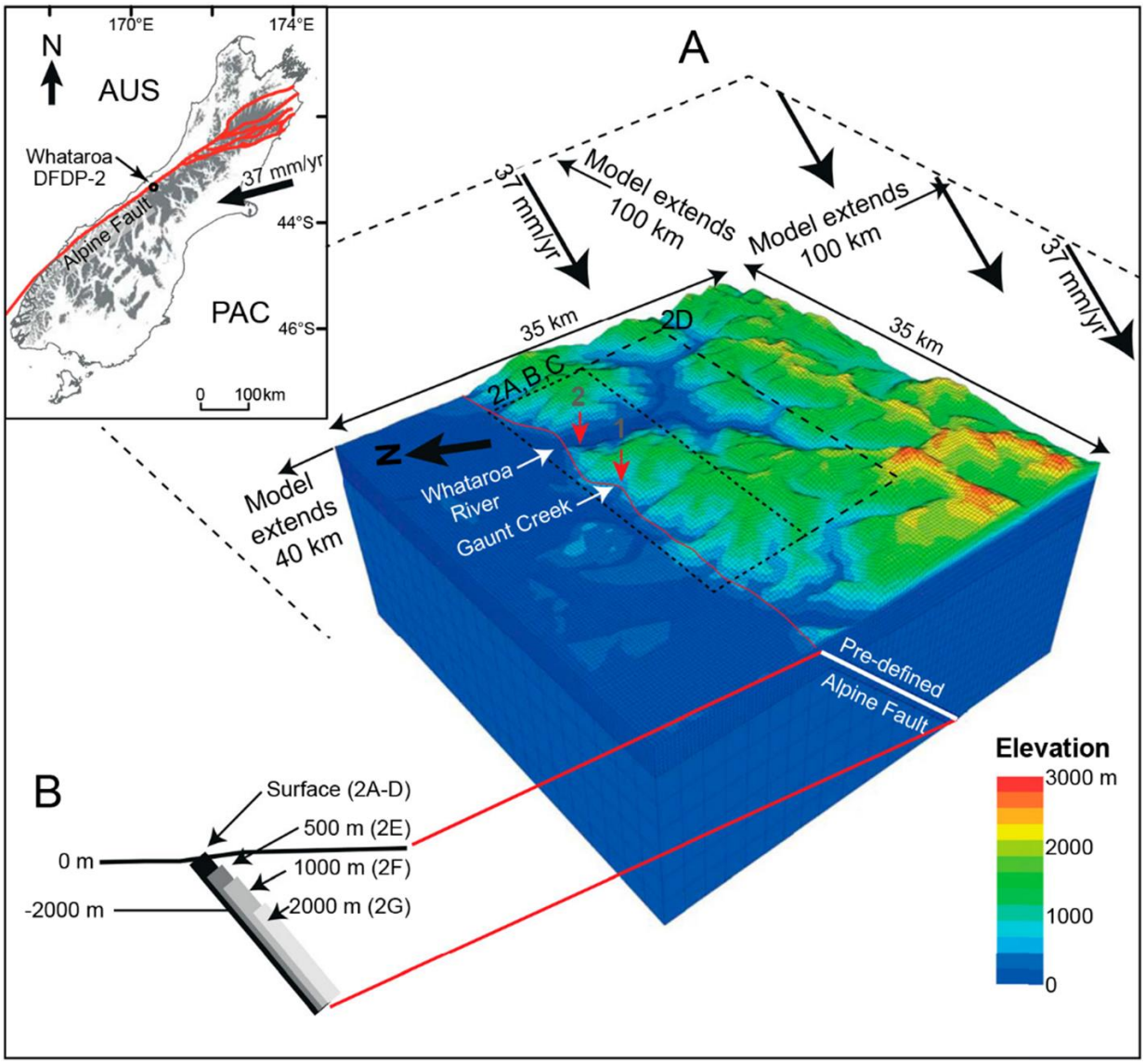

Figure B.1 Model setup for the Alpine fault. (a) Model geometry based on a 200 m digital elevation model (contour interval 200 m) of a 35 × 35 km region including the Whataroa River and Gaunt Creek. The region of interest is embedded into a larger model with dimensions of 175 km × 135 km × 25 km and velocity conditions are imposed on the boundaries as shown by the black arrows. Red arrows show the DFDP-1 and 2 drill holes (Sutherland et al. 2012, 2017). The Alpine fault is included as a pre-existing weakness dipping at 50° southeast to depths ranging from 0 m to 2000 m. The red line shows the trace of the Alpine fault from the Active Faults Database (Langridge et al. 2016). Dashed boxes show regions plotted in Figure B.2. (b) Detail of weaker Alpine fault material, each line is offset for illustrative purposed only, letters in brackets refer to Figure B.2. (Inset) Plate boundary setting showing the Alpine fault, Whataroa and the plate motion vector (DeMets et al. 1994).

B.3. Model Methodology

To explore the relationships between topographic relief, fault partitioning and fault strength, we solved simultaneously the motion and stress relations for a 3D deforming crust using a field-constrained rheological model. We solved a series of 3D mechanical models using the continuum code FLAC^{3D} (Itasca 2014).

B.3.1. Model Geometry and Boundary Conditions

Our model consists of a high-resolution region (x = 35 km, y = 35 km, depth = 10 km and 200 m resolution) centred on the mouth of the Whataroa gorge, shown in Figure B.1a. This is embedded into a larger low-resolution region which has the dimensions 175 km normal to and 235 km parallel to the Alpine fault, extending to a depth of 25 km. Only the high-resolution part of the model includes topography (Figure B.1a). The model boundaries are placed at a considerable distance from the high-resolution region to ensure that boundary effects do not influence our results. Velocity boundary conditions, derived from GPS and plate reconstructions (DeMets et al. 1994; Wallace et al. 2007) are imposed on the model edges. The material representing the Australian Plate is held still, whereas that representing the Pacific Plate moves at a rate of 37 mm/yr (Figure B.1a). All models have a pre-existing dipping (50° southeast) structure representing the Alpine fault (Figure B.1a). The strength of the structure and its initial geometry are varied for different models as described below.

B.3.2. Material Properties Used in the Models

The models assume a two-layered crust, similar to that in previously published modelling studies (Upton and Koons 2007; Upton et al. 2009; Koons et al. 2012; Roy et al. 2016). We set the model 'frictional viscous transition' 15 km below sea-level (b.s.l.) at a distance from the Alpine fault and elevated to 10 km b.s.l. adjacent to the fault (Koons 1987; Boese et al. 2012). We use a thermally activated mid-lower crust with material properties identical to previous modelling efforts (Upton and Koons 2007; Upton et al. 2009; Koons et al. 2012; and references therein). The upper crust of the hanging wall is modelled using a strain-

softening elastoplastic Mohr–Coulomb rheology based on measured fault rock strength from Haast Schist at the Cromwell Gorge in central Otago (Thomson 1993). This material has an initial friction angle (ϕ) of 35°, cohesion of 50 MPa, and the capacity to strain soften to a friction angle of 15° and cohesion of 100 kPa after 3% total strain (Thomson 1993; Koons et al. 2012; Roy et al. 2016). The friction angle of the pre-existing model Alpine fault is varied in the models from 10° to 25°. The friction angle is a measure of the shear strength of a material, measuring its resistance to sliding. In this study, we are interested in the relative strengths of the deformed (faulted) rock and undeformed hanging wall, and their evolution. The strain softening nature of the material modelled means there is a direct relationship between the amount of deformation (faulting) and the final value of the friction angle. For this reason, we use the friction angle (as a measure of strength) to illustrate where faulting has occurred in the models (e.g., Figure B.2).

Interpreting models of a highly evolved system, such as valley/ridge topography and segmentation along the Alpine fault, is challenging because we need to strike a balance between over- and under-defining the constraints on the models. In this case, we know that the Alpine fault is segmented in the uppermost crust and we have hypothesised that both fault strength and topography play a role in determining the nature of the segmentation. If we predefine the fault structure completely, we cannot watch its evolution. However, we need to pre-define enough of the fault structure for the deformation to occur in the areas that we know it does. We ran two sets of models to try and unpack these different controls.

Model Set 1 was aimed at the impact of fault strength on the development of strain localisation and fault segmentation. In these models, the pre-existing structure representing the Alpine fault extends all the way to the surface. Its friction angle was varied from 10° to 25°. These geometries were run to explore how weak a dipping structure must be for both components of deformation—fault normal and fault parallel—to be taken up along it. Models that produced strain patterns unlike those observed along the Alpine fault tell us what rheological parameters are unlikely. We then reduced the number of constraints on the models in Model Set 2. These models were run to explore the evolution of strain partitioning and fault segmentation relative to topography and fault strength. To do so, we varied the friction angle as above. We also varied the depth to which the weakness extends toward the surface from 2000 m b.s.l. to 500 m b.s.l. (Figure B.1b)

to explore the development of fault segmentation relative to topography. These models are not meant to imply that the Alpine fault suddenly goes from weak to strong in the shallow crust. They are designed so that we can observe how near-surface fault segmentation develops in the absence of pre-defined weaknesses at the surface. We varied the depth of the tip of the pre-defined Alpine fault to find the model that most closely matches field observations. By using a strain softening rheology for the hanging wall material, we can see where strain is localised in relation to other features in the model.

B.3.3. Model Limitations

The resolution of the central part of the models is 200 m, thus we can explore localisation of deformation only at scales > 200 m. We are unable to model features such as the anisotropy of the schist, the width of the fault damage zone or the footwall rheology. The latter two were called upon by Barth et al. (2012) as constraints on partitioning and the geometry of the hanging wall fault wedges. Our resolution is too coarse to resolve sediments thicknesses of <50–200 m. We also make assumptions about initial conditions and geometries. To avoid complex and difficult to code geometries, which can lead to numerical instabilities, we assume that the Alpine fault can be modelled as a straight line at 2 km or 500 m b.s.l. in Model Set 2. Given the non-linear nature of the range front at this scale, this is obviously a simplification and we note that in comparing our results with field observations. Finally, no surface processes are imposed in the models.

B.4. Model Results

B.4.1. Model Set 1

Varying the friction angle of the pre-defined weakness representing the Alpine fault had a significant impact on the nature of strain partitioning. A weak structure (ϕ = 10 or 15°) precludes any partitioning (Figures B.2a and B.2b) with both fault-parallel and fault-normal velocity components taken up along this weak structure, whereas a stronger (ϕ = 25°) dipping structure took up almost none of the fault-parallel velocity and only a portion of the fault-normal velocity (Figure B.2d). In the strong fault case, a series of

structures developed in the hanging wall, some parallel to the model Alpine fault and others at a high angle to it, generally along topographic lows. Fault-parallel motion was largely taken up on two structures, one 2–3 km inboard of the Alpine fault and a series of sub-parallel high strain zones 8–10 km inboard which form in the upper Whataroa and its tributaries. A second structure developed along the western side of the Whataroa valley (referred to as the Whataroa-model fault). It took up both strike-slip (sinistral) and reverse motion perpendicular to the model Alpine fault.

B.4.2. Model Set 2

In this model set, we explored the development of partitioning relative to topography by varying the depth to which we pre-define the Alpine fault weakness. As discussed above, this is not because we think that the Alpine fault suddenly strengthens in the near-surface, but so that we can observe how fault segmentation evolves unconstrained by pre-existing weaknesses. Boundary-parallel motion was taken up on vertical structures that develop in the hanging wall above the top of the pre-defined weakness. Where this depth is greater, vertical structures developed further from the range front (Figures B.2e–B.2g and B.3–B.5). The boundary-normal component was influenced by the topographic relief, especially where the depth to the top of the pre-defined model Alpine fault is greater (Figures B.3–B.5). Structures developed along the edge of the Whataroa and Waitangitaona valleys, which take up a considerable portion of the boundary-normal deformation. These structures are seen in the ϕ plots as zones of weakness that curve into the river valleys from the north (Figures B.3–B.5).

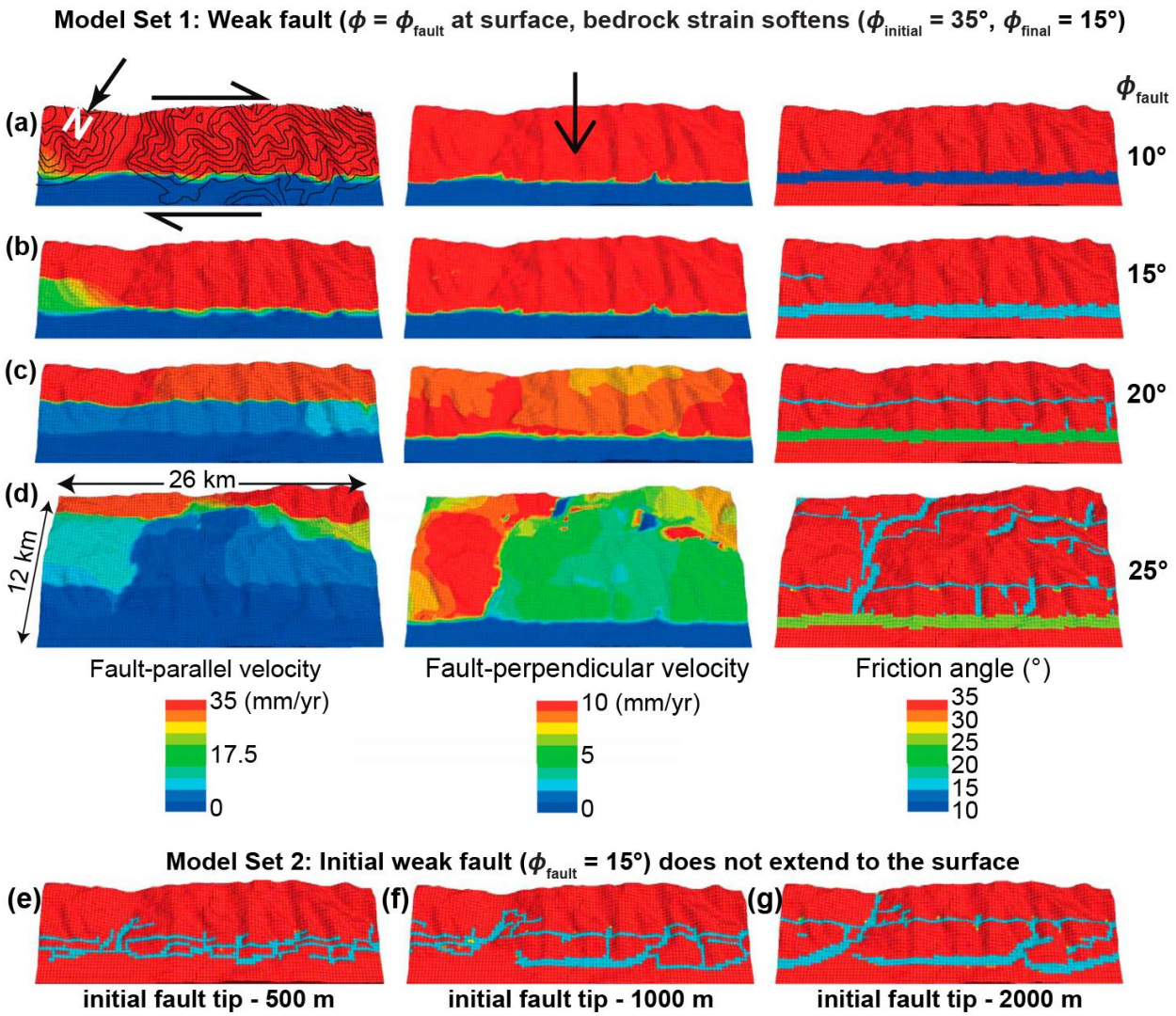

Figure B.2 Model results shown as fault-parallel velocity, fault-normal velocity and friction angle (ϕ) looking down on the models as shown by dashed boxes in Figure B.1a. Note that (d) includes a larger region as the zones of localisation in this model are more widespread than for (a)–(c). The material strain softens thus ϕ is representative of strain localisation. (a)–(d) The pre-existing Alpine fault extends to the surface. The black arrows in the left and middle columns of (a) show the relative motion that each column is illustrating. Boundary parallel or strike-slip motion in the left-hand column and boundary perpendicular or thrust motion in the middle column. (a) and (b) ϕ = 10 and 15° respectively. Both fault-parallel and perpendicular velocity components are taken up on that structure. (c) ϕ = 20°, a vertical structure develops c. 2–3 km southeast of the Alpine fault which takes up about half of the fault-parallel motion. Fault-normal motion is still taken up along the dipping Alpine fault. (d) ϕ = 25° is unfavourable for fault-par- allel motion while half of the fault-normal motion is still taken up along it. Several shear zones develop east of the Alpine fault. (e)–(g) Strain localisation above an initial weak Alpine fault (ϕ = 15°) that extends to within 500 m (e) 1000 m (f) or 2000 m (g) below the surface. In all cases, strain localises onto a series of structures which partition the motion in the near surface.

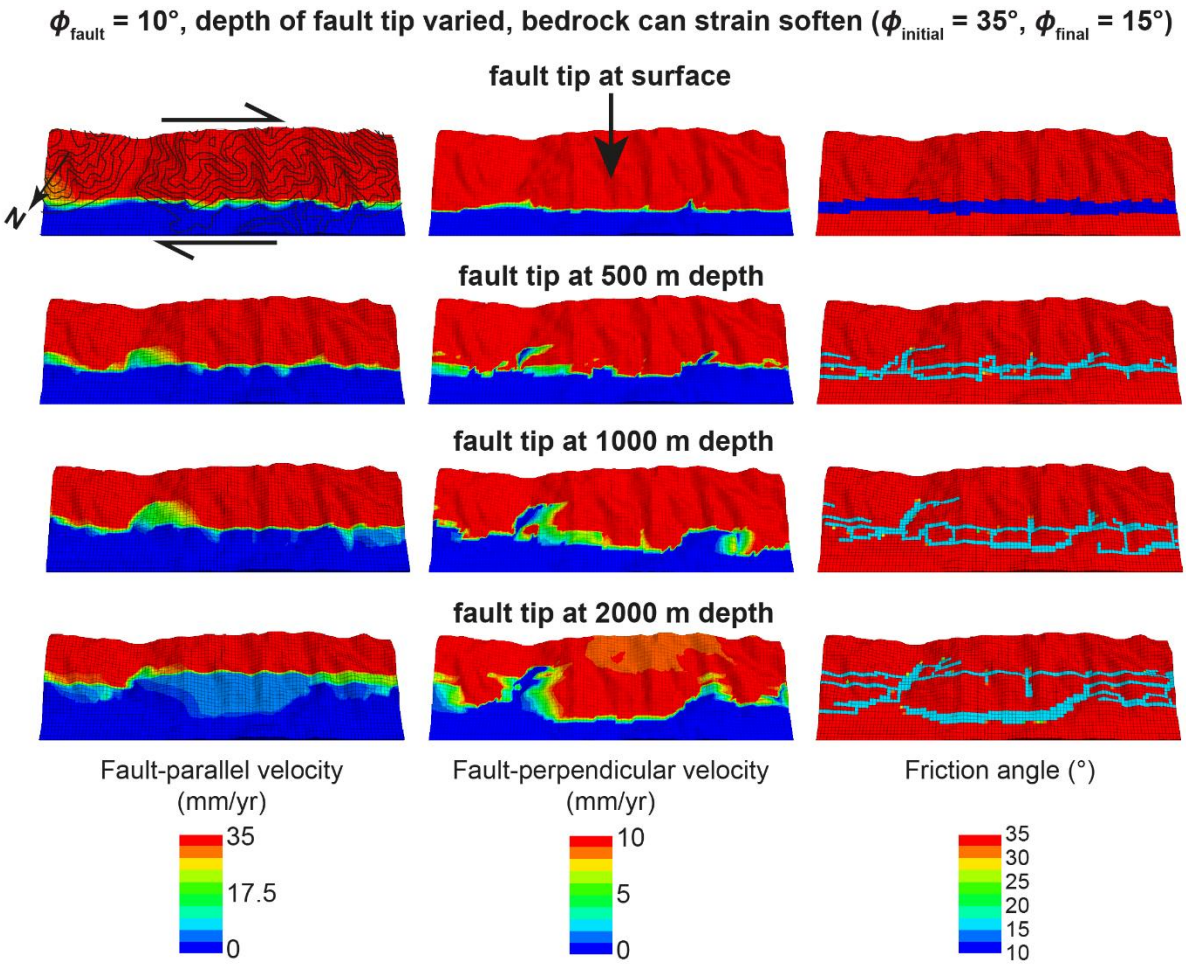

Figure B.3 Model results, boundary-parallel velocity, boundary-normal velocity and friction angle (representation of strain localisation) for a pre-existing fault strength of ϕ = 10° with the depth to the top of the fault zone varied from being at the surface to 2000 m b.s.l.

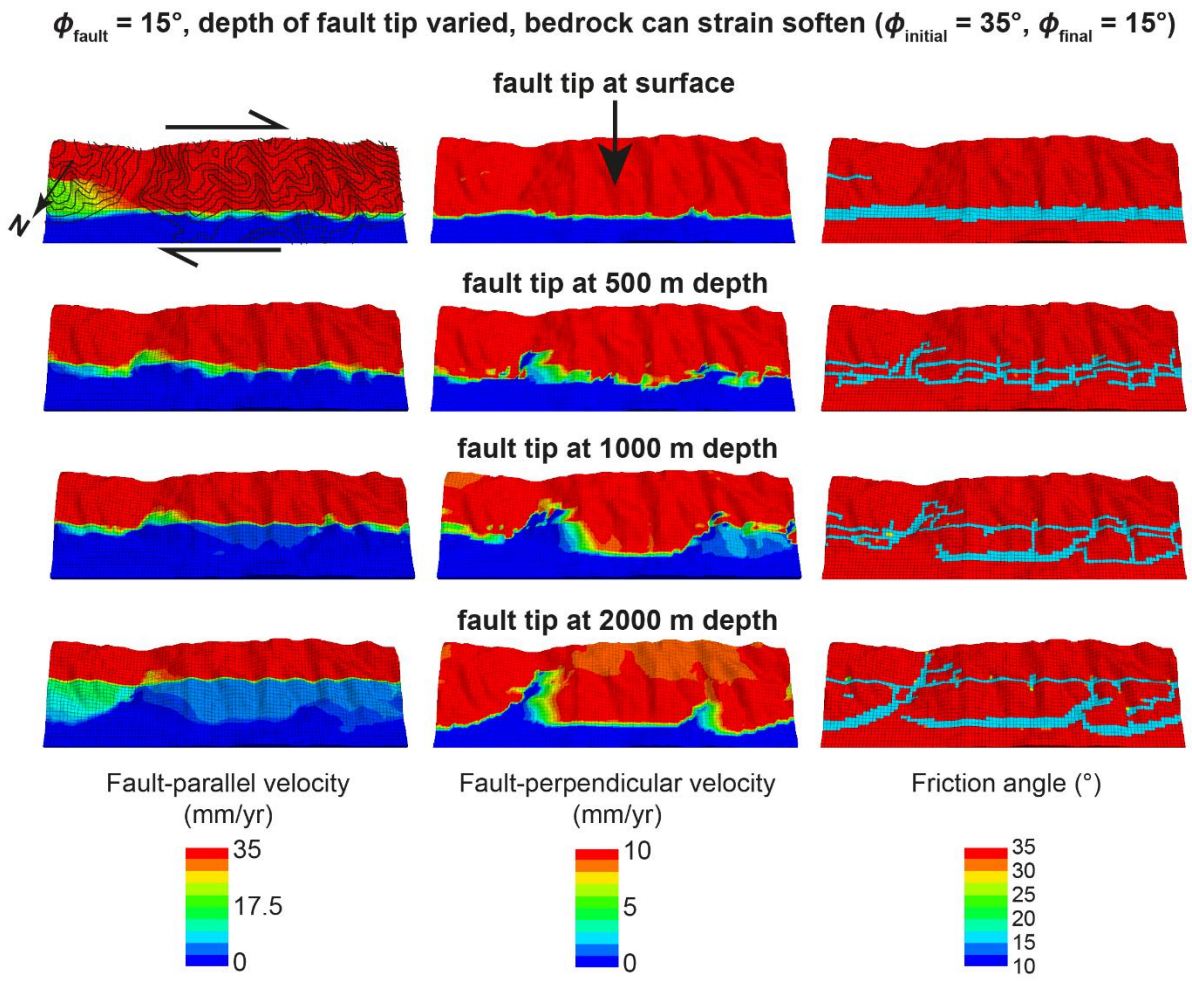

Figure B.4 Model results, boundary-parallel velocity, boundary-normal velocity and friction angle (representation of strain localisation) for a pre-existing fault strength of ϕ = 15° with the depth to the top of the fault zone varied from being at the surface to 2000 m b.s.l.

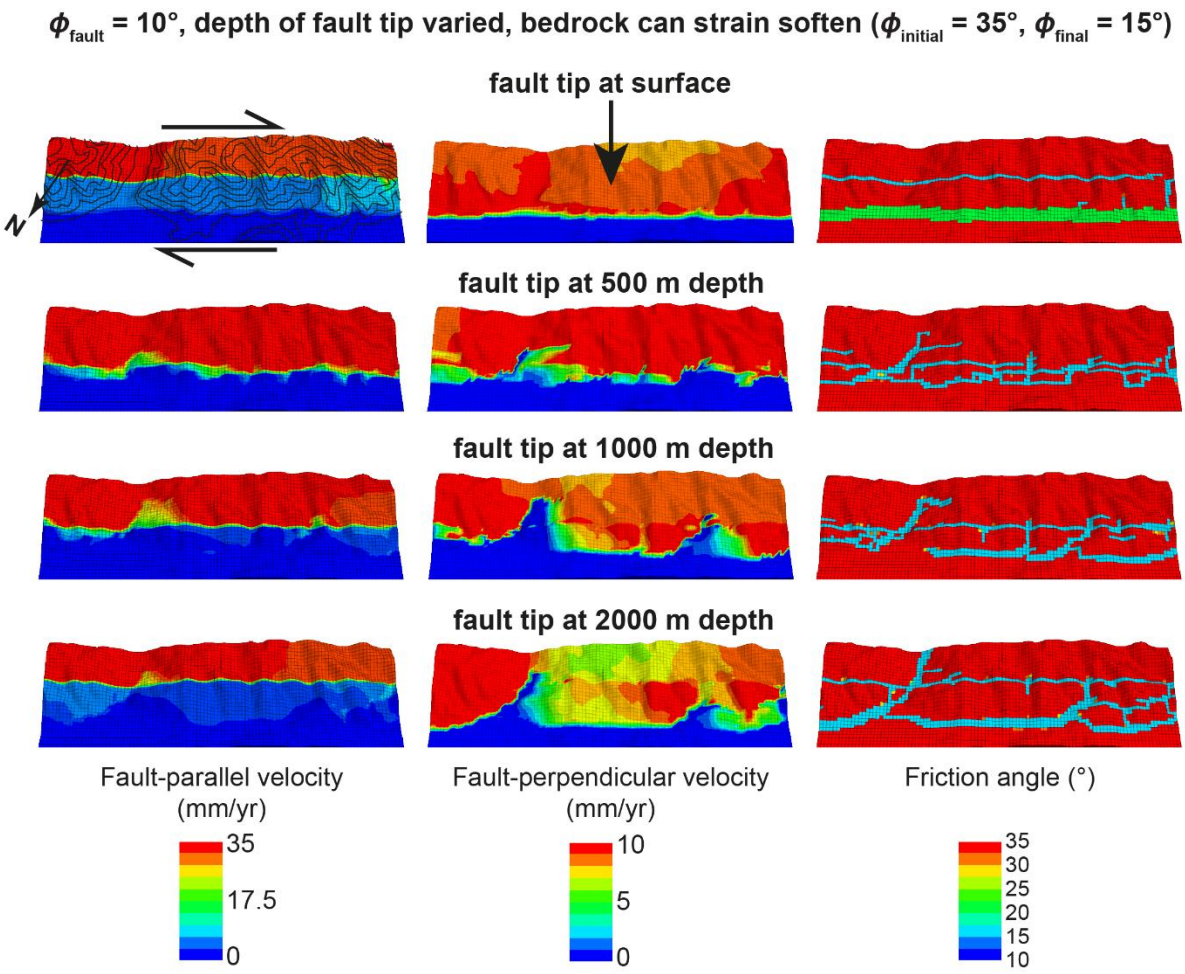

Figure B.5 Model results, boundary-parallel velocity, boundary-normal velocity and friction angle (representation of strain localisation) for a pre-existing fault strength of ϕ = 20° with the depth to the top of the fault zone varied from being at the surface to 2000 m b.s.l.

B.5. Discussion

B.5.1. Partitioning of Strain and Segment Characteristics

Varying the strength of the Alpine fault and the depth of the pre-defined weak dipping structure in the models produced a variety of patterns of strain localisation at the surface. As the strength ratio between the bedrock and the model Alpine fault decreased or the up-dip top of the pre-defined weak dipping structure was at greater depth, the development of vertical, dominantly strike-slip structures developed further southeast of the Alpine fault. Under these conditions, the Alpine fault is not favourably oriented to take up the highly oblique motion and deformation is strongly partitioned. Field observations and LiDAR suggest, based on the assumption that thrust segments dip at c. 45° and strike-slip segments are close to vertical, that strain partitioning in the shallow brittle crust is restricted to within c. 500 m of the range front (Barth et al. 2012; Langridge et al. 2014). Vertical strike-slip sections found crossing the toe of ridges c. 500 m inboard of the range front strongly suggest that individual structures merge into a single structure at shallow depths (Norris and Cooper 1995, 1997; Barth et al. 2012; Langridge et al. 2014). The field observations best fit a model with a single weak fault plane to c. 500 m b.s.l. and segmentation of the fault into shallow vertical and dipping structures at about this depth. A comparison with structures mapped from LiDAR also suggests this depth is <500 m (Figure B.6). Our model cannot capture all the complexity of the natural system and assumes that the Alpine fault at depth is planar. Where our model deviates most from the mapped features, northeast of Gaunt Creek, it is possible that the weak Alpine fault in the near-surface extends further northwest than in our simplified model geometry (Figure B.6).

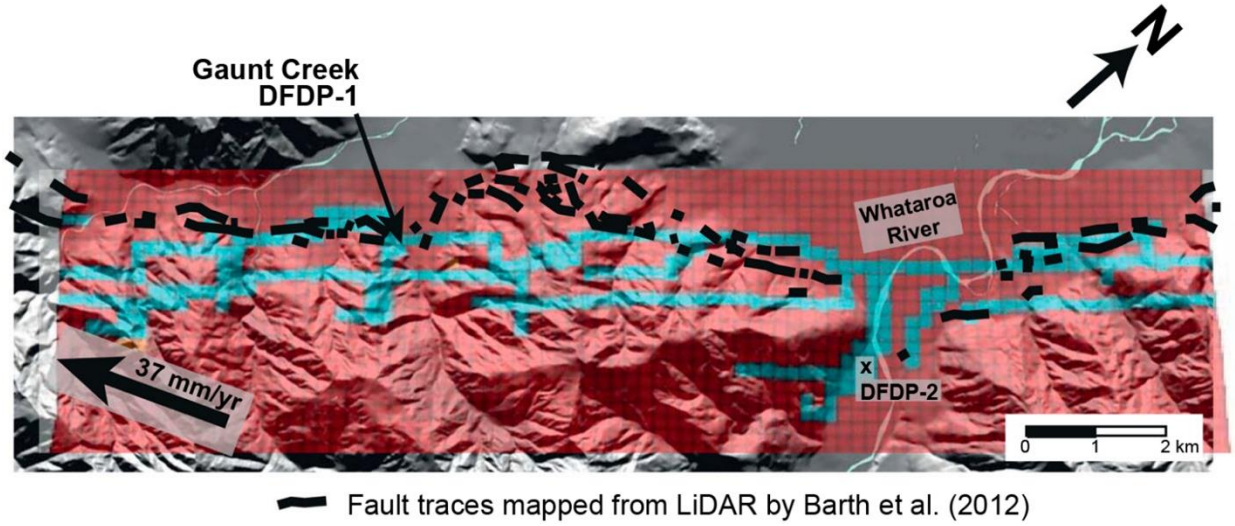

Figure B.6 Comparison of model (Figure B.2e) results with LiDAR observations (from Barth et al. 2012).

B.5.2. Stress State in the Near-Surface and its Relationship to Topography

The model stress state varies along strike (Figures B.7 and B.8). Beneath the ridges, the stress state is close to the regional stress regime where σ_2 is near vertical, i.e., far-field tectonic driving forces dominate the stress regime (Koons 1994; Boese et al. 2012). Beneath the valleys, the intermediate principal stress, σ_2, is rotated to near-horizontal by the topographic relief, reflecting a thrust stress regime rather than oblique strike-slip. Along the model Alpine fault, we observe rotation of the stress state and partitioning of deformation onto oblique thrust and oblique strike-slip structures. At the valley mouth, a thrust segment curves into the valley and the stress state is one of almost pure thrusting (Figure B.7c). Along strike to the south, parallel partitioning is obvious with a strike-slip segment (Figure B.7f) and a thrust segment (Figure B.7e). σ_1 for this segment is very close to the regional maximum horizontal stress observed by Boese et al. (2012). As well as rotation of the stress state, field observations from Franz Josef, 20 km south of our field area, suggest that the magnitudes of the σ_2 and σ_3 are close and readily switch (Enlow and Koons 1998). The youngest shallow-level vein sets in the Franz Josef river valley are both sub-horizontal and sub-vertical and these two sets are mutually cross-cutting. This implies that σ_2 and σ_3 are of similar magnitude and there was some switching between the two in the deformation history (Hanson et al. 1990).

The Whataroa valley and its tributaries are the largest erosional hole along the western Southern Alps, representing a major departure from the dominant topography of the steep and high Southern Alps. We might expect to see rotation of the stress state and strain concentration along the Whataroa, as a consequence of slope-generated shear and normal stresses which reduce the amount of tectonic stress required to reach failure (Koons and Kirby 2007). Where the Alpine fault is strong (ϕ = 20 or 25°), our models do predict significant perturbation of the stress state. They also predict that tectonic stresses in the hanging wall combine with slope-generated stresses to form a structure we have called the Whataroa-model fault, which extends c. 10 km along the western Whataroa valley (Figure B.5).

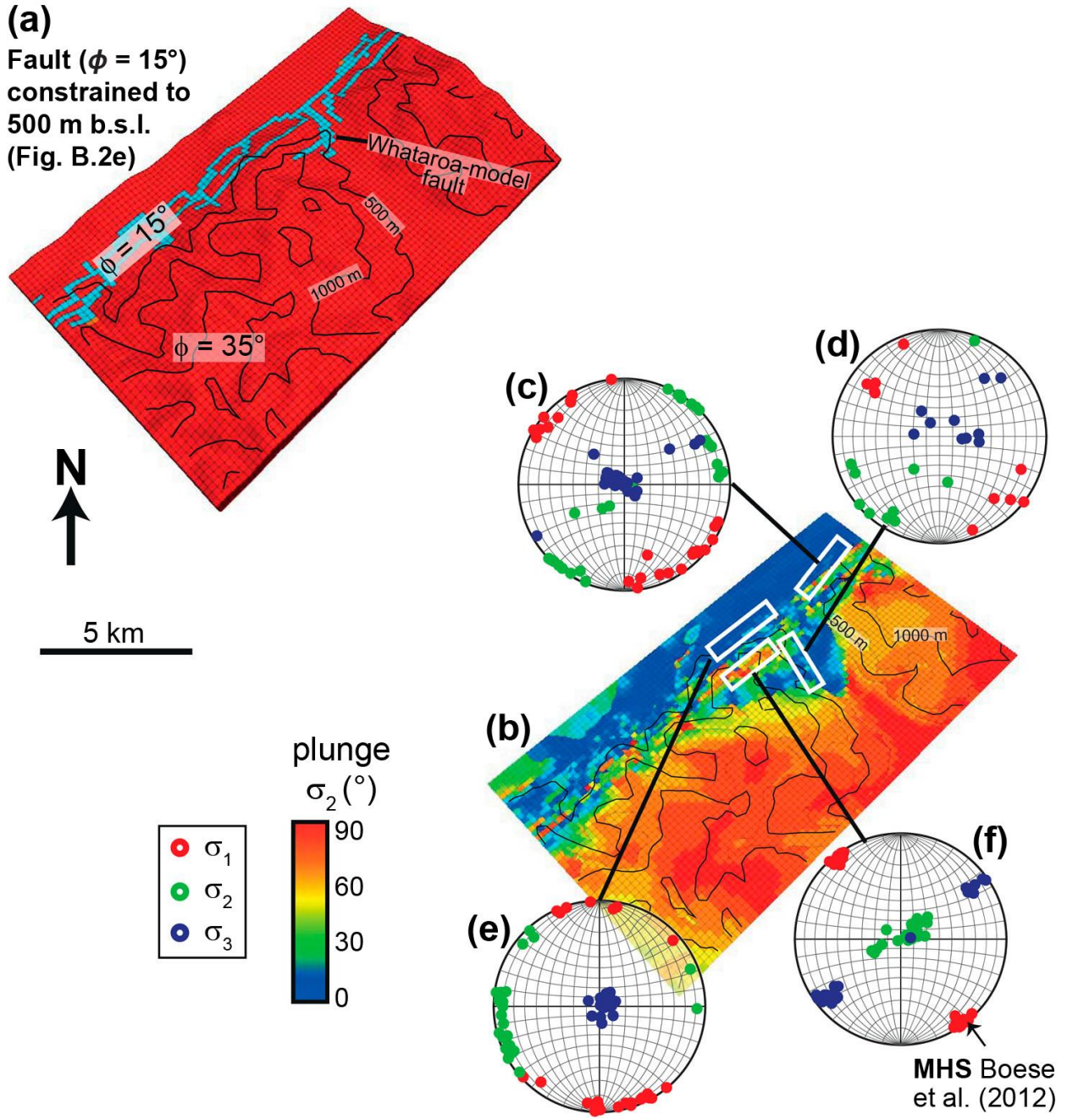

Figure B.7 States of stress along the model Alpine fault extending to 500 m b.s.l. (a) The friction angle at the surface above an initial planar Alpine fault weakness extending to 500 m b.s.l. Light blue: where the hanging wall has strain softened to $\phi = 15°$, shows the location of high strain zones in the models. (b) Plunge of σ_2 on a horizontal slice at sea-level though the model shown in (a). Blue: σ_2 is near horizontal. Red: σ_2 is near vertical. (c)–(f) Stereonet plots showing the stress state within regions outlined by the white boxes. (c) and (e) Thrust segments close to the range front. (d) Whataroa-model fault which forms as an oblique sinistral strike-slip structure along the western edge of the Whataroa Valley. (f) A strike-slip segment where motion is partitioned between here and the thrust segment shown in (e). MHS = Maximum horizontal stress determined by Boese et al. (2012).

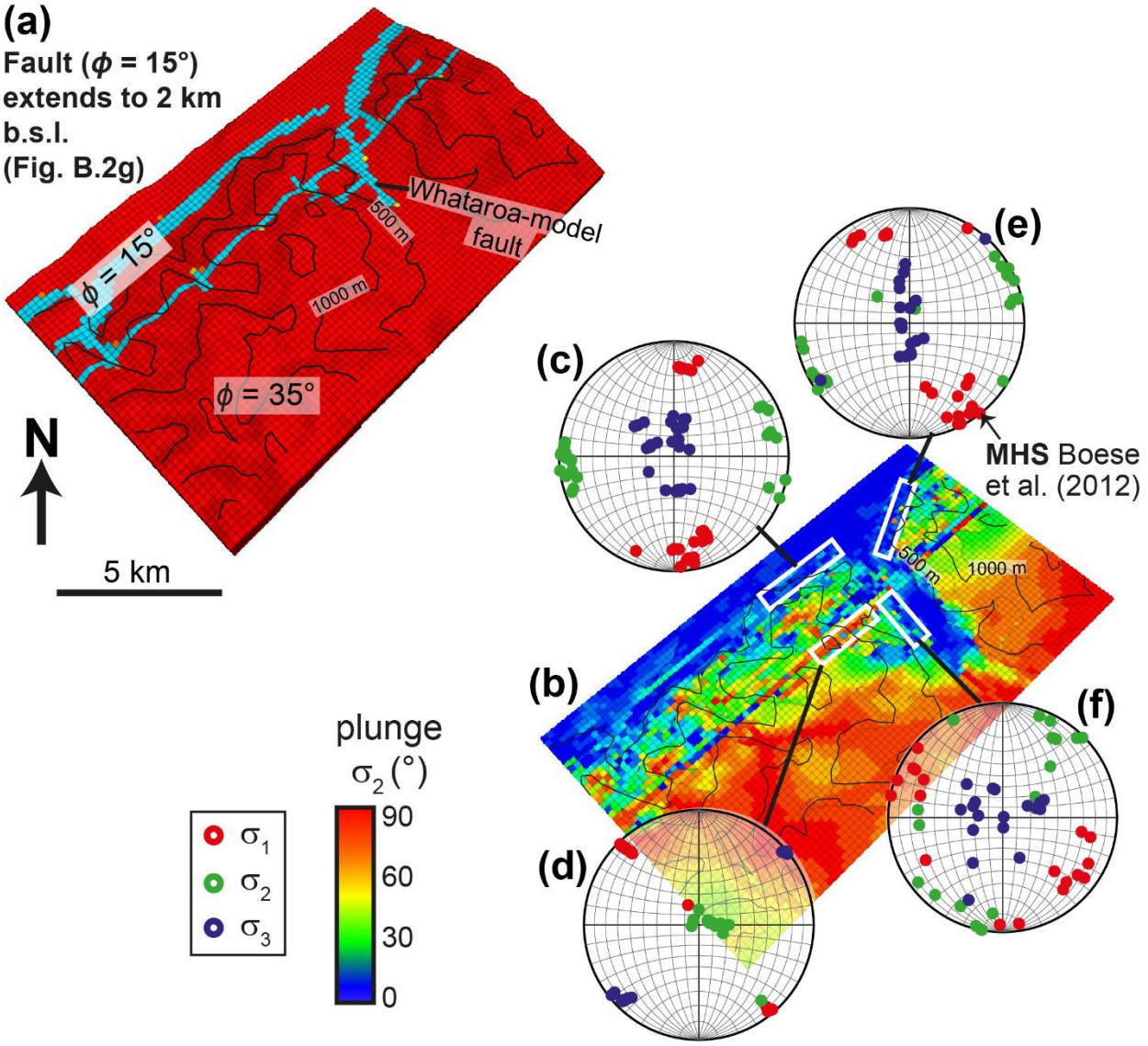

Figure B.8 States of stress along the model Alpine fault extending to 2000 m b.s.l. (a) The friction angle at the surface above a pre-defined Alpine fault weakness extending to 2000 m b.s.l. (b) Plunge of σ_2 on a horizontal slice at sea-level through the model shown in A. Blue: σ_2 is near horizontal. Red: σ_2 is near vertical. (c)–(f) Stereonet plots showing the stress state within regions outlined by the white boxes. (c) A near pure thrust segment close to the range front. (d) A strike slip segment where motion is partitioned between here and the thrust segment shown in (g). (e) An oblique thrust segments close to the range front. (f) Whataroa-model fault which forms as an oblique sinistral strike-slip structure along the western edge of the Whataroa valley. MHS = Maximum horizontal stress determined by Boese et al. (2012).

B.5.3. Controls on the Strength of the Shallow Alpine Fault

The lack of field evidence for (1) major active structures parallel to the large valleys, and (2) vertical strike-slip structures at distances > 500 m from the range front provides a robust constraint on the strength of the Alpine fault. The lack of these two suggest the Alpine fault is sufficiently weak (ϕ < 20°) that the topographic stress perturbation of the Whataroa valley and its tributaries is insufficient to shift significant failure away from the dipping fault plane. In these models, tectonic stresses in the hanging wall still combine with slope-generated stresses to form a shorter version of the Whataroa-model fault (Figure B.7) which extends c. 2 km along the western Whataroa valley. This modelled structure is predicted to have minor oblique sinistral strike-slip motion, up to the east (Figures B.3 and B.7d). A structure such as this might explain the bedrock geometry at the DFDP-2B drill site where the depth to basement far exceeded expectations (Sutherland et al. 2017). This could be due to one or both of the following processes. Motion along the structure dropping the western side of the valley down relative to the eastern side or enhanced erosion of a weakened fault zone by successive glaciations during the Pleistocene resulting in an over-steepened valley (Roy et al. 2015).

B.5.4. Comparison with Other Models

Barth et al. (2012) propose that the width, extent and geometry of the fault wedges are controlled by the thickness of the footwall sediments and the width of the fault damage zone. We cannot test these two attributes as constraints because the resolution of our models is too coarse to include them. We do show that stress perturbations, which result from topography, as first mooted by Norris and Cooper (1995, 1997), produce a combination of serial and parallel partitioning along the range front of the Southern Alps. We would argue that it is not necessary to appeal to footwall rheology to explain the observations, but we cannot discount the suggestion that it does play a role in controlling the details of individual fault segments, as suggested previously (Barth et al. 2012). Our models differ from Norris and Cooper (1995, 1997) in that they have no pure strike-slip segments, instead a combination of serial and parallel partitioning develops, as also noted by Langridge et al. (2014) in their interpretation of LiDAR observations.

B.6. Appendix Conclusions

In mountainous regions, topography perturbs the stress state, and couples with rheology to influence the localisation of strain, particularly in regions of oblique deformation. We used 3D mechanical models to show that as the strength ratio between the bedrock and an oblique dipping fault is decreased, or the depth to the up-dip tip of a single weak dipping structure is increased, two effects are observed. First, vertical, dominantly strike-slip structures develop further and further into the hanging wall. Second, strain is localised into significant topographic perturbations. We use field and LiDAR observations, our 3D models and the perturbation to the stress field from topography to evaluate the strength and stress regime of the Alpine fault. A strong model Alpine fault or a situation where boundary-parallel motion is able to bleed off a single dipping structure onto vertical strike-slip faults at depths >500 m does not match the observations. A weak model Alpine fault, which is a single structure at depths >500 m, predicts that both vertical strike-slip structures and structures following topo- graphic lows are restricted to within c. 500 m of the range front, consistent with field and LiDAR observations. At shallower depths, rather than pure serial or parallel partitioning occurring, the interaction of a weak fault and the topography produces a complex pattern that is a combination of both serial and parallel partitioning. Strike-slip segments occur within the hanging wall of the range front, while oblique thrusting is taken up at the range front.

B.7. Appendix Acknowledgements

This work was supported by the NZ Ministry for Business Innovation and Employment and National Science Foundation grants 1009626 and 1324637 to P. O. Koons; Division of Earth Sciences. The models and analysis presented in this manuscript are built on the considerable contribution of the late Richard Norris to our understanding the Alpine fault and we are grateful for the many discussions with Richard over several years. We also acknowledge useful feedback and discussions with Alan Cooper, Rupert Sutherland and Susan Ellis. Tim Little, Rob Langridge, Virginia Toy and two anonymous reviewers all provided constructive feedback. Nick Mortimer is thanked for his editorial oversight.

APPENDIX C. ENERGY PARTITIONING, DYNAMIC FRAGMENTATION, AND OFF-FAULT DAMAGE IN THE EARTHQUAKE SOURCE VOLUME[4]

C.1. Appendix Abstract

Seismological fracture or breakdown energy represents energy expended in a volume surrounding the advancing rupture front and the slipping fault surface. Estimates are commonly obtained by inverting ground motions and using the results to model slip on the fault surface. However, this practice cannot identify contributions from different energy-consumption processes, so our understanding of the importance of these processes comes largely from field- and laboratory-based studies. Here we use garnet fragment size data to estimate surface-area energy density with distance from the fault core in the damage zone of a deeply exhumed strike-slip fault/shear zone. Estimated energy densities per fragmentation event range from 2.87×10^3 to 2.72×10^5 J/m^3 in the outer and inner portions of the dynamic damage zone, respectively, with the dynamic zone being inferred from the fractal dimensions of fragment size distributions and other indicators. Integrating over the ~105 m width of the dynamic damage zone gives fracture surface-area energy per unit fault area ranging from a lower bound of 6.63×10^5 J/m^2 to an upper bound of 1.63×10^7 J/m^2 per event. This range overlaps with most geological, theoretical, and kinematic slip-model estimates of energy expenditure in the source volume for earthquakes characterized by seismic moments $>10^{17}$ N·m. We employ physics-based fragmentation models to estimate equivalent tensile strain rates associated with garnet fragmentation, which range from 5.42×10^2 to 1.04×10^4 s^{-1} per earthquake in the outer and inner portions of the dynamic damage zone, respectively. Our results suggest that surface-energy generation is a non-negligible component of the earthquake energy budget.

[4] The content of this chapter has been published in: Johnson, S.E., Song, W.J., Vel, S.S., Song, B.R, Gerbi, C.C., 2021, Journal of Geophysical Research 126, e2021JB022616, https://doi.org/10.1029/2021JB022616.

C.2. Appendix Plain Language Summary

Less than 20% of the total energy released from most earthquakes radiates away from the fault as seismic waves that cause ground shaking. Thus, a large portion of the total energy is expended in surrounding rocks as frictional heat and a variety of damage processes. The partitioning of energy into these rocks directly modulates patterns of rupture and slip, and therefore earthquake intensity. Estimates of earthquake energy are commonly obtained from ground motions recorded by seismometers located long distances from the fault. This method cannot differentiate between energy consumed as damage versus frictional heat. Thus, the relative roles of these two energy sinks remain an open question of fundamental importance for understanding seismic hazards and the earthquake energy budget top to bottom. Here we use fragmented garnet grains to estimate the energy partitioned into the damaged rock volume. Our results suggest that surface-energy generation is a non-negligible component of the earthquake energy budget.

C.3. Appendix Introduction

During an earthquake, released elastic strain energy U_{rel} is converted to the energy U_{conv} required to advance the rupture and to overcome the frictional resistance to slip on the trailing fault (see Table C.1 for notation used in this paper). The rest radiates away as elastodynamic waves U_{rad} that produce ground shaking. U_{rad} is the only quantity that can be directly measured and generally comprises less than 15–20% of U_{rel} (e.g., McGarr et al., 1979; Lockner and Okubo, 1983; Lachenbruch and McGarr, 1990; McGarr, 1999; Shi et al., 2008; Okubo et al., 2019). U_{conv} can be divided (e.g., Kanamori and Brodsky, 2004) into the energy of frictional heat U_{fh} and a variety of inelastic physical and chemical processes U_{sa} that include on- and off-fault fracturing and dilatancy in the broader source volume. U_{sa} can be equated to seismological fracture energy (e.g., Kanamori and Rivera, 2006) or breakdown work (Tinti et al., 2005), depending on its mathematical definition and how off-fault damage is treated. Thus, a simplified energy balance, displayed graphically in Figure C.1a, can be written as:

$$U_{\mathrm{rel}} = U_{\mathrm{conv}} + U_{\mathrm{rad}} = U_{\mathrm{sa}} + U_{\mathrm{fh}} + U_{\mathrm{rad}} \tag{C1}$$

The energy balance in Figure C.1a represents the time-dependent evolution of stress and slip for a unit area of fault surface. Figure C.1b puts this energy balance into the context of the larger earthquake source volume by considering a point "A" adjacent to a strike-slip fault at ~10 km depth during subshear rupture propagation. Following nucleation, the rupture tip moves from right to left at km/s rates with the upper lobe of stress concentration associated with locally divergent particle motion and therefore tensile (T) stresses. As the rupture front propagates, point A reaches the peak stress τ_{p} and fails. As it is engulfed by the region of tensile stress concentration surrounding the rupture front, the released elastic strain energy is converted to surface energy through intense fracturing among other energy-consuming processes, and the stress drops along the thick curve with arrowheads in Figure C.1a. When the rupture front has passed, point A is subjected to additional dynamic stresses associated with slip at m/s rates on the rough trailing fault surface and continues to consume energy in the form of additional fracture plus frictional heat among other energy sinks until the residual stress τ_1 is reached at the critical slip distance $\mathrm{D_c}$.

U_{sa} is the energy consumed in breaking down the rocks during rupture and slip and determines the radiation efficiency $U_{\mathrm{rad}}/(U_{\mathrm{rad}} + U_{\mathrm{sa}})$, directly modulating patterns and rates of slip and rupture propagation, near-fault particle velocities, and earthquake intensity (e.g., Walsh, 1965; Husseini et al., 1975; Andrews, 1976, 2005; Lockner et al., 1977; Harris and Day, 1997; Spudich and Olsen, 2001; Kanamori and Brodsky, 2004; Dunham et al., 2011; Huang et al., 2014b; Ben-Zion et al., 2015; Nielsen et al., 2016; Lambert and Lapusta, 2020). U_{fh} also modulates rupture dynamics by driving processes that affect the dynamic frictional resistance to fault slip such as flash heating (Rice, 2006; Goldsby and Tullis, 2011; Brantut and Platt, 2017; Brantut and Viesca, 2017; Sleep, 2019), frictional melting (Hirose and Shimamoto, 2005; Di Toro et al., 2006, 2009), high-temperature crystal plasticity (Bestmann et al., 2012; Verberne et al., 2013), superplastic flow (Green et al., 2015), thermal pressurization of pore fluids (Sibson, 1973; Wibberley and Shimamoto, 2005; Rice, 2006; Noda and Lapusta, 2010; Viesca and Garagash, 2015; Brantut and Platt, 2017; Acosta et al., 2018), and mineral phase transformations (Schubnel et al., 2005;

Brantut et al., 2011). Most of these thermally driven processes are localized along or directly adjacent to slipping surfaces, but because they can influence rupture dynamics, they can also contribute to on- and off-fault damage and therefore U_{sa}.

Understanding the relative magnitudes and roles of U_{sa} and U_{fh} is a first-order problem in earthquake mechanics. However, when evaluating the geological processes that occur during rupture propagation and fault slip, it is difficult to quantitatively separate and estimate U_{sa} and U_{fh} (Shipton et al., 2006). In addition, while U_{sa} can be derived from estimates of moment magnitude, stress drop, and radiated energy (e.g., Abercrombie and Rice, 2005; Viesca and Garagash, 2015), U_{fh} is effectively transparent in seismological observables. Thus, there is deep uncertainty regarding the relative magnitudes of U_{sa} and U_{fh} (e.g., Kanamori, 1994; Shipton et al., 2006; Beeler et al., 2012, 2016; Ben-Zion and Sammis, 2013; Nielsen et al., 2016; Scholz, 2019; Brodsky et al., 2020). Very few geological studies have directly estimated the value of U_{sa} (Olgaard and Brace, 1983; Chester et al., 2005; Reches and Dewers, 2005; Wilson et al., 2005; Ma et al., 2006; Pittarello et al., 2008), with results ranging from negligible to major contributions to U_{conv}. Even fewer geological studies have estimated U_{fh} (Matsumoto et al., 2001; Reches and Dewers, 2005; Pittarello et al., 2008; Fulton et al., 2013 updated by Brodsky et al., 2020), the results also spanning a range of U_{conv}. High-strain-rate experimental estimates of U_{sa} and/or U_{fh} are equally sparse (e.g., Doan and Billi, 2011; Aben et al., 2016, 2020; Barber and Griffith, 2017; Liu and Zhao, 2021).

Our focus in the present study is U_{sa}. Geological evidence for U_{sa} around mature continental strike-slip faults is well preserved in the uppermost crust as highly fragmented and pulverized rock (e.g., Chester et al., 2005; Wilson et al., 2005; Dor et al., 2006, 2009; Rockwell et al., 2009; Mitchell et al., 2011; Wechsler et al., 2011; Lin and Yamashita, 2013; Rempe et al., 2013). A few studies in these and other faults provide estimates of the energy expended in generating new surface area by calculating total surface area of fragments, typically using optical and electron-beam imaging (e.g., Sammis et al., 1987; Chester et al., 2005; Ma et al., 2006; Keulen et al., 2007; Muto et al., 2015), or laser methods (e.g., Olgaard and Brace, 1983; Reches and Dewers, 2005; Wilson et al., 2005; Rockwell et al., 2009; Wechsler et al., 2011). These

highly fragmented and pulverized rocks have provided the motivation for numerous experimental studies seeking to quantify the stresses and strain rates required to impart such damage under relatively low confining pressures (e.g., Xia et al., 2008; Doan and Gary, 2009; Doan and Billi, 2011; Yuan et al., 2011; Doan and d'Hour, 2012; Aben et al., 2016, 2017a, 2020; Barber and Griffith, 2017; Griffith et al., 2018). We conclude from this experimental work, along with theoretical (e.g., Poliakov et al., 2002; Reches and Dewers, 2005; Rice et al., 2005) and numerical (e.g., Andrews, 2005; Dunham et al., 2011; Shi and Day, 2013; Ampuero and Mao, 2017; Xu and Ben-Zion, 2017; Thomas and Bhat, 2018; Okubo et al., 2019) studies, that consumption of U_{sa} in intense off-fault fragmentation and pulverization involves dynamic coseismic stresses superimposed on whatever preexisting quasistatic or dynamic damage might already be present. An important point made above in relation to Figure C.1 is that these transient stress pulses may not be restricted to the process zone around the advancing rupture front but may also occur during the slipping phase behind the advancing rupture from stress peaks associated with, for example, roughness, asperities, bends, and barriers that may lead to individual rock volumes experiencing multiple, rapid stress pulses large enough to cause multiple fracturing and fragmentation stages during a single earthquake.

In contrast to the near-surface exposures referenced above, very little is known about U_{sa} at depths corresponding to the base of the seismogenic zone. Early numerical models of rupture along strike-slip faults suggested that intense damage might be limited to the uppermost crust (e.g., Ben-Zion and Shi, 2005), but recently-developed numerical approaches predict significant off-fault damage at depth (e.g., Shi and Day, 2013; Ampuero and Mao, 2017; Okubo et al., 2019), consistent with increasingly high-resolution seismological imaging of damaged rocks at depths of up to 20 km in, for example, New Zealand (e.g., Li et al., 2014a) and southern California, USA (e.g., Cochran et al., 2009; Ben-Zion and Zaliapin, 2019). Geological evidence for U_{conv} in the deeper seismogenic zone is elusive, available only from deeply exhumed faults and underlying shear zones. Quenched friction melt, or pseudotachylyte (e.g., Sibson, 1975; Sibson and Toy, 2006; Di Toro et al., 2009), has until recently (Rowe and Griffith, 2015) been the only widely accepted evidence for coseismic energy consumption in crystalline rocks at depth. However, intense fragmentation of feldspar (Pittarello et al., 2008; Johnson, 2015; Sullivan and Peterman, 2017; Petley-

Regan et al., 2018; Soda and Okudaira, 2018; Campbell et al., 2020; B. R. Song et al., 2020) and garnet (e.g., Trepmann and Stöckhert, 2002; Austrheim et al., 2017; Hawemann et al., 2019; Jamtveit et al., 2019; Petley-Regan et al., 2019; B. R. Song et al., 2020), intense kinking of micas (Bestmann et al., 2011; Anderson et al., 2021), mechanical twinning of jadeite (Trepmann and Stöckhert, 2001), unusual quartz microstructures (e.g., Trepmann and Stöckhert, 2003; Bestmann et al., 2011, 2012; Price et al., 2016), and variations in fluid-inclusion abundance (W. J. Song et al., 2020) in the deeper seismogenic zone have more recently been attributed to coseismic loading. Existing experimental, theoretical, and numerical work points to dynamic stresses being largely responsible for this damage, although high-strain-rate, quasistatic loading during post-seismic creep may also make a measurable contribution.

An example of fragmentation from near the base of the seismogenic zone is presented by B. R. Song et al. (2020) who described fragmented garnet grains in the damage zone of a deeply exhumed, seismogenic, strike-slip shear zone in the Norumbega Fault system, Maine, USA. This work was designed to provide our group with a data set that could be used to estimate fracture surface-area energy density U_s (J/m^3) and fracture surface-area energy per unit fault area U_{sa} (J/m^2) associated with the fragmentation. In the present study, we use the fragment size data of B. R. Song et al. (2020) to estimate U_s across the on- and off-fault damage zone and integrate the values to obtain U_{sa}, and in this way our analysis differs from most other geological studies that estimated U_{sa} from single or spatially limited samples. Additionally, for the first time, we apply physics-based fragmentation models to estimate strain rates associated with the fragmentation in the earthquake source volume. *In the present study, we equate the surface-area energy estimated from the garnet fragment size distributions to* U_{sa} *(thus the use of "*sa*")* with the understanding that additional energy of unknown magnitude was consumed by processes that we are not currently able to assess from the preserved rock record. We compare our results with 55 previous studies that estimate U_{conv}, U_{fh} or U_{sa} from theoretical, numerical and kinematic-slip models, pseudotachylyte geometry, electron spin

resonance, heat flow measurements, and fragment surface area measurements from modern and ancient faults. Our analyses provide new information about the earthquake energy budget and rupture dynamics in the deeper reaches of the seismogenic zone.

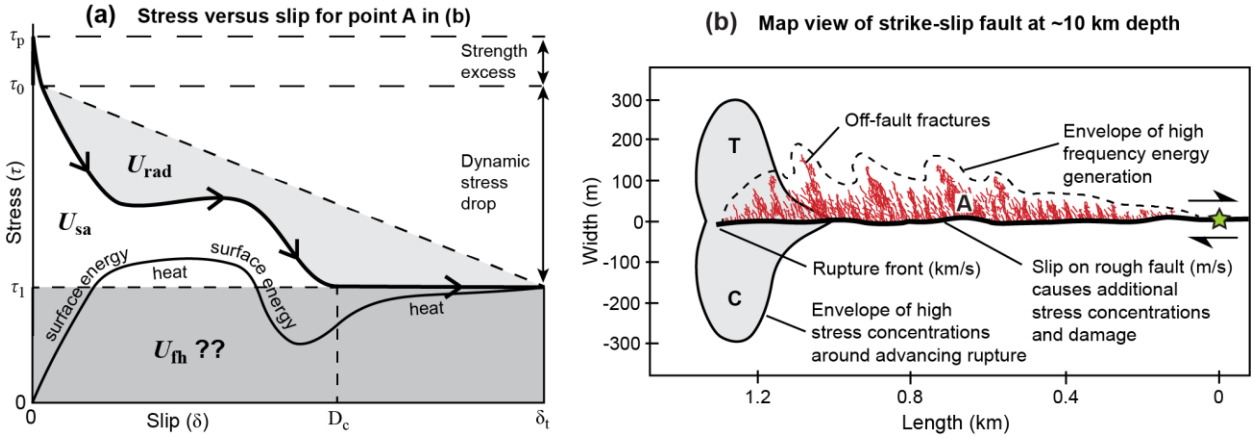

Figure C.1 Earthquake energy budget and fracture distribution for rupture propagation along a strike-slip fault. (a) Idealized slip-weakening model of the earthquake energy budget for point A in (b). Shear stress (τ) is shown as a function of slip (δ) for a total slip of δ_t. τ_p is the peak stress at which the earthquake nucleates. The total released elastic strain energy per unit fault area is the area under the diagonal dashed line extending from the initial stress τ_0 to δ_t. The converted energy per unit fault area is the area under the thick black curve with arrowheads. U_{rad} is the radiated elastodynamic wave energy. U_{sa} is the energy consumed in advancing the rupture and slipping on the rough/complex fault to reach the residual friction level τ_1 at the critical slip distance D_c. U_{sa} includes off-fault damage. The work below τ_1 is often assumed to be dissipated as frictional heat U_{fh}, but as noted by Cocco et al. (2006), there is no requirement for this assumption. Along these lines, the thin black curve (after Tinti et al., 2005) attempts to illustrate that U_{sa} likely includes some heat dissipation, and U_{fh} likely includes some surface-energy generation, with additional energy sinks also needing to be considered. (b) Schematic map view of the left half of bilateral Mode II subshear rupture propagating from right to left at ~10 km depth in a homogeneous medium (after Okubo et al., 2019). Green star indicates nucleation point; red lines along upper edge of the fault indicate coseismic fractures. Off-fault fracturing occurs primarily on the tensile (T) rather than compressional (C) side of the rupture front, and different fracture patterns are expected in bimaterial subshear ruptures (Xu and Ben Zion, 2017). The off-fault fracturing results primarily from stress concentrations surrounding the rupture front but also from stresses associated with slip on the rough and/or complex fault surface. High-frequency energy generated by the off-fault damage is a likely source of dilatant isotropic radiation (e.g., Cheng et al., 2021).

Table C.1 Notation used in the present study.

Symbol	Description
U_{rel}	Total released elastic energy per unit fault area
U_{conv}	Converted non-radiated energy per unit fault area
U_{rad}	Radiated energy per unit fault area
U_{fh}	Frictional heat energy per unit fault area
U_{sa}	Fracture surface-area energy per unit fault area
U_{s}	Fracture surface-area energy density
τ	Shear stress
τ_0	Initial shear stress
τ_1	Residual shear stress
τ_{p}	Peak shear stress at which an earthquake nucleates
δ	Slip distance
δ_{t}	Total slip distance
$\mathrm{D_c}$	Critical slip distance
A	Surface area of a particle aggregate
V	Volume of a particle aggregate
n_i	Number of particles for size s_i
s	Particle size (e.g., spherical diameter or cube edge)
s_i	Spherical diameter for bin i
$\bar{s}_{\mathrm{avg}}$	Area-averaged spherical diameter (= L)
γ	Specific surface energy
λ	Surface-area correction factor
$C(>s)$	Fraction of particles with size greater than s
$n(s)$	Count fraction of particles for size s
s_{min}	Minimum particle size
s_{max}	Maximum particle size
D	Exponent of a power-law distribution of particle size
k	Constant of a power-law distribution of particle size
$N(>s)$	Number of particles greater than size s
$U_{\mathrm{s}}^{\mathrm{garnet}}$	Fracture surface-area energy density of garnet
$U_{\mathrm{s}}^{\mathrm{rock}}$	Fracture surface-area energy density of the surrounding rock
V^{garnet}	Volume fraction of garnet
V^{rock}	Volume fraction of the surrounding rock ($V^{\mathrm{garnet}} + V^{\mathrm{rock}} = 1$)

Symbol	Description
γ^{garnet}	Specific surface energy of garnet
$\gamma^{\mathrm{plagioclase}}$	Specific surface energy of plagioclase
$\dot{\varepsilon}$	Strain rate
$\dot{\varepsilon}_0$	Characteristic strain rate
$\bar{\dot{\varepsilon}}$	Normalized strain rate
L	Area-averaged fragment size (e.g., spherical diameter or cube edge)
L_0	Characteristic length scale for a fragment
$\bar{L}$	Normalized average fragment size of a model
$\bar{L}_{\mathrm{Grady}}$	Normalized average fragment size of Grady (2006) model
$\bar{L}_{\mathrm{GC}}$	Normalized average fragment size of Glenn & Chudnovsky (1986) model
$\bar{L}_{\mathrm{ZMR}}$	Normalized average fragment size of Zhou et al. (2006a, 2006b) model
$\bar{L}_{\mathrm{LM}}$	Normalized average fragment size of Levy & Molinari (2010) model
$\bar{\hat{L}}_{\mathrm{Grady}}$	Modified normalized average fragment size of Grady (2006) model
$\bar{\hat{L}}_{\mathrm{GC}}$	Modified normalized average fragment size of Glenn & Chudnovsky (1986) model
$\hat{L}_{\mathrm{Grady}}$	Modified average fragment size of Grady (2006) model
E	Young's modulus
ρ	Mass density
c	Longitudinal wave speed in the material
t	Time
t_0	Characteristic time
t_{l}	Loading time required to absorb the applied strain energy
t_{f}	Failure time required to dissipate the applied strain energy
M	Ratio of loading time to failure time (= $t_{\mathrm{l}}/t_{\mathrm{f}}$)
Γ	Fracture energy
K_{Ic}	Fracture toughness
B	Geometrical factor (2 for 2D problem; 3 for 3D)
v_{c}	Effective fracture propagation velocity
σ_{c}	Quasistatic uniaxial compressive strength of a material
σ_{t}	Quasistatic tensile strength of a material
α	Ratio of compressive strength to tensile strength (= $\sigma_{\mathrm{c}}/\sigma_{\mathrm{t}}$)
N_{EQ}	Number of earthquake events
$\dot{\varepsilon}^{\mathrm{cor}}$	Corrected strain rate for a single earthquake

C.4. The Norumbega Fault System and Sandhill Corner Shear Zone

The Norumbega fault system in Maine, USA (Figure C.2) represents the roots of a long-lived, Paleozoic, right-lateral, strike-slip fault system (Ludman and West, 1999). The Sandhill Corner shear zone is one of the longest continuous strands of the Norumbega fault system, and a kinematic vorticity number of 0.97 determined from recrystallized quartz veins in the shear zone combined with other kinematic constraints (Johnson et al., 2009) is consistent with approximately strike-slip displacement. Rocks in the shear zone show little to no exhumation-related deformational or metamorphic overprint of the microstructures that formed while the shear zone was seismically active at temperatures of 350–500 °C based on quartz (dislocation creep and subgrain rotation recrystallization) and feldspar (fracturing) deformation mechanisms (Price et al., 2016). A traverse (cross-section in Figure C.2) from NW to SE across the Sandhill Corner shear zone reveals a ~205 m transition from coarse-grained quartzo-feldspathic host rocks through mylonite and ultramylonite before reaching the shear-zone core. Emerging from the SE side of the core, ~25 m of highly sheared schist transitions rapidly to schist host rocks (Figure C.2). The shear zone is therefore much wider in the quartzo-feldspathic rocks NW of the core than it is in the schist SE of the core, the core being located at the quartzo-feldspathic/schist contact.

Rocks within the shear zone show evidence for dynamic coseismic conditions including deformed (Figure C.3), and less abundant undeformed, pseudotachylyte that is concentrated within ~40 m of the shear-zone core in the quartzo-feldspathic rocks, and within ~5 m of the core in the schist rocks (Price et al., 2012; W. J. Song et al., 2020). The fact that pseudotachylyte is not restricted to the core, and that it is found as far as ~40 m into the quartzo-feldspathic rocks, has implications for the history and distribution of coseismic damage in the shear zone and will be revisited in Section 6.1. Abundant pseudotachylyte was documented in the Ray Corner mylonite zone (Rowe et al., 2018), which is ~56 km northeast along strike of the Sandhill Corner shear zone and may be the same structure (the rocks documented by Rowe et al., 2018 were in a quarry and have subsequently been blasted and removed). The shear-zone rocks also contain intensely fragmented grains of garnet and feldspar (Figure C.3), which are used in the energy and strain-rate calculations below.

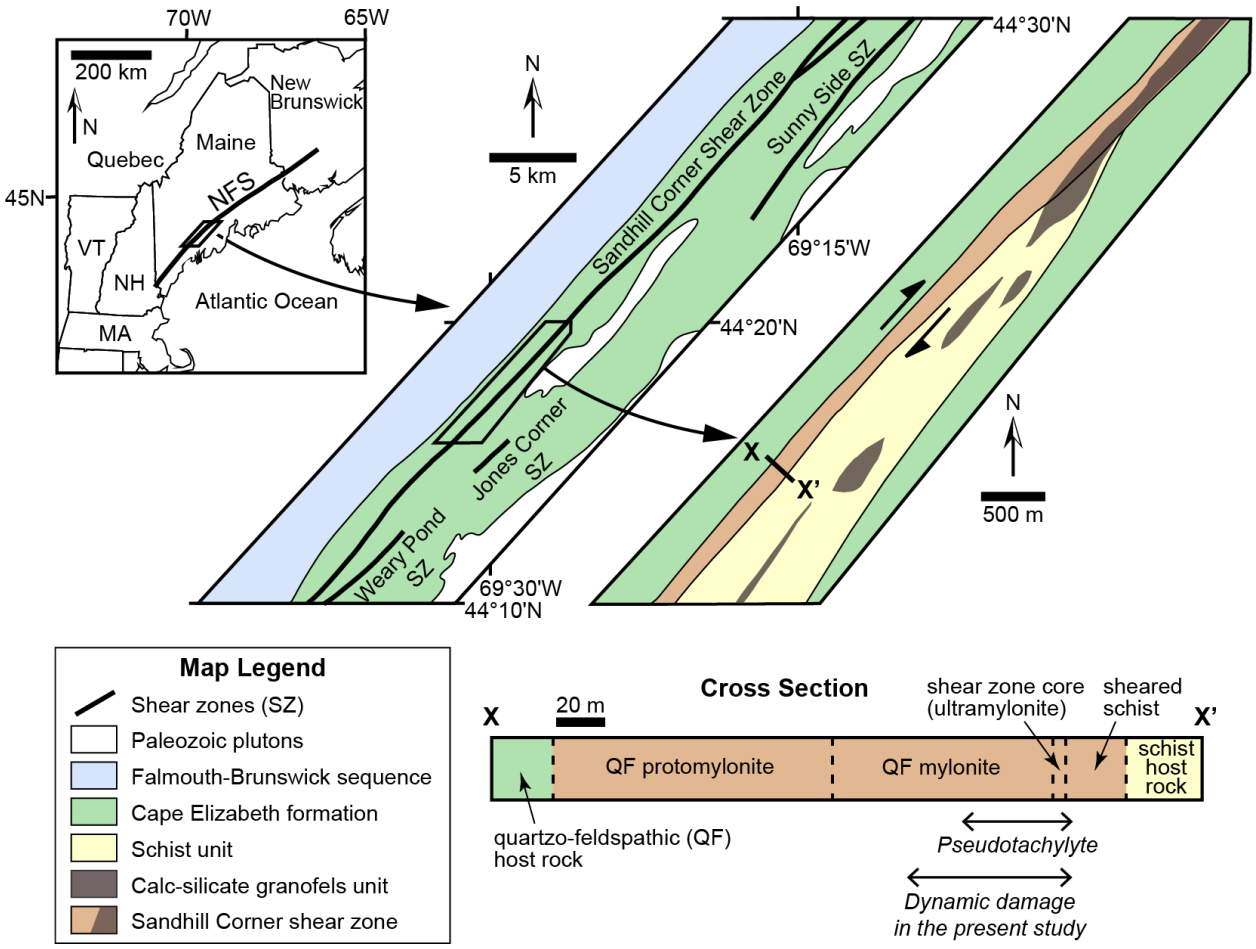

Figure C.2 Regional geologic setting and cross section of the study area in the Sandhill Corner shear zone of the Norumbega Fault system (NFS). Modified after Price et al. (2016). QF = quartzo-feldspathic. Note asymmetric development of the shear zone around the core in the cross-section X–X'. Spatial distribution of pseudotachylyte (Price et al., 2012; W. J. Song et al., 2020), and the dynamic damage zone (B. R. Song et al., 2020) used for estimating fracture surface-area energy in the present study are marked in the cross section (see Figure C.8). Although pseudotachylyte is distributed over ~40 m in the QF rocks, it is concentrated in the shear-zone core.

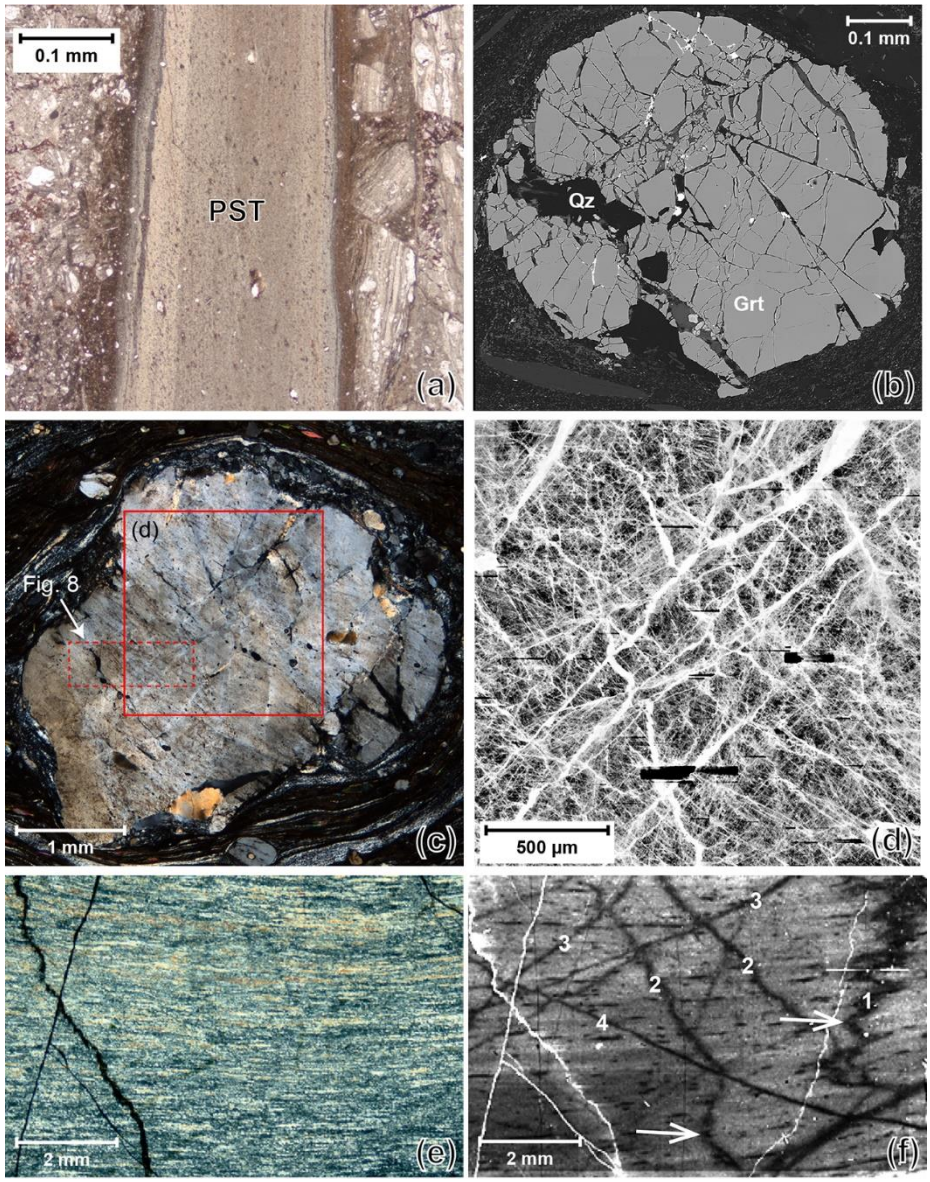

Figure C.3 Microstructures from the Sandhill Corner shear zone showing evidence for dynamic coseismic stresses. (a) Viscously deformed pseudotachylyte vein (PST) surrounded by pre-melt cataclasite. Plane-polarized light. (b) Backscattered electron image of fragmented garnet (sample BB12). Grt – garnet; Qz – quartz. (c) Oligoclase grain (sample BB16) showing patchy extinction and microcracks healed with feldspar and quartz. Cross-polarized light. (d) Inverted cathodoluminescence (CL) image of area in (c) showing extreme fragmentation and feldspar/quartz healing. Microstructural examination favors tensile (Mode I) microcracking although we cannot rule out mixed-mode behavior. (e) Optical photomicrograph of a fine-grained (<40 µm), recrystallized quartz ribbon. Optically, the ribbon shows a typical recrystallized microstructure. Cross-polarized light. (f) CL image of (e) showing a history of multiple overprinting Mode I fractures preserved as dark bands in the quartz (numbers indicate the sequence of microcracking, 1 being earliest). Remarkably, the two earliest generations (1 and 2), indicated by the arrows, have been deformed and folded during viscous flow of the polycrystalline aggregate, suggesting at least four cycles of microcracking, each under a different transient stress field leading to different orientations, followed by viscous flow. Healed microcracks are typically lined with fluid inclusions. White lines in the CL image are open cracks, also visible optically in (e).

C.5. Calculation of Fragment Size for Surface Energy and Strain Rate Estimates

C.5.1. General Concepts

When estimating surface energies from natural fragment size data, it is important that the average fragment size *L* be representative of *average surface area* as opposed to mean diameter (or other spatial measure such as cube edge) of the population. Consider the surface area per unit volume (A/V) of an aggregate consisting of n_i spheres of diameter s_i for bin *i*:

$$\left(\frac{A}{V}\right)_{sphere} = \frac{\sum n_i \left[4\pi \left(\frac{s_i}{2}\right)^2\right]}{\sum n_i \left[\frac{4}{3}\pi \left(\frac{s_i}{2}\right)^3\right]} = \frac{6\sum n_i s_i^2}{\sum n_i s_i^3} = \frac{6}{\bar{s}_{\text{avg}}} = \frac{6}{L} \tag{C2}$$

In this case, $\bar{s}_{\text{avg}}$ or *L* represents the area-averaged sphere diameter. The surface-area energy density U_s (J/m^3) can then be obtained by $(A/V) \times \gamma$ where γ is the specific surface energy (J/m^2). Since fragments are never perfect spheres or cubes, it is necessary to apply a surface-area correction factor λ, which is the ratio of fragment surface area to equivalent-volume spherical surface area. We calculate the surface area correction factor λ for the garnet samples (see Section C.5.1.1) using the method proposed by Davies et al. (2019, 2021). To apply the correction factor, U_s is multiplied by the total average value of λ (~1.5; Table C.2) for all garnet samples. Thus, the corrected U_s is:

$$U_s = \frac{6\gamma\lambda}{L} \tag{C3}$$

In the case of brittle materials for which specific surface energy is not available, theoretically derived fracture energy Γ (J/m^2) could be used instead of γ (Tromans and Meech, 2002).

Equation (C2) also provides a convenient form for *L* as:

$$L = \frac{\sum n_i s_i^3}{\sum n_i s_i^2} \tag{C4}$$

which states that a population of spheres with diameters s_i can be used to find *L* by dividing the sum of the cubes of the diameters by the sum of the squares of the diameters of all the fragments in the population of

interest. In the event a cumulative particle size distribution $C(> s)$ has a perfect power-law variation with exponent D and constant k, then:

$$C(> s) = \int_{s_{\min}}^{s_{\max}} n(s)\, ds = k s^{-D} \tag{C5}$$

where s is particle size (diameter here) between the minimum ($s_{\min}$) and maximum ($s_{\max}$) for the power-law distribution, $C(> s)$ is the fraction of particles with size greater than s, and $n(s)$ is the particle count fraction per unit length. Taking the derivative of Equation (C5) and applying the Leibniz integral rule, we obtain the count fraction of a power-law cumulative distribution:

$$n(s) = kDs^{-D-1} \tag{C6}$$

Thus, we can show from Equations (C4) and (C6) that:

$$L = \frac{\sum n_i s_i^3}{\sum n_i s_i^2} = \frac{\int_{s_{\min}}^{s_{\max}} n(s) s^3\, ds}{\int_{s_{\min}}^{s_{\max}} n(s) s^2\, ds} = \frac{\int_{s_{\min}}^{s_{\max}} kDs^{-D+2}\, ds}{\int_{s_{\min}}^{s_{\max}} kDs^{-D+1}\, ds} \tag{C7}$$

The solutions for Equation (C7) are as follows:

$$L = \left(\frac{2-D}{3-D}\right)\left[\frac{s_{\max}^{(3-D)} - s_{\min}^{(3-D)}}{s_{\max}^{(2-D)} - s_{\min}^{(2-D)}}\right] \quad \text{if } D \neq 2 \text{ and } D \neq 3$$

$$L = \frac{s_{\max} - s_{\min}}{\ln\left(s_{\max}/s_{\min}\right)} \quad \text{if } D = 2 \tag{C8}$$

$$L = \frac{\ln\left(s_{\max}/s_{\min}\right)}{s_{\min}^{-1} - s_{\max}^{-1}} \quad \text{if } D = 3$$

Equation (C8) is the only derivation we are aware of that explicitly gives L and therefore U_s as a function of the power-law exponent D, which is commonly referred to as the fractal dimension. Area-averaged fragment size L is also used in estimating strain rates in Section 5.

Table C.2 Summary of three-dimensional *D*-value (D), microfracture density, minimum ($s_{\min}$) and maximum ($s_{\max}$) fragment size, area-averaged fragment size (L) with standard deviation, and surface-area correction factor (λ) for fragmented garnet and plagioclase samples.

Lithology	Sample	Distance from the lithologic contact[a] (m)	D[b]	Microfracture density[c] (mm^{-1})	$s_{\min}$ (μm)	$s_{\max}$ (μm)	L[d] (μm)	λ[e] average
QF[f]	71 (garnet)	−96.06	1.938	61.42	10	199.53	65.91 ± 46.60	1.49
QF	56 (garnet)	−62.98	2.555	120.12	10	89.13	29.22 ± 16.30	1.63
QF	BB16-a (garnet)	−15.47	2.956	113.59	10	56.23	21.23 ± 8.52	1.40
QF	BB16 (garnet)	−15.47	3.357	155.07	10	79.43	21.14 ± 9.52	1.36
QF	BB16 (plagioclase)	−15.47	3.010	154.69	10	123.00	27.19 ± 15.32	1.5[g]
QF	BB12 (garnet)	−12.72	2.897	94.11	10	112.20	27.80 ± 15.25	1.35
Contact	41 (garnet)	0.00	2.879	113.72	10	63.10	22.62 ± 10.21	1.40
Schist	305 (garnet)	5.46	2.713	123.01	10	177.83	36.61 ± 21.03	1.51
Schist	28 (garnet)	9.01	2.370	60.51	10	223.87	52.32 ± 34.01	1.58

[a]Perpendicular distance is measured from the lithologic contact between the QF[f] and schist rocks, and negative values indicate the QF rocks.
[b]Three-dimensional *D*-values are calculated by adding 1.0 to the two-dimensional *D*-values of B. R. Song et al. (2020).
[c]Microfracture density is measured by a linear scanline method (B. R. Song et al., 2020), in which 6 randomly oriented scanlines are drawn across each grain, and the microfractures in the grain intersected with scanlines are counted. An average microfracture density for each sample is defined by the total number of the microfractures divided by the total scanline length.
[d]L is calculated using Equation (C8) in the text. The standard deviation is obtained from the variance between L and each bin of the fragment size distribution.
[e]λ is derived from backscattered electron images (Davies et al., 2019, 2021), and the total average value (~1.5) for all the garnet samples is used in estimating surface area energy density and energy per unit fault area. See Section C.5.1.1.
[f]QF = quartzo-feldspathic.
[g]λ for plagioclase was not obtained because real shapes of fragments are not measured by an electron backscatter diffraction method. Instead, the total average λ value (~1.5) of garnet is used in estimating surface area energy density of the plagioclase grain.

C.5.1.1. Calculation of Surface Area Correction Factor (λ)

We calculate the surface area correction factor λ (also called surface roughness factor) for the fragmented garnet samples using the method proposed by Davies et al. (2019, 2021 Corrigendum) to correct the surface-area energy density of the modeled spherical fragments.

λ is defined by the surface area ratio of the 3D fragment ($S_{3\mathrm{df}}$) to the 3D equivalent sphere ($S_{3\mathrm{des}}$) having the same volume:

$$\lambda = \frac{S_{3\mathrm{df}}}{S_{3\mathrm{des}}} \tag{C9}$$

To estimate 3D surface areas from 2D fragment measurements using scanning electron microscope images, Davies et al. (2019) used the relationship between 3D surface area and 2D perimeter of known regular

shapes with aspect ratio from 1 to 10. A 2D rectangle of $h \times \beta h$ and a 3D square-section bar of $h \times h \times \beta h$ are considered where h is the length of a side of the shapes and β is the aspect ratio from 1 to 10. This range of aspect ratio is observed in the fragmentation experiment of borosilicate glass (Pyrex) conducted by Davies et al. (2019) and in our garnet fragments (e.g., Figure C.4). Davies et al. (2019) calculated ratios of (1) the 2D rectangle perimeter (P_{r}) to the perimeter of the equivalent circle (P_{rec}) having the same area, and (2) the 3D bar surface area (S_{b}) to the equivalent sphere surface area (S_{bes}) having the same volume:

$$\frac{P_{\mathrm{r}}}{P_{\mathrm{rec}}} = \frac{(1+\alpha)}{(\beta\pi)^{0.5}} \text{ and } \frac{S_{\mathrm{b}}}{S_{\mathrm{bec}}} = \frac{2(1+2\beta)}{\pi^{1/3}(6\beta)^{2/3}} \tag{C10}$$

These two ratios for the regular shapes are then used to estimate λ for 3D fragments from the perimeters of 2D fragment images ($P_{2\mathrm{df}}$) and the equivalent circle for fragments ($P_{2\mathrm{dec}}$) by assuming the following:

$$\left(\frac{S_{\mathrm{b}}}{S_{\mathrm{bec}}}\right)\Big/\left(\frac{P_{\mathrm{r}}}{P_{\mathrm{rec}}}\right) = K = \left(\frac{S_{3\mathrm{df}}}{S_{3\mathrm{des}}}\right)\Big/\left(\frac{P_{2\mathrm{df}}}{P_{2\mathrm{dec}}}\right) \tag{C11}$$

From Equations (C9) and (C11),

$$\lambda = K\left(\frac{P_{2\mathrm{df}}}{P_{2\mathrm{dec}}}\right) \tag{C12}$$

The factor K for the regular shapes is calculated for $1 \leq \beta \leq 10$ using Equations (C10) and (C11) in Table C.3. With an increase in aspect ratio β of the regular shapes, the two ratios of $S_{\mathrm{b}}/S_{\mathrm{bec}}$ and $P_{\mathrm{r}}/P_{\mathrm{rec}}$ increase, but the factor K is relatively constant, close to 1 (e.g., K = 1.10 for β = 1 and K = 0.95 for β = 10). Thus, from Equation (C12), the surface area correction factor λ for aspect ratio between 1 and 10 can be written as:

$$\lambda \approx \left(\frac{P_{2\mathrm{df}}}{P_{2\mathrm{dec}}}\right) \tag{C13}$$

This allows the surface areas of fragments to be corrected by measuring the perimeters of 2D fragment images. Using Equation (C13), we estimate λ for the fragmented garnet samples in the Sandhill Corner shear zone (e.g., Figure C.5). The average λ for the garnet samples ranges from 1.35 to 1.63 (Table C.2), and we used the total average λ value of 1.5 to calculate the surface-area energy density U_{s}.

Our calculated average value of λ = 1.5 is comparable to the values of Davies et al. (2019, 2021) as their Pyrex fragmentation experiment yields average λ of 1.3–1.4 when the factor K = 1 is used. Freshly crushed and relatively unweathered minerals have λ = 2 to 10 (White, 1995). For example, using the gas adsorption method for surface area measurement, Parks (1990) found λ = 2.2 for crushed quartz, and White and Peterson (1990) obtained an average λ of 7 for clays, oxides and freshly crushed silicates such as quartz, feldspar and calcite. Studies of fault gouge also show similar λ value range but slightly higher than ours. In a South African gold mine, Olgaard and Brace (1983) measured surface areas of 'fresh' gouge (exposed for 3 days) and 'old' gouge (exposed to the mine atmosphere for 6 yrs), and obtained λ values of 3.75 and ~4.4, respectively, which are obtained by dividing the specific surface area of gas absorption (0.75 m^2/g for 'fresh' and 2.0 m^2/g for 'old') by that of X-ray sedimentation assuming a sphere (0.20 m^2/g for 'fresh' and 0.45 m^2/g for 'old') in Table 2 of Olgaard and Brace (1983). Wilson et al. (2005) reported $\lambda = 6.6 \pm 1.5$ for gouge from the San Andreas fault in the Tejon Pass region, but their particle size results, necessary to calculate λ, have been questioned by Rockwell et al. (2009) who produced markedly different particle sizes and suspected errors in the laser analyzer results of Wilson et al. (2005). It appears that the relatively low λ value of our fragmented garnet is at least partly explained by the relatively smooth fragment boundaries (Figure C.6) compared to fault gouge (e.g., Olgaard and Brace, 1983; Sammis et al., 1987; Wilson et al., 2005).

Table C.3 S_b/S_{bec}, P_r/P_{rec}, and K for $1 \leq \beta \leq 10$.

β	S_b/S_{bec}	P_r/P_{rec}	K
1	1.24	1.13	1.10
2	1.30	1.20	1.09
3	1.39	1.30	1.07
4	1.48	1.41	1.05
5	1.56	1.51	1.03
6	1.63	1.61	1.01
7	1.70	1.71	0.99
8	1.76	1.80	0.98
9	1.82	1.88	0.97
10	1.87	1.96	0.95

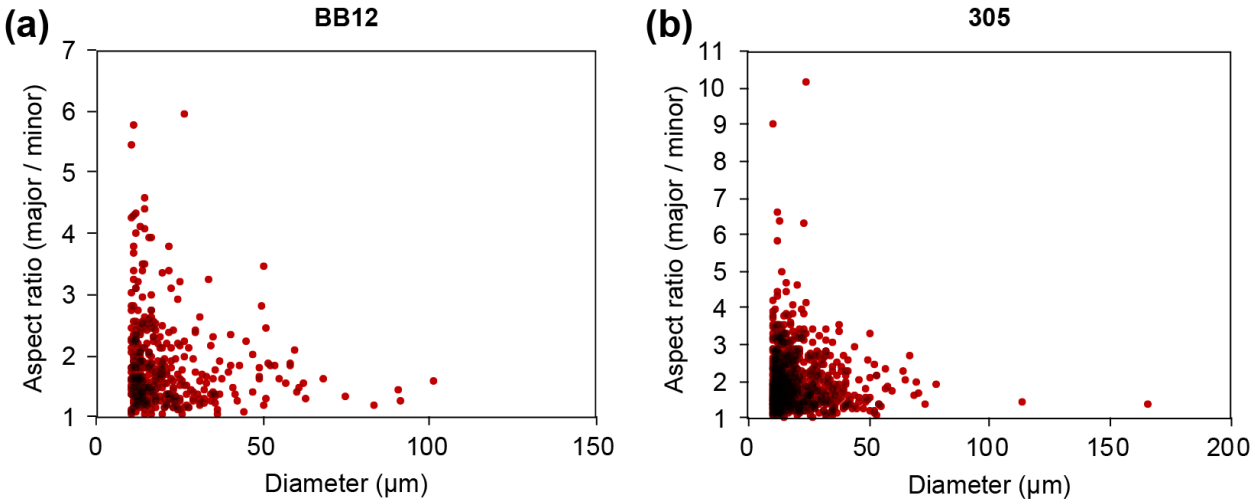

Figure C.4 Examples of aspect ratio for garnet fragments ≥ 10 μm in the Sandhill Corner shear zone. (a) Sample BB12 from the quartzo-feldspathic rocks (see Figure C.7a for the microstructure). (b) Sample 305 from the schist (see Figure C.7b for the microstructure). Aspect ratio (major axis / minor axis) was calculated from best-fit ellipse of each fragment. Darker color represents more overlapping data points.

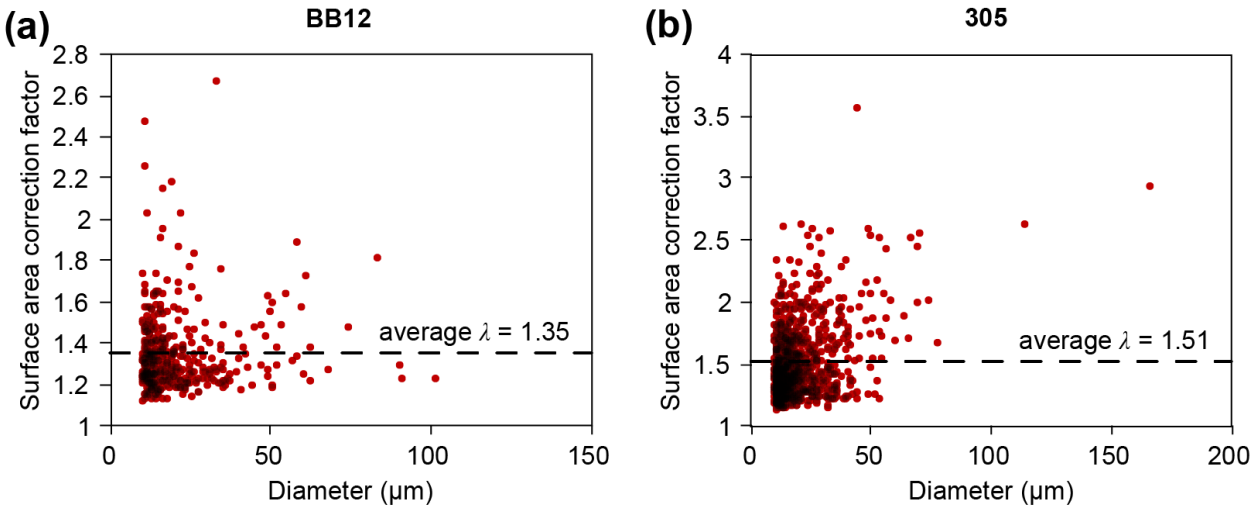

Figure C.5 Examples of surface-area correction factor λ for garnet fragments ≥ 10 μm in the Sandhill Corner shear zone. (**a**) Sample BB12 from the quartzo-feldspathic rocks (see Figure C.7a for the microstructure), showing λ range of 1.1–2.7 and average λ = 1.35 (dashed line). (**b**) Sample 305 from the schist (see Figure C.7b for the microstructure), showing λ range of 1.1–3.6 and average λ = 1.51 (dashed line). Darker color represents more overlapping data points.

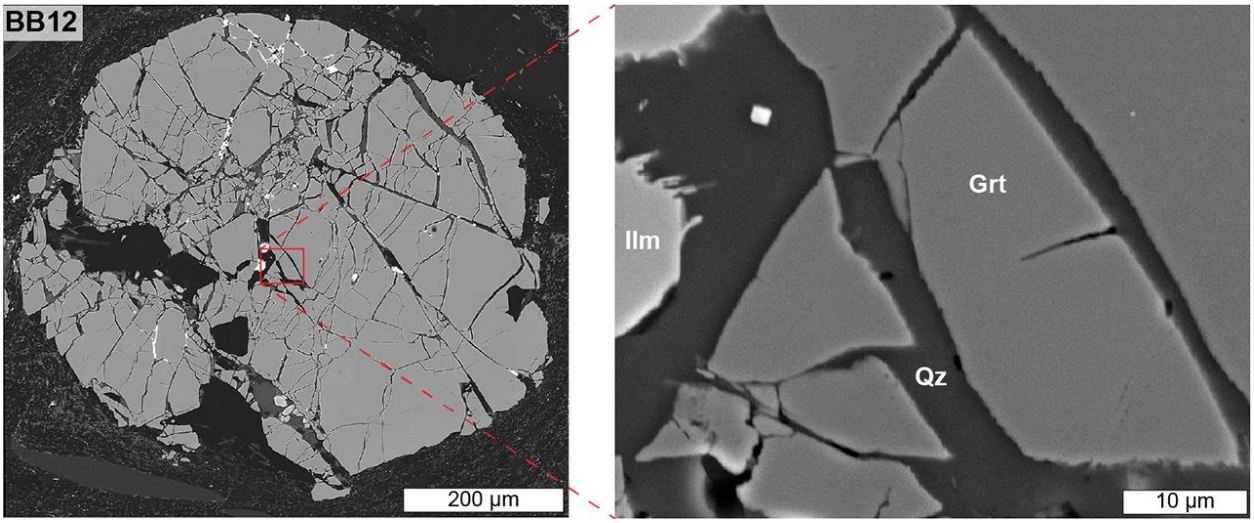

Figure C.6 Backscattered electron image of fragmented garnet (sample BB12) in the Sandhill Corner shear zone, showing relatively smooth and straight boundaries of garnet fragments. Ilm – ilmenite; Grt – garnet; Qz – quartz.

C.5.2. Fragment Sizes and Integration Length Scales Used in the Present Study

In the inner Sandhill Corner shear zone, B. R. Song et al. (2020) found that the fragment size distribution defined two power-law trends (two slopes, or *D*-values, in a log–log plot) that intersect at a value of s = ~10 µm (Figure C.7). Such "bifractal" distributions are observed in a wide range of different processes from drilling, brecciation, crushing and milling of rock (Carpinteri and Pugno, 2002; Barnett, 2004; Farris and Paterson, 2007; Taşdemir, 2009; Roy et al., 2012) to rapid shock fragmentation of brick, glass, quartz, rock and ceramic (Fujiwara et al., 1977; Capaccioni et al., 1986; Suteanu et al., 2000; Barnett, 2004; Keulen et al., 2007; Roy et al., 2012; Davydova et al., 2014; Hossain and Kruhl, 2015). Bifractal distributions are sometimes interpreted as identifying a grinding limit (e.g., Keulen et al., 2007), but 10 µm is far too large for the grinding limit of garnet (~0.26 µm for almandine-pyrope; B. R. Song et al., 2020). Thus, we follow the interpretation of such distributions found in other fragmentation studies (e.g., Carpinteri and Pugno, 2002; Wittel et al., 2008; Taşdemir, 2009; Hogan et al., 2012, 2016) in which the fragments larger than ~10 µm represent a dynamic *volume* fragmentation event (through-going in 3D) leading to the larger size distribution with *D*-values ≥2.5 (Figure C.7). The second stage is a lower-energy

(lower strain rate and stress rate) *surface* fragmentation event with *D*-values <2.5 (Figure C.7). Thus, for our study, 10 μm is taken as the lower limit of the dynamic fragment size, and the upper limit is defined by the largest fragment in each garnet sample. In taking 10 μm as the lower limit, we ignore the possibility that fragments <10 μm were once part of the larger *D*-value distribution but have been modified by secondary physical or chemical processes (e.g., Roy et al., 2012). Including smaller fragments would significantly increase our estimates of energy and strain rate calculated below.

Selecting one highly fragmented garnet grain from each sample, B. R. Song et al. (2020) analyzed the garnet fragment size distributions (Figure C.8a) and microfracture densities (Figure C.8b) across the Sandhill Corner shear zone and applied a power-law fit to the fragment size data (Figure C.7). Figure C.8c and Table C.2 show the area-averaged garnet fragment size *L* used for our calculations. Following B. R. Song et al. (2020), *D*-values ≥2.5 in the inner shear zone are interpreted as indicating dynamic coseismic fragmentation. High strain-rate fragmentation of brittle solids typically leads to a self-similar, scale-invariant relationship between fragment size and cumulative number or mass (e.g., Fujiwara et al., 1977; Schoutens, 1979; Matsui et al., 1982; Turcotte, 1986; Sammis et al., 1987; Redner, 1990; Ishii and Matsushita, 1992; Kaminski and Jaupart, 1998; Ching et al., 2000; Chester et al., 2004; Genç et al., 2004; Chester et al., 2005; Zhou et al., 2006b; Grady, 2009, 2010, 2017; Taşdemir, 2009; Levy and Molinari, 2010; Hogan et al., 2012, 2015; Price et al., 2012; Roy et al., 2012; Kolzenburg et al., 2013; Liu and Zhao, 2021). This fragment size distribution can be described by the equation $N(> s) = ks^{-D}$ where $N(> s)$ is the number of particles greater than size s (see Rockwell et al., 2009 and Phillips and Williams, 2021 for deviations from this relationship). The *D*-value, sometimes called the fractal dimension, has been shown in many studies to be proportional to the magnitude and rate of loading (e.g., Fujiwara et al., 1977; Matsui et al., 1982; Turcotte, 1986; Nagahama and Yoshii, 1994; Jébrak, 1997; Kaminski and Jaupart, 1998; Ching et al., 2000; Barnett, 2004; Cui et al., 2006; Zhou et al., 2006b; Taşdemir, 2009; Hogan et al., 2012; Hou et al., 2015; Liu and Zhao, 2021), so it can be used, with appropriate care, to infer the type of process associated with fragmentation (e.g., quasistatic versus dynamic).

To understand the difference between quasistatic and dynamic fragmentation, consider a brittle material such as garnet that contains flaws that vary in size, orientation, and distribution. Under slow, quasistatic loading, the most favorable flaws are triggered first, and growth of the resulting fractures leads eventually to macroscopic failure. In contrast, dynamic loading also triggers the most favorable flaws, but the rate of loading outpaces fracture growth (Figure C.9; Strassburger et al., 2008) so that additional flaws are triggered before macroscopic failure occurs. Thus, dynamic loading of a brittle material involves rapid growth in elastic strain energy, greatly exceeding the levels required for quasistatic fracture formation and propagation. Because fracture-generated surface energy is a relatively weak conversion process, fractures rapidly nucleate and grow, branching into finer and finer length scales until a minimum length scale is reached where the excess elastic energy can be consumed (Sharon et al., 1996; Grady, 2010). This dynamic fracture branching controls the range of fragment sizes—the more rapid the loading, the more energy expended, the more abundant the smaller fragments, and the higher the *D*-value.

Following B. R. Song et al. (2020), *D*-values ≥2.5 *that are not the product of shearing comminution* (e.g., Sammis et al., 1987) suggest that the inner shear zone experienced dynamic fragmentation as the result of coseismic energy release whereas the outer shear zone with *D*-values <2.5 appears to have undergone lower-energy fragmentation possibly also owing to dynamic coseismic energy release, although quasistatic post-seismic creep may have contributed. To capture the transition from higher-energy to lower-energy loading, we consider those samples with *D*-values ≥2.5, plus the first sample outside the higher-energy dynamic loading zone. Thus, we include sample 71 in the quartzo-feldspathic rocks and sample 28 in the schist rocks, so our analysis covers ~96 m in the quartzo-feldspathic rocks and ~9 m in the schist (Figure C.8). In support of our selection using *D*-values, W. J. Song et al. (2020) used spatial abundance of fluid inclusions introduced during coseismic deformation to define a coseismic damage zone up to ~90 m wide in the quartzo-feldspathic rocks (Figure C.8), which also corresponds to the mylonite–protomylonite transition (W. J. Song et al., 2020). Pseudotachylyte occurs in the quartzo-feldspathic rocks within ~40 m of the core (W. J. Song et al., 2020). Anderson et al. (2021) documented 7 samples in the quartzo-feldspathic rocks within ~60 m of the core containing muscovite grains with kink-band geometries indicating dynamic

strain rates. Taken together, these observations indicate a boundary within the quartzo-feldspathic rocks related to dynamic coseismic strain rates lying between samples 56 and 71, so we take sample 71 as the outer boundary of our integration of U_s to determine U_{sa}. In the schist rocks, pseudotachylyte is concentrated within ~5 m of the core (e.g., Price et al., 2012) and the gradients in other parameters are very steep (Figure C.8) consistent with the choice of sample 28 as the outer boundary for integration of U_s.

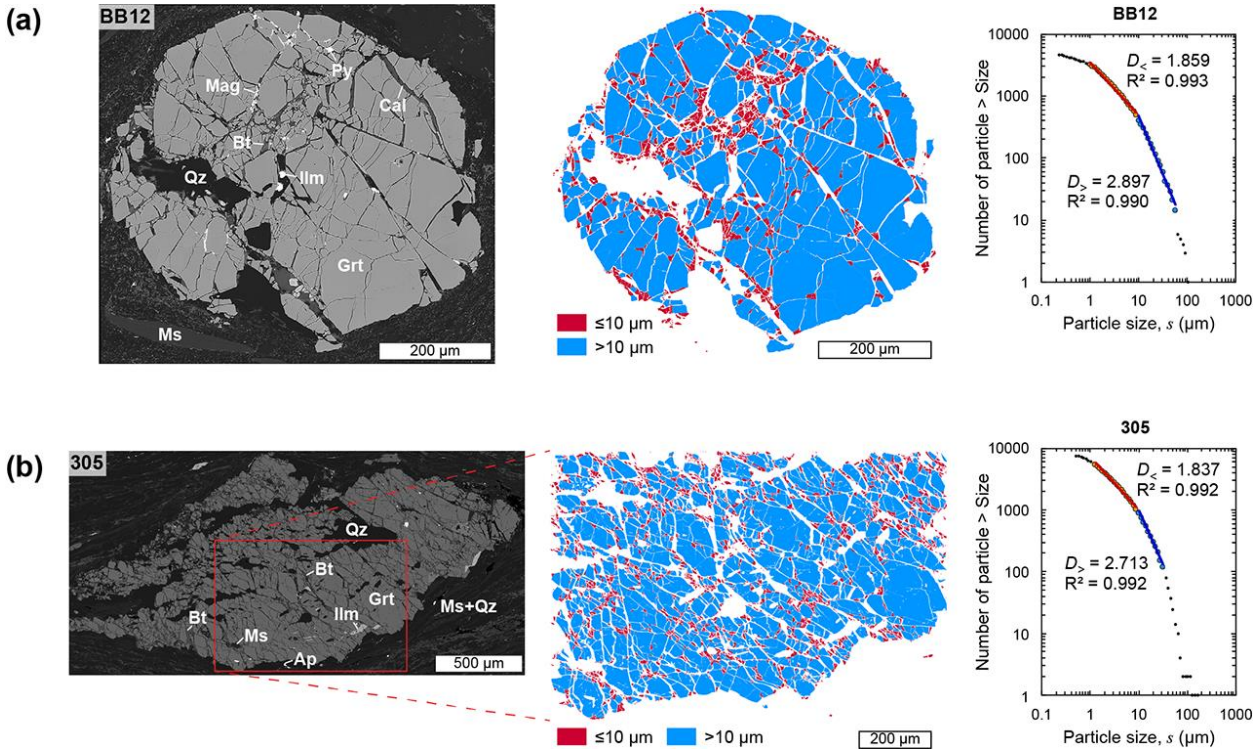

Figure C.7 Examples of fragmented garnet in the Sandhill Corner shear zone showing "bifractal" fragment size distribution. Microcracks are filled primarily with quartz. (a) Sample BB12 from the quartzo-feldspathic rocks. (b) Sample 305 from the schist. Bicolor maps (*center*) of the backscattered electron images (*left*) highlight fragment distributions for two different size ranges with a breakpoint at 10 μm. Red and blue colors in the maps indicate fragments ≤10 μm and >10 μm, respectively, corresponding to $D_<$ and $D_>$ in the particle size distribution plot (*right*). $D_>$ is used as D to calculate area-averaged fragment size L. D-values are in 3D. The change in slope for fragments ≤1 μm reflects loss of resolution at finer fragment sizes. After B. R. Song et al. (2020). Mineral abbreviations are: Ap = apatite, Bt = biotite, Cal = calcite, Grt = garnet, Ilm = ilmenite, Mag = magnetite, Ms = muscovite, Py = pyrite, Qz = quartz.

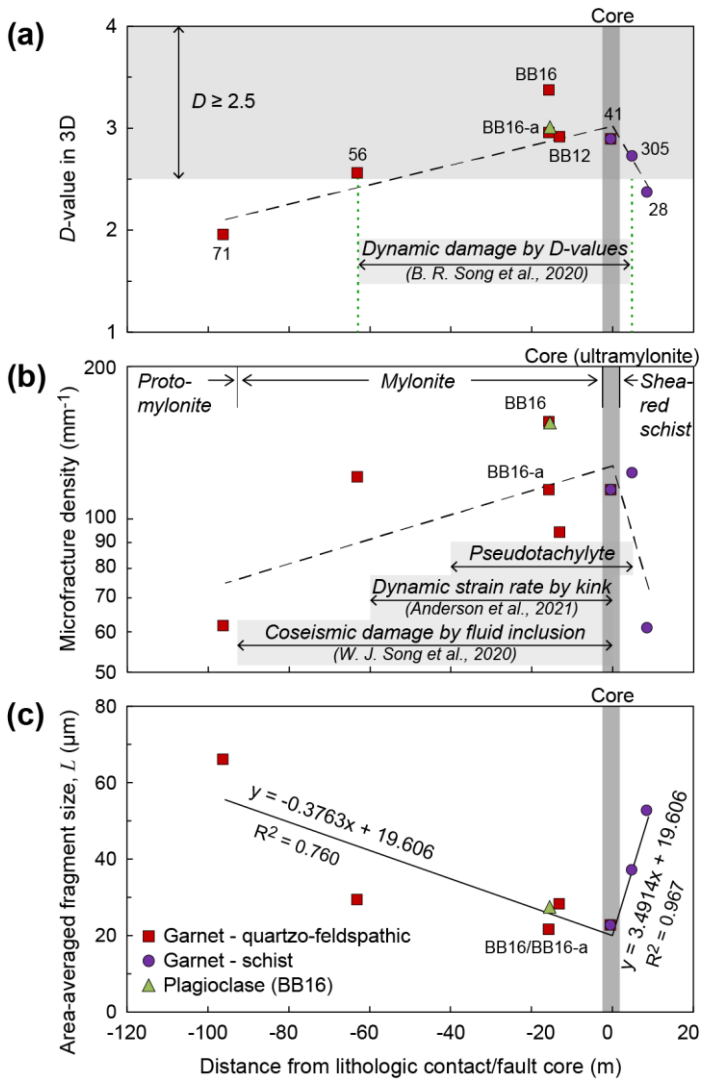

Figure C.8 Data for the fragmented garnet samples against distance from the quartzo-feldspathic/schist contact in the Sandhill Corner shear zone. Also included for comparison is plagioclase from sample BB16. Note highly asymmetric distribution of all data types around the shear-zone core. (a) Three-dimensional *D*-values showing general increase toward the core. Each *D*-value is estimated from a power-law fit to fragment size distribution of each sample (B. R. Song et al., 2020). Dashed line shows qualitative trend. (b) Microfracture density showing general increase toward the core. The densities were measured in the same grains that were used to calculate *D*-values (B. R. Song et al., 2020). Dashed line shows qualitative trend. The distribution of rock types is also displayed. (c) Area-averaged fragment size L showing decrease toward the core. The best-fit equations are used to calculate surface-area energy density U_s and strain rate in the dynamic damage zone. Samples BB16 and BB16-a overlap with the difference in L much smaller than the symbol size. Symbol legend is displayed in (c). Sample numbers are shown in (a), and only two sample numbers at the same distance are provided in (b) and (c). Sample BB16 garnet shows elevated *D*-value (a) and microfracture density (b) owing to post-fragmentation viscous flow (B. R. Song et al., 2020). See Table C.2 for individual data. The widths of coseismic deformation documented in other studies are indicated in (a) and (b) to support our selection of the dynamic damage zone for integration of U_s from sample 71 to sample 28. These include pseudotachylyte distribution (Price et al., 2016; W. J. Song et al., 2020), dynamic strain rate using kinked muscovite (Anderson et al., 2021), and fluid-inclusion abundance (W. J. Song et al., 2020).

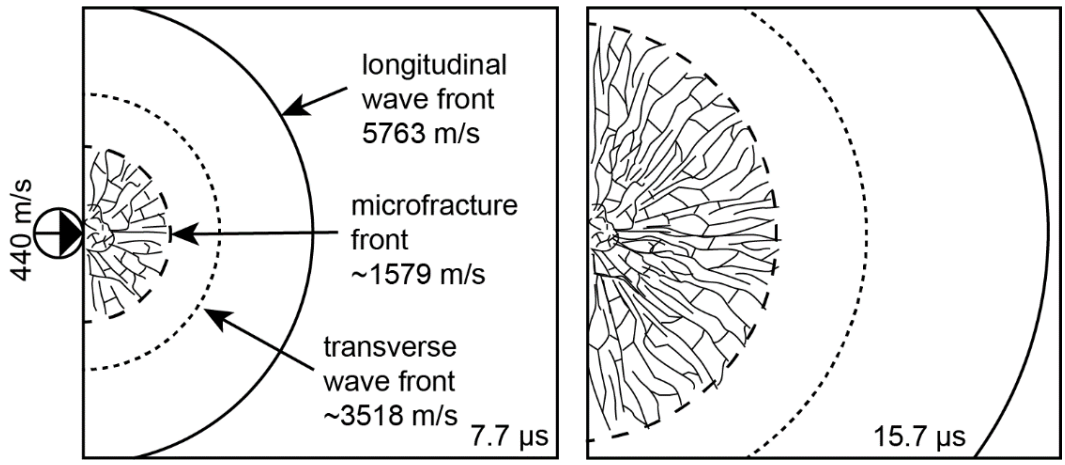

Figure C.9 Illustration of dynamic fragmentation in which the loading rate outpaces the material response rate. Impact on Starphire glass with steel ball at 440 m/s produces a microfracture front that lags the longitudinal and transverse wave fronts at 7.7 and 15.7 microseconds. After Figure 3 of Strassburger et al. (2008).

C.6. Estimates of Fracture Surface-Area Energy Density (U_s) and Fracture Surface-Area Energy per Unit Fault Area (U_{sa})

If the average fragment size distribution for each sample of interest across the Sandhill Corner shear zone on either side of the core can be described by a continuous function, as shown in Figure C.8c, then the fracture surface-area energy per unit fault area U_{sa} (J/m^2) is readily calculated by integrating the surface-area energy density U_s (J/m^3) from Equation (C3) arising from the distribution across the damage-zone width. There are volume-fraction bounds to consider in our energy estimates because our analysis is based on the fragmentation of garnet grains that make up ~1% of the quartzo-feldspathic rocks and ~5% of the schist. Considering the surface-area energy density from Equation (C3), we can calculate an energy density in the damage zone based on the volume fractions of garnet and the remaining rock as $U_s = U_s^{\text{garnet}} V^{\text{garnet}} + U_s^{\text{rock}} V^{\text{rock}}$, where V^{garnet} and V^{rock} are the volume fractions of garnet and the surrounding rock, respectively, and $V^{\text{garnet}} + V^{\text{rock}} = 1$. A lower volume-fraction bound would be $U_s = U_s^{\text{garnet}} V^{\text{garnet}}$, where V^{garnet} = 0.01 and 0.05 for the quartzo-feldspathic and schist rocks, respectively. To calculate a rigorous upper volume-fraction bound, we would need to know how much of the surrounding rock was fragmented, and the material properties and average fragment sizes (L) for all relevant minerals.

These parameters are difficult to evaluate in highly deformed mylonites and ultramylonites, so for our current analysis, we use 100% garnet for an upper volume-fraction bound $U_s = U_s^{\text{garnet}} V^{\text{garnet}}$, where $V^{\text{garnet}} = 1$. Also note that the lower and upper volume-fraction bounds of U_s are *total* surface-area energy densities recorded in the shear zone.

To estimate U_s *for a single earthquake*, we must estimate the number of earthquakes contributing to the fragmentation. Chester et al. (2005), Wilson et al. (2005) and Ma et al. (2006) divided their energy estimates by the number of earthquakes required to accumulate the total coseismic fault displacement. Total displacement on the Sandhill Corner shear zone is unknown so we cannot employ this method. Additionally, the Sandhill Corner shear zone was seismically active at temperatures consistent with the base of the seismogenic zone, so an unknown amount of displacement would have been accommodated by viscous flow in the post- and interseismic phases of the seismic cycle, and this would need to be subtracted from the total to estimate the coseismic displacements. A more direct method is to estimate the number of overprinting microfracture events in the mineral grains used for the analysis. In examining the garnet grains used for Figure C.8, we have identified 2 overprinting microfracture events, so the lower volume-fraction bound on U_s per earthquake is $U_s = \frac{1}{2}\left(U_s^{\text{garnet}} V^{\text{garnet}}\right)$, where V^{garnet} = 0.01 and 0.05 for the quartzo-feldspathic and schist rocks, respectively. To estimate the number of earthquake events for the upper volume-fraction bound, we examined the number of overprinting microfracture events preserved in plagioclase grains and quartz ribbons near the shear-zone core owing to their high modal abundance in the surrounding rock volume. As shown in Figure C.3, plagioclase grains and quartz ribbons experienced multiple generations of microfracturing followed by tight healing/sealing. Examining cathodoluminescence images of fragmented plagioclase and recrystallized quartz (e.g., Figures C.3d and f), we have found up to 6 sets of microfractures, so the upper volume-fraction bound on U_s per earthquake is $U_s = \frac{1}{6}\left(U_s^{\text{garnet}} V^{\text{garnet}}\right)$, where $V^{\text{garnet}} = 1$.

Given the above approach with its associated assumptions and using γ^{garnet} = 3.551 J/m^2 for almandine garnet (Table C.4; Tromans and Meech, 2002), we present lower and upper bound estimates on U_s over the dynamic damage zone in Figure C.10a. The surface-area energy density U_s for the two bounds, using the best-fit equations for L in Figure C.8c, ranges from 2.87×10^3 to 2.72×10^5 J/m^3. Integrating U_s over the dynamic damage-zone width in the Sandhill Corner shear zone leads to lower and upper bounds on the fracture energy per unit fault area U_{sa} of 6.63×10^5 J/m^2 and 1.63×10^7 J/m^2, respectively. Because plagioclase preserves an excellent record of fragmentation in these rocks, we could potentially evaluate the associated energy bounds for comparison with garnet. However, fragment size distributions for feldspar are more challenging than garnet because fragment boundaries are not resolved in optical or backscattered electron images, and in our experience, the resolution of cathodoluminescence images may be too low for determining reliable fragment size distributions. An alternative is to use electron backscatter diffraction (EBSD) methods. Figure C.11 shows application of EBSD (see Methods in B. R. Song et al., 2020) to the BB16 plagioclase grain in Figure C.3c, giving an area-averaged fragment size L of 27.19 μm (Figure C.8c; Table C.2). Using $\gamma^{\text{plagioclase}}$ = 2.739 J/m^2 for anorthite plagioclase (Table C.4; Tromans and Meech, 2002) and the surface area correction factor λ (~1.5) determined for garnet (Table C.2), the upper bound for U_s per earthquake of the plagioclase grain (1.51×10^5 J/m^3) is very close to the value for garnet BB12 (1.92×10^5 J/m^3) near the fault core (Figure C.10a; Table C.5), despite the good cleavage in plagioclase that might compromise results (see Figure C.8 and Table C.2 for other measured/calculated parameters of the BB16 plagioclase).

Table C.4 Material properties used for computation of fracture surface-area energy density, tensile strain rate, normalized strain rate, and normalized average fragment size for fragmented garnet and plagioclase samples.

	Garnet		Plagioclase	
Property[a]	Value	Reference	Value	Reference
γ (J/m^2)	3.551	Almandine (Tromans & Meech, 2002)	2.739	Anorthite (Tromans & Meech, 2002)
ρ (kg/m^3)	4,132	Almandine-rich garnet (Jiang et al., 2004)	N/A[b]	
E (Pa)	2.4173×10^{11}	Almandine (Hearmon,1979)	1.0328×10^{11}	Anorthite (Hearmon,1979)
K_{Ic} (Pa·m$^{1/2}$)	1.310×10^{6}	Almandine (Tromans & Meech,2002)	7.52×10^{5}	Anorthite (Tromans & Meech,2002)
v_{c} (m/s)	250–1,000	Zhang & Zhao (2014); Hogan et al. (2016)	250–1,000	Zhang & Zhao (2014); Hogan et al. (2016)
σ_{c} (Pa)	1.014×10^{9}	Static-loading strength of yttrium aluminum garnet (Jiang et al., 2019)	N/A[b]	
σ_{t} (Pa)	1.014×10^{8}	$\sigma_{\mathrm{t}} = \sigma_{\mathrm{c}}/10$ (e.g., Hogan et al., 2016)	N/A[b]	
M	2	Hogan et al. (2016)	2	Hogan et al. (2016)
B	3	Volumetric problem (Hogan et al., 2016)	3	Volumetric problem (Hogan et al., 2016)

[a]See Table C.1 for the definition of each symbol.
[b]These properties (ρ, σ_{c} and σ_{t}) are not used for plagioclase because normalized strain rate and normalized average fragment size for plagioclase are not calculated.

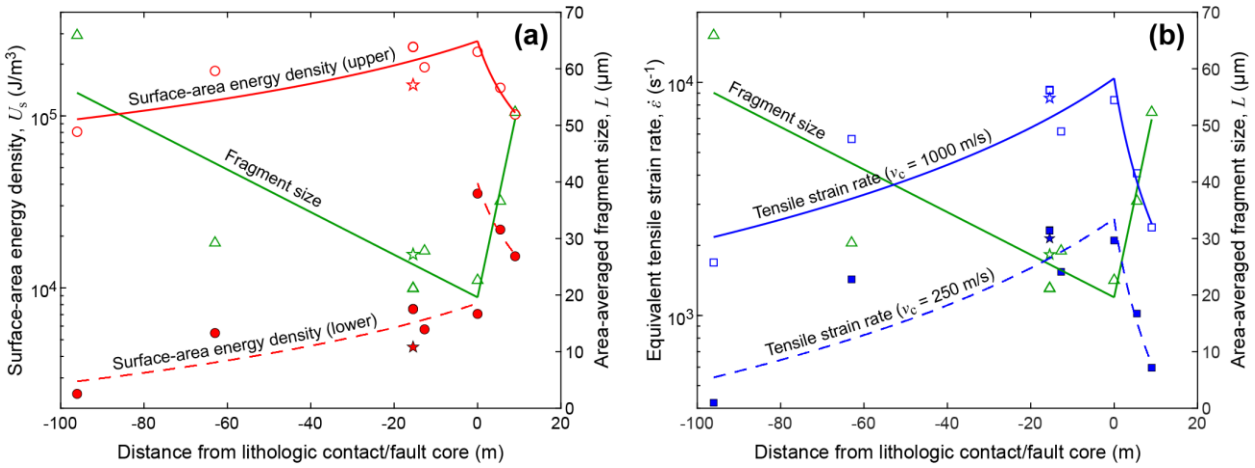

Figure C.10 Plots of surface-area energy density (U_s) and equivalent tensile strain rate ($\dot{\varepsilon}$), for a single earthquake, calculated from area-averaged garnet fragment size (L) across the dynamic damage zone of the Sandhill Corner shear zone. Symbols indicate results for individual garnet samples (see Table C.5). (a) Upper and lower bounds of U_s plotted on a logarithmic scale. Green line and triangles – L (from Figure C.8c); red solid line and circles – upper bound on U_s assuming 100% garnet and 6 microfracture events; red dashed line and filled circles – lower bound on U_s assuming 1% and 5% garnet in the quartzo-feldspathic and schist rocks, respectively, and 2 microfracture events. The discontinuity in the lower bound on U_s across the core is caused by the different modal percentages of garnet. (b) Upper and lower bounds of $\dot{\varepsilon}$ plotted on a logarithmic scale. Green line and triangles – L (from Figure C.8c); blue solid line and squares – $\dot{\varepsilon}$ for crack propagation velocity (v_c) = 1000 m/s, blue dashed line and filled squares – $\dot{\varepsilon}$ for v_c = 250 m/s. BB16 plagioclase data for L, upper and lower values of U_s, and upper and lower values of $\dot{\varepsilon}$ are also plotted for comparison (marked by stars). Note the strongly asymmetric distribution across the lithologic contact (shear-zone core).

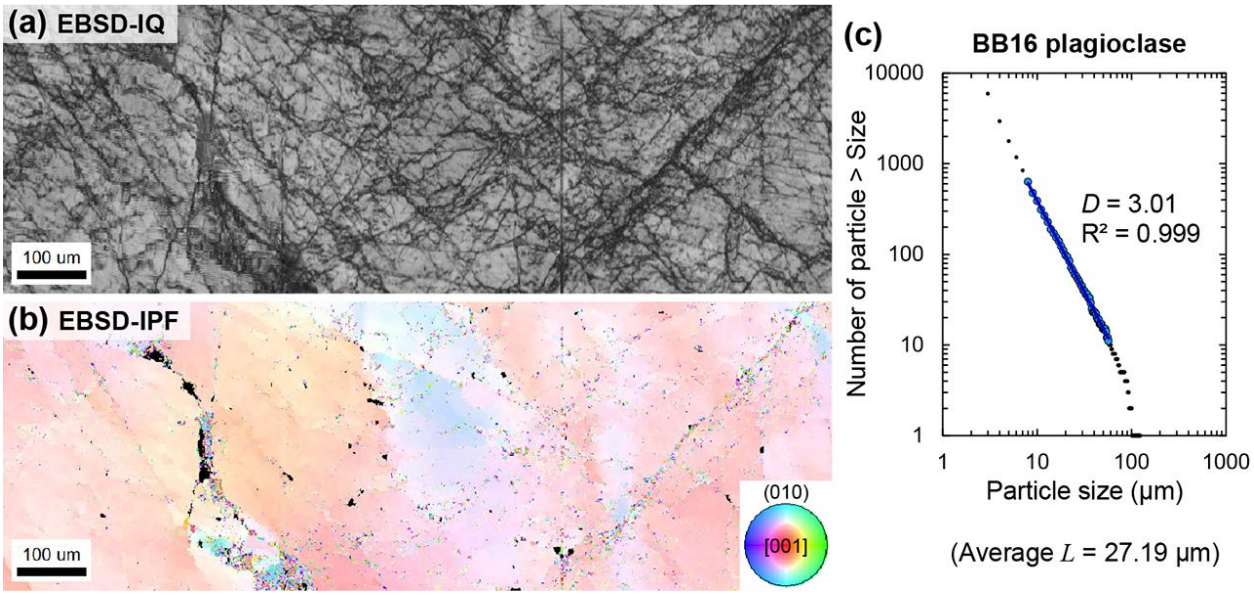

Figure C.11 EBSD analysis of fragment size distribution of BB16 plagioclase in Figure C.3c. (a) Image quality (IQ) map showing microfractures. (b) Inverse pole figure (IPF) map showing crystallographic orientations, acquired using 1 μm step size. (c) Cumulative size distribution of plagioclase fragments (>3 μm), defined by >0.5° misorientation. *D*-value, microfracture density and average fragment size for 10 μm ≤ Size ≤ Max are shown in Figure C.8.

Table C.5 Summary of fracture surface-area energy density (U_s) and tensile strain rate ($\dot{\varepsilon}$) for fragmented garnet and plagioclase samples.

				U_s per EQ[b]		Total $\dot{\varepsilon}$		$\dot{\varepsilon}$ per EQ[f]	
Lithology	Sample	Distance[a] (m)	Total U_s (J/m^3)	Upper bound[c] (J/m^3)	Lower bound[d] (J/m^3)	v_c[e] = 1,000 (s^{-1})	v_c = 250 (s^{-1})	v_c = 1,000 (s^{-1})	v_c = 250 (s^{-1})
QF[g]	71 (garnet)	-96.06	4.849×10^5	8.082×10^4	2.425×10^3	2.481×10^4	2.481×10^4	1.688×10^3	4.220×10^2
QF	56 (garnet)	-62.98	1.094×10^6	1.823×10^5	5.469×10^3	8.405×10^4	8.405×10^4	5.719×10^3	1.430×10^3
QF	BB16-a (garnet)	-15.47	1.506×10^6	2.510×10^5	7.529×10^3	1.358×10^5	1.358×10^5	9.237×10^3	2.309×10^3
QF	BB16 (garnet)	-15.47	1.512×10^6	2.519×10^5	7.558×10^3	1.366×10^5	1.366×10^5	9.291×10^3	2.323×10^3
QF	BB16 (plagioclase)	-15.47	9.067×10^5	1.511×10^5	4.534×10^3	1.258×10^5	1.258×10^5	8.561×10^3	2.140×10^3
QF	BB12 (garnet)	-12.72	1.149×10^6	1.916×10^5	5.747×10^3	9.054×10^4	9.054×10^4	6.160×10^3	1.540×10^3
Contact	41 (garnet)	0.00	1.413×10^6	2.355×10^5	7.065×10^3 [3.532×10^4]	1.234×10^5	1.234×10^5	8.397×10^3	2.099×10^3
Schist	305 (garnet)	5.46	8.730×10^5	1.455×10^5	[2.183×10^4]	5.993×10^4	5.993×10^4	4.078×10^3	1.019×10^3
Schist	28 (garnet)	9.01	6.109×10^5	1.018×10^5	[1.527×10^4]	3.508×10^4	3.508×10^4	2.387×10^3	5.967×10^2

[a]Perpendicular distance was measured from the lithologic contact between the QF[g] and schist rocks, and negative values indicate the QF rocks.

[b]U_s calculated for a single earthquake (EQ).

[c]Upper bound on U_s per EQ assumes 100% garnet (or plagioclase) volume and 6 earthquake events, so it is calculated by dividing the total U_s by the number of earthquakes.

[d]Lower bound on U_s per EQ assumes 1% and 5% garnet volumes (V^{garnet} = 0.01 and 0.05, respectively) in the QF and schist rocks, respectively and 2 earthquake events, so it is calculated by $\left(U_s^{\text{total}} \times V^{\text{garnet}}\right)/2$ where U_s^{total} is the total U_s. The values in brackets represent U_s per EQ using 5% garnet volume. Sample 41 from the lithologic contact between the QF and schist rocks has both U_s per EQ for 1% and 5% garnet volumes. Lower bound for the plagioclase sample is calculated by the same approach as garnet and presented for the purpose of comparison.

[e]v_c is effective fracture propagation velocity (m/s). 1,000 and 250 m/s are used for upper and lower bounds for $\dot{\varepsilon}$, respectively.

[f]$\dot{\varepsilon}$ per EQ assumes 6 earthquake events (N_{EQ} = 6) and is calculated, using the nonlinear relationship between strain rate and fragment size in the text, and by$\dot{\varepsilon} \times N_{\text{EQ}}{}^{(-3/2)}$.

[g]QF = quartzo-feldspathic.

C.7. Estimating Strain Rate ($\dot{\varepsilon}$) from Fragmented Minerals in the Earthquake Source Volume

Here we present a novel application of physics-based fragmentation models for estimating strain rates from fragmented minerals collected in the earthquake source volume. Many processes cause brittle fragmentation including meteorite impact, volcanic eruption, brecciation, shear cataclasis, projectile penetration, thermoelastic stresses, and munitions explosions, and it has long been postulated that an underlying energy principle plays a central role in fragmentation (see Grady, 2017 for a comprehensive review). Most quantitative relationships between strain rate and fragment size distribution have been made for tensile stresses, focusing largely on the problem of a thin expanding ring (reviewed by Grady, 2017 and Ramesh et al., 2015). In the present paper, we focus on the work of Grady (1982 and later work), Glenn and Chudnovsky (1986), Zhou et al. (2006a, 2006b), and Levy and Molinari (2010). Grady (1988) derived a length scale $L = 2ct$, where c is the longitudinal wave speed (m/s) in the material and t is time (s). This equation states that any region within the spherical radius ct surrounding a defect that acts as the locus of failure will fail independently of areas outside this radius. L can therefore be treated as estimating the average fragment size for high strain-rate loading based on the local balancing of kinetic and fracture energy. Because it is based on an energy balance that includes fracture surface-area energy, L is the fragment size that represents the average surface area of the fragment population, not the mean size of the population (Section 3). Glenn and Chudnovsky (1986) adjusted Grady's length scale to account for the fact that stored elastic strain energy dominates over kinetic energy in the quasistatic regime, which has recently been employed by Griffith et al. (2018).

The works of Grady (1982 and later work) and Glenn and Chudnovsky (1986) are based on instantaneous, macroscale energy balances and do not account for the role of heterogeneously distributed microstructural attributes such as flaws, nor the time-dependent processes of fracture initiation/growth and internal elastic wave reflections/interactions that occur during dynamic fragmentation. Zhou et al. (2006a) employed finite element techniques to incorporate a dynamic fracture initiation criterion and a cohesive fracture growth model that includes time-dependent wave interactions to describe the fragmentation of an expanding, homogeneous ring. Levy and Molinari (2010) extended the work of Zhou et al. (2006a) by

including the distributions of flaws (material heterogeneity) in the material and their influence on local stress concentrations, as well as the influence of stress relief waves upon fracture initiation and growth. A fundamental finding of these later numerical works is that the energy-based macroscale approaches of Grady (1982 and later work) and Glenn and Chudnovsky (1986) overestimate the fragment size for a given strain rate in the dynamic regime. Hogan et al. (2016) modified the instantaneous, energy-based expressions of Grady (1982 and later work) and Glenn and Chudnovsky (1986) to allow better comparison with the time-dependent models of Zhou et al. (2006a, 2006b) and Levy and Molinari (2010). Because Hogan et al. (2016) conducted compressional experiments, they also derived an expression for converting their compressional strain rates to equivalent tensile strain rates for comparison with the above tensile fragmentation models. We briefly review all six models (the four original models plus the two modified models presented by Hogan et al., 2016), and select one to compute our garnet strain rates.

Each of the models cited above retrieves the same general relation $L \propto \dot{\varepsilon}^{(-2/3)}$ at high strain rates where L is the area-averaged fragment size and $\dot{\varepsilon}$ the strain rate. The proportionality relation assumes an ideal continuum in which energy consumption is purely by fracture. Natural rock materials such as oil shale (Grady, 1982) and Westerly Granite (Ghaffari et al., 2019) may deviate from the ideal relation owing to additional energy-consumption mechanisms. Although the different models give somewhat different predictions, if the results are normalized by characteristic values, then they can be directly compared. Zhou et al. (2006b) compiled the appropriate characteristic values as follows. A characteristic length scale L_0 is:

$$L_0 = ct_0 \tag{C14}$$

which represents the statistical size of a fragment when the available excess potential energy is converted to fracture energy. A characteristic time t_0 defined by Camacho and Ortiz (1996) is:

$$t_0 = \frac{E\Gamma}{\sigma_t^2 c} \tag{C15}$$

where E is Young's modulus (Pa), Γ is the Mode I fracture energy for plane stress conditions (J/m^2) which is effectively the same value as specific surface energy γ for brittle materials, σ_t is the quasistatic tensile

strength of the material (Pa), and $c = \sqrt{E/\rho}$ is the longitudinal wave speed (m/s) in the material where ρ is mass density (kg/m^3). This equation can be interpreted as the time needed for elastic waves released by a cohesive element to encompass the characteristic fragment size L_0 (Levy and Molinari, 2010). Γ is given as:

$$\Gamma = \frac{K_{\mathrm{Ic}}^2}{2E} \tag{C16}$$

where K_{Ic} is the Mode I fracture toughness (Pa·m$^{1/2}$). And finally, from Equations (C15) and (C16), a characteristic strain rate $\dot{\varepsilon}_0$ defined by Drugan (2001) is:

$$\dot{\varepsilon}_0 = \frac{\sigma_{\mathrm{t}}}{E t_0} = \frac{2\sigma_{\mathrm{t}}^3 c}{E K_{\mathrm{Ic}}^2} \tag{C17}$$

which can be interpreted as the strain rate required to fully open a cohesive element in characteristic time t_0. The normalized strain rate $\bar{\dot{\varepsilon}}$ and the normalized average fragment size $\bar{L}$ are then defined as (Zhou et al., 2006b):

$$\bar{\dot{\varepsilon}} = \frac{\dot{\varepsilon}}{\dot{\varepsilon}_0} \text{ and } \bar{L} = \frac{L}{L_0} \tag{C18}$$

Using these characteristic values, we arrive at the normalized relations between average fragment size and strain rate for the fragmentation models above, adopting the form proposed by Grady (2006, Equation 5.16). Thus, the Grady (2006) normalized fragment size is:

$$\bar{L}_{\mathrm{Grady}} = \left(\frac{24}{\bar{\dot{\varepsilon}}^2}\right)^{1/3} \tag{C19}$$

The Glenn and Chudnovsky (1986) normalized fragment size is:

$$\bar{L}_{\mathrm{GC}} = \frac{4}{\bar{\dot{\varepsilon}}} \sinh\left(\frac{1}{3}\sinh^{-1}\left(\frac{3}{2}\bar{\dot{\varepsilon}}\right)\right) \tag{C20}$$

The Zhou et al. (2006a, 2006b) normalized fragment size is:

$$\bar{L}_{\mathrm{ZMR}} = \frac{4.5}{1 + 4.5\bar{\dot{\varepsilon}}^{2/3}} \tag{C21}$$

And the Levy and Molinari (2010) normalized fragment size is:

$$\bar{L}_{\mathrm{LM}} = \frac{3}{1 + 4.5\bar{\dot{\varepsilon}}^{2/3}} \tag{C22}$$

The coefficients in the models by Grady (2006) and Glenn and Chudnovsky (1986) are based on energy balances whereas the coefficients in the numerical models of Zhou et al. (2006a, 2006b) and Levy and Molinari (2010) were obtained by data-fitting. As noted above, Hogan et al. (2016) developed modified versions of the models by Grady (2006) and Glenn and Chudnovsky (1986) to compare the results of their compression experiments with fragmentation models based on tensile fragmentation. The modified normalized Grady equation (Hogan et al., 2016) is:

$$\bar{\bar{L}}_{\mathrm{Grady}} = 2\left(\frac{2Bv_{\mathrm{c}}^2}{M^2c^2\bar{\dot{\varepsilon}}^2}\right)^{1/3} \tag{C23}$$

where B is a geometrical factor (2 for a 2D problem, 3 for a 3D problem), v_{c} is the effective fracture propagation velocity (m/s), and $M = t_{\mathrm{l}}/t_{\mathrm{f}}$ where t_{l}, the loading time, is the time required to absorb the applied strain energy and t_{f}, the failure time, is the time required to dissipate the applied energy. M is generally valid for dynamic loads as it would approach infinity at tectonic loading rates. Similarly, the modified normalized Glenn and Chudnovsky equation (Hogan et al., 2016) is:

$$\bar{\bar{L}}_{\mathrm{GC}} = \sqrt{\frac{2B}{3}}\frac{4v_{\mathrm{c}}}{Mc\bar{\dot{\varepsilon}}}\sinh\left(\frac{\theta}{3}\right) \quad \text{where } \theta = \sinh^{-1}\left[\sqrt{\frac{3}{2B}}\frac{3Mc\bar{\dot{\varepsilon}}}{2v_{\mathrm{c}}}\right] \tag{C24}$$

Of the six normalized models, the modified Grady ($\bar{\bar{L}}_{\mathrm{Grady}}$) and the modified Glenn and Chudnovsky ($\bar{\bar{L}}_{\mathrm{GC}}$) models are dependent on material properties whereas the other four models are not.

Hogan et al. (2016) compared their experimental results on five different materials with the six models, using the material properties of silicon carbide (SiC-N) to plot the curves of the modified Grady and the modified Glenn and Chudnovsky models, and found that the modified Grady model provided the

best fit to the data. We replotted all the model curves using the properties of the five materials presented in Hogan et al. (2016) and confirm that, overall, the modified Grady model does a good job of predicting fragment size for each material at a given strain rate, although our garnet data are equally well fit with the Zhou et al. (2006a, 2006b), Levy and Molinari (2010), and modified Glenn and Chudnovsky (1986) models. Using Equations (C19)–(C24) and appropriate properties for garnet (Table C.4), Figure C.12 illustrates how our garnet data plot in relation to the experimental results from Hogan et al. (2016). The large range bars stem from the uncertainties associated with the mechanical properties and the standard deviation of average fragment size L (see the caption of Figure C.12). Values of v_c for garnet have not been reported to our knowledge, so we use a value of v_c = 1,000 m/s to illustrate the relationships. We use a value of 3 for B as we are interested in volume fragmentation of garnet, and M is taken as 2 following Hogan et al. (2016). We assume the relationship $\sigma_t = \sigma_c/\alpha$ where σ_c is the quasistatic uniaxial compressive strength (Pa), and the handbook by Harper (2001) indicates that α typically lies between 8 and 12. Following Hogan et al. (2016), we choose a value of α = 10.

Given these results, we use the modified Grady model to calculate dimensional strain rates from our garnet fragment size data. From the modified normalized Grady model in Equations (C14)–(C18) and (C23) and, the dimensional strain rate as a function of L is:

$$\dot{\varepsilon} = \frac{4v_c}{M}\sqrt{\frac{B\Gamma}{E\hat{L}^3_{\mathrm{Grady}}}} \tag{C25}$$

It is important to note that the calculated strain rate using $\hat{L}_{\mathrm{Grady}}$ is an *equivalent tensile strain rate*, which is based on the rate expected by equating strain energies in the compressional experiments to equivalent tensile strain energies (Hogan et al., 2016): *it does not imply that the micromechanical processes are the same in the two types of failure, nor that we are assuming macroscale tension in the damage zone*. Extension of this approach to field conditions is not trivial owing at least partly to the likely spatial variability of the dynamic stress tensor depending on position in the damage zone and time during a coseismic event, which will impact the nature and extent of fragmentation and choice of appropriate model (e.g., Barber and

Griffith, 2017; Bhat et al., 2012; Thomas and Bhat, 2018; Xu and Ben-Zion, 2017; Okubo et al., 2019). We use this approach with appropriate caution, noting that options are few, and suggest that additional theoretical, experimental, and numerical work is needed to better understand the extension of these models to dynamic coseismic fragmentation.

In estimating the equivalent tensile strain rate for a single earthquake in the Sandhill Corner shear zone, we apply the same correction for the number of earthquake events (N_{EQ} = 6) as we used for the upper bound on U_{s} (Figure C.10a). Unlike the correction applied to U_{s}, the relationship between $\dot{\varepsilon}$ and $\hat{L}_{\mathrm{Grady}}$ is nonlinear, so the corrected strain rate for a single earthquake $\dot{\varepsilon}^{\mathrm{cor}} = \dot{\varepsilon} N_{\mathrm{EQ}}{}^{(-3/2)}$. The surface area correction factor λ used to calculate U_{s} is not applicable to the strain rate calculation. Using Equation (C25) and applying $\dot{\varepsilon}^{\mathrm{cor}}$, Figure C.10b shows the distribution of equivalent tensile strain rate for a single earthquake either side of the core of the Sandhill Corner shear zone. The upper and lower bounds use the effective fracture propagation velocity v_{c} = 1,000 and 250 m/s, respectively. Dynamic fracture propagation velocities in rocks and minerals are poorly known, spanning large ranges for given materials (e.g., Hogan et al., 2016; Zhang and Zhao, 2014) and fluctuating broadly as a function of fracture branching (e.g., Sharon et al., 1996); *we choose these values of v_{c} to illustrate the relations between v_{c}, $\dot{\varepsilon}$ and L.* The equivalent tensile strain rate for a single earthquake using the best-fit equations for *L* in Figure C.8c ranges from 2.17×10^{3} to 1.04×10^{4} s^{-1} for v_{c} = 1,000 m/s and 5.42×10^{2} to 2.60×10^{3} s^{-1} for v_{c} = 250 m/s. In addition, uncertainties in the value of M in Equation (C25) could lead to a factor of ±0.5 difference in these estimates. Owing to the current uncertainties in the various parameters in Equation (C25) and the way that the equivalent tensile strain rate is calculated (Hogan et al., 2016), these estimates should be treated as preliminary. Nevertheless, the method appears to have promise and the results are within range of what might be expected from theory and laboratory experiments.

Peak tensile strain rates of order 10^{5} s^{-1} have been predicted in previous theoretical work (e.g., Reches and Dewers, 2005), and compressional strain rates of order 10^{3} s^{-1} were required in single-event tests to pulverize Arkansas Novaculite in weakly confined conditions (Barber and Griffith, 2017) and

Westerly Granite at 60 MPa confining pressure (Yuan et al., 2011). Aben et al. (2016) have noted that pulverization can be related to total strain accumulation. They assigned a threshold value of ~1.2% finite strain and have shown that this threshold can be achieved by a single high-energy compression event or an accumulation of multiple lower-energy compression events. On the other hand, Griffith et al. (2018) found that relatively coarse (>2 mm), columnar-shaped fragments form in Westerly Granite during what they interpreted as radial isotropic tension at tensile strain rates of <50 s^{-1}, suggesting that extensive damage zones may reflect multiple applications of macroscale tension. Although we are not necessarily advocating for macroscale dynamic tension, there are good reasons to consider the possibility, some of which are presented below.

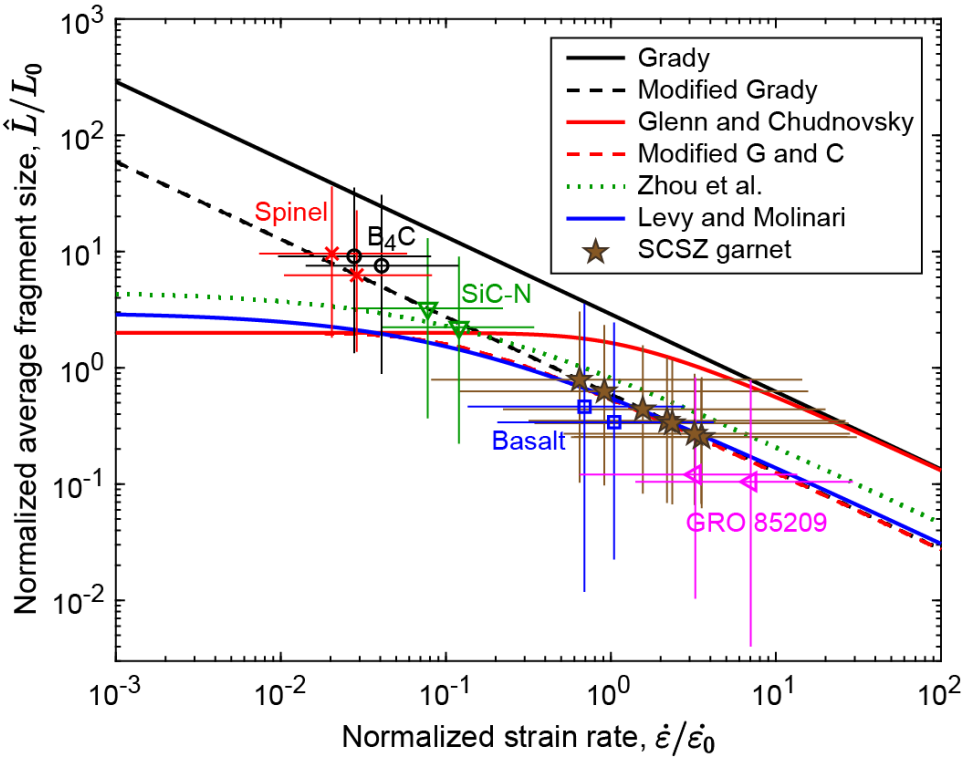

Figure C.12 Comparison of normalized average fragment size against normalized strain rate for the garnet data in the Sandhill Corner shear zone (SCSZ garnet marked by stars) with the experimental data (spinel, boron carbide – B_4C, silicon carbide – SiC-N, basalt, and meteorite – GRO 85209) of Hogan et al. (2016) and the six models of Grady (2006), modified Grady (Hogan et al., 2016), Glenn and Chudnovsky (1986), modified Glenn and Chudnovsky (G and C; Hogan et al., 2016), Zhou et al. (2006a, 2006b), and Levy and Molinari (2010). The two curves of the modified Grady and the modified G and C are plotted using garnet properties (Table C.4). The SCSZ garnet data are computed using the modified Grady model and the area-averaged fragment size (Figure C.5c; Table C.2). We use v_c of 1000 m/s to illustrate relations. Value ranges on non-garnet data are from Hogan et al. (2016), and we computed range bars the same way for the garnet data—by combining the uncertainties associated with determination of physical properties and the range of fragment size ± its standard deviation (Table C.2). For physical properties, following Hogan et al. (2016), an uncertainty of 20% was assumed for σ_t and K_{Ic}, and 5% was assumed for E and ρ.

C.8. Discussion

C.8.1. Comparison to Other Estimates of U_{conv}, U_{sa} and U_{fh}

Different estimates of U_{conv}, U_{sa} and U_{fh} are found in the literature and here we divide them into three groups for comparison with our results: (1) geological estimates of U_{sa} (Olgaard and Brace, 1983; Chester et al., 2005; Reches and Dewers, 2005; Wilson et al., 2005; Ma et al., 2006; Pittarello et al., 2008) and U_{fh} (Matsumoto et al., 2001; Reches and Dewers, 2005; Pittarello et al., 2008; Brodsky et al., 2020);

(2) theoretical and numerical estimates of U_{sa} or U_{conv} (Aki, 1979; Li, 1987; Guatteri et al., 2001; Poliakov et al., 2002; Ide, 2003; Abercrombie and Rice, 2005; Di Toro et al., 2005; Rice et al., 2005; Lancieri et al., 2012; Kozdon and Dunham, 2013; Malagnini et al., 2014; Brodsky et al., 2020) and (3) estimates of U_{sa} or U_{conv} from inversion of ground motion waveforms using kinematic slip models (Tinti et al., 2005, 2008; Ma et al., 2006; Cocco and Tinti, 2008). Because our geological estimates of U_{sa} arise from integration of U_s across the entire damage zone, they are macroscale values and therefore can be directly compared with seismological estimates (Cocco and Tinti, 2008).

Figure C.13 shows our upper and lower bounds of U_{sa} for a single earthquake compared to 55 other estimates of U_{conv}, U_{sa} and U_{fh}. The average value of ~1.4×10^7 J/m^2 considers only the lower-bound and single estimates. Where the values are known, all but two of these earthquakes or faults have seismic moments M_0 ranging from 2.5×10^{17} to 4.8×10^{22} N·m, which corresponds to moment magnitude M_w ranging from 5.5 to 9.1 (Table C.6). For completeness, we include two studies (Olgaard and Brace, 1983; Reches and Dewers, 2005, the data from which was used by Wilson et al., 2005) that estimate U_{sa} from much smaller earthquakes with local magnitudes M_L = 2.1 and 3.7, respectively. We note that most of the geological estimates of U_{sa} come from thin gouge and cataclasite/ultracataclasite layers that experienced significant shearing comminution, whereas the garnet grains used in the present study display primarily Mode I microfractures and are distributed through the off-fault damage zone. In addition, except for Pittarello et al. (2008), these other geological estimates were made in rocks exhumed from a maximum depth of 2–4 km, whereas the Sandhill Corner shear zone was seismically active at the base of the seismogenic zone. Surface-energy generation through Mode I microfracture versus shearing comminution involves different processes so it is not clear whether the surface energy generated by the two processes can be directly compared. Similarly, it is not clear whether we can make direct comparisons of surface-energy generation in rocks exhumed from different depths. With these caveats in mind, we briefly discuss some of these previous studies.

Wilson et al. (2005) calculated U_{sa} (2.0–3.6×10^6 J/m^2) for a portion of the San Andreas fault at Tejon Pass, California for a 10-mm thick gouge zone generated by each earthquake, and they estimated that 7,000–10,000 earthquakes formed the total observed damage zone 70–100 m wide. The U_{sa} values of Wilson et al. (2005) have been questioned by Rockwell et al. (2009) who were unable to reproduce their laser-determined particle size distributions. Presumably this also calls into question the results from Reches and Dewers (2005) for the Bosman fault, South Africa, formed during a 1997 M_L = 3.7 earthquake.

For the Chester et al. (2005) data, assuming no fragmented grains were healed/sealed and refractured, the total estimated U_{sa} around the Punchbowl fault in California is 7×10^8 J/m^2. They divided this number by 10,000 (estimated number of earthquakes responsible for the estimated 44 kms of fault displacement) to arrive at a value of U_{sa} per earthquake of 7×10^4 J/m^2. They noted that if 50% of the ultracataclasite in the mm-thick principal slip surface was healed/sealed and then refractured during an earthquake, and the energy to refracture a grain boundary is half of that required to fracture an intact grain, then this would lead to a value of ~5×10^5 J/m^2 per earthquake. In Figure C.13, we report their total energy estimate of 7×10^8 J/m^2, their minimum estimate of 7×10^4 J/m^2 per earthquake, and their intermediate estimate of 5×10^5 J/m^2 per earthquake given healing and refracturing of the mm-thick principal slip surface. For purposes of discussion, we apply the same calculation to the entire 0.3 m-wide ultracataclasite bounding the mm-thick principal slip surface. Following the calculation by Chester et al. (2005), if 50% of the ultracataclasite was healed/sealed, and the energy to refracture a grain boundary is half of that required to fracture an intact grain, we obtain a value of ~1.6×10^8 J/m^2 per earthquake. We do not plot this value in Figure C.13, but it does show how sensitive the energy calculations are to fragment healing/sealing and refracturing and we note that healing/sealing (including fluid-inclusion planes) was extensive in these rocks (Wilson et al., 2003). The Chester et al. (2005) estimate of 5×10^5 J/m^2 has been used is some studies (e.g., Cocco and Tinti, 2008) to infer that surface-area energy generation is a negligible energy sink in the source, but the uncertainties in this estimate are large and it should be interpreted with appropriate care.

For the Ma et al. (2006) data, the geological estimate of U_{sa} per earthquake (6.5×10^5 J/m^2) was obtained by dividing the total calculated U_{sa} (4.3×10^6 J/m^2) by ~6.6 earthquakes assuming that no fragmented grains were healed/sealed. Ma et al. (2006) did not quantify the off-fault component, measuring fragment sizes in a single, 2-cm-wide slip zone in a drill core so their reported U_{sa} in total, and per earthquake, should be considered minimum estimates. If we make the same assumption for fragment healing/sealing as for the Punchbowl fault example above considering the entire 2-cm-wide slip zone, we obtain a value of ~1.4×10^6 J/m^2 per earthquake, without considering off-fault surface-area energy. We do not plot this value in Figure C.13, but again we note the sensitivity of the energy calculations to fragment healing/sealing.

The Pittarello et al. (2008) geological estimates of U_{sa} were obtained by using fragments in plagioclase survivor clasts *within* pseudotachylyte veins as well as fractured wall rocks adjacent to pseudotachylyte veins in rocks exhumed from ~10 km depth and ambient temperature of ~250 °C. Owing to the direct proximity of friction melt, this fragmentation could represent thermal shock loading in whole or part (e.g., Papa et al., 2018, 2021), so the results of Pittarello et al. (2008) may not be directly comparable to results obtained by mechanical fragmentation processes.

Seismological calculations from kinematic slip models reanalyzed for breakdown work by Tinti et al. (2005, 2008) and Cocco and Tinti (2008) show a wide range of U_{sa} values as a function of calculated slip on the fault. For these models, we show a range from a lower value that represents the whole-fault average (the lowest value they reported) to an upper value that represents the parts of the fault that slipped greater than 90% of the maximum calculated slip. For the data from Rice et al. (2005) and Abercrombie and Rice (2005), the maximum value was calculated as they did—twice the minimum value. All others are single-value or stated-range estimates of U_{conv}, U_{sa}, or U_{fh}.

The results of our analysis overlap well with the 55 other estimates and, if correct, provides new evidence for the role of surface energy in the deeper source volume. Overlap of our geological estimates of U_{sa} with those from the three large-displacement faults (Chester et al., 2005; Wilson et al., 2005; Ma et al.,

2006) is particularly interesting given that we selected garnet grains from across the ~105-m-wide dynamic damage zone of the Sandhill Corner shear zone whereas most of the surface energy in these studies was apparently stored in thin cataclasite and ultracataclasite layers within or adjacent to principal slip zones/surfaces in shallowly-exhumed fault rocks. The degree of off-fault damage in the uppermost crust along mature faults may potentially be minimized through time by the development of these thin principal slip surfaces that are weak owing to low-cohesion fault gouge and/or low-friction fault material (Shipton et al., 2006). However, this is unlikely to hold in the deeper reaches of the seismogenic zone where transient porosity and permeability are rapidly healed/sealed by processes like quartz-vein infill, metamorphic reactions, grain sintering, and recrystallization. Given the rock compositions and seismic activity at temperatures of ~350–500 °C in the Sandhill Corner shear zone, most healing/sealing of microfractures was accomplished primarily by quartz deposition (Figures C.3 and C.7). Healing/sealing times for quartz at such temperatures are extremely rapid (e.g., Brantley et al., 1990), so the rocks were almost certainly fully healed/sealed in the interseismic periods and fresh rock needed to be broken down during each earthquake. For this reason, surface-energy generation may be a more important energy sink at depth than it is near the surface where the fault rocks may not be fully healed/sealed in the interseismic periods. This highlights the importance of integrating observations from top to bottom in the seismogenic zone when considering the earthquake energy budget.

Recognizing an enhanced role of microscale damage surrounding the fault/shear-zone core allows U_{rad}, as it is measured in the far field, to accommodate a small fraction of the total energy released without the vast majority of the remaining energy needing to be dissipated as frictional heat, for which there is limited geological/geophysical evidence (e.g., Lachenbruch and McGarr, 1990). For a recent well-constrained example, Brodsky et al. (2020) note that for the 2011 M_w 9.1 Tohoku earthquake in Japan, the energy dissipated as frictional heat U_{fh}, based on direct heat-flow measurements of Fulton et al. (2013), ranges from 20–86 MJ/m^2 given a conservative estimate of stress drop (2 MPa). This contrasts with their range of plausible U_{conv} values of 46–300 MJ/m^2. A significant range of plausible U_{conv} values exceed the range of U_{fh}, opening the possibility of off-fault energy consumption (U_{sa}) of similar magnitude to that

dissipated as heat; a larger estimate of stress drop would further increase the discrepancy. The Tohoku results contrast, for example, with Pittarello et al. (2008) who compared pseudotachylyte thicknesses with fragment sizes in plagioclase and rock enclosed by or adjacent to pseudotachylyte from the Gole Larghe fault in the Italian Alps to infer that 97–99% of U_{conv} went into heat. These large variations in estimates of U_{fh} as a percentage of U_{conv} exemplify the need for additional geological, theoretical, numerical, and experimental studies of energy consumption/dissipation at different depths in the seismogenic zone.

Fracture or breakdown energy is heterogeneously distributed around faults as shown for example in kinematic slip models (e.g., Tinti et al., 2005), microstructural observations in drill core (e.g., Wechsler et al., 2011), and field investigations (e.g., Johnson et al., 1994; Chester and Chester, 1998; Chester et al., 2004; Dor et al., 2006; Bistacchi et al., 2010; Griffith et al., 2010; Rempe et al., 2013; Smith et al., 2013; Milliner et al., 2015; Ostermeijer et al., 2020). This should be expected in the source volume owing to non-linear elastic responses, body-wave reflections and interactions in the anisotropic heterogeneous material, and localized failure events, all leading to spatial and temporal heterogeneity in the distribution of U_{sa}. In the Sandhill Corner shear zone, such heterogeneity is reflected in the variable intensity of fragmentation in garnet and plagioclase grains throughout the damage zone, with some grains showing more intense fragmentation than others at a similar distance from the shear-zone core. Thus, the total stress history at a fixed distance from the core of the Sandhill Corner shear zone appears to have differed from other positions the same distance from the core. This same point was made by Short (1966) who studied the microstructures associated with the 1962 Hardhat nuclear explosion and noted that natural discontinuities and inhomogeneities can cause shock wave perturbation, differential movements, and heterogeneous failure and fragmentation. Thus, multiple transects across a given damage zone would likely lead to a more robust analysis of U_{sa}.

The occurrence of pseudotachylyte as far as 40 m from the core of the Sandhill Corner shear zone raises the additional possibility of multiple slip surfaces operating at depth during individual and/or successive earthquakes, and similar observations of dispersed pseudotachylyte have been made by other workers (e.g., Wenk et al., 2000; Edwards and Ratschbacher, 2005; Allen and Shaw, 2013; Smith et al.,

2013). Most, though not all, of the off-fault pseudotachylyte in the Sandhill Corner shear zone has been viscously deformed during post- and inter-seismic periods (e.g., Figure C.3a), so may reflect the early evolution of the fault zone before a well-established core was developed (e.g., Scholz et al., 1993; Chester and Chester, 1998; Ben-Zion and Sammis, 2003; Chester et al., 2004; Chester et al., 2005; Shipton et al., 2006; Vallée et al., 2008; Brodsky et al., 2011; Perrin et al., 2016, 2021; Ross et al., 2017). However, the spatial gradients in *D*-values, microfracture density and garnet fragment sizes relative to the shear-zone core (Figure C.8) are consistent with the core being the long-term locus of rupture. The occurrence of off-fault friction melts raises the question of whether the garnet grains used for fragment size analysis reflect temporally and spatially distinct event. If this were the case, then integrating the energy density values across the dynamic damage zone might overestimate U_{sa}. We have no direct evidence to support or refute this, so it remains an additional uncertainty in our estimates.

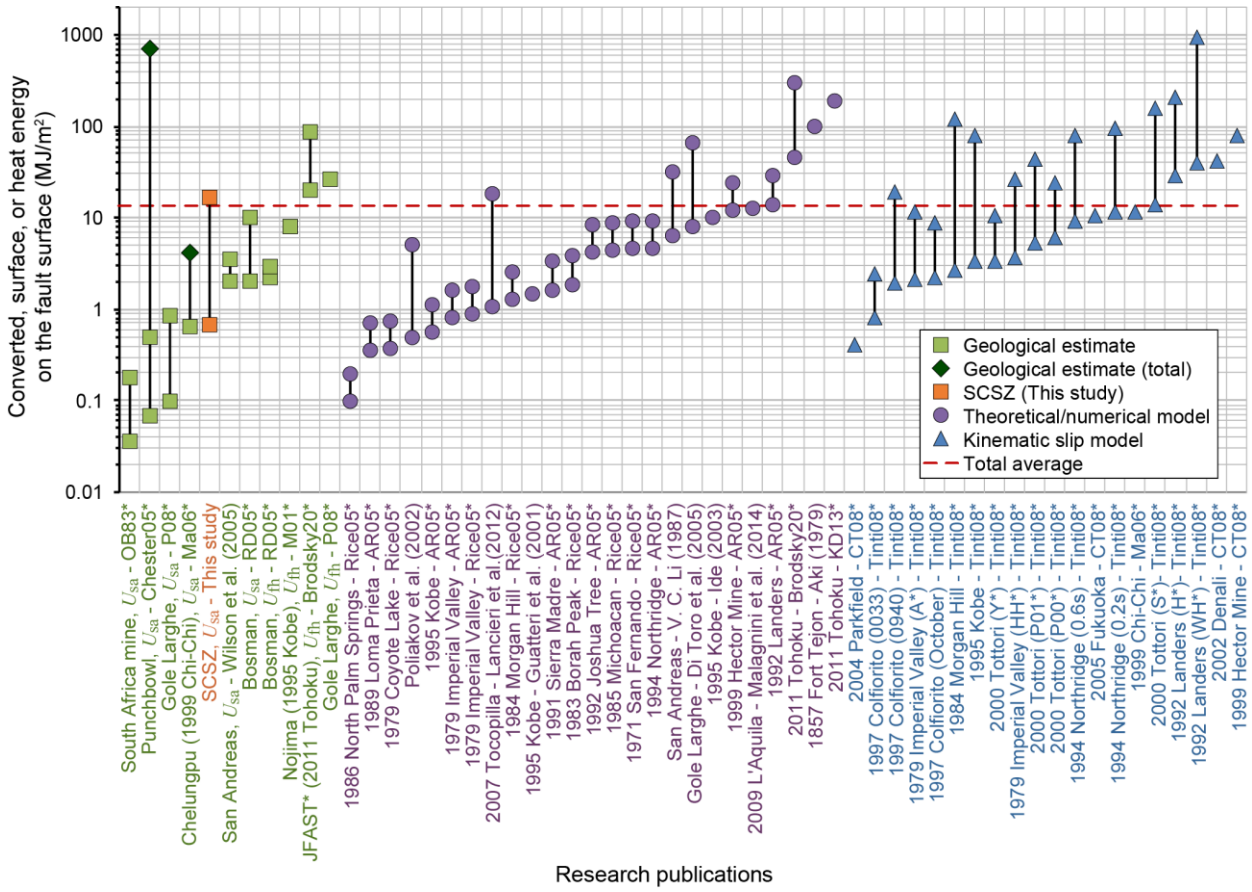

Figure C.13 Comparison of converted, surface, or heat energy estimates, for a single earthquake, from 56 sources including our garnet results (orange squares) for the Sandhill Corner shear zone (SCSZ). See Table C.6. For the geological estimates of Chester et al. (2005) and Ma et al. (2006), we show both their total surface energy estimates (marked by dark green diamonds) and their minimum estimates per earthquake. In addition, for Chester et al. (2005), we add an intermediate estimate that they reported (see Section 6.1). Uncertainties in the number of earthquakes responsible for the surface-energy generation in both studies and limited spatial analysis in Ma et al. (2006) precludes confident assignment of a single-earthquake energy value. The total average (dashed red line) of 13.80 MJ/m^2 is for lower bounds and single estimates only – does not include upper-bound values. *OB83 – Olgaard and Brace (1983); Chester05 – Chester et al. (2005); P08 – Pittarello et al. (2008); Ma06 – Ma et al. (2006); RD05 – Reches and Dewers (2005); M01 – Matsumoto et al. (2001); JFAST – Japan Trench Fast Drilling Project; Brodsky20 – Brodsky et al. (2020); Rice05 – Rice et al. (2005); AR05 – Abercrombie and Rice (2005); KD13 – Kozdon and Dunham (2013); CT08 – Cocco and Tinti (2008); Tinti08 – Tinti et al. (2005, 2008); A – Archuleta's model; Y – Yagi's model; HH – Hartzel and Heaton's model; P01 – Piatanesi's model-01; P00 – Piatanesi's model-00; S – Sekiguchi's model; H – Hernandez et al.'s model; WH – Wald and Heaton's model.

Table C.6 Comparison of fracture surface-area energy per unit fault area (U_{sa}) using fragmented garnet to other published studies of converted non-radiated energy per unit fault area (U_{conv}), frictional heat energy per unit fault area (U_{fh}), or U_{sa}, for a single earthquake with two exceptions[a].

Method	Earthquake (EQ) / Location	Type of converted energy[b]	Converted energy value (MJ/m^2)	Seismic moment, M_0 (10^{18} N·m)	Moment magnitude, M_w[c]	Reference
Geological	Gold mine, South Africa (EQ at Boksburg on September 23, 1970)	U_{sa}	0.037–0.185		2.1[d]	Olgaard & Brace (1983)
Geological	Punchbowl fault, Calif., US	U_{sa}	0.07–700[a]			Chester et al. (2005)
Geological	San Andreas fault (Tejon Pass), Calif., US	U_{sa}	2–3.6			Wilson et al. (2005)
Geological	Bosman fault, South Africa (1997 Hartebeestfontein gold mine EQ)	U_{sa}	2–10		3.7[d]	Reches & Dewers (2005)
Geological	Bosman fault, South Africa (1997 Hartebeestfontein gold mine EQ)	U_{fh}	2.2–3		3.7[d]	Reches & Dewers (2005)
Geological	Gole Larghe fault, Italy	U_{sa}	0.10–0.85			Pittarello et al. (2008)
Geological	Gole Larghe fault, Italy	U_{fh}	27			Pittarello et al. (2008)
Geological	Nojima fault, Japan (1995 Kobe EQ)	U_{fh}	8	24	6.9	Matsumoto et al. (2001) for U_{fh} ; Wald (1996) for M_0
Geological	Chelungpu fault, Taiwan (1999 Chi-Chi EQ)	U_{sa}	0.65–4.3[a]	270	7.6	Ma et al. (2006) for U_{sa} ; Ji et al. (2003) for M_0
Geological	Japan Trench Fast Drilling Project (2011 Tohoku EQ)	U_{fh}	20–86	48,000	9.1	Brodsky er al. (2020) for U_{fh} ; Yue & Lay (2011) for M_0
Geological	**SCSZ[e], Maine, US**	$\boldsymbol{U_{\mathrm{sa}}}$	**0.66–16.25**			**This study**
Theoretical/ Numerical	1991 Sierra Madre EQ, Calif., US	$U_{\mathrm{conv}}/U_{\mathrm{sa}}$	1.66–3.32	0.25	5.5	Abercrombie & Rice (2005)
Theoretical/ Numerical	1979 Coyote Lake EQ, Calif., US	$U_{\mathrm{conv}}/U_{\mathrm{sa}}$	0.38–0.76	0.35	5.6	Rice et al. (2005)
Theoretical/ Numerical	1986 North Palm Springs EQ, Calif., US	$U_{\mathrm{conv}}/U_{\mathrm{sa}}$	0.10–0.20	1.8	6.1	Rice et al. (2005)
Theoretical/ Numerical	(Major earthquakes)	$U_{\mathrm{conv}}/U_{\mathrm{sa}}$	0.5–5			Poliakov et al. (2002)
Theoretical/ Numerical	1992 Joshua Tree EQ (main shock), Calif., US	$U_{\mathrm{conv}}/U_{\mathrm{sa}}$	4.24–8.48	1.9	6.1	Abercrombie & Rice (2005)
Theoretical/ Numerical	2009 L'Aquila EQ (main shock), Italy	$U_{\mathrm{conv}}/U_{\mathrm{sa}}$	12.9	1.95	6.1	Malagnini et al. (2014)
Theoretical/ Numerical	1984 Morgan Hill EQ, Calif., US	$U_{\mathrm{conv}}/U_{\mathrm{sa}}$	1.3–2.6	2.1	6.1	Rice et al. (2005)
Theoretical/ Numerical	1979 Imperial Valley EQ, Calif., US	$U_{\mathrm{conv}}/U_{\mathrm{sa}}$	0.88–1.76	5	6.4	Rice et al. (2005)
Theoretical/ Numerical	1979 Imperial Valley EQ, Calif., US	$U_{\mathrm{conv}}/U_{\mathrm{sa}}$	0.82–1.64	6.7	6.5	Abercrombie & Rice (2005)
Theoretical/ Numerical	1971 San Fernando EQ, Calif., US	$U_{\mathrm{conv}}/U_{\mathrm{sa}}$	4.6–9.2	7	6.5	Rice et al. (2005)
Theoretical/ Numerical	1994 Northridge EQ, Calif., US	$U_{\mathrm{conv}}/U_{\mathrm{sa}}$	4.66–9.32	13	6.7	Abercrombie & Rice (2005)
Theoretical/ Numerical	1983 Borah Peak EQ, Idaho, US	$U_{\mathrm{conv}}/U_{\mathrm{sa}}$	1.9–3.8	23	6.8	Rice et al. (2005)
Theoretical/ Numerical	1995 Kobe EQ, Japan	$U_{\mathrm{conv}}/U_{\mathrm{sa}}$	0.57–1.14	23	6.8	Abercrombie & Rice (2005)

Table C.6 (Continued)

Method	Earthquake (EQ) / Location	Type of converted energy[b]	Converted energy value (MJ/m^2)	Seismic moment, M_0 (10^{18} N·m)	Moment magnitude, M_w[c]	Reference
Theoretical/ Numerical	1995 Kobe EQ, Japan	U_{conv}/U_{sa}	1.5	24	6.9	Guatteri et al. (2001) for U_{conv}/U_{sa}; Wald (1996) for M_0
Theoretical/ Numerical	1995 Kobe EQ, Japan	U_{conv}/U_{sa}	10	24	6.9	Ide (2003) for U_{conv}/U_{sa}; Wald (1996) for M_0
Theoretical/ Numerical	1989 Loma Prieta EQ, Calif., US	U_{conv}/U_{sa}	0.36–0.71	31	6.9	Abercrombie & Rice (2005)
Theoretical/ Numerical	San Andreas fault (Parkfield), Calif., US	U_{conv}/U_{sa}	6.3–32			Li (1987)
Theoretical/ Numerical	Gole Larghe fault, Italy	U_{conv}/U_{sa}	8–67			Di Toro et al. (2005)
Theoretical/ Numerical	1999 Hector Mine EQ, Calif., US	U_{conv}/U_{sa}	12.19–24.37	63	7.1	Abercrombie & Rice (2005)
Theoretical/ Numerical	1992 Landers EQ, Calif., US	U_{conv}/U_{sa}	14.25–28.50	80	7.2	Abercrombie & Rice (2005)
Theoretical/ Numerical	2007 Tocopilla EQ, Chile (main shock)	U_{conv}/U_{sa}	1.1–18.6[f]	368	7.6	Lancieri et al. (2012) for U_{conv}/U_{sa}; Peyrat et al. (2010) for M_0
Theoretical/ Numerical	1857 Fort Tejon EQ, Calif., US	U_{conv}/U_{sa}	100	870	7.9	Aki (1979) for U_{conv}/U_{sa}; Sieh (1978) for M_0
Theoretical/ Numerical	1985 Michoacan EQ, Mexico	U_{conv}/U_{sa}	4.4–8.8	1500	8.0	Rice et al. (2005)
Theoretical/ Numerical	2011 Tohoku EQ, Japan	U_{conv}/U_{sa}	46–300	48,000	9.1	Brodsky er al. (2020) for U_{conv}/U_{sa}; Yue & Lay (2011) for M_0
Theoretical/ Numerical	2011 Tohoku EQ, Japan	U_{conv}/U_{sa}	190	48,000	9.1	Kozdon & Dunham (2013) for U_{conv}/U_{sa}; Yue & Lay (2011) for M_0
Kinematic slip model	1997 Colfiorito EQ (0033 UTC 26 September), Italy	U_{conv}/U_{sa}	0.80–2.40	0.4381	5.7	Tinti et al. (2005, 2008)
Kinematic slip model	1997 Colfiorito EQ (1523 UTC 14 October), Italy	U_{conv}/U_{sa}	2.22–8.76	0.6478	5.8	Tinti et al. (2005, 2008)
Kinematic slip model	1997 Colfiorito EQ (0940 UTC 26 September), Italy	U_{conv}/U_{sa}	1.94–19.16	1.039	5.9	Tinti et al. (2005, 2008)
Kinematic slip model	2004 Parkfield EQ, Calif., US	U_{conv}/U_{sa}	0.42	1.08	6.0	Cocco & Tinti (2008)
Kinematic slip model	1984 Morgan Hill EQ, Calif., US	U_{conv}/U_{sa}	2.72–121.52	2.62	6.2	Tinti et al. (2005, 2008)
Kinematic slip model	1979 Imperial Valley EQ (Archuleta's model), Calif., US	U_{conv}/U_{sa}	2.12–11.64	6.4	6.5	Tinti et al. (2005, 2008)
Kinematic slip model	1979 Imperial Valley EQ (Hartzel & Heaton's model; T_{box}[g] = 0.3s), Calif., US	U_{conv}/U_{sa}	3.64–26.34	8.64	6.6	Tinti et al. (2005, 2008)
Kinematic slip model	2005 Fukuoka EQ, Japan	U_{conv}/U_{sa}	10.68	11.5	6.6	Cocco & Tinti (2008)
Kinematic slip model	2000 Tottori EQ (Yagi's model), Japan	U_{conv}/U_{sa}	3.38–10.66	11	6.6	Tinti et al. (2005, 2008)
Kinematic slip model	2000 Tottori EQ (Piatanesi's model-00), Japan	U_{conv}/U_{sa}	6.04–24.22	11.58	6.6	Tinti et al. (2005, 2008)
Kinematic slip model	2000 Tottori EQ (Piatanesi's model-01), Japan	U_{conv}/U_{sa}	5.46–44.62	11.952	6.6	Tinti et al. (2005, 2008)

Table C.6 (Continued)

Method	Earthquake (EQ) / Location	Type of converted energy[b]	Converted energy value (MJ/m^2)	Seismic moment, M_0 (10^{18} N·m)	Moment magnitude, M_w[c]	Reference
Kinematic slip model	2000 Tottori EQ (Sekiguchi's model), Japan	U_{conv}/U_{sa}	14.26–161.04	19	6.8	Tinti et al. (2005, 2008)
Kinematic slip model	1994 Northridge EQ (T_{box}[g] = 0.6s), Calif., US	U_{conv}/U_{sa}	9.22–80.00	12.2	6.7	Tinti et al. (2005, 2008)
Kinematic slip model	1994 Northridge EQ (T_{box}[g] = 0.2s), Calif., US	U_{conv}/U_{sa}	11.5–95.9	12.2	6.7	Tinti et al. (2005, 2008)
Kinematic slip model	1995 Kobe EQ, Japan	U_{conv}/U_{sa}	3.32–79.50	24.4	6.9	Tinti et al. (2005, 2008)
Kinematic slip model	1999 Hector Mine EQ, Calif., US	U_{conv}/U_{sa}	81.2	67	7.1	Cocco & Tinti (2008)
Kinematic slip model	1992 Landers EQ (Wald & Heaton's model), Calif., US	U_{conv}/U_{sa}	40.52–947.72	92.6	7.2	Tinti et al. (2005, 2008)
Kinematic slip model	1992 Landers EQ (Hernandez et al.'s model), Calif., US	U_{conv}/U_{sa}	29.14–209.68	102	7.3	Tinti et al. (2005, 2008)
Kinematic slip model	1999 Chi-Chi EQ, Taiwan	U_{conv}/U_{sa}	11.6	270	7.6	Ma et al. (2006) for U_{conv}/U_{sa}; Ji et al. (2003) for M_0
Kinematic slip model	2002 Denali EQ, Alaska, US	U_{conv}/U_{sa}	41.4	757	7.8	Cocco & Tinti (2008)

[a]Two exceptions include total U_{sa} of 700 MJ/m^2 for the Punchbowl fault (Chester et al., 2005) and total U_{sa} of 4.3 MJ/m^2 for the Chelungpu fault (1999 Chi-Chi EQ; Ma et al., 2006). All the other estimates are for a single earthquake.

[b]The type of converted energy includes U_{conv}, U_{sa}, and U_{fh}. $U_{conv} = U_{sa} + U_{fh}$; see Equation (C1) in the text. We indicate U_{conv}/U_{sa} for the theoretical, numerical, and kinematic slip model owing to the different definitions of energy in these studies (e.g., fracture energy versus breakdown work) and how off-fault damage is treated.

[c]$M_w = \frac{2}{3}(\log M_0 - 9.1) \approx \frac{2}{3}\log M_0 - 6.07$ where M_0 (N·m) is seismic moment (Hanks and Kanamori, 1979; Kanamori and Brodsky, 2004).

[d]This magnitude is on the Richter scale (local magnitude M_L).

[e]SCSZ, Sandhill Corner shear zone.

[f]This range of the converted energy for 2007 Tocopilla EQ incorporates both Brune's spectral model (Brune, 1970; Lancieri et al., 2012) and the Abercrombie and Rice (2005) formulation with uncertainties (see Figure 10 of Lancieri et al., 2012).

[g]T_{box} denotes the duration of the box car (rectangular) function, or the running mean, which is used in smoothing a slip velocity time function (see Tinti et al., 2005).

C.8.2. Sources of Off-Fault Damage

The obvious spatial association of off-fault damage gradients relative to seismogenic fault cores combined with experimental, theoretical, and numerical results has led to a general view that this damage is largely coseismic in origin (Figure C.1). For damage well off the principal slip surface, this means stress waves from the rupture front and rough/complex slipping surface(s) with large enough energy content to cause fracturing and fragmentation. These high-energy stress waves may require unusually high frequencies and amplitudes to cause severe local damage (e.g., Uenishi, 2021). Potential sources of such stress waves include: (a) the rupture front where elastic strain energy is converted to the fracture/breakdown energy needed to advance the rupture (e.g., Madariaga, 1977; Kostrov and Das, 1988; Andrews, 2005; Rice et al., 2005; Xu et al., 2012a, 2012b; Okubo et al., 2019); (b) constructive coalescence of shear waves into a coherent Mach front during supershear rupture (e.g., Bernard and Baumont, 2005; Bhat et al., 2007; Dunham, 2007; Doan and Gary, 2009; Andrews, 2010; Yuan et al., 2011; Bruhat et al., 2016; Shlomai et al., 2020a); (c) sliding on a rough fault surface (e.g., Kostrov, 1974; Chester and Chester, 2000; Dieterich and Smith, 2009; Sagy and Brodsky, 2009; Griffith et al., 2010; Dunham et al., 2011; Shi and Day, 2013; Goebel et al., 2014; Neilsen et al., 2016; Allam et al., 2019; Okubo et al., 2019, 2020; Withers et al., 2019); (d) rapid acceleration and deceleration of the rupture front (e.g., Madariaga, 1977; Vallée et al., 2008; Thomas et al., 2017), possibly caused by head waves in strongly damaged fault zones (e.g., Huang et al, 2014a; Huang et al., 2016); (e) complex rupture styles and supershear transitions related to the degree of off-fault material heterogeneity (e.g., Ma and Elbanna, 2015; Albertini and Kammer, 2017) or fault roughness (Bruhat et al., 2016); (f) dynamic reduction of fault-normal compressive stress (e.g., Brune et al., 1993; Brune, 2001; Ben-Zion and Huang, 2002; Reches and Dewers, 2005), possibly owing to propagation of a self-healing slip-pulse (e.g., Heaton, 1990; Ben-Zion and Shi, 2005; Xu et al., 2012a, 2012b; Xu and Ben-Zion, 2017 Shlomai et al., 2020b, 2021;); (g) dynamic displacements and velocity oscillations associated with rapidly changing elastic stiffness of rocks in the process of becoming damaged

(Julian et al., 1998; Thomas et al., 2017; Thomas and Bhat, 2018; Petley-Ragan et al., 2019); and (h) high-frequency stress waves generated by elastic collisions at a variety of scales related to fault-zone structure (e.g., Tsai and Hirth, 2020).

The work of Xia et al. (2008), Doan and Gary (2009), Yuan et al. (2011), Aben et al. (2016), and Barber and Griffith (2017) suggests that intense fragmentation of intact rock requires local compressional strain rates greater than ~150–1500 s^{-1} depending on rock type and confining pressure. In contrast, Griffith et al. (2018) have shown that fragmentation of intact rock may occur at much lower stresses and strain rates if macroscale tension is achieved during rupture (e.g., Xu and Ben-Zion, 2017). Barber and Griffith (2017) have shown in weakly confined dynamic compression experiments that Arkansas Novaculite produces ~86 times more surface area per unit mass (~6.0 m^2g^{-1}) than Westerly Granite (~0.07 m^2g^{-1}), highlighting the important role played by material properties and microstructure. Several experimental studies have shown that rapid dynamic stress cycling reduces dynamic strength and more easily leads to intense fragmentation (Badge and Petroš, 2005; Braunagel and Griffith, 2019; Li et al., 2021; Liu and Zhao, 2021). Additionally, material contrast across a fault may strongly amplify dynamic effects (e.g., Ben-Zion and Rice, 1997; Shi et al., 2008; Thomas et al., 2017; Shlomai et al., 2020b, 2021), and the background stress orientation can markedly influence the spatial scale of the damage zone (Xu et al., 2012a, 2012b). With notable exceptions (e.g., Mckay et al., 2019), current theoretical and numerical models treat the on- and off-fault volume as elastically isotropic; adding realistic anisotropic elastic properties would likely impact model results, and we address this point further in Section 6.3.

A key characteristic of our fragmented garnet grains is preservation of original crystal shape where post-fragmentation viscous extension of the fragments is minor (e.g., Figure C.7a). The microfractures in these garnet grains typically show little or no shear displacement, lack a strong preferred orientation, commonly meet at approximately right angles, and the fragments are quite angular with planar faces (Figures C.7 and C.6) all of which favor tensile failure (Sammis et al., 1987; Sammis and Ben-Zion, 2008). These same characteristics are observed for fragmented garnet, feldspar, diopside and other minerals in deeply exhumed damage zones (Trepmann and Stöckhert, 2002; Pittarello et al., 2008; Austrheim et al.,

2017; Sullivan and Peterman, 2017; Petley-Regan et al., 2018, 2019; Hawemann et al., 2019; Jamtveit et al., 2019; Campbell et al., 2020), and for quartz, feldspar and other minerals in damage zones around active, large-displacement, strike-slip faults (e.g., Dor et al., 2006, 2009; Rockwell et al., 2009; Wechsler et al., 2009; Mitchell et al., 2011; Rempe et al., 2013; Muto et al., 2015), and provide an explanation for dilatant isotropic radiation which is particularly prevalent in the near field (e.g., Ben-Zion and Ampuero, 2009; Cheng et al., 2021). In contrast, Dor et al. (2009) noted Hertzian-type fracturing in fragmented sandstone but not crystalline rocks, and they attributed this to compressional interaction of neighboring grains. These observations raise the important question of whether such fragmentation requires a macroscale tensile dynamic stress field (e.g., Rockwell et al., 2009; Lin and Yamashita, 2013; Aben et al., 2017a; Thomas et al., 2017; Xu and Ben-Zion, 2017; Griffith et al., 2018; Okubo et al., 2019).

Tensile stresses at various scales are possible during rupture. For example, Brune et al. (1993) and Brune (2001) argued for vibrations during rupture leading to cycles of dynamic fault-normal stress reduction which could potentially lead to macroscale tension. Xu and Ben-Zion (2017) have shown that subshear and supershear ruptures at 3 km depth along strike-slip faults separating rocks with different elastic stiffnesses can generate near-isotropic tensile stresses large enough to cause damage at >100 m from the rupture surface. In contrast, Thomas et al. (2017) and Thomas and Bhat (2018) have modeled formation of Mode I fractures as wing cracks associated with activation of shear fractures. Sammis et al. (1987) and Rice et al. (2005) have noted that tensile failure can also form in triaxial compression by the stress chains that transmit forces in granular media (the confined comminution model of Sammis et al., 1987). As noted above, Dor et al. (2009) attributed Hertzian-type fracturing in fragmented sandstone to this type of process. The confined comminution model requires that grains be in contact with one another to establish force chains. This explanation cannot be directly applied to the fragmented garnet grains documented by B. R. Song et al. (2020) because they are surrounded by a matrix composed of grains and fragments of different minerals (e.g., quartz, feldspar and mica) that are typically smaller in size by one or more orders of magnitude (see Figure 3 of B. R. Song et al., 2020). Thus, the garnet grains represent relatively large, isolated heterogeneities compared to the surrounding matrix. The equivalent tensile strain rates that we

estimated in the dynamic portion of the damage zone (Figure C.10b) are significantly higher (~100 times) than those achieved in split-Hopkinson pressure bar experiments aimed at investigating radial isotropic tensile stresses as a cause of fragmentation (Griffith et al., 2018), but the garnet fragment sizes in the damage zone are significantly smaller (~100 times) than the experimental fragments as well indicating higher energy or multiple events. More detailed geological studies of exhumed seismogenic faults and shear zones are required to better understand the causes of extreme off-fault fragmentation, and the results of these studies can be used to help inform experimental, theoretical, and numerical investigations into the same phenomena.

C.8.3. Elastic Anisotropy, Stress Amplification, and Failure

As noted earlier, extensive off-fault damage appears to be caused primarily by high-energy stress waves emanating from the rupture front, secondary off-fault rupture splays, and slip on rough/complex fault surfaces. Although shearing and comminution are typically isolated to rocks near principal slip surfaces, more distant off-fault damage generally expresses as Mode I microfractures at very small macroscale strains. The question arises as to whether these Mode I microfractures require macroscale tension in the source volume, constrained comminution during compression, wing-crack formation during compression, or a combination of these mechanisms. Here we introduce another possible mechanism by showing that grain-scale tensile stresses large enough for tensile microfracturing can arise simply from the interactions of anisotropic mineral grains in a variety of macroscale stress states.

Rocks are composed of individual anisotropic mineral grains, and the elastic interactions of these grains during the passage of stress waves would lead to marked heterogeneity in stress magnitudes and distributions. As an example of how elastic anisotropy impacts local stresses, Figure C.14 shows maximum principal stress σ_{1P} for a real microstructure of schist (Naus-Thijssen et al., 2011) under macroscale loading approximating that adjacent to the San Andreas fault at 7.5 km depth (stress tensor from Vel et al., 2016). The rock microstructure was captured using EBSD techniques (see Johnson et al., 2021a, for details), and the mechanical analysis employed the ThermoElastic and Seismic Analysis (TESA) Toolbox (Vel et al.,

2016; Cook et al., 2018; Johnson et al., 2021a), with each grain assigned its stiffness tensor in the crystal coordinate reference frame. All calculations are 3D with the 2D microstructure extended into the third dimension. The number of grains in the microstructure is 238 and the ratio of finite elements to grains is 288. Thus, we classify our microstructure as a representative volume element in the sense that analyzing a larger area would not significantly change our results (see Appendix A of Johnson et al., 2021a).

Figure C.14a shows a phase map of the chosen microstructure. Figure C.14b shows the state of stress (compression is negative) for a volume of rock near, but not within, the San Andreas fault. Figure C.14c shows grain-scale values of σ_{1P} under the macroscale loading condition (SAF), and Figures C.14d and e show the same for an instantaneous normal stress (σ_{22}) increase of 400 MPa (i.e., −360 + 400 = 40 MPa of tension) normal to the fault, and an instantaneous shear stress (σ_{12}) increase of 200 MPa (90 + 200 = 290 MPa) parallel to the fault, respectively. Figure C.14f shows histograms of σ_{1P} for all quadrature points in the finite element mesh for the macroscale loading (SAF) and instantaneous fault-normal (σ_{22}) stress increases of 100, 200, 300 and 400 MPa. Figure C.14g shows the same for instantaneous fault-parallel shear stress (σ_{12}) increases of 50, 100, 150 and 200 MPa. Figures C.14f and g show what percentage of the quadrature points in the finite element mesh instantaneously exceed quasistatic tensile strength thresholds of 10 and 50 MPa (e.g., Mardon et al., 1990; You, 2015; Lan et al., 2019), and a dynamic tensile strength threshold of 100 MPa (e.g., Griffith et al., 2018). The results in Figures C.14f and g show that the percentage of quadrature points exceeding the tensile strength thresholds increases with increasing σ_{22} and σ_{12}. These are macroscale tensile strength thresholds for macroscopic tensile failure, so they are significant overestimates of the tensile stresses required for the development and growth of Mode I microfractures (e.g., Hoek and Martin, 2014).

Our work (e.g., Figure C.14; Vel et al., 2016; Johnson et al., 2021a) shows that grain-scale stresses are highly heterogeneous in magnitude and spatial distribution in polymineralic rocks owing to anisotropic grain interactions. In this way, pervasive tensile microfracturing can occur in dynamic 3D compression

without appealing strictly to force-chain or wing-crack mechanisms. Such stress amplification may also be important for earthquake nucleation and the failure of relatively strong rock patches/asperities required to initiate and advance the rupture (e.g., Dresen et al., 2020).

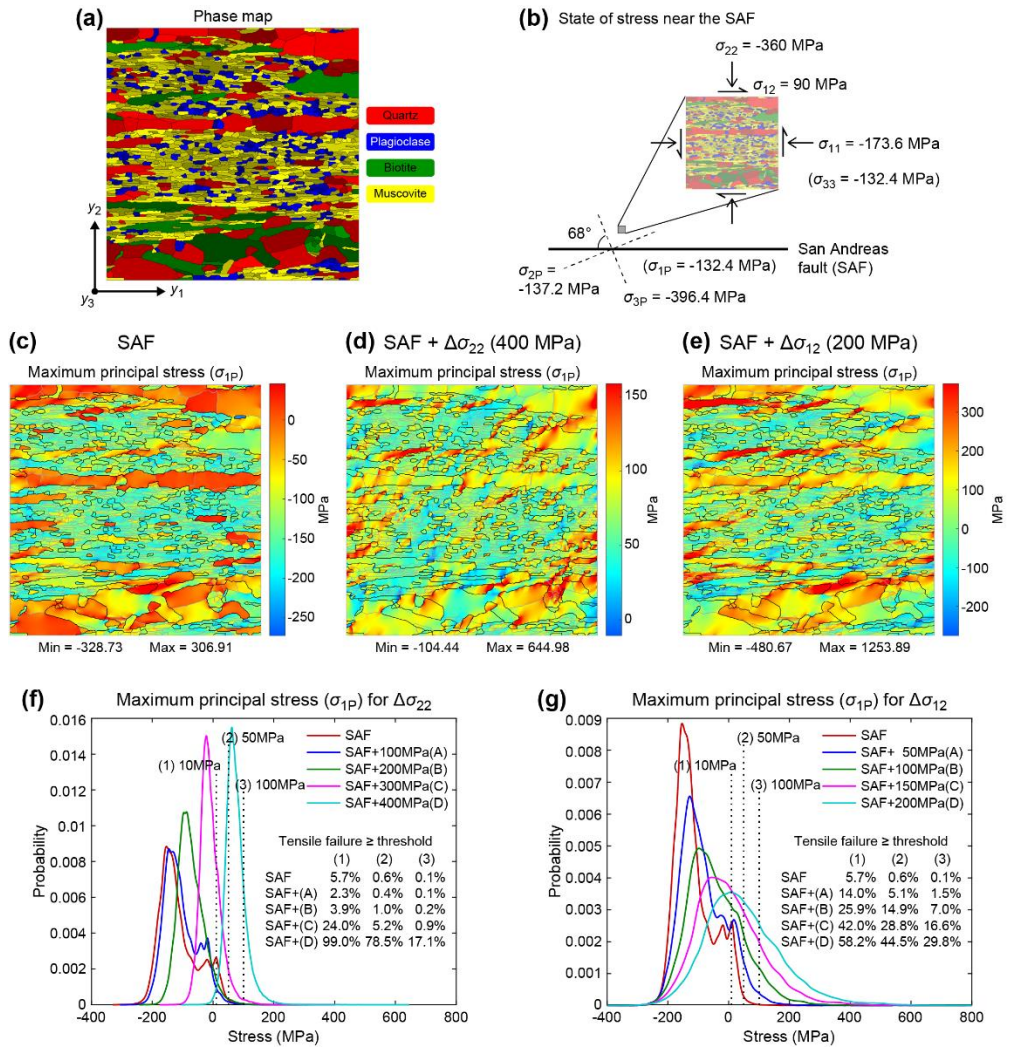

Figure C.14 Impact of elastic anisotropy on grain-scale stresses. (a) Phase map with smoothed grain boundaries (as a result of meshing) for a schist (Naus-Thijssen et al., 2011) derived from electron backscatter diffraction and the TESA Toolbox. Different shades of the same colors indicate differently oriented grains of the same phase. The analysis coordinate system (y_1-y_2-y_3) is also displayed. (b) State of stress at 7.5 km depth near the San Andreas fault (SAF) applied to the schist. Nonzero macroscale stress components are displayed, noting that all three macroscale principal stresses (σ_{1P}, σ_{2P} and σ_{3P}) are compressive (compression is negative). See Vel et al., (2016) for the macroscale stress tensor. (c) Maximum principal stress (σ_{1P}; tension is positive) in MPa at the SAF macroscale stress loading. (d) Maximum principal stress for a 400 MPa stress increase normal to the fault ($\Delta\sigma_{22}$ = 400 MPa). (e) Maximum principal stress for a 200 MPa shear stress increase ($\Delta\sigma_{12}$ = 200 MPa). (f) Histograms showing the distributions of maximum principal stress σ_{1P} for $\Delta\sigma_{22}$ = 100, 200, 300, and 400 MPa. (g) Histograms showing the distributions of maximum principal stress σ_{1P} for $\Delta\sigma_{12}$ = 50, 100, 150, and 200 MPa. The vertical dotted lines in (f) and (g) represent tensile strength thresholds of 10, 50 and 100 MPa for reference. Tensile failure percentage in the histogram plots is calculated by counting the number of analysis points that exceed the tensile strength threshold. Note the increases in tensile failure in the perturbed conditions compared to the SAF stress loading and the wide range of σ_{1P} values in the microstructure owing to the interactions of the elastically anisotropic minerals. The grain-scale stresses were calculated using the TESA Toolbox and the elastic properties of α-quartz (Ohno et al., 2006), plagioclase (An_{25}; Brown et al., 2016), biotite (Aleksandrov and Ryzhova, 1961), and muscovite (Vaughan and Guggenheim, 1986).

C.9. Appendix Summary and Conclusions

- We use garnet fragment size data to estimate coseismic surface-area energy density distributions across the ~105 m-wide dynamic damage zone of the Sandhill Corner shear zone and integrate the energy density to estimate the fracture surface-area energy per unit fault area. We also apply physics-based fragmentation theory to the fragment size data to estimate equivalent tensile strain rates associated with the fragmentation.
- Calculated surface-area energy densities U_s for a single earthquake across the dynamic damage zone range from 2.87×10^3 to 2.72×10^5 J/m^3. Integrating over the width of the dynamic damage zone gives fracture surface-area energy per unit fault area U_{sa} ranging from 6.63×10^5 to 1.63×10^7 J/m^2. This range in U_{sa} overlaps favorably with geological, theoretical, numerical, and kinematic slip-model estimates for earthquakes characterized by seismic moments greater than ~10^{17} N·m. Calculated equivalent tensile strain rates $\dot{\varepsilon}$ range from 5.42×10^2 to 1.04×10^4 s^{-1} depending on the assumed microfracture velocity v_c, and these are broadly compatible with theoretical, numerical, and experimental estimates.
- Geological estimates of heat and surface energy in coseismically fragmented rocks are few in number and are affected by uncertainties regarding: (1) number and relative timing of events responsible for the estimated surface energy; (2) heterogeneity of structures and microstructures in the damage zone; (3) degree of fault-rock healing/sealing after each event; (4) spatial resolution and other limitations imposed by methods for determining fragment size distributions; and (5) relationships among *D*-values, energies and strain rates, and the interpretation of *D*-values that result from multiple events. Despite these limitations, geological estimates provide an important bridge between the simplified macroscale view of energy consumed/dissipated on a frictional sliding surface and the geological reality of intensely and heterogeneously fractured, fragmented, and pulverized damage zones that can reach 100s of meters in width.

- Additional limitations of our analysis include not having comprehensive data for fragmentation of the rock surrounding the garnet grains. Feldspar grains are intensely fragmented and were rapidly healed/sealed by feldspar and quartz, thus being available for refragmentation. Preliminary analysis of feldspar fragment size distributions and number of overprinting microfracture events using electron backscatter diffraction and cathodoluminescence methods give promising results making one of the most common minerals in the continental crust available for fragment size analysis. Quartz also shows abundant evidence of coseismic brittle failure, but post-failure viscous flow of quartz in the Sandhill Corner shear zone precludes its use in fragment size analysis.
- Much of the literature on the earthquake energy budget points to frictional heat as the most important component of energy consumption/dissipation during an earthquake, but there is little observational basis for this. The tightest constraints we are aware of, and they are few, do not rule out an important contribution from the surface energy associated with on- and off-fault fracture, fragmentation and damage.
- We employ numerical techniques with a natural rock microstructure to show that elastic stresses are strongly amplified by the interactions of elastically anisotropic minerals, and that these interactions can lead to grain-scale tensile stresses exceeding macroscale dynamic and quasistatic tensile strength thresholds even when all macroscale principal stresses are compressional. Incorporating more realistic rock properties into models may better align geological observations and model results, although this may require a multi-scale approach.

C.10. Appendix Acknowledgments and Data

We gratefully acknowledge support from National Science Foundation grants EAR-0820946, EAR-1347087 and EAR-1727090. Correspondences with James Hogan and Hiroo Kanamori were very helpful, and reviews by Simone Papa and Anonymous greatly improved the final manuscript. Data used to produce Figures C.8a and b are available in B. R. Song et al. (2020). The data contained in Tables C.2, C.5 and C.6 are available at Figshare via https://doi.org/10.6084/m9.figshare.16752682.

BIOGRAPHY OF THE AUTHOR

Bo Ra Song was born in Seoul, South Korea. She was raised in the same city and graduated from Yeouido Girl's High School. She attended the Korea University, Seoul, South Korea and graduated in 1998 with a Bachelor's degree in Earth and Environmental Sciences. While teaching Earth Science to high school students, she entered the Geology graduate program at the Korea University and received a Master of Science degree in 2005. Bo Ra Song is a candidate for the Doctor of Philosophy degree in Earth and Climate Sciences from the University of Maine in August 2022.